PACIFIC EARTHQUAKE ENGINEERING
RESEARCH CENTER

Computational Modeling of Progressive Collapse in Reinforced Concrete Frame Structures

Mohamed M. Talaat

and

Khalid M. Mosalam

University of California, Berkeley

PEER 2007/10
MAY 2008

Computational Modeling of Progressive Collapse in Reinforced Concrete Frame Structures

Mohamed M. Talaat

and

Khalid M. Mosalam

Department of Civil and Environmental Engineering
University of California, Berkeley

PEER Report 2007/10
Pacific Earthquake Engineering Research Center
College of Engineering
University of California, Berkeley

May 2008

ABSTRACT

The progressive collapse of structures during severe loading caused by earthquakes, blasts, and other effects causes catastrophic loss of life. Such collapse is typically caused by the inability of the structural system to redistribute its loads following the failure of one or more structural members to carry gravity loads. In reinforced concrete (RC) structures, the loss of gravity load-carrying capacity in columns has been observed to trigger a chain of collapse events. This is especially true for structures built according to older building code provisions and thus possessing non-ductile reinforcement details. The evaluation of the vulnerability of these buildings to collapse in the event of an earthquake, and its expected improvement as a result of applying proposed seismic retrofit measures, e.g., using fiber-reinforced polymer (FRP) composites, is an important prerequisite in policy decisions and emergency preparedness. The objective of this report is to develop simulation tools for progressive collapse assessment.

The methodology of the research presented in this report is divided into the development of simulation tools on the component and system levels. Component-level developments refer to modeling the behavior of seismically deficient RC columns, and establishing criteria for their collapse and removal from the computational finite element (FE) model of the structural system. System-level developments refer to modeling the mechanics of removing a structural element from the FE model during the simulation.

Computational component models are developed and experimentally calibrated for the distribution of confining stresses in fiber-discretized cross sections of RC columns and for the confinement-sensitive constitutive material behavior of three common seismically deficient details: (1) inadequately confined core concrete, (2) buckling-prone longitudinal reinforcement, and (3) insufficiently developed lap-splices. Thus, a pseudo-solid modeling approach is pursued at the higher computational efficiency of uniaxial material models. Cross-section damage indices are formulated by aggregating the effects of hysteretic damage from the constituent fibers according to their respective constitutive models, and used to identify the collapse limit state and to establish removal criteria for the class of RC columns dominated by axial-flexure interaction. An existing analytical model from the literature is used to identify the collapse limit state and to establish removal criteria for the class of RC columns dominated by shear-axial interaction. The

developed computational models are implemented in an extensible form using an object-oriented software framework. The computational models are used to simulate a number of previous experimental studies on as-built and FRP-retrofitted RC columns with seismically deficient details. The results of the simulation exhibit the ability to predict not only the as-built response but also the effects and utility limit of the FRP retrofit.

An analytical formulation is developed for the time-dependent problem of sudden removal of a structural element from a FE model using the principles of dynamic force equilibrium. An automatic element removal algorithm is analytically formulated, computationally implemented, and numerically tested for robustness using an idealized benchmark problem. This formulation is extended to include a simplified account of collision between the collapsed columns and the rest of the structure.

The report concludes by presenting demonstration applications of the developed progressive collapse simulation tools using two test-bed structural systems representing older one- and five-story RC frame buildings partially infilled with unreinforced masonry (URM) walls. The applications include: (1) the deterministic assessment of progressive collapse response (i.e., the interaction between the URM wall and the RC frames, element collapse mode and sequence, the resulting change in system dynamic properties, and the eventual global collapse mechanisms); (2) the analysis of sensitivity in the progressive collapse response in terms of time to collapse and story drift ratios to uncertain structural system parameters and ground motion intensity; and (3) the probabilistic evaluation of the effect of intra-event variability (i.e., site location and building orientation) in ground motion records on the fragility of four limit states in one of the test-bed structures, namely the partial and the complete collapse of both the URM wall and the RC frame structure.

ACKNOWLEDGMENTS

The research conducted in this report was sponsored primarily by the Pacific Earthquake Engineering Research (PEER) Center through the Earthquake Engineering Research Centers Program of the National Science Foundation under award number EEC-9701568. Any opinions, findings, and conclusions or recommendations expressed in this material are those of the authors and do not necessarily reflect those of the funding agencies.

CONTENTS

LIST OF FIGURES

LIST OF TABLES

1 Introduction

1.1 GENERAL

The progressive collapse of building structures is a field of research that has been receiving increasing attention. “Progressive collapse” is defined as a disproportionately large structural failure resulting from a relatively local event such as the failure of a gravity load-carrying structural member and the subsequent inability of the structural system to redistribute the resulting overload through a path that can maintain overall stability and integrity. One major discipline where the ability to simulate and predict the extent of structural collapse is of particular importance is the emerging field of performance-based earthquake engineering (PBEE). PBEE represents a paradigm shift for the earthquake-resistant structural design procedure, from the process of adhering to prescriptive code-based design requirements toward a more holistic approach where an engineered structure has to satisfy a set of performance (functionality, life safety, cost of repair, etc.) benchmarks decided upon by the building’s stakeholders (PEER 1997). The risk of progressive collapse due to the loss of gravity load-carrying capacity during a seismic event is particularly a concern for older structures, designed and detailed prior to the current knowledge about structural response to seismic excitation and the requirements of ductile design. The ability to assess that risk and to quantify the improvements resulting from proposed retrofit measures represents an important decision variable. Policymakers can use this risk evaluation data to make planning decisions, establish priorities, and allocate resources. In addition to assessing the vulnerability of existing structures, progressive collapse analysis can play a significant role in performing tradeoffs between structural design alternatives for new structures and in identifying potential weak links in a proposed structural design from a PBEE perspective.

In the past decade, extensive research has been conducted to understand the behavior of individual structural components during cases of extreme loading in order to identify their

prevalent modes of failure and to establish the corresponding collapse limit states. Of relevance to this report is the work conducted on reinforced concrete (RC) columns with several non-ductile details including deficient shear reinforcement by Elwood (2002), deficient and retrofitted lap splices by Xiao and Ma (1997) and by Ma and Xiao (1999), deficient and retrofitted transverse confinement for core concrete by Sheikh and Yau (2002), and inadequately restrained longitudinal reinforcement by Dhakal and Maekawa (2002a,b). In addition, relevant studies have been conducted on RC frames infilled with unreinforced masonry URM walls (Hashemi and Mosalam 2007), and RC shear walls (Massone and Wallace 2004), as well as other typical building components, in a trend that is likely to continue and further address more complex building components. The results from these studies have often been used either to calibrate phenomenological models or (less successfully) to construct physics-based models that reproduce degrading component response until the collapse limit state is imminent.

Meanwhile, there has been limited research aimed at establishing a conceptual framework for performing analysis of progressively collapsing structures. For example, Kaewkulchai and Williamson (2004) proposes a simple approach based on static condensation of collapsed elements but that redistributes internal forces from collapsed elements as external nodal forces applied at the subsequent time step, an approach that is sensitive to the integration time step of the analysis. In contrast, Powell (2005) follows an energy balance method to characterize the dynamic behavior of a system attempting to reach a new equilibrium configuration following the collapse of a column. However, the integration of computational platforms that can perform progressive collapse analysis in an efficient and reliable manner with calibrated component models that can identify failure mode-specific collapse limit states and establish material-based criteria for removal of collapsed elements has been absent in the literature. Instead, macro-level damage indicators such as dissipated hysteretic energy Kaewkulchai and Williamson (2004) are often used. *The construction of such a computational platform and populating it with a library of increasingly sophisticated component models and relevant collapse limit-state criteria are the ultimate objectives of this report.*

1.2 CONTEXT AND SCOPE

This report is envisioned as a component of a collaborative study program aimed at furthering the understanding of the dynamic structural response in deteriorating collapse-prone structural systems. The collaborative study program, as outlined in Figure 1.1, comprises experimental and analytical phases centering around—but not limited to—a prototype structural system composed of RC frames with and without URM infill wall. The components illustrated in the boxes numbered 1, 2, 4, 5, 6, 10, 14, and 16 in Figure 1.1 are addressed in Hashemi (2007) and focus on experimentally establishing the dynamic structural response data representing the interaction between the RC frames and the URM infill wall, and between the bare and infilled frames being connected by a RC slab. Furthermore, Hashemi (2007) establishes the damage progression in the respective structural members with the objective of calibrating existing computational models—including strut-and-tie (SAT) idealizations—of the test structure for subsequent use in evaluating the uncertainties involved in assessing the structural safety of this type of structure using the techniques of structural reliability. The components illustrated in the boxes numbered 3, 7, 11, 12, 17, and 18 in Figure 1.1 are addressed in Elkhoraibi (2007) and focus on developing improved hybrid simulation techniques to enable pseudo-dynamic testing of structures experiencing abrupt variation in stiffness during the seismic response. To achieve that goal, Elkhoraibi (2007 develops testing algorithms employing mixed-variable (displacement and force) control and error-compensating displacement control, with applications to steel, timber, RC, and masonry structures.

This report focuses on the tasks outlined in the boxes numbered 8, 9, 13, and 15 in Figure 1.1. These can be collectively described as the development and implementation of new computational models and procedures to simulate the progression of structural deterioration and collapse under extreme seismic loading. The computational solution strategy proposed in this research for structural systems experiencing possible loss of elements during the analysis is illustrated in Figure 1.2, where italicized text denotes the component models and procedures required in addition to those commonly available in conventional computational platforms for nonlinear time history analysis of structural systems. The computational tools developed in this report can be divided into two groups: component-level and system-level developments.

Component-level modeling aims at developing constitutive models on the material, the cross section, and the element levels, capable of accurately reproducing the response of concrete and reinforcing steel bars in structural elements suffering from deficiencies and/or extreme forces/deformations. *This report focuses on structural collapse resulting from the loss of gravity load-carrying capacity and, in the applications it presents, explicitly considers the role of RC columns, as well as URM infill walls*. The behavior and collapse potential of RC columns is considered in the distinct cases of ductile and non-ductile detailing. Moreover, the report considers columns externally retrofitted by fiber reinforced polymer (FRP) jacketing as an option to mitigate the effect of non-ductile design details. The examples of non-ductile behavior of the RC columns that are considered in this report include the inadequacy and failure of transverse confining reinforcement, buckling of reinforcing bars, inadequately developed lap-splices in reinforcing bars, and premature shear failure. These deficiencies are handled by the development of a confined fiber-discretized cross-section model that takes into account the internal distribution of confining stresses resulting from transverse reinforcement, along with confinement-sensitive uniaxial material constitutive models for concrete, buckling-prone reinforcing steel bars, and lap-spliced reinforcing steel bars. In addition to modeling the cyclically degrading structural response, these component models are coupled with energy- and deformation-based damage models to quantify the spread of material failure into the structural element and identify the element's collapse limit state.

System-level modeling starts from the establishment of criteria for element removal dependent on the material damage information and the element's governing mode of failure. Upon violating any of its removal criteria at the end of an analysis time step, the element is eliminated from the structural model and is considered collapsed. Most importantly, accurate handling of dynamic load redistribution from the collapsed element to the remaining structure is essential in predicting the sequence and extent of system collapse. This is attributed to the path-dependent nature of the collapse process and its sensitivity to initial conditions. Also important is the redistribution of masses and element-associated loads, especially after the collapse of horizontal structural elements such as beams. Elimination of elements and possibly nodes is conducted in a manner that ensures the connectivity and integrity of the remaining structural model and its applied gravity loads. The elimination procedure is performed using an adaptive

time-stepping algorithm to allow the continuation of the analysis in a robust and accurate manner and to minimize the potential of numerical non-convergence unless overall collapse takes place. The developed procedures are employed in applications involving structural collapse in shear-damaged columns, flexure-damaged columns, and axially brittle truss members.

Both component-level and system-level development follow a path starting by the formulation of an analytical model (or procedure) or the adoption of an existing one with possible modifications. Parametric study-style simulations are then performed to reproduce the solutions of benchmark problems or the observations from experiments performed on reduced-scale specimens as a means to calibrate the analytical model parameters and better understand their characteristics and functionality. The analytical models and procedures are then implemented as new classes in an object-oriented computational modeling platform and integrated into a finite element (FE) structural analysis code. The advantages of the new classes in capturing the effect of local detailing on the simulated structural response of RC columns are individually demonstrated using experimental data from several experimental studies. Moreover, the ability of these new classes to interact smoothly in performing progressive collapse analysis of a redundant structural system with deficient columns is illustrated. Finally, the integration of these new classes into a PBEE study to conduct collapse assessment is demonstrated through examples of representative seismically deficient residential structural systems.

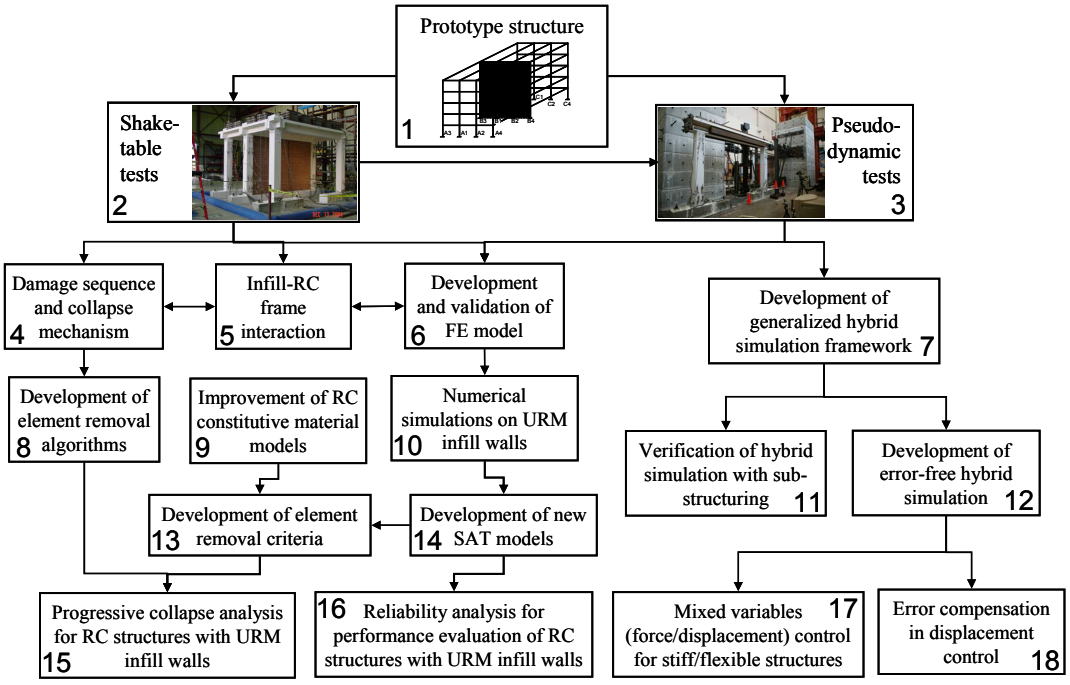

Fig. 1.1 Overview of collaborative study program.

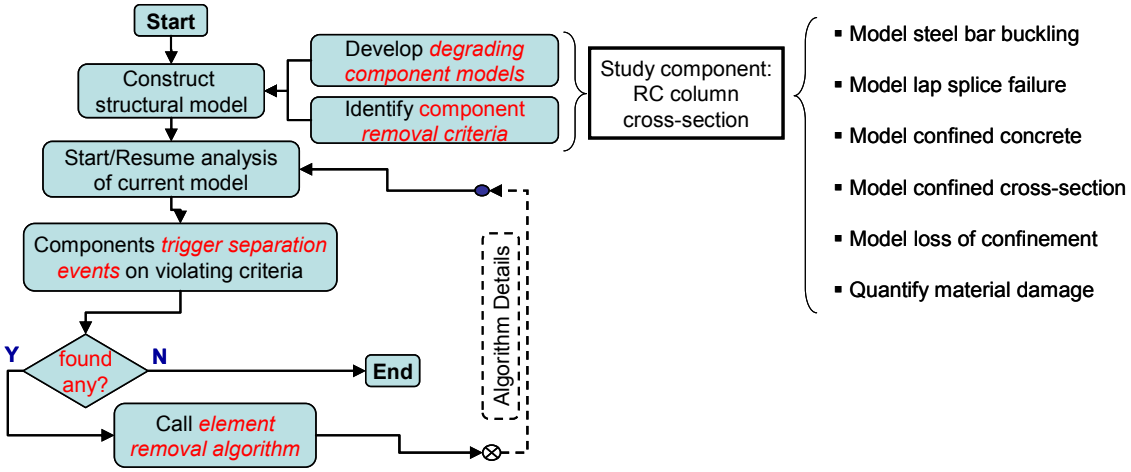

Fig. 1.2 Proposed global solution algorithm for progressive collapse simulation.

1.3 CONTRIBUTIONS

The ultimate objectives of this research are to establish and to validate a framework for conducting progressive collapse analysis of RC framed structures subjected to extreme dynamic loading. To achieve these objectives, this report presents the following main contributions:

- A new constitutive material model for reinforcing steel bars susceptible to buckling. This model accounts for the lateral confining stiffness of transverse ties.
- A constitutive material model for lap-spliced reinforcing steel bars, constructed by assembling and modifying previously developed models for monotonic response under prescribed confinement, hysteretic response, and hysteretic strength and stiffness degradation.
- A constitutive material model for passively confined concrete, constructed by assembling and modifying previously developed models for monotonic response under variable confinement, hysteretic response under prescribed confinement, tension softening, and hysteretic strength degradation.
- An analytical model for the spatial distribution of confining stresses within a circular RC column cross section based on assumption of a uniform confining jacket and a linear-elastic relationship governing bond-stress at the interface. The resulting distribution can be approximated using a simple polynomial function for computational efficiency.
- A material-based damage metric for tracking failure propagation and establishing the criteria for reaching the collapse limit state in columns controlled by flexure-axial interaction.
- An algorithm for direct removal of collapsed elements during the analysis of a computational structural model and accounting for load and mass redistribution.
- An implementation of the developed computational models into an extensible and modifiable object-oriented environment that facilitates further development and linkage to a wider set of structural engineering applications.
- An importance ranking of the uncertainty in structural model parameters on the collapse response of the class of five-story RC frame buildings with URM infill walls, developed using deterministic sensitivity analysis.

- An investigation of the effect of site-to-site ground motion record variability (i.e., intra-event variability) on the probability of structural collapse, developed using fragility plots.

1.4 ORGANIZATION

This report is organized into eight chapters and two appendices. Chapter 1 presents the background and motivation for the research, its scope, and its main contributions. It introduces the target computational solution procedure and sets in relative position the various component-level and system-level developments presented henceforth. Chapter 2 presents the analytical formulations developed for the component modeling of uniaxial material response in buckling-prone reinforcing steel bars and deficient lap splices. Chapter 3 presents the analytical formulation developed for the component modeling of confined fiber-discretized cross sections and the uniaxial material response of confined and unconfined concrete. The component models developed in Chapters 2 and 3 are calibrated using comparisons with the measured results obtained from several experimental investigations of individual steel bars, bar-pullout specimens, and concrete cylinders. These comparisons are used to identify typical ranges for model parameter values.

Chapter 4 presents the implementation details of the component models as new classes into an object-oriented computational modeling platform and discusses the relevant aspects of the computational environment. This implementation is carried out within the modeling software OpenSees (open system for earthquake engineering simulation), whose open-source code and user's manual are freely available on the internet (Mazzoni et al. 2004). In Chapter 5, the implemented classes are used to construct FE structural models of several experimentally investigated RC columns, and computationally reproduce the observed global and local responses under cyclic lateral loading. The aims of these simulations are to conduct a macroscopic verification of the implementation procedure and to verify the ability of the developed component models to integrally model structural behavior more complex than that of the simple test specimens used in their individual calibration (as discussed in Chapters 2 and 3), such as the interaction of multiple structural deficiencies in a column cross section and the effects of external FRP retrofit. Furthermore, these simulations are used to demonstrate the

contribution to the accuracy of the modeling process presented by the newly developed component models, and to establish system-dependent guidelines for their use in the modeling process (e.g., choice of type of finite element(s) and numerical integration parameters).

Following the presentation of component-level developments, Chapter 6 outlines the analytical background for the dynamically compatible element removal procedure. In addition, it presents the element removal criteria adopted for the different modes of failure under investigation. It discusses the implementation details for automatically removing an element in the course of an ongoing analysis, and the necessary checks and adjustments to the analyzed structural system to maintain numerical and structural stability as well as physical relevance. Finally, the chapter concludes by presenting a benchmark example of a progressively collapsing trussed-beam structure subjected to seismic excitation. The simulation results validate the implementation of the automatic element removal algorithm and demonstrate the robustness and accuracy of the proposed procedure, while being performed independently of the developed component models discussed in Chapters 2–5 and the removal criteria based on their associated limit states discussed at the end of Chapter 6.

In Chapter 7, the element removal algorithm is employed in the setting of more complex structural systems. In conjunction with the developed component models, the report proceeds to investigate the progressive collapse response in one-story and five-story URM-infilled RC structural systems representative of seismically deficient residential buildings. First, the performance of the element removal procedure is investigated in an application of a one-story structure for which experimental data are available. This offers an opportunity for model interpretation and for establishing a more transparent understanding of the response in the absence of such confounding factors as higher mode effects. Second, the element removal procedure is applied to a multi-story building to quantitatively establish its progressive collapse behavior and sensitivity to uncertainty in unknown system parameters during a major seismic event. Finally, a preliminary probabilistic study using the framework of PBEE is conducted on the one-story structural system to quantitatively assess the effect of intra-event variability (i.e., site location and building orientation) on its probability of collapse.

Chapter 8 presents a summary of this report, lists its major findings, and points out directions for further investigation. Appendix A lists and identifies input parameters for the script

commands necessary to generate progressively collapsing model components and analyses within OpenSees. Appendix B presents the theoretical assumptions and analytical formulations developed for handling the impact by free-falling bodies on a progressively collapsing structure whose results are utilized in the analysis of the benchmark structural system in Chapter 6.

2 Modeling of Column Longitudinal Reinforcement

This chapter deals with constitutive material modeling of reinforcing steel bars in RC columns. Of particular interest is the performance of deficient reinforcing bars due to non-ductile detailing leading to bar buckling in compression and lap-splice failure in tension. Of equal interest is the ability of the developed computational models to account for the anticipated improvement in the structural performance due to the application of local retrofit measures through external confinement of the deficient RC column cross sections. First, a review of the available literature on longitudinal reinforcement modeling with an emphasis on non-ductile details is conducted. Next, an analytical material model for the uniaxial response of steel bars laterally restrained by uniformly spaced transverse reinforcement is developed. The analytical model uses the concept of strain decomposition to solve the large-deformation problem of a buckled reinforcing bar in terms of axial stress-strain response while condensing the transversal and rotational degrees of freedom (DOFs). This model is calibrated by reproducing the experimentally reported behavior from several published investigations of reinforcing steel bars subjected to monotonic and cyclic axial loading. Finally, an analytical material model for the uniaxial response of lap-spliced steel bars is constructed by juxtaposing two analytical models from published literature, namely a model for confinement-sensitive monotonic lap-splice behavior and another model for cyclic bond-slip behavior. Components from both models are jointly utilized and developed further, along with the addition of a hysteretic damage rule. The developed lap-splice model is calibrated by reproducing the experimentally reported behavior from investigations of reinforcing steel bars embedded in concrete and subjected to monotonic and cyclic pull-out loading.

2.1 REVIEW OF PUBLISHED LITERATURE

The literature reviewed in this chapter pertains to the role of longitudinal steel reinforcement as follows:

1. Modeling of yielding and plasticity in steel bars
2. Modeling of buckling in steel bars
3. Modeling of lap-splice and bond-slip behavior in steel bars

The body of literature on these topics is extensive, and this review does not pretend to be inclusive. Rather, only previous work that informs the background of the analytical models and modeling schemes conducted in the current study is reviewed.

2.1.1 Modeling of Yielding and Plasticity in Steel Bars

Reinforcing steel bars generally follow a linear-elastic response until their yielding strain is reached. Following yielding, nonlinear behavior characterized by elongation with little corresponding change in stress is typically observed, followed by a period of hardening up to a peak stress, which is followed by softening and, ultimately, fracture of the bar. The observed hysteretic behavior of the bars cannot be accounted for by isotropic hardening alone, but exhibits the so-called Bauschinger's effect, which is an evidence of kinematic hardening as well (Bauschinger 1886). Accordingly, previous yielding under tensile stress reduces the compressive yielding stress and the corresponding unloading stiffness upon strain increment reversal. Similarly, previous yielding under compressive stress reduces the tensile yielding stress and the corresponding unloading stiffness.

Analytical models for steel bars include the most simple bilinear model where the bar response is idealized by a high-stiffness linear elastic branch prior to yielding and a low-stiffness linear hardening (or perfectly plastic) branch until fracture. Upon strain increment reversal, the higher stiffness is restored until subsequent yielding is detected. This model can be adapted to reproduce both kinematic and isotropic types of hardening. More sophisticated multi-linear plasticity models have also been developed, with independent branches representing the elastic, yielding, hardening, and/or softening phases of the response, together with complex hysteretic rules. Examples of these models can be reviewed in Shames and Cozzarelli (1997). Upon careful

selection of parameters, these models can provide estimates of the stress in the bar throughout a given strain history with acceptable accuracy. However, these models are inaccurate in estimating the bar stiffness throughout the analysis under general loading history with the same accuracy, which plays a significant role in the accuracy of a dynamic analysis and in predicting the structural behavior at the onset and after bar buckling.

Models for steel bar inelastic behavior which include explicitly nonlinear functions and can thus be used with greater accuracy to estimate the bar stiffness at any point along the loading history have been developed as well by several researchers. Early efforts include Mander et al. (1984) and Menegotto and Pinto (1973). The latter model is still widely used in modeling the cyclic behavior of steel bars because it is easy to implement and control using few physically meaningful parameters. It can be complemented by the work of Chang and Mander (1994) for a better representation of the nonlinear monotonic behavior and the yield plateau. Later work by Filippou and Zulfiqar (1990) and Balan et al. (1998) has the advantage of using an invertible stress-strain relationship. It should be stated that most of these analytical models do not explicitly account for low-cycle fatigue and fracture of reinforcing bars. Rather, a limit is imposed on the cyclic response (e.g., the plastic energy dissipation) after which the bar material is assumed to have fractured. Among the widely used damage models in engineering applications the Coffin-Manson metal fatigue equations (Coffin 1962; Manson 1979) have been recently reviewed in Brown and Kunnath (2004) in the context of modeling low-cycle fatigue in reinforcing steel bars.

2.1.2 Modeling of Buckling in Steel Bars

Longitudinal bar buckling has received considerable attention from researchers in the last decade, resulting in different proposed modeling approaches. Experimental investigations were conducted on individual reinforcing bars by several researchers including Monti and Nuti (1992), Rodriguez et al. (1999), Bayrak and Sheikh (2001), and Dhakal and Maekawa (2002b). These experiments established monotonic and cyclic response data for bars with different strengths, slenderness (length to diameter) ratios, and axial load eccentricities. These data led to a number of analytical models to predict the onset of bar buckling and describe post-buckling behavior.

First, attention is given to models that predict the onset of buckling. Rodriguez et al. (1999) assumes that the buckling length is known a priori (e.g., equal to tie spacing) and calculates the critical buckling stress based on the classic Euler's equation of stability and an experimentally calibrated effective length factor to account for the non-ideal boundary conditions. This model tracks the changes in bar stiffness by employing the reduced bar modulus, E_r (Timoshenko and Gere 1961), defined as

$$E_r = \frac{4E_s E_{st}}{\left(\sqrt{E_s} + \sqrt{E_{st}}\right)^2} \tag{2.1}$$

where E_s is the elastic (Young's) modulus of the bar and E_{st} is the tangent modulus of the bar at the current strain level. To compute these moduli, Rodriguez et al. (1999) adopts the mechanical stress-strain relationship proposed by Mander et al. (1984).

Experimental observations from RC column tests demonstrate that bar buckling can occur over multiple transverse tie spacings. Therefore, a variable buckling length as well as the lateral restraining effect of these ties should be explicitly considered in predicting the buckling load. In the unpublished preliminary study of Terenzani et al. (2001) the problem of the longitudinal bar supported by discrete lateral ties is idealized as a beam-column supported on uniformly distributed springs. An energy-minimization approach is then used to determine the effect of the restraining ties on the buckling length and the corresponding critical stress. This approach employs a strong theoretical background, and provides a practical closed-form analytical expression for estimating the buckling length. Certain simplifications are made, such as neglecting the confining effect of the dilating concrete as secondary to that of the transverse reinforcement, and the use of a simple bilinear material law for estimating the stress state of the longitudinal and transverse reinforcement. During the course of the studies presented in this report, a preliminary assessment suggested that the predictive accuracy of this model is sensitive to the choice of idealized tangent modulus and to how adequately it represents the actual bar stiffness at the onset of buckling. The study in Dhakal and Maekawa (2002c) is based on a setup similar to that of Terenzani et al. (2001) assuming a sinusoidal buckled shape function and minimizing the strain energy to calculate the critical load. However, Dhakal and Maekawa (2002c) elects to use discrete springs to model individual ties. This necessitates the use of

iterative procedures to determine the critical number of ties and the corresponding critical stress, which is computationally demanding. In addition, Dhakal and Maekawa (2002c) uses a simplified fracture energy-based approach to predict the compressive stress in steel bars corresponding to spalling of the cover concrete, whose lateral confining effect is neglected. The unpublished study of Terenzani et al. (2001) provides the motivation and background for the analytical developments presented in this report, and will be discussed in full detail in the following section.

In contrast to the above studies, Bayrak and Sheikh (2001) proposes a more complex formulation, which considers the dilation forces imposed by the cover concrete prior to spalling (assumed to be sinusoidally varying in the longitudinal direction) and the resultant forces from the distribution of transverse ties within the cross section. Hence, Bayrak and Sheikh (2001) presents a solution of the longitudinal bar as a beam-column subjected to axial, shear, and bending actions to compute the buckled shape and the deflection at mid-height under a set of idealized end-conditions. While the resulting analytical expression is moderately complex, it is based on an ideal set of assumptions, and its applicability is restricted to the considered geometry and tie configuration. In contrast, Berry and Eberhard (2005) proposes a straightforward empirical expression for the RC column lateral drift ratio at the onset of bar buckling, which incorporates the lateral drift at yield, axial load, cross-section area, concrete strength, transverse reinforcement ratio and strength, and a cross-section shape factor accounting for confinement effectiveness. The statistical analysis included in Berry and Eberhard (2005) employs results from 40 tests of flexure-critical RC columns, and results in a fit with 28% coefficient of variation (COV).

Second, attention is given to models that predict the post-buckling behavior of reinforcing bars. Two distinct approaches exist. The first approach describes the behavior based on the average strain in the neighboring concrete. In this case, the material model is in effect a structural model of the reinforcing bar, and the model parameters need to be calibrated for the bar geometry. Justification for this average strain approach is presented in Bayrak and Sheikh (2001), arguing that while the buckled bar loses its bond with the neighboring concrete, the assumption of sustained bond can be maintained at transverse tie locations at the ends of a buckled bar. After calculating the mid-height lateral deflection of the buckled bar, Bayrak and

Sheikh (2001) resorts to a compiled library of experimental stress-average strain responses of bars subjected to different load eccentricities to define the monotonic post-buckling behavior. This procedure is tedious to implement in a general-purpose FE code, and is therefore further developed in Bae et al. (2005) by using the aforementioned experimental library to define a set of empirical relationships between lateral deflection and axial stress for variable bar diameter and buckling length.

Other published research works which follow the average strain approach include Monti and Nuti (1992), Gomes and Appleton (1997), and Attolico et al. (2000). The original compressive stress-strain relationship of the bar is modified beyond the buckling stress to include a softening branch. Monti and Nuti (1992) uses an empirical four-parameter stress-strain relationship that explicitly includes the slenderness of the bar as well as kinematic and isotropic hardening. In an extension of this research, Attolico et al. (2000) proposes a modification to eliminate the anomaly of stress overshooting during brief unloading-reloading cycles. By assuming a plastic deformation mechanism for buckled bars and using equilibrium of local stresses, Gomes and Appleton (1997) proposes an analytical modification to the Menegotto-Pinto model (1973) to account for the non-uniform distribution of inelastic stresses across the bar cross section, and use it to predict the uniaxial response.

In contrast to the above approach of dealing directly with average strain, Dhakal and Maekawa (2002a,b) use a micro-analytical approach to solve the nonlinear stability problem using local second-order strains of the buckled bar. This is performed to determine the monotonic softening behavior of buckled bars using solid modeling. Based on such simulations, made for a variety of bar geometry and strength configurations, this softening relationship is then parameterized using average strain quantities and included in a FE code. The cyclic behavior rules are adopted from Menegotto and Pinto (1973) after modifying the compressive loading envelope, as well as reducing the axial stiffness of buckled bars upon unloading from a compression stress state.

2.1.3 Modeling of Lap-Splice and Bond-Slip Behavior in Steel Bars

Bond stress between reinforcing steel and neighboring concrete is the mechanism through which the straining actions are transferred along a RC column. In standard fiber section analysis, which relies on the Euler-Bernoulli beam assumption, perfect bond between a reinforcing bar and the neighboring concrete is typically assumed (Spacone et al. 1996a). However, this assumption is violated by steel bars bridging flexural cracks in concrete, deformation in embedded steel bars along their anchoring length, and lap-spliced bars. The transfer of interface shear stresses along a uniaxially loaded bar toward its stress-free end must be accompanied by relative displacements along the interface, i.e., slip. The amount of slip deformation in a RC column is a function of the stress gradient developed along the bar-concrete interface and does not induce stress-generating mechanical strain in the bar. Hence, it results in a more flexible column response than would take place in the absence of slip. Failure of the bond results in a reduced ability to develop stresses in the reinforcing bar and the degradation of the RC column's lateral force capacity, as well as hysteretic pinching and reduction in stiffness and energy-dissipation capacity (Cho and Pincheira 2006).

Several attempts have been made to model the bond-slip mechanisms; Ngo and Scordelis (1967) and Nilson (1971) are pioneering examples. Experimental investigations have been conducted on bars embedded in concrete blocks and exhibiting hysteretic degradation in Viwathanatepa (1979) and a preliminary analytical model proposed. A later study by Eligehausen et al. (1983) proposes a multi-linear constitutive model to describe the hysteretic relationship between bond stress and slip deformation in an anchored bar as a function of the concrete strength, confinement, and interface geometry. Another multi-linear bond-slip constitutive model is proposed in Hawkins et al. (1982) based on measurements of slip in ribbed bars partially embedded in concrete blocks. The bars are loaded within their elastic range and therefore measured displacements can be converted to slip displacements by subtracting the elastic elongation at each stress level. The experimental setup spares the analytical model the need to make assumptions regarding the bond stress distribution along the interface by limiting the bonded length within the concrete blocks to one or few lugs. Hence the measured slip displacements are constant along the bonded length (Hawkins et al. 1982).

In Huang et al. (1996) and Engstrom et al. (1998), experimental pull-out tests are conducted on individual deformed bars located at the centers, edges, and corners of concrete blocks. The experimental observations are used to calibrate a constitutive model for monotonic bond-slip behavior whose parameters depend on the perceived adequacy of confinement, with a nonlinear ascending branch and multi-linear softening. A fully nonlinear relationship is proposed in Xiao and Ma (1997) for monotonic bond-slip behavior, which has the advantage of explicitly incorporating the amount of transverse confinement within the cross section. This latter feature enables the use of the model in applications, including externally retrofitted columns without the need for empirical modifications. A more recent bond-slip model is developed in Lowes et al. (2004) which uses non-local modeling to describe the dependence of the bond strength on the concrete and steel stress states.

The bond model developed in Eligehausen et al. (1983) has been used in several modeling studies. In Monti et al. (1997a,b), this model is used together with a numerical integration scheme based on stress field interpolation to develop a bond-slip element for anchored bars in RC beams. Subsequently, Monti and Spacone (2000) modifies the force-based fiber element developed by Spacone et al. (1996a,b) to take advantage of the bond-slip element by Monti et al. (1997a,b) in modeling RC column behavior. In a similar modeling approach, Ayoub and Filippou (1999) follows a mixed integration scheme—interpolating both stress and slip along the finite element. The modeling efforts mentioned above rely upon re-formulating the bond-slip model in terms of stress-strain quantities in the context of fiber elements by using an adequate localization length that represents the size of the stress transfer region. Next, an equivalent of a strain decomposition scheme is followed, which splits the computed strain in the concrete fiber adjacent to a spliced bar along the stress transfer length between two materials (i.e., reinforcing bar and bond interface) acting in series. After satisfying the equilibrium of stresses in the two materials, according to the constitutive model of each, the cross-section resisting force vector and stiffness matrix are assembled. The choice of a localization length is affected by the numerical integration parameters and the anchoring length. A similar approach is followed in Xiao and Ma (1997) to model the monotonic lateral response of as-built and retrofitted RC columns containing deficient lap-splices, with the localization length being related to the splice length. An improvement on this model is proposed in Binici and Mosalam (2007) by

assuming an admissible linear distribution of bond stresses along the transfer length instead of the original assumption of a constant value in Xiao and Ma (1997). For all the models described in this paragraph, comparisons with experimental results are satisfactory. However, these formulations, while reasonably accounting for the effect of bond-slip occurring along the length of a single column, could not handle bond-slip occurring in joints connecting multiple members, e.g., beam-column joints. Research is currently ongoing in this field (Mitra and Lowes 2007).

In contrast to using strain decomposition, Rubiano-Benavides (1998) proposes the addition of rotational springs at the column end nodes to account for the additional flexibility generated by bond-slip in anchored bars. This relies on a subjective procedure in calibrating the behavior of the added rotational spring. Another study (Cho and Pincheira 2006) uses a local bond-slip model to independently calibrate the backbone moment-rotation envelope of a rotational spring, and then adds multi-linear hysteretic unloading-reloading rules. A more recent and physics-based approach is adopted in Zhao and Sritharan (2007), where the rotational spring being used is composed of a fiber-discretized section that incorporates a bond-slip constitutive material model to explicitly estimate the amount of slip deformation. A more complex formulation can be found in Salem and Maekawa (2004), which follows a three-dimensional (3D) solid modeling approach. This model is highly accurate but is computationally demanding and not suitable for use with fiber elements. The models mentioned above assume that the bond failure mechanism involves shearing of the concrete keys between the deformed bar lugs, and do not explicitly account for bond failure due to splitting of the cover concrete surrounding the steel bar. This latter failure mode has been first investigated in Tepfers (1979). A number of fracture energy-based models have been developed to estimate the bond strength for this failure mode, e.g., Reinhardt and Van der Veen (1992). A comparative study and a deterministic sensitivity analysis of several such models for estimating bond strength due to concrete cover splitting was recently conducted in Talaat and Mosalam (2007)

2.2 ANALYTICAL MODEL FOR BUCKLING-ENABLED STEEL BARS

The proposed uniaxial material model for buckling-enabled steel bars is composed of several components as discussed in the following sections. The first component is the estimation of

critical buckling stress and corresponding buckling length in the presence of transverse ties. The effect of these ties is modeled as a continuous support of uniform, generally nonlinear, stiffness. The second component is the prediction of monotonic post-buckling behavior and softening, which is modeled using a strain decomposition approach. The third component is the prediction of cyclic behavior, which includes accounting for the reduced unloading stiffness of previously buckled bars. The fourth component is estimating hysteretic stress reduction and bar fracture, which is modeled as a low-cycle fatigue phenomenon.

2.2.1 Geometric Setup

The geometric setup and free-body diagram of the buckling-prone longitudinal steel bar encased within a RC column is shown in Figure 2.1, which are similar to those adopted in Terenzani et al. (2001) and Dhakal and Maekawa (2002c). The present model assumes that buckling takes place in the perpendicular direction away from the column cross section in a bar of diameter d_b over a buckling length L_b spanning more than one transverse tie spacing s_t, and that the restraining effect of the transverse ties can be modeled by uniformly distributed nonlinear springs of axial stiffness α_t for each tie. The concrete cover is assumed to spall prior to bar buckling and its restraining effect on the bar is not modeled. The kinematic boundary conditions are assumed such that the bar is prevented from translation or rotation at the beginning and end of the buckling length. The figure shows the free-body diagram of the buckled bar at equilibrium in a deformed configuration with buckling-induced lateral displacement δ_n at mid-height. This results in bending moments M_1 and M_2 as shown, in addition to the axial load P satisfying equilibrium. The stress gradient of the buckling-prone longitudinal steel bar along the buckling length is ignored because in the relevant case of post-yield buckling within a plastic hinge region, the stress along the bar in this region is nearly constant. The inclusion of the stress gradient in the formulation, while offering little advantage, requires an iterative solution of the critical buckling length instead of the closed-form analytical expression derived in Equation (2.10). The buckled shape of the reinforcing bar is assumed to follow an infinite series of harmonic shape function as follows:

$$y(x) = \sum_{n=1}^{\infty} (\delta_n / 2)[1 - \cos(2\pi n x / L_b)] \tag{2.2}$$

which describes the lateral displacement $y(x)$ at location x along the buckling length L_b. Moreover, the bar is assumed to have an initial imperfection (initial deformed shape) that results in an infinitesimal lateral displacement δ_i at mid-height. A series of harmonic functions similar to Equation (2.2) is assumed to describe the initial deformed shape.

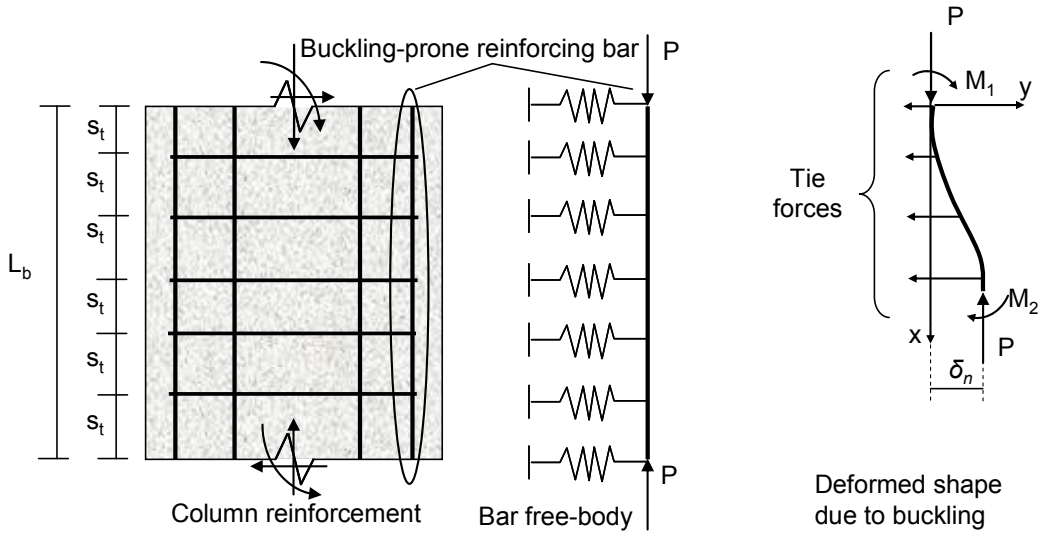

Fig. 2.1 Geometry and free-body diagram of buckling-prone longitudinal bar.

2.2.2 Detecting Onset of Buckling

The elastic strain energy stored in the system due to the increase in axial load on the bar can be evaluated by algebraically adding the contributions from two terms. The first term is derived from the bending moment $M(x)$ and curvature $\phi(x)$ along the buckling length L_b, where $M(x) = E_s J_b \phi(x)$, J_b is the moment of inertia of the bar cross section, and

$$\phi(x) = \frac{\partial^2 y(x)}{\partial x^2} = \sum_{n=1}^{\infty} \frac{2(n\pi)^2}{L_b^2} \delta_n \cos(2\pi n x / L_b) \tag{2.3}$$

Accordingly, the first term in the strain energy equation can be evaluated by making use of the orthogonal characteristic of trigonometric integrals as

$$\Delta U_{bar} = \frac{1}{2}\int_0^{L_b} M\phi\, dx = \frac{E_s J_b}{2}\int_0^{L_b}\left(\frac{\partial^2 y}{\partial x^2}\right)^2 dx = \frac{E_s J_b}{2}\sum_{n=1}^{\infty}\frac{4(n\pi)^4}{L_b^4}\delta_n^2\frac{L_b}{2} = \frac{E_s J_b}{L_b^3}\pi^4\sum_{n=1}^{\infty}n^4\delta_n^2 \tag{2.4}$$

where E_s is the elastic modulus of the bar material (i.e., steel) and the explicit reference to functional dependence on the location (x) has been dropped. For inelastic increments, E_s is replaced by the reduced modulus E_r from Equation (2.1), with E_{st} being the current tangent modulus of the bar material.

The second term in the strain energy equation is derived from the stretching in the uniform springs representing the transverse tie stiffness. Introducing $\beta_t = \alpha_t / s_t$ as the uniform spring stiffness per unit length, and noting that the stretch in a spring at a distance x is given by $y(x)$, the second term in the strain energy equation evaluates to

$$\Delta U_{ties} = \frac{\beta_t}{2}\int_0^{L_b} y^2 dx = \frac{\beta_t}{2}\sum_{n=1}^{\infty}\delta_n^2\frac{3L_b}{8} = \frac{3\beta_t}{16}L_b\sum_{n=1}^{\infty}\delta_n^2 \tag{2.5}$$

Combining Equations (2.4) and (2.5) leads to the elastic strain energy in Equation (2.6). It is worth mentioning that the strain energy stored in the axial deformation of the bar is considered negligible compared with the bending deformation.

$$\Delta U_e = \Delta U_{bar} + \Delta U_{ties} = \sum_{n=1}^{\infty}\frac{E_s J_b}{L_b^3}\left(n^2\pi^2\right)^2\delta_n^2 + \sum_{n=1}^{\infty}\frac{3\beta_t}{16}L_b\,\delta_n^2 \tag{2.6}$$

The external work done by the applied force P is evaluated by computing the resulting change (shortening) in the bar length ΔL. The updated length is evaluated by integration along the deformed shape and can be evaluated using the following first-order expansion:

$$\Delta L = \int_0^{L_b}\left(\sqrt{1+\left(\frac{dy}{dx}\right)^2}-1\right)dx \approx \frac{1}{2}\int_0^{L_b}\left(\frac{dy}{dx}\right)^2 dx = \frac{1}{2}\sum_{n=1}^{\infty}\frac{(\pi\delta_n)^2}{L_b^2}\frac{L_b}{2} = \frac{\pi^2}{4L_b}\sum_{n=1}^{\infty}\delta_n^2 \tag{2.7}$$

Hence, the external work can be evaluated as

$$\Delta W = P\Delta L \approx \frac{P\pi^2}{4L_b}\sum_{n=1}^{\infty}\delta_n^2 \tag{2.8}$$

Equations (2.6) and (2.8) are derived using elastic material properties. However, unless the transverse reinforcement spacing is severely inadequate, longitudinal bar buckling often takes place after yielding and during inelastic bar behavior. This fact can be addressed using

incremental forms of Equations (2.6) and (2.8). Hence, equating the expressions for internal and external work increments, substituting current material properties, and setting $n=1$ for the critical case, leads to the following non-monotonic relationship between the critical buckling load P_{cr} and the buckling length L_{cr}:

$$P_{cr}=\frac{4\pi^2 E_r J_b}{L_{cr}^2}\left(1+\frac{3\beta_t L_{cr}^4}{16\pi^4 E_r J_b}\right) \tag{2.9}$$

which is minimized with respect to L_{cr} to find the minimum critical load $P_{cr,\min}$ and the corresponding critical length $L_{cr,\min}$.

$$L_{cr,\min}=\left\{L_{cr}:\frac{\partial P_{cr}}{\partial L_{cr}}=\frac{-8\pi^2 E_r J_b}{L_{cr}^3}+\frac{3\beta_t L_{cr}}{2\pi^2}=0\right\}=2\pi\sqrt[4]{\frac{E_r J_b}{3\beta_t}}\geq s_t \tag{2.10}$$

$$P_{cr,\min}=\left\{P_{cr}:L_{cr}=L_{cr,\min}\right\}=\begin{cases}\dfrac{8\pi^2 E_r J_b}{L_{cr,\min}^2} & \text{if} \quad L_{cr,\min}>s_t \\ \dfrac{4\pi^2 E_r J_b}{s_t^2} & \text{if} \quad L_{cr,\min}=s_t\end{cases} \tag{2.11}$$

The constraint $L_{cr}\geq s_t$ checks and verifies the initial assumption that the tie spacing is such that buckling takes place over multiple ties. In the case of wider tie spacing, $L_{cr}<s_t$ is inadmissible and buckling is assumed to take place between two adjacent ties ($L_{cr,\min}=s_t$). In this case, the critical buckling load is corrected to exclude contribution to the strain energy by transverse tie stiffness, i.e., the second term in the parenthesis of Equation (2.9) becomes zero; hence the discontinuity in Equation (2.11) at $L_{cr,\min}=s_t$. Hence, for a bar with cross-sectional area A_b, it is more convenient to evaluate a critical buckling stress (compression is treated negative throughout this report unless otherwise noted) at any stage during the analysis as

$$\sigma_{cr,\min}=\begin{cases}-\dfrac{2\sqrt{3\gamma_{cr}}}{A_b} & \text{if} \quad L_{cr,\min}>s_t \\ -\dfrac{4\pi^2 E_r J_b}{A_b s_t^2} & \text{if} \quad L_{cr,\min}=s_t\end{cases} \tag{2.12}$$

where $\gamma_{cr}=E_r J_b \beta_t$ is a quantity that reflects the effect of inelasticity in the bar and transverse ties on the critical buckling stress. Since the inelasticity is a function of the imposed

strain history, Equation (2.12) therefore describes a critical surface in the bar stress-strain space that when violated by the current compressive stress in the bar during the analysis determines the onset of buckling. This critical surface is generated by evaluating the value of $\sigma_{cr,\min}$ at each axial strain increment. This procedure is demonstrated in Figure 2.2 for a bar buckling over a single tie-spacing length $L_{cr,\min} = s_t$, where the mechanical stress-strain behavior of the bar is assumed to follow Chang and Mander (1994), with yield stress σ_y and ultimate stress σ_u (see Fig. 2.5). It can be observed from the above formulation that inelasticity in the bar will reduce its stiffness modulus and therefore reduce its buckling stress. Similarly, inelasticity or failure of the transverse ties will lead to a larger buckling length and therefore a lower critical stress. If it is desired that the bar constitutive material model include a yield plateau where the tangent modulus value is zero, the critical surface definition has to be modified in that yield plateau region. This can be achieved by using the secant instead of the tangent modulus in Equation (2.1) during the perfectly plastic region to avoid an unrealistic zero value of the critical stress.

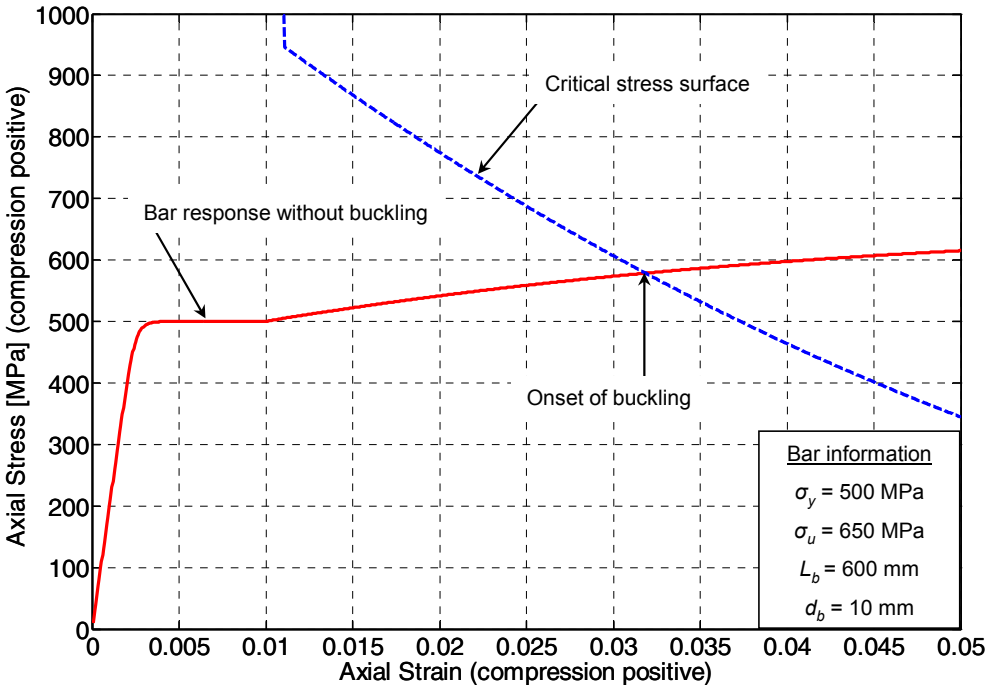

Fig. 2.2 Onset of bar buckling and effect of bar inelasticity.

2.2.3 Monotonic Post-Buckling Behavior

Upon detection of buckling in a longitudinal reinforcing bar, the post-buckling behavior is modeled based on a strain-decomposition scheme. First, consider the linear-elastic behavior of a classic axially loaded steel bar with time-invariant boundary conditions, i.e., no lateral supports due to transverse ties, and buckling length L_{cr} corresponding to a critical compressive stress $\sigma_{cr} = -4\pi^2 EJ_b / A_b L_{cr}^2$. The initial conditions of the bar correspond to no axial load and stress-free ends. An initial imperfection in the bar is assumed that results in a mid-height lateral deflection δ_i. The initially deflected profile of the bar along its buckling length can be described by a harmonic function $y_i(x)$, where

$$y_i(x) = \frac{\delta_i}{2}\left[1 - \cos\left(\frac{2\pi}{L_{cr}}x\right)\right] \tag{2.13}$$

As a result, the length of the bar along the deflected profile is different from the shortest distance measured between the ends of the bar, which can be interpreted as an initial shortening corresponding to an initial stress-free strain ε_{fi} expressed as follows:

$$\varepsilon_{fi} = \frac{\Delta L_i}{L_{cr}} = -\frac{1}{L_{cr}}\int_0^{L_{cr}}\left(\sqrt{1+\left(\frac{dy}{dx}\right)^2} - 1\right)dx \approx -\frac{1}{L_{cr}}\int_0^{L_{cr}}\frac{1}{2}\left(\frac{dy}{dx}\right)^2 dx = -\frac{\pi^2\delta_i^2}{4L_{cr}^2} \tag{2.14}$$

When the bar is loaded with an axial load P, the resulting deflected profile $y(x)$ is the algebraic sum of the initial profile $y_i(x)$, which represents a particular solution to the differential equation of a beam, and a profile $y_1(x)$ obtained from the general second-order equilibrium solution of a beam with fixed ends.

$$y_1(x) = \frac{1}{\left(4\pi^2/k_b^2 L_{cr}^2 - 1\right)}\frac{\delta_i}{2}\left[1 - \cos\left(\frac{2\pi}{L_{cr}}x\right)\right] \tag{2.15}$$

where $k_b^2 = P/EJ_b$. Next, define the ratio α_P such that

$$\alpha_P = \frac{\sigma}{\sigma_{cr}} = \frac{P}{4\pi^2 EJ_b/L_{cr}^2} = k_b^2 L_{cr}^2/4\pi^2 \tag{2.16}$$

and substitute in Equation (2.15) to get (2.17), and then add (2.13) to get (2.18).

$$y_1(x) = \frac{\delta_i}{2}\left[1 - \cos\left(\frac{2\pi}{L_{cr}}x\right)\right]\frac{\alpha_P}{(1-\alpha_P)} \tag{2.17}$$

$$y(x) = y_i(x) + y_1(x) = \frac{\delta_i}{2}\left[1 - \cos\left(\frac{2\pi}{L_{cr}}x\right)\right]\frac{1}{(1-\alpha_P)} = \frac{y_i(x)}{(1-\alpha_P)} \tag{2.18}$$

The physical significance of the previous derivation represents an interesting concept. An applied stress on the bar σ results in amplification of the deflected shape resulting from the initial imperfection by a factor dependent on the ratio $\alpha_P = \sigma/\sigma_{cr}$. As a result, the measured strain ε along the buckling length of the bar comprises two components: the stress-inducing mechanical strain ε_s in the steel material and an additional stress-free shortening ε_f due to amplification of the initial imperfection. In the linear elastic range, the first term is dominant, and can typically be computed as $\varepsilon_s = \sigma/E_s$. The second term is computed by making use of Equations (2.14) and (2.18):

$$\varepsilon_f = \frac{\varepsilon_{fi}}{(1-\alpha_P)^2} \tag{2.19}$$

The total strain measured along the bar is $\varepsilon_t = \varepsilon_s + \varepsilon_f$. Given the small typical values of α_p in the elastic range and the small common values for initial imperfection, the value of ε_f is insignificant prior to buckling or yielding in compression and can be neglected in estimating the linear response without any notable loss of accuracy.

However, yielding or buckling of the bar significantly changes its stiffness and alters the value of α_P. Hence, when the bar reaches either limit case, the structural system is redefined according to the new material constants, and the initial boundary conditions are set to the current configuration of the deflected and loaded bar. Consider the case of a bar that has reached its yielding strain and is starting to exhibit hardening behavior (i.e., not yet into the hardening range). The initial conditions are taken from the solution of Equation (2.18) with the applied stress and strain being set to the yield point in compression $\left(-\sigma_y, -\varepsilon_y = -\sigma_y/E_s\right)$. These initial conditions are listed with a superscript h to denote that loading is taking place in the hardening phase:

$$\sigma_i^h = -\sigma_y \tag{2.20}$$

$$\varepsilon_{fi}^h = -\varepsilon_y + \varepsilon_{fi} \Big/ \left(1 - \sigma_y / \sigma_{cr}\right)^2 \approx -\varepsilon_y \tag{2.21}$$

The approximation in Equation (2.21) is valid, since the stress-free strain can be ignored in the elastic range as discussed above. This has the advantage of eliminating the model's sensitivity to the estimated value of the initial imperfection δ_i. Next, the strain decomposition relationships are re-written to reflect the new boundary conditions:

$$\varepsilon_t = \left(\varepsilon_s - \varepsilon_{fi}^h\right) + \varepsilon_f^h \tag{2.22}$$

$$\varepsilon_f^h = \frac{\varepsilon_{fi}^h}{\left(1 - \alpha_{\Delta P}^h\right)^2} \tag{2.23}$$

where $\alpha_{\Delta P}^h$ is a redefinition of the ratio α_P according to

$$\alpha_{\Delta P}^h = \frac{\sigma(\varepsilon_s) - \sigma_i^h}{\sigma_{cr}^h - \sigma_i^h} \geq 0 \tag{2.24}$$

where $\sigma(\varepsilon_s)$ represents the bar's constitutive material law and the updated critical stress σ_{cr}^h is computed using (2.12) and the reduced stiffness modulus E_r from (2.1). Equations (2.22)–(2.24) can be satisfied using an iterative solver. Note that ε_t and ε_s represent the total and mechanical strains in the bar and are not affected by the hardening regime, hence the absence of superscript h. If the updated critical stress σ_{cr}^h is lower than the yield stress and the bar therefore buckles prematurely, the material effectively unloads, while the observed (total) strain increases due to the amplification factor in Equation (2.23). Otherwise, the stress in the bar will continue to increase until it reaches the buckling stress. However, the bar's stress-total strain response will exhibit reduced hardening stiffness due to the decomposition of total strain between a mechanical component that generates stress and a stress-free buckling-induced component.

Finally, consider the case of a general material law for a steel bar with nonlinear inelastic behavior and laterally restrained by uniform transverse ties of nonlinear stiffness. Once buckling is detected according to Equation (2.12), define σ_b and ε_b, the compressive stress at the onset of buckling and the corresponding compressive strain magnitude, respectively. Then an updated

structural system with new boundary conditions can be approximately defined, following the example of Equations (2.20) and (2.21). The new set of boundary conditions are listed (with superscript b to denote the buckling phase) by

$$\sigma_i^b = \sigma_b = \max_{\varepsilon_s}\left\{\sigma(\varepsilon_s) : \sigma(\varepsilon_s) \le \sigma_{cr,\min}\right\} \tag{2.25}$$

$$\varepsilon_{fi}^b = \varepsilon_b = \sigma^{-1}(\sigma_b) - \sigma^{-1}(0) \tag{2.26}$$

where σ^{-1} refers to the inverse stress-strain relationship of the bar's constitutive material law and $\sigma^{-1}(0)$ is the strain corresponding to the beginning of the current compressive stress cycle ($\sigma^{-1}(0) = 0$ for monotonic loading). Next, approximate σ_{cr}^b as the terminal critical stress of the buckled bar at large deformations $\sigma_{cr|\infty}$, corresponding to asymptotic material tangent stiffness moduli (or rupture, if applicable) in the bar and transverse ties.

$$\sigma_{cr}^b \approx \sigma_{cr|\infty} = \left\{\sigma_{cr,\min} : \left(|\varepsilon_s| >> \varepsilon_y, \gamma_{cr} = \min_{\varepsilon_s}\{\gamma_{cr}\}\right)\right\} \tag{2.27}$$

Therefore, equations similar to (2.22)–(2.24) are proposed with the substitution of superscript h by b and making the necessary adjustments (e.g., for the definition of $\alpha_{\Delta P}^b$). The redefinition of boundary conditions and initial stress-free strain requires the addition of a residual strain term ε_r to preserve strain compatibility of the decomposition equation. This residual strain is equivalent to the stress-free strain ε_f^h in Equation (2.23) at the point where Equations (2.22)–(2.24) are redefined (i.e., at the onset of buckling). The updated equations describing post-buckling stress-strain behavior are written in terms of the redefined boundary conditions making use of Equations (2.25)–(2.27).

$$\varepsilon_t = (\varepsilon_s - \varepsilon_b) + \varepsilon_f^b \tag{2.28}$$

$$\varepsilon_f^b = \varepsilon_r + \frac{\varepsilon_b}{\left(1 - \alpha_{\Delta P}^b\right)^2} \tag{2.29}$$

$$\alpha_{\Delta P}^b = \frac{\sigma(\varepsilon_s) - \sigma_b}{\sigma_{cr|\infty} - \sigma_b} \ge 0 \tag{2.30}$$

The main components and behavioral features of this model are illustrated in Figure 2.3. The mechanical stress-strain model for the bar is assumed to follow Chang and Mander (1994).

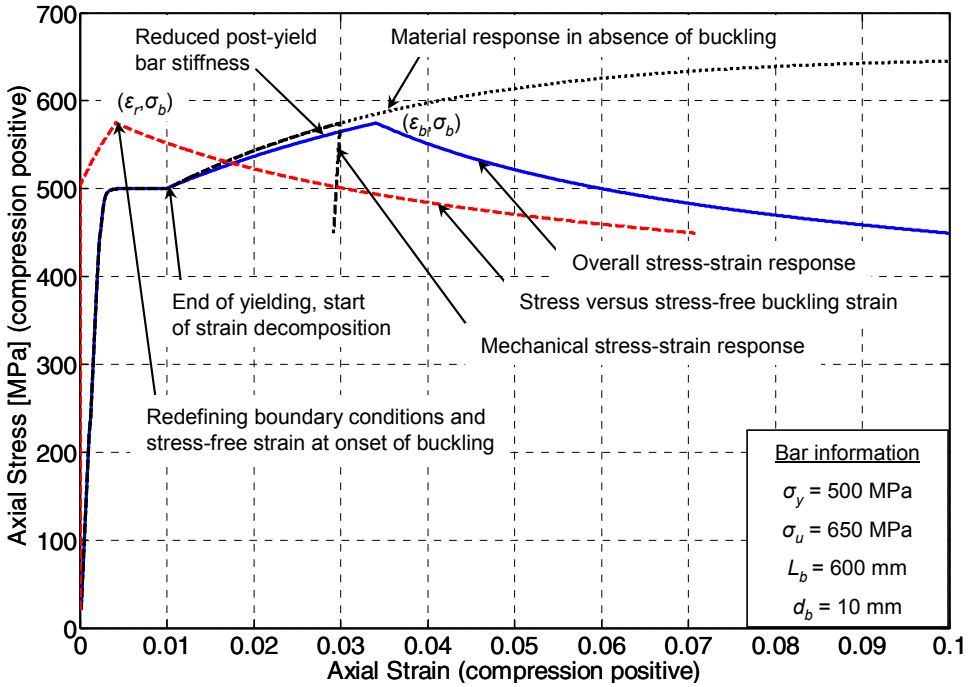

Fig. 2.3 Model illustration of monotonic post-buckling behavior.

2.2.4 Cyclic Post-Buckling Behavior

The point $\left(\varepsilon^{un}, \sigma^{un}\right)$ on the stress-strain path marks the end of a loading half-cycle and the start of an unloading one. An unloading half-cycle is defined as the path starting at peak strain and ending at zero stress (or earlier, if strain reversal takes place prior to reaching zero stress), while a loading half-cycle is defined as the stress-strain path starting at zero stress (or from the end of the preceding unloading half-cycle in which zero stress had not been reached) and ending at the peak strain. The end of a compression (negative) loading half-cycle is detected when the algebraic sign of the total strain increment $\Delta\varepsilon_t$ is reversed from negative to positive. Following a loading half-cycle during which buckling has been detected, experimental results reported in the literature show that bars exhibit reduced axial stiffness, the buckling-induced shortening decreases, and the bar straightens out (Monti and Nuti 1992). This behavior can be modeled consistently using the strain decomposition approach employed in modeling post-buckling behavior. The recovered buckling-induced shortening can be expressed in terms of a positive

stress-free strain increment $\Delta\varepsilon_f$. Hence, the bar material temporarily follows its constitutive law with a reduced mechanical strain increment $\Delta\varepsilon_s = \Delta\varepsilon_t - \Delta\varepsilon_f$. This results in a reduced overall unloading stiffness $E^{un} = \partial\sigma(\varepsilon_s)/\partial\varepsilon_t$ up to the point when $\varepsilon_f = 0$ and $\Delta\varepsilon_s = \Delta\varepsilon_t$. Afterwards, the relationship $\varepsilon_t = \varepsilon_s$ is restored and the bar material follows its constitutive law in the original manner until subsequent buckling is detected.

The relationship governing the distribution of strain increments is formulated to ensure continuity over its range as follows:

$$\Delta\varepsilon_f = \eta_f \frac{\varepsilon_f}{\varepsilon_f^{un}} \Delta\varepsilon_t \le \Delta\varepsilon_t \text{ with } 0 \le \eta_f \le 1 \tag{2.31}$$

where ε_f and ε_f^{un} are the stress-free strains corresponding to the current and unloading stress states, respectively. Moreover, for numerical stability, the resulting change in bar stiffness is gradual and continuous along the regime in which the stress-free strain varies from $\varepsilon_f = \varepsilon_f^{un}$ to $\varepsilon_f = 0$, allowing a smooth transition to the constitutive material law. The choice of η_f should be made such that bars suffering from severe buckling should exhibit softer axial stiffness upon strain reversal as discussed above. The analytical study in Dhakal and Maekawa (2002b) suggests that the tangent stiffness at the beginning of the compression unloading half-cycle E_i^{un} can be assumed as follows:

$$E_i^{un} = E_s \left(\sigma^{un} / \sigma\left(\varepsilon_t^{un}\right)\right)^2 \tag{2.32}$$

where $\sigma\left(\varepsilon_t^{un}\right)$ is the bar material's mechanical stress at the unloading strain without considering the effects of buckling, as illustrated in Figure 2.4. Note that the effective bar stiffness is given by

$$E^{un} = \frac{d\sigma}{d\varepsilon_t} = \frac{d\sigma}{d\varepsilon_s}\frac{d\varepsilon_s}{d\varepsilon_t} = E_s \frac{d\varepsilon_s}{d\varepsilon_t} \tag{2.33}$$

During a compression unloading half-cycle, the derivative in the last term is expressed using Equation (2.31) as follows:

$$\frac{d\varepsilon_s}{d\varepsilon_t} = \frac{d}{d\varepsilon_t}\left(1 - \eta_f \frac{\varepsilon_f}{\varepsilon_f^{un}}\right)\varepsilon_t = 1 - \eta_f \frac{\varepsilon_f}{\varepsilon_f^{un}} + O\left(\eta_f^2\right) \approx 1 - \eta_f \frac{\varepsilon_f}{\varepsilon_f^{un}} \tag{2.34}$$

where $O(\eta_f^2)$ follows the usual asymptotic notation. Substituting Equation (2.34) in (2.33) and equating to (2.32) when $\varepsilon_f = \varepsilon_f^{un}$ yields

$$\eta_f = 1 - \left(\sigma^{un} / \sigma(\varepsilon_t^{un})\right)^2 \tag{2.35}$$

At the end of the tension loading half-cycle, the stress-free strain ε_f is checked for full recovery. Unless fully recovered, the non-zero value of ε_f is designated as the current residual strain ε_r during the subsequent load cycle. At the end of the tension unloading half-cycle, the corresponding mechanical strain $\varepsilon_s(\sigma = 0)$ is stored in order to be used in Equation (2.26) and the increasing compressive stresses are monitored and checked for buckling. Once detected, an updated σ_b and ε_b are defined, and an updated set of Equations (2.25)–(2.30) is enforced until subsequent strain reversal. The main components and behavioral features of this model are illustrated in Figure 2.4. For clarity of illustration, the mechanical stress-strain behavior of the bar is assumed to follow the nonlinear model in Menegotto and Pinto (1973) without including a yield plateau.

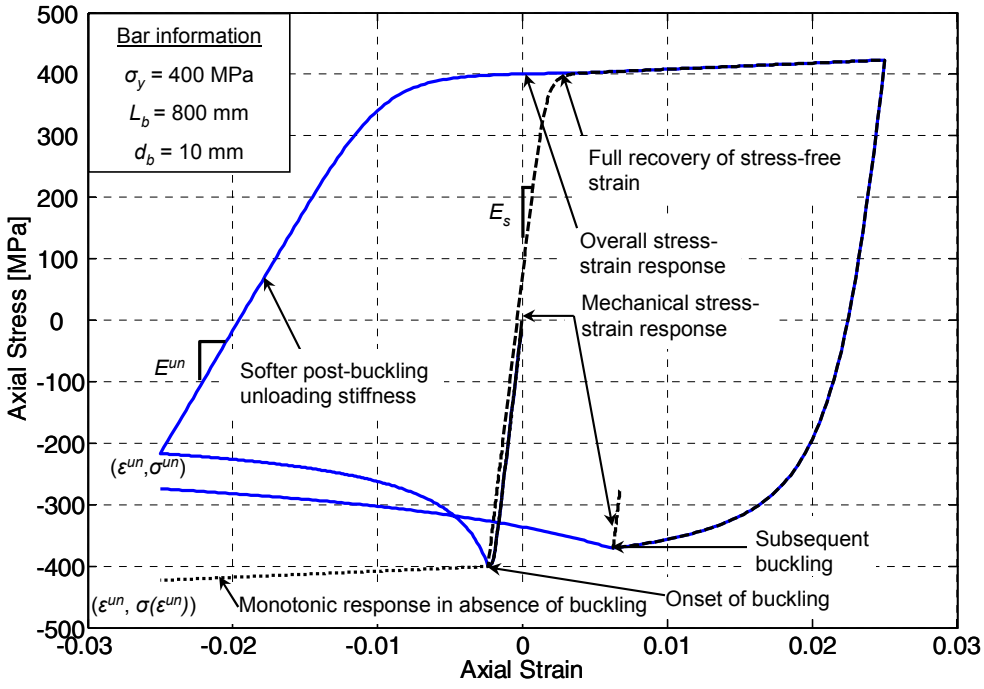

Fig. 2.4 Model illustration of cyclic post-buckling behavior.

2.2.5 Hysteretic Stress Reduction and Bar Fracture

The Coffin-Manson fatigue model (Coffin 1962; Manson 1979) is employed as described by Brown and Kunnath (2004) to model the hysteretic degradation of reinforcing steel bars and subsequent fracture. This model is based on the accumulation of plastic strain. It defines a cumulative damage index calculated at the end of each loading half-cycle according to

$$D_s = \sum_{half\ cycles} \left(\frac{\varepsilon_p}{2M_f} \right)^{1/\alpha_{cm}} \leq 1 \tag{2.36}$$

where ε_p is the plastic strain accumulated between strain reversals. It is assumed to be equal to the strain amplitude after subtracting an elastic strain value equal to the stress amplitude $\left(\sigma_s^{\max} - \sigma_s^{\min}\right)$ divided by the elastic stiffness modulus E_s. M_f is the strain corresponding to fracture in monotonic tension, and α_{cm} is a model calibration parameter (typically 0.5–0.7 for metals). The damage index calculated after each loading half-cycle is used to compute a hysteretic stress reduction factor for subsequent loading half-cycles as follows:

$$R_s = (1 - D_s)^{a_s} \tag{2.37}$$

where a_s is another model calibration parameter. When the damage index value is equal to zero prior to damage, the stress reduction factor is equal to unity causing no reduction in stress. When the damage index value reaches unity, the stress reduction factor becomes zero and the bar becomes inactive. The study in Brown and Kunnath (2004) suggests calibrated values of $M_f = 0.130$ and $\alpha_{cm} = 0.506$ for reinforcing steel bars. The parameter α_s is calibrated in the next section.

In order to use the Coffin-Manson fatigue model discussed above and the calibration in Brown and Kunnath (2004) with the current reinforcing steel bars buckling model, a modification is suggested in Equation (2.38) for the definition of strain amplitude to account for the relatively rapid hysteretic degradation caused by buckling. The strain amplitude is therefore redefined as one composed of the mechanical axial strain amplitude $\left(\varepsilon_s^{\max} - \varepsilon_s^{\min}\right)$ and the maximum compressive strain in the buckled bar's cross section. The latter is computed from the maximum curvature $\phi_{\max}$ of the deformed (buckled) shape assuming Bernoulli-compliant

bending as $\phi_{\max} \times d_b/2$. Thus strains accumulated mechanically are treated differently in assessing damage than those observed due to buckling-induced shortening. Reversing Equation (2.14) to compute the lateral offset δ from the stress-free strain ε_f, substituting in Equation (2.3) to compute the corresponding curvature at mid-height of the buckled bar ($x = L_{cr}/2$), using $n = 1$, multiplying by half the bar diameter, modifying ε_f with the residual strain ε_r according to the discussion at the end of the previous section, adding the mechanical strain amplitude, and subtracting the elastic strain value yields

$$\varepsilon_p^b = \left(\varepsilon_s^{\max} - \varepsilon_s^{\min}\right) + \frac{2\pi d_b}{L_{cr}}\sqrt{\varepsilon_f - \varepsilon_r} - \frac{\left(\sigma^{\max} - \sigma^{\min}\right)}{E_s} \tag{2.38}$$

This plastic strain quantity can be used along with experimental data to calibrate fatigue models similar to Brown and Kunnath (2004) for bars suffering from multiple instances of buckling prior to fracture as discussed in the next section.

2.2.6 Parameter Calibration and Experimental Verification

In this section, the buckling-enabled model for longitudinal reinforcing steel bars developed in the present section is compared to experimental results published in Monti and Nuti (1992), Rodriguez et al. (1999), and Bae et al. (2005) to assess its validity and calibrate the parameter α_s. Calibration of the parameter α_{cm} using the definition of plastic strain from Equation (2.38) requires experimental data of steel bars cyclically loaded until fracture while suffering from multiple instances of buckling, which proved difficult to find in the literature. Thus, the value calibrated in Brown and Kunnath (2004) is adopted for simplicity. The simulated experimental investigations include individual steel bars subjected to monotonically increasing compressive strains or cyclically increasing strains. The end conditions for all bars are such that they are prevented from rotation and lateral translation at both ends. Analytical simulation is performed using the proposed bar-buckling model and a mechanical stress-strain material model for the reinforcing steel. Unless otherwise mentioned, the mechanical stress-strain model in Chang and Mander (1994) is used. The stress-strain parameter values used in the analytical simulation for each group of experiments are listed in Table 2.1 and defined in Figure 2.5, where the subscript

sh refers the onset of strain-hardening, and the subscript u refers to ultimate stress state. In the case of some material properties not being reported such as the initial strain hardening modulus, or the cyclic behavior parameters, they are estimated within the range of typical steel properties and calibrated when applicable to the bars' response observed prior to buckling. In the case of several parameters not being reported, the constitutive law in Menegotto and Pinto (1973) is used for the mechanical stress-strain relationship of the steel bars. The values of the parameter α_s used in calibrating the simulated cyclic load tests are listed in Table 2.1. Due to the small number of experiments, no statistics are computed. However, the observed model response exhibited robust (little) sensitivity to small perturbations in α_s values.

Table 2.1 Parameter values in simulations using the bar-buckling model.

Experiment	(Bae et al. 2005)	(Rodriguez et al. 1999)	(Monti and Nuti 1992)
E_s [GPa]	200	200	200
E_{sh} [GPa]	5	10	8
σ_y [MPa]	440	409	490
σ_u [MPa]	640	700	Not Available
ε_{sh}	0.005	0.005	Not Available
ε_u	0.16	0.18	Not Available
α_s (for cyclic loading only)		0.30	0.10

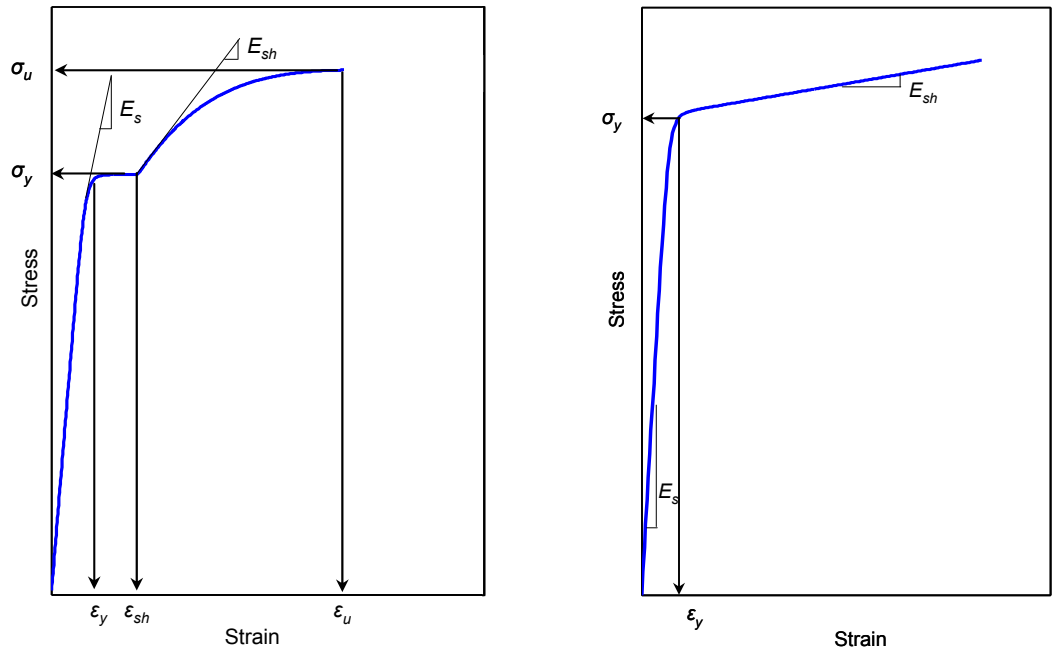

(a) Model in Chang and Mander (1994) (b) Model in Menegotto and Pinto (1973)

Fig. 2.5 Basic parameters of existing mechanical stress-strain models for steel.

Figure 2.6 illustrates the comparison between the model predictions and the monotonic compression tests reported in Bae et al. (2005) for nine levels of the bar slenderness ratio $L_b/d_b = 4,5,...,12$. The simulation is successful in capturing the buckling stress for the majority of bars except for bars that buckle prior to reaching the yield stress, i.e., with very high slenderness ratio $L_b/d_b \geq 10$. This is because the critical buckling surface during the yielding plateau is not well-defined as previously described in Section 2.2.2. The model is moderately successful in reproducing the reduction in hardening stiffness between yielding and buckling. In that region, the analytical model shows higher stiffness than the experimental results, and as a result the predicted strains at the peak stress prior to softening are underestimated. The model is generally successful in describing the post-buckling softening in the bars. The analytically simulated softening branches show discontinuity and steeper gradients at the onset of buckling that cannot be observed in the experiments due to the load-application control process and average strain calculation method. The experimentally computed strains are averaged over a

gage length of 200 mm, which is less capable of capturing the sudden effects of strain localization.

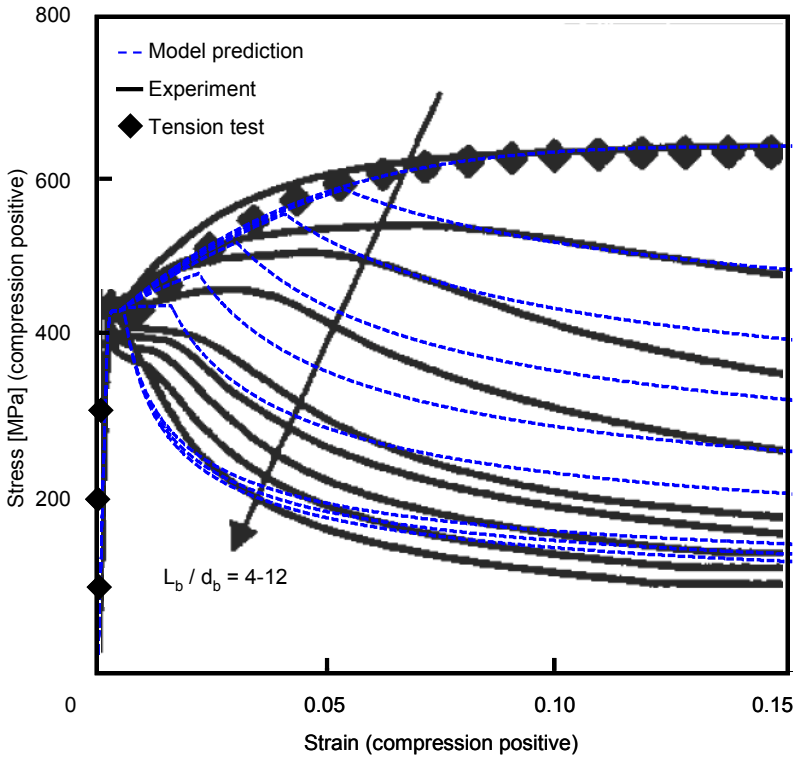

Fig. 2.6 Model simulations of Bae et al. (2005) bar-buckling experiments.

Figure 2.7 illustrates the comparison between the model prediction and the cyclic loading experiments conducted in Rodriguez et al. (1999) for two bars representing the compression (concave) and tension (convex) sides of an axially loaded RC column subjected to cyclic lateral displacement. Both bars have a slenderness ratio of 6. The simulation is successful in estimating the cycles where buckling is observed and the subsequent softening. The simulation is also successful in estimating the reduced stiffness moduli of the buckled bars upon unloading from compression, and is largely successful in reproducing the following hysteretic loops in tension and compression except for occasional overestimation of the hysteretic loop size during unloading from loading half-cycles of high strain magnitude. The simulation slightly overestimates the reduction in unloading stiffness following brief buckling sessions in Figure 2.7b.

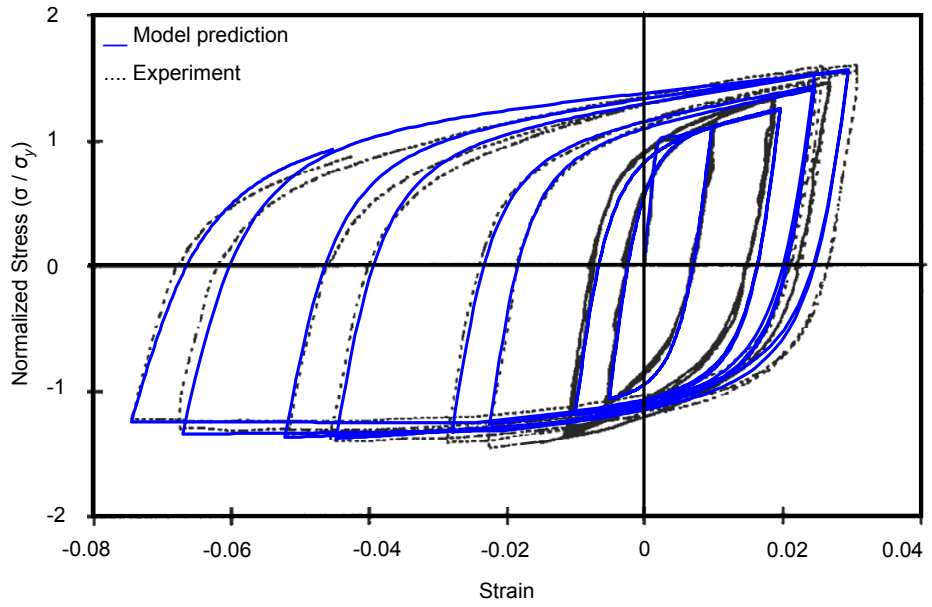

(a) Bar representing RC column's concave side

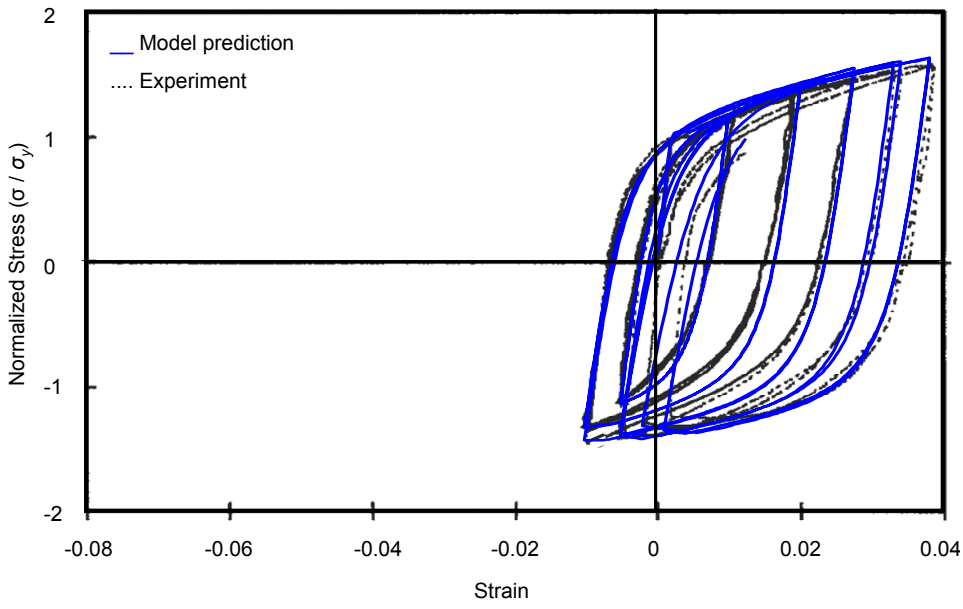

(b) Bar representing RC column's convex side

Fig. 2.7 Model simulations of Rodriguez et al. (1999) bar-buckling experiments.

Figure 2.8 illustrates the comparison between the model prediction and the cyclic loading tests conducted in Monti and Nuti (1992) for steel bars with slenderness ratios of 8 and 11. The pre-buckling response of the steel bars is supposed to follow the mechanical stress-strain model in Menegotto and Pinto (1973) due to the limited material properties reported in Monti and Nuti (1992). The simulation is successful in estimating the cycles where buckling is observed and the subsequent softening in stress. The simulation is also successful in estimating the reduced stiffness moduli of the buckled bars upon unloading from compression and in reproducing the subsequent hysteretic behavior in tension. The area of the hysteretic loops in compression is underestimated in the simulation while unloading from the 0.03 strain cycle due to the limitations of the mechanical stress-strain model. This can be calibrated in the presence of additional material property data and more detailed mechanical stress-strain models, e.g., the model in Chang and Mander (1994). Superimposed on the response is the estimation of the stress-strain response in the absence of buckling using the steel material model in Dhakal and Maekawa (2002b). The comparison illustrates the significance of the developed bar-buckling model in estimating the effect of buckling on the uniaxial response of longitudinal reinforcement. Moreover, similar to the present buckling model, an underestimation of the area of the hysteretic loops in compression especially for $L_b/d_b = 11$ is also observed in the simulations based on the steel material model in Dhakal and Maekawa (2002b) without buckling.

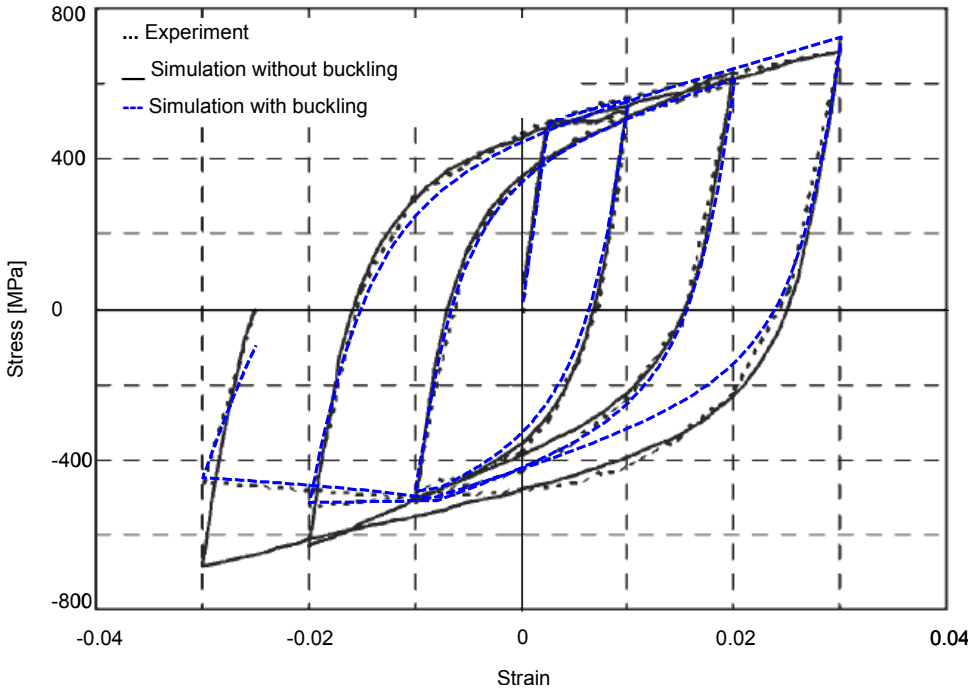

(a) Bar with length-to-diameter ratio of 8

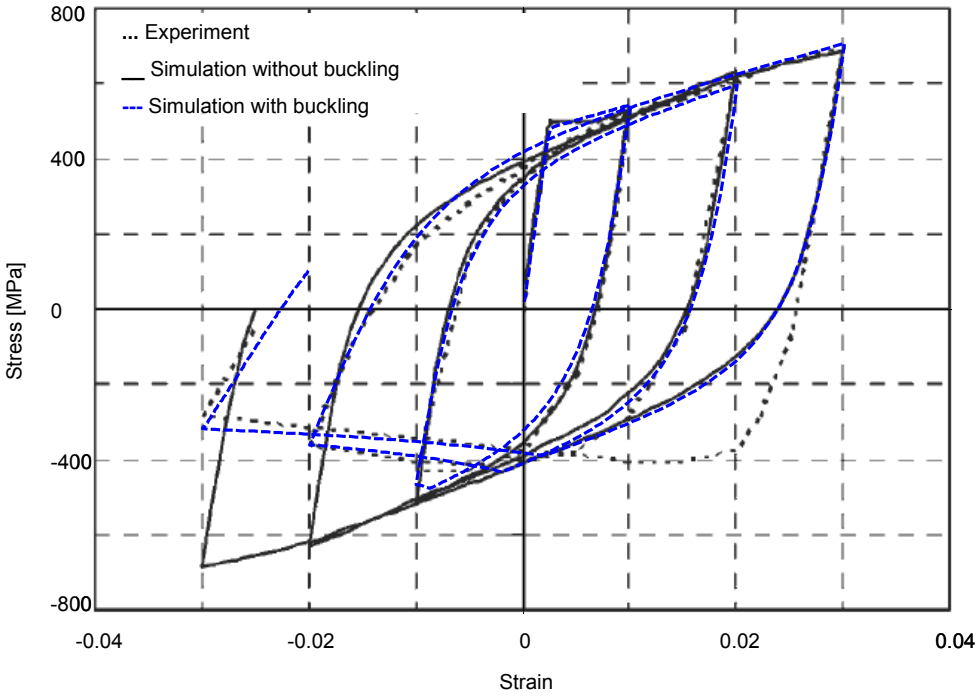

(b) Bar with length-to-diameter ratio of 11

Fig. 2.8 Model simulations of Monti and Nuti (1992) bar-buckling experiments.

2.3 ANALYTICAL MODEL FOR LAP-SPLICED STEEL BARS

The proposed uniaxial material model for lap-spliced steel bars is based on a number of components. The first component is an admissible interpolation of bond stresses within the splice region. The second component is a strain decomposition approach. The third component is a constitutive bond-slip material model which combines a confinement-sensitive constitutive law for monotonic bond-slip behavior with multi-linear hysteretic unloading-reloading rules. The fourth component consists of an analytical model for hysteretic damage and stress reduction.

2.3.1 Geometric Setup

The geometric setup and assumed stress fields of two longitudinal steel bars lap-spliced within a RC column as adopted from Binici and Mosalam (2007) are shown in Figure 2.9. The spliced bar is referred to as "1," while the starter bar is referred to as "2" in illustrations and subscripts. The distribution of bond shear stresses τ along the splice length is assumed to vary linearly from zero at the stress-free end of each bar to a maximum stress τ_m at a distance L_s, which satisfies the equilibrium of stresses at the stress-free end. At any location along the splice at a distance l_1 from the stress-free end of the spliced bar, the equilibrium of axial stresses in each bar and bond stresses transferred to it can be respectively expressed using the following two equations:

$$\sigma_{s1}\pi\frac{d_b^2}{4}=\frac{\tau_1}{2}\pi d_b l_1=\tau_m\pi d_b\frac{l_1^2}{2L_s} \tag{2.39}$$

$$\sigma_{s2}\pi\frac{d_b^2}{4}=\frac{\tau_2}{2}\pi d_b\left(L_s-l_1\right)=\tau_m\pi d_b\frac{\left(L_s-l_1\right)^2}{2L_s} \tag{2.40}$$

Solving Equations (2.39) and (2.40) for the axial stresses in the bars σ_{s1} and σ_{s2} and then algebraically adding them, one obtains the total steel stress σ_s at a distance l_1 as follows:

$$\sigma_s=\sigma_{s1}+\sigma_{s2}=2\tau_m\frac{\left(L_s-l_l\right)^2+l_l^2}{d_b L_s} \tag{2.41}$$

which corresponds to the parabolic axial stress distribution along the splice length illustrated in Figure 2.9. In FE analysis, the spatial variation in the total steel stress is computed as a function of the integration point location within the splice length.

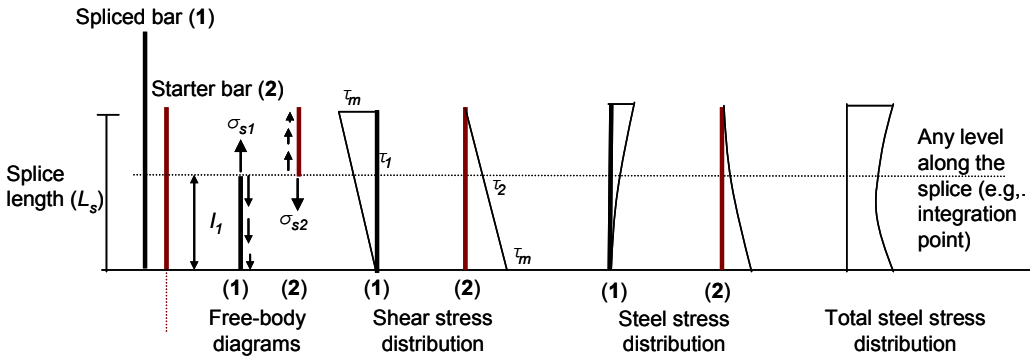

Fig. 2.9 Geometry and stress-strain distribution along spliced steel bars.

2.3.2 Monotonic Lap-Splice Behavior

The monotonic bond-slip relationship proposed in Xiao and Ma (1997) with minor modifications is briefly presented in this section. This relationship relates the bond stress τ_m to the slip displacement u_s given the compressive strength f_c' of the adjoining concrete, the maximum bond strength in the absence of lateral confinement τ', the lateral confining stress acting on the spliced bars σ_3, and a non-dimensional factor r_o representing the reinforcing bar grade. This bond-slip model follows the equation:

$$\tau_m = \frac{\tau_{\max} r\left(u_s / u_{s,\max}\right)}{r - 1 + \left(u_s / u_{s,\max}\right)^r} \tag{2.42}$$

where Xiao and Ma (1997) proposes the following definitions for the model parameters:

$$\tau_{\max} = \tau' + 1.4\sigma_3 \tag{2.43}$$

$$u_{s,\max} = 0.25\left(1 + 75\,\sigma_3 / f_c'\right) \text{ [mm]} \tag{2.44}$$

$$r = r_o - 13\,\sigma_3 / f_c' \geq 1.1 \tag{2.45}$$

where r_o is 2 for Grade 60 and 1.5 for Grade 40 steel, and in the absence of experimental measurement, it is assumed that

$$\tau' = 20\sqrt{f_c'}/d_b \text{ [N, mm units]} \tag{2.46}$$

The confining stress σ_3 is computed from the transverse reinforcement and its maximum value is assumed to correspond to a concrete dilation strain $\varepsilon_{dl} \approx 0.0010 \text{ to } 0.0015$ (Seible et al. 1997), after which confinement is experimentally observed to have insignificant effect on clamping the splices (Xiao and Ma 1997). Note that Hawkins et al. (1982) proposes a different relationship for $u_{s,\max}$ in well-confined steel bars (see the following equation) that explicitly takes into account the diameter of the bar but not the magnitude of the confining pressure.

$$u_{s,\max} = 8\left(\frac{f_c'}{1000 d_b}\right)^{1/3} + \frac{310}{d_b f_c'} \text{ [N, mm units]} \tag{2.47}$$

Together Equations (2.44) and (2.47) present lower and upper bounds, respectively.

A strain decomposition approach similar to the one described in Section 0 is used in this section. The monotonic bond material described above is coupled as a uniaxial material in series with another uniaxial material representing the mechanical stress-strain response of reinforcing steel bars. Hence,

$$\varepsilon_t = \varepsilon_s + \varepsilon_{sl} \quad \text{with} \quad \varepsilon_{sl} = u_s / L_s \tag{2.48}$$

where ε_s is the mechanical strain such that $\sigma_s = \sigma(\varepsilon_s)$ represents the total axial stress in the spliced bars according to their mechanical stress-strain constitutive law, and ε_{sl} represents normalized slip deformation. Equations (2.42), (2.48), and the mechanical stress-strain constitutive law are solved iteratively to satisfy the equilibrium of stresses along the splice region while preserving the kinematic compatibility of strain components and the constitutive law. Typically, due to the relative uniformity in spatial distribution of steel total stress along the splice length (σ_s in Fig. 2.9), one integration point is deemed sufficient and computationally economical. The main components and behavioral features of this model are illustrated in Figure 2.10. The mechanical stress-strain model for the bar is assumed to follow Menegotto and Pinto (1973) for simplicity of illustration. The figure illustrates the concept of using strain decomposition to simulate softening in the overall response following failure of the lap-splice while the spliced bars unload elastically.

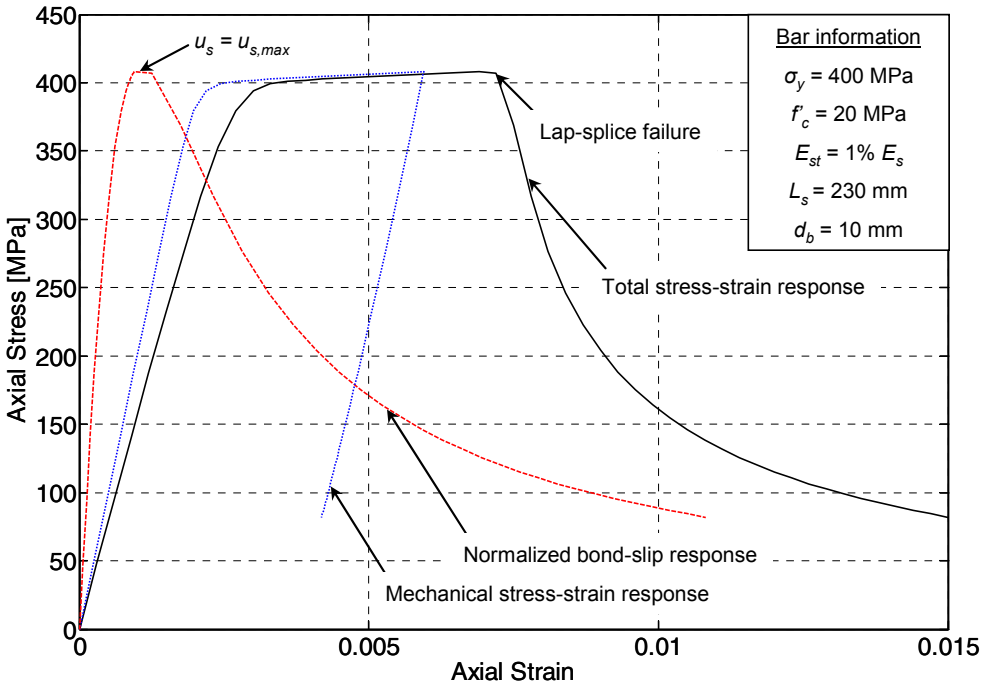

Fig. 2.10 Model illustration of monotonic lap-splice behavior.

Figure 2.11 illustrates an example simulation for the response of lap-spliced bars compared to that of bars with perfectly rigid bond, i.e., no lap-splice. Three lap-splice length-to-diameter ratios $L_s/d_b = 40, 20, 10$ are simulated to represent cases of adequate and inadequate designs. The first set of plots—shown in solid lines— illustrates the response of the lap-spliced bars in their as-built condition, i.e., no external confinement. The second set of plots—shown in dashed lines—illustrates the response of the lap-splice if retrofitted by external confinement of 3-mm diameter circular spirals at a spacing of 25 mm in a cross section of 75 mm diameter. The simulated behavior of the retrofitted splices exhibits lower initial stiffness due to the increase in slip displacement $u_{s,\max}$ in Equation (2.44) more than the corresponding increase in bond-stress capacity $\tau_{\max}$ in Equation (2.43). In this simulation, the mechanical stress-strain model of the bars follows Menegotto and Pinto (1973). Note that the bond-slip relationship is independent of the lap-splice geometric setup and can therefore be used to model the bond-slip of the anchored bars. This can be achieved if the free-body diagram in Figure 2.9 is modified to eliminate the

starter bar and include the proper stress condition at the embedded end of the anchored bar, with Equations (2.39) and (2.41) updated accordingly.

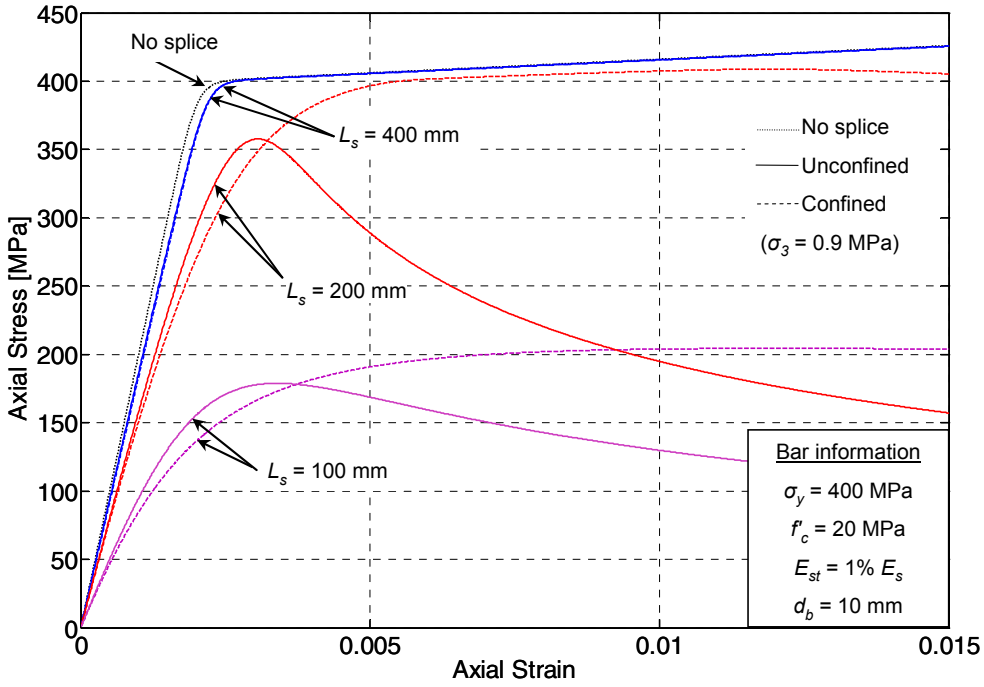

Fig. 2.11 Effect of splice length and confining stress on spliced bar response.

2.3.3 Cyclic Lap-Splice Behavior

Modeling the cyclic response of the lap-spliced bars involves modeling the cyclic bond-slip behavior. In addition to friction and interlocking between the interface concrete and the lugs on a deformed bar surface, compression loading on the spliced bars leads to direct bearing on concrete and alters the assumption of stress-free bar ends. Moreover, several researchers report that the bond-slip behavior and strength exhibit stiffer and stronger response if the bars are pushed toward each other and into the concrete instead of being pulled apart and out due to the additional confining action of the encasing concrete (Viwathanatepa 1979). However, in RC column cross sections subjected to flexural deformations, the primary role of the reinforcing steel bars is to transfer tensile stresses; the role of the reinforcing bars is secondary to the concrete in resisting compressive stresses. Moreover, a cross section whose lap-spliced bars had failed in tension will not be able to develop its bending moment capacity and—consequently—will

impose hardly any demand on the reinforcing steel bars located in its compression (concave) side. Thus, the effect of slip direction on the lap-splice behavior is not explicitly modeled. The concept of strain decomposition and equilibrium of stresses as illustrated in Figure 2.10 is used together with a hysteretic material model to represent the bond-slip behavior. The model consists of the envelope curve described by Equation (2.42), an unloading branch, a pinching branch, a reloading branch, and a hysteretic damage model. This section presents the cyclic response rules. Section 2.3.4 introduces the hysteretic damage model, while Section 2.3.5 presents comparison with experimental data and identifies typical value ranges for the calibrated model parameters.

The proposed cyclic response rules draw their inspiration from Hawkins et al. (1982) and use some of the parameter values reported therein for guidance. The unloading branch follows an unloading modulus S_{un} from the unloading point $\left(u_s^{un}, \tau^{un}\right)$ until stress reversal. The value of S_{un} is assumed equal to the initial tangent modulus S_i of the envelope, obtained by differentiating Equation (2.42) as follows:

$$S_{un} = S_i = \left.\frac{\partial \tau_m}{\partial u_s}\right|_{u_s=0} = \frac{\tau_{\max} r}{(r-1) u_{s,\max}} \tag{2.49}$$

Following stress reversal, the unloading branch continues linearly up to a residual bond stress τ_r depending on the present level of bond integrity (reflected by the unloading stress) as follows:

$$\tau_r = -k_r \tau^{un} \tag{2.50}$$

A value of $k_r = 0.15$ is suggested in Hawkins et al. (1982). Hence the corresponding residual slip displacement is expressed by

$$u_{s,r} = u_s^{un} - \left(\tau^{un} - \tau_r\right)/S_{un} \tag{2.51}$$

Subsequently, the response follows a pinching branch whose stiffness modulus S_{pin} depends on the unloading slip displacement u_s^{un} according to one of the two cases discussed in the following paragraph.

The first case occurs if the bond response prior to unloading is mainly elastic, identified by unloading $\left(u_s^{un}, \tau^{un}\right)$ from the envelope with $\left|u_s^{un}\right| \le u_s^e$, where the superscript e denotes the mainly elastic bond behavior and u_s^e is a model parameter. The pinching branch in this case

coincides with a reloading branch whose stiffness modulus targets the point $\pm\left(u_s^e, \tau^e\right)$ on the opposite-sign envelope curve, i.e.,

$$S_{pin}^e = \frac{\tau^e - \left|\tau_r\right|}{u_s^e + \left|u_{s,r}\right|} \tag{2.52}$$

The response follows the stiffness modulus S_{pin}^e until it returns to the envelope without intermediate changes in stiffness, see Figure 2.12. The second case occurs if the bond response prior to unloading $\left(u_s^{un}, \tau^{un}\right)$ exhibits significant inelasticity, i.e., $\left|u_s^{un}\right| > u_s^e$. In this case, the response follows a reduced stiffness modulus S_{pin}^i (the superscript i denotes inelastic bond behavior). The extent of the inelastic pinching is assumed to depend on the unloading secant modulus and thus reflects the severity of bond deterioration. For simplicity, this latter relationship is assumed linear as follows:

$$S_{pin}^i = \beta_p \frac{\overline{\tau}^{un}}{\overline{u}_s^{un}} \tag{2.53}$$

$$\overline{u}_s^{un} = \left\{ u_s : \max_{u_s \tau^{un} > 0} \left(u_s \tau^{un} \right) \right\} \tag{2.54}$$

where $\beta_p \leq 1$ and can be calibrated by fitting to experimental measurements (see Section 2.3.5). Equation (2.54) retrieves the largest previously recorded slip displacement in the direction of the envelope to which τ_{un} belongs (see Fig. 2.12). The pinching regime ends when the pinching branch intersects the reloading secant modulus S_{sec}. This secant connects the origin to the farthest previous unloading point $\left(\hat{u}_s^{un}, \hat{\tau}^{un}\right)$ on the opposite envelope after reducing the target stress by a factor γ_p.

$$S_{\text{sec}} = \gamma_p \frac{\hat{\tau}^{un}}{\hat{u}_s^{un}} \tag{2.55}$$

$$\hat{u}_s^{un} = \left\{ u_s : \max_{u_s \tau^{un} < 0} \left(-u_s \tau^{un} \right) \right\} \tag{2.56}$$

Equation (2.56) retrieves the largest previously recorded slip displacement in the direction opposite to the envelope to which τ_{un} belongs. The form of the expression for γ_p in Hawkins et al. (1982) is adopted and modified to

$$\gamma_{p,\min} \le \gamma_p = \gamma_{p,\max} - \left(\gamma_{p,\max} - \gamma_{p,\min}\right)\frac{\left(\max|u_s| - u_s^e\right)}{u_{s,ult}} \le \gamma_{p,\max} \tag{2.57}$$

where $u_{s,ult}$ is the slip displacement corresponding to the loss of bond stiffness and can be determined experimentally or estimated according to an existing model, e.g., based on Eligehausen et al. (1983) as a multiple of $u_{s,\max}$ (depending on confinement and bar surface conditions; see Section 2.3.5). The values of $\gamma_{p.\min}$ and $\gamma_{p.\max}$ are assumed equal to 0.65 and 0.90, respectively, in Hawkins et al. (1982). After returning to the target point where the pinching branch intersects the reloading secant branch, the latter branch continues until it intersects the envelope and then follows the envelope until the next unloading occurs.

Figure 2.12 illustrates schematically the hysteretic response of the bond-slip model. The loading path follows the roman letters a-b-c-d-e-f-g-h. The roman letters a-b-c-d′-e′-f′-g′-h′ describe a loading path for the case where the effect of hysteretic degradation is included, which is discussed in the next section. Note that the loading history in Figure 2.12 is such that the first unloading occurs while the bond behavior is mainly elastic, and as a result the pinching and reloading branches coincide following stress reversal. Loading takes place along the envelope curve a-b until unloading at b, which should temporarily be designated (u_s^{un}, τ^{un}) and, at the same time, $(\overline{u}_s^{un}, \overline{\tau}^{un})$, until subsequent unloading (for clarity, designations not shown on the plot). The response then follows the slope S^{un} in Equation (2.49) along b–c before it starts elastic pinching at c, which is defined by Equations (2.50)–(2.51). The first pinching branch follows c–d according to Equation (2.52) until it intersects the envelope curve at d and continues along d–e.

When unloading at e, the unloading point (u_s^{un}, τ^{un}) is designated $(\overline{u}_s^{un}, \overline{\tau}^{un})$ and the farthest unloading point on the opposite-sign envelope (i.e., point b) is designated $(\hat{u}_s^{un}, \hat{\tau}^{un})$ as the target of the subsequent reloading. This is opposite to the case when unloading first took place at b. Note that throughout the loading history, the designations $(\overline{u}_s^{un}, \overline{\tau}^{un})$ and $(\hat{u}_s^{un}, \hat{\tau}^{un})$

interchange as the direction of loading switches, whereas (u_s^{un}, τ^{un}) always denotes the most recent unloading point. Unloading from e follows the slope S^{un} in Equation (2.49) until f, defined by Equations (2.50) and (2.51). Subsequently, inelastic pinching starts with the pinching slope S_{pin}^{i} in Equation (2.53) until it intersects the linear reloading branch of slope S_{sec} in Equation (2.55) at g, and then follows the reloading branch along g–h until it intersects the envelope curve at h. Subsequently, the response follows the envelope curve until further unloading.

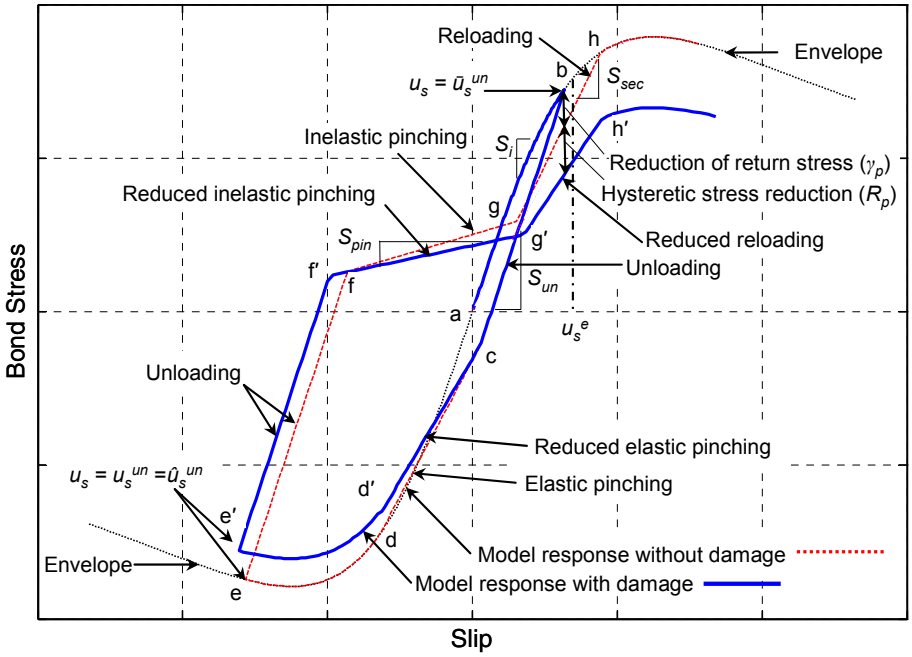

Fig. 2.12 Hysteretic reduction of bond-slip envelope curve and reloading stiffness.

An exceptional case occurs when unloading takes place from one direction of loading when the other direction has not been previously loaded or only loaded to a relatively low stress which results in an undefined or unrealistically high value of S_{sec} that can never converge back to the envelope. This will often be the case at the first instance of unloading to be followed by inelastic pinching. In this case, the pinching branch continues until it intersects the envelope curve and the linear reloading branch with slope S_{sec} is ignored. The hysteretic response to this exceptional case is illustrated in Figure 2.13 for one cycle of inelastic bond behavior prior to

unloading. The loading path follows the roman letters a-b-c-d-e, with the inelastic pinching branch c-d returning directly to the envelope at d and then continuing along d–e as discussed.

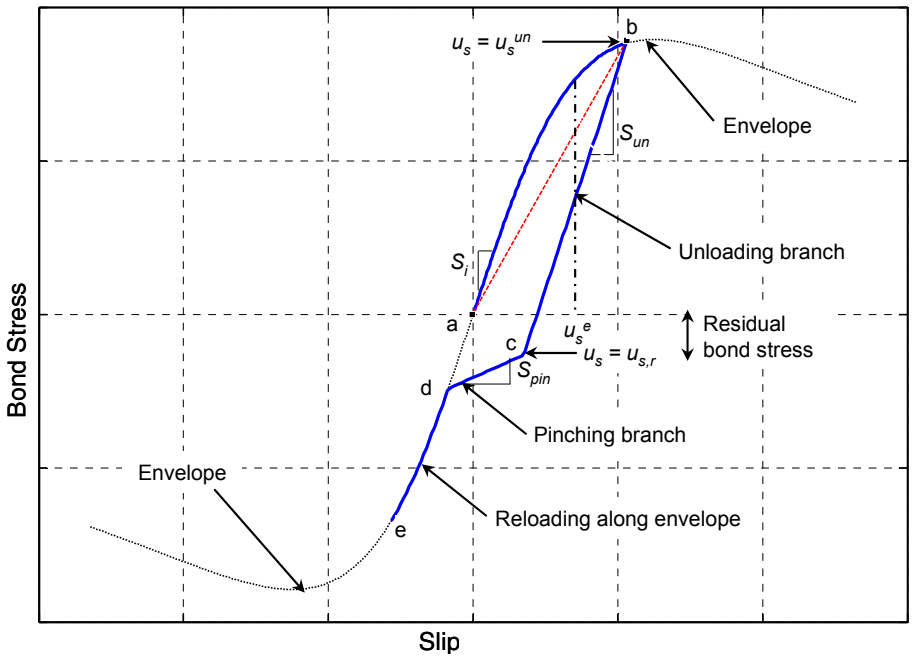

Fig. 2.13 Model illustration of hysteretic bond-slip behavior.

2.3.4 Hysteretic Stress Reduction

A hysteretic damage component is added to the bond-slip model to reduce the envelope curve and reloading stiffness due to hysteretic degradation. First, the following maximum slip displacement-based damage index is proposed:

$$D_p = \max\left\{\left|\hat{u}_s^{un}\right|, \left|\bar{u}_s^{un}\right|\right\} / u_{s,ult} \tag{2.58}$$

Next, the following reduction factor is defined and multiplied by the bond stress:

$$R_p = 1 - D_p^{\alpha_p \left(1-\alpha_{pn}\left(1-1/n\right)\right)} \text{ with } 0 < \alpha_p \text{ and } 0 \le \alpha_{pn} < 1 \tag{2.59}$$

where α_p and α_{pn} are model parameters to be calibrated by fitting to experimental measurements (see Section 2.3.5), and n is the number of minor loading half-cycles following the maximum slip level. A minor loading half-cycle is defined as one in which subsequent unloading takes place during pinching or reloading and before returning to the reduced envelope.

The effect of hysteretic stress reduction is illustrated in Figure 2.12 along the loading path designated by the roman letters a-b-c-d′-e′-f′-g′-h′. Loading along a-b and unloading along b-c are unaffected by hysteretic degradation. The branch d-e along the envelope curve is reduced to d′-e′ via multiplying the bond stresses at d and e by R_p in Equation (2.59), and so the elastic pinching slope along c-d is reduced. The unloading slope of e′-f′ is the same as e-f. Hysteretic degradation results in reduction of the envelope curve starting from h according to Equation (2.59), and therefore both the inelastic pinching slope along f′-g′ and the linear reloading slope along g′-h′ are consequently reduced.

2.3.5 Parameter Calibration and Experimental Verification

In this section, the lap-splice model developed for longitudinal reinforcing steel bars is compared to the experimental results published in Viwathanatepa (1979) and Hawkins et al. (1982) to assess its validity. In addition, the calibration process involved in performing the comparison is intended to inform the selection of default parameter values for the model. Table 2.2 lists the range and statistics of values used for every parameter in reproducing 15 cyclic and monotonic bar pull-out experiments. For monotonic model response, the sole important parameter is $u_{s,\max}$, which affects the initial stiffness. The calibrated results show that this parameter can be estimated with little uncertainty as bounded by Equations (2.44) and (2.47). For the hysteretic response, the parameters $u_s^e/u_{s,\max}$, k_r, β_p, $\gamma_{p,\max}$, and $\gamma_{p,\min}$ have a secondary effect on the shape of pinching and reloading branches. They can be estimated with reasonable flexibility without significantly affecting the peak stress and the general profile of the response. The parameters $u_{s,ult}/u_{s,\max}$ and α_p play a primary role in determining the rate of hysteretic decay. The calibrated values of $u_{s,ult}/u_{s,\max}$ reflect considerable uncertainty and should be carefully evaluated taking into consideration the bar surface and confinement conditions. Finally, the parameter α_{pn} can be estimated with little uncertainty and has secondary influence on the model output.

Table 2.2 Calibrated bond-slip model parameter ranges.

Parameter	Minimum value	Maximum value	Mean Value	COV
$u_{s,\max}$ [mm]	1.15	1.40	1.34	0.075
$u_{s,ult}/u_{s,\max}$	8.00	25.00	13.91	0.416
$u_s^e/u_{s,\max}$	0.10	0.20	0.16	0.313
k_r	0.15	0.20	0.16	0.150
β_p	0.05	0.20	0.14	0.534
$\gamma_{p,\max}$	0.90	0.95	0.91	0.015
$\gamma_{p,\min}$	0.70	0.85	0.75	0.042
α_p	1.20	2.00	1.54	0.238
$\alpha_p - \alpha_{pn}$	0.60	1.10	0.93	0.167

The experiments reported in Hawkins et al. (1982) include individual steel bars bonded to anchored concrete blocks over a short length (only 1–4 lugs) and subjected to increasing push-pull displacements. The bars are subjected to stresses lower than their yield strength in order to enable the reproduction of the local bond-slip behavior from the recorded forces and displacements by subtracting the elastic elongation of the bars. Slip deformations and stresses are assumed uniform along the bonded length. The experiments include monotonic and cyclic—both symmetric and asymmetric—displacement histories. The primary investigated variable in the experimental study is the concrete compressive strength, which varied between 18 and 47 MPa. The majority of the experiments are conducted using deformed bars of 25 mm diameter, while a few experiments are conducted on deformed bars of 19, 32, 36, 38, and 40 mm diameter and plain bars of 19 and 25 mm diameter. All bars used in testing are of 60 MPa nominal yield strength.

Analytical simulation is performed using the proposed lap-splice model and the reported material properties. The experimental setup reported in Hawkins et al. (1982) results in reinforcing bars that are better-confined than typical column reinforcement yet provides no direct

means to estimate the confining stress. Therefore, the monotonic bond strengths were obtained as reported from the monotonic loading experiments, while $u_{s,\max}$ was estimated using Equation (2.47). The bond-slip model was then verified and calibrated by reproducing measurements from the cyclic loading experiments. Figure 2.14a illustrates the comparison between the proposed model and the experiment of an asymmetric tension-only load history as well as the monotonic response of a 25 mm deformed bar embedded over two lugs in a 34 MPa concrete block. The simulated monotonic envelope successfully reproduces the pre-peak monotonic response and slightly underestimates the slope of the softening branch. The simulated cyclic response successfully estimates the peak stress, reproduces the hysteretic degradation, and predicts the residual bond stress capacity at the end of the experiment. However, the model overestimates the experimentally observed reloading stiffness due to its linear approximation.

Figure 2.14b illustrates the comparison between the proposed model and the experiment of a symmetric load history as well as the monotonic response of a 25 mm deformed bar embedded over two lugs in a 47 MPa concrete block. The simulated response successfully reproduces the pre-peak monotonic response (while slightly underestimating the softening branch), the peak stress, and the hysteretic degradation on the tension (pull or positive) side. However, since the effect of slip direction has not been incorporated in the model, the simulated stresses in the early stages of the compression (push or negative) direction are underestimated. The comparison suggests that the error in estimation is not likely to have a significant effect on modeling of concrete column response, and that the error decreases with the increase of hysteretic bond degradation which is common during seismic loading. Moreover, the later post-peak response of the model is of higher interest in modeling collapse-prone problems as is the case in this report than the early post-peak behavior. Also noted is a discrepancy between the simulated and measured residual bond stress directly after unloading in the push side, since the measured stresses show a temporary spike in the direction opposite to the preceding push loading and then decreases in magnitude to a level equal to the simulated stresses. It is thought that this spike exists due to the higher value of the static friction coefficient between the deformed bar and the neighboring concrete at the beginning of the deformation reversal than the kinematic friction later. The inclusion of such a spike in a computational model is numerically problematic and constitutes very little practical importance. It is observed that the linear pinching and

reloading branches in the model cannot accurately reproduce the nonlinear reloading behavior in all the experimentally observed reloading branches, yet this is considered an acceptable simplification.

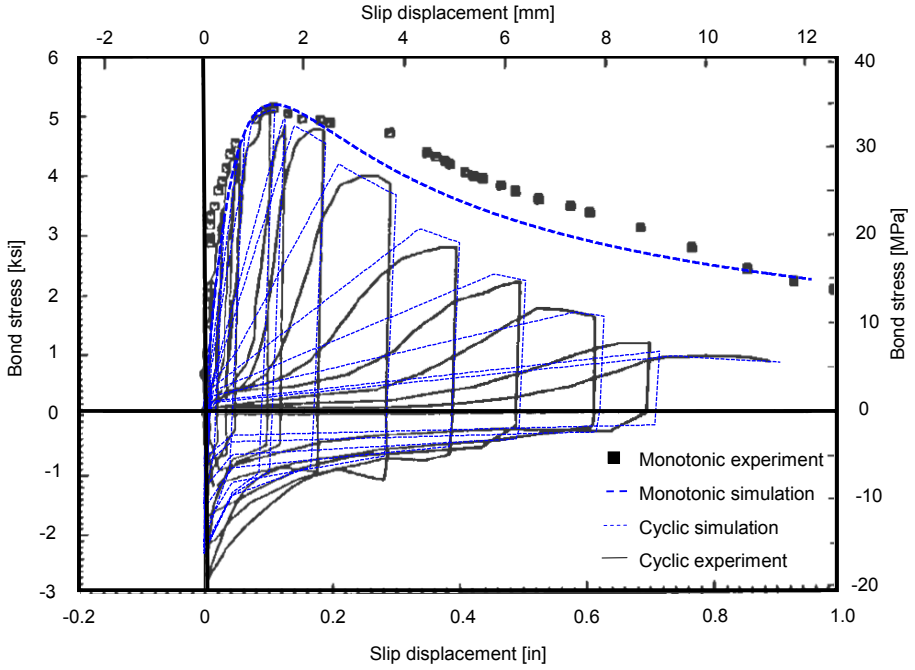

(a) Asymmetric (one-sided) cyclic displacement history

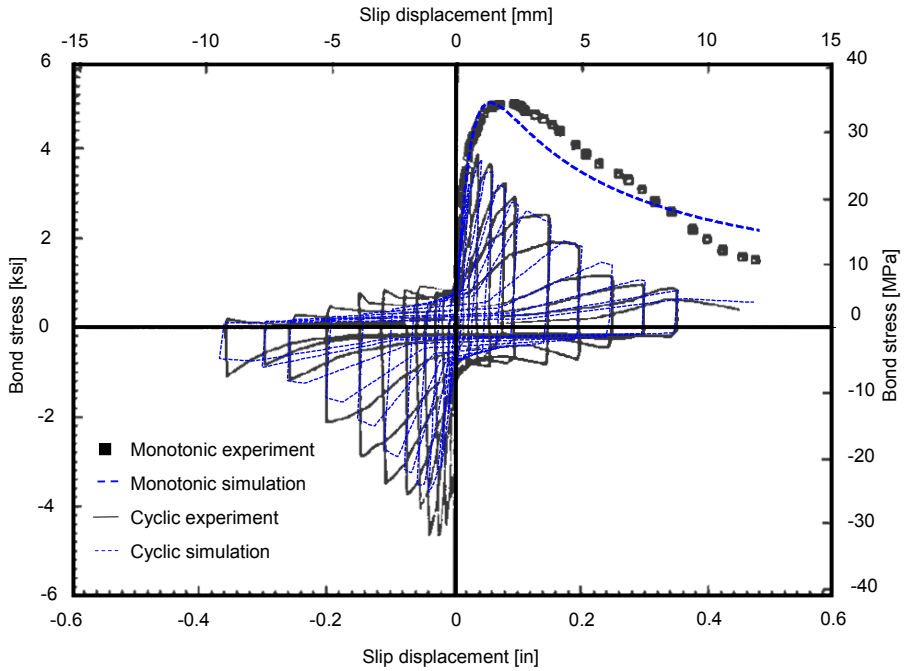

(b) Symmetric cyclic displacement history

Fig. 2.14 Model simulation of Hawkins et al. (1982) bond-slip experiments.

The experiments reported in Viwathanatepa (1979) include individual deformed steel bars embedded in column stubs over a variable anchorage length and subjected to increasing push-pull displacement histories. Bar diameter ranges from 19 to 32 mm, and the column stub (anchorage) length ranges from 381 to 635 mm. The bars are embedded in the center of the column stubs which are transversally reinforced to provide confinement. The applied force on the bar (from which the bar's axial stress is computed) and the relative displacement between the bar at the end of the embedded length and the stub face are recorded. The strains in the bar along the embedded length are also recorded to reproduce the spatial distribution of slip deformation along the bar. The experiments include monotonic and symmetric cyclic displacement histories. Average concrete strength is 33 MPa, and steel material properties are reproduced in Table 2.3.

Table 2.3 Steel properties used in modeling (Viwathanatepa 1979) experiments.

Experiment	25 mm (#8) bar	32 mm (#10) bar	13 mm (#4) bar (ties)
E_s [GPa]	201	201	203
E_{sh} [GPa]	15	15	20
σ_y [MPa]	469	471	493
σ_u [MPa]	738	738	745
ε_u	0.13	0.13	0.12
Tie spacing [mm]			100
Number of branches in each tie			4

Analytical simulation is performed using the proposed lap-splice model and the reported or estimated material properties. The mechanical stress-strain behavior of the steel bars is assumed to follow the model in Chang and Mander (1994). The confining pressure due to transverse reinforcement can be computed from the geometry and material properties of the transverse reinforcement according to the procedure outlined in Mander et al. (1988) and by assuming a transverse dilation strain of $\varepsilon_{dl} = 0.00125$ according to Xiao and Ma (1997). The total confining stress on the bars during the experiment is expected to be larger than those computed due to the effect of placement at the center of the column stub instead of the sides or corners.

However, the effect of this discrepancy was evaluated and found to be tolerable by comparing the simulated and measured peak stresses at bond failure in the cases of monotonic loading. Since the lap-splice model is developed for the geometric setup shown in Figure 2.9 where two bars slide relative to each other, the average total strain involved in its constitutive model is a sum of mechanical elongation and slip-induced strains in two bars, whereas the reported experiments involve one bar slipping relative to a fixed column stub. Therefore, the analytical model has to be manipulated in order to reflect the geometry of the experimental setup. This is achieved by multiplying by a factor of two the experimental displacement history before inputting it to the simulation in order to result in the correct slip-induced strains and corresponding stresses in the serially coupled materials' respective constitutive models (i.e., steel bar and bond-slip). Experimental records of bar strains in Viwathanatepa (1979) illustrate that the distribution of slip displacement along the embedded length of the bar can be adequately interpolated as linearly varying from zero at the stress-free end to a maximum at the other end of the embedded length, which supports the computational procedure discussed above based on the geometric setup of Figure 2.9.

Figure 2.15a illustrates the comparison between the simulation and the experimental results for a 25 mm bar embedded in a 635 mm column stub. The simulated response successfully identifies the peak stress cycle and estimates the peak stress in the pull direction. The reproduction of hysteretic degradation is generally successful. However, the simulated unloading stiffness is sometimes lower than its experimental counterpart, and the residual stress at unloading is underestimated for large displacement magnitudes. Figure 2.15b illustrates the comparison between the simulation and the experimental results for a 32 mm bar embedded in a 635 mm column stub. Similar observations to those made for Figure 2.15a can be made for Figure 2.15b. However, the simulated unloading stiffness and residual stresses at unloading exhibit a better match to the experimental observations in Figure 2.15b than in Figure 2.15a. However, in Figure 2.15b the maximum stresses at the end of a few displacement cycles are overestimated relative to the experimental observations, which is not the case in Figure 2.15a. In both cases, the simulated stiffness and strength of the pre-peak response in the push direction are underestimated, but the post-peak response does not seem affected by neglecting the possibly asymmetric bond-slip behavior in the constitutive model.

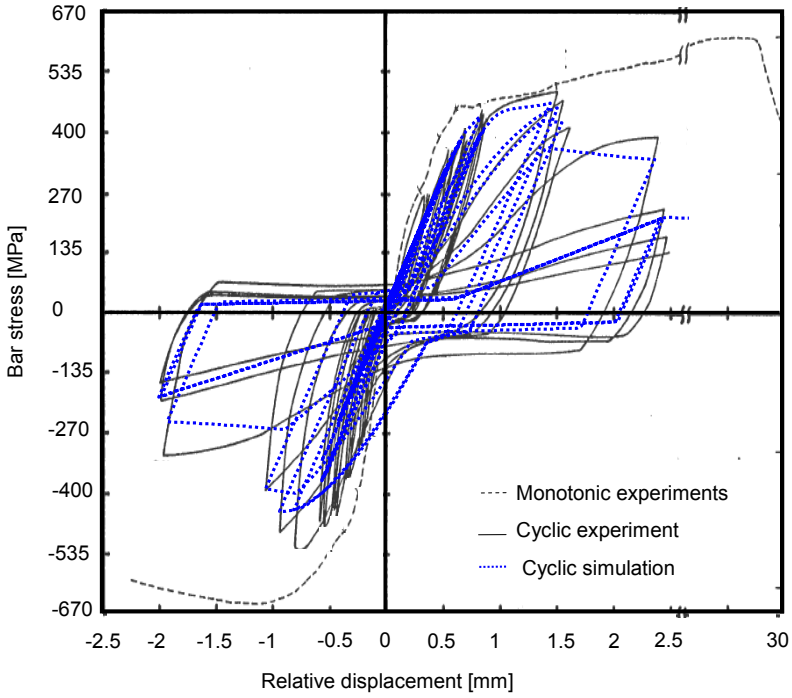

(a) 25 mm (#8) bar embedded in 635 mm (25″) column stub

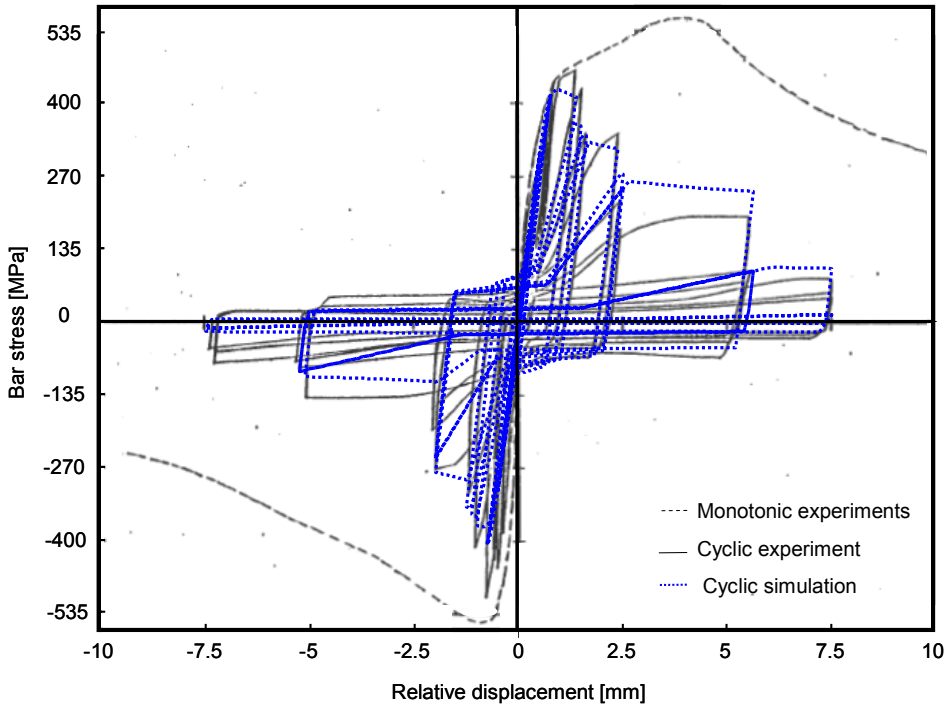

(b) 32 mm (#10) bar embedded in 635 mm (25″) column stub

Fig. 2.15 Model simulation of Viwathanatepa (1979) bond-slip experiments.

2.4 SUMMARY

In this chapter, analytical material models were proposed to model the confinement-dependent axial stress-strain response of buckling-prone and lap-spliced reinforcing steel bars. Closed-form analytical expressions for estimating the critical buckling length and corresponding stress were derived using an energy approach that incorporates the restraining effect of the transverse ties. The post-buckling stress-strain behavior of steel bars was modeled using a strain decomposition approach based on an assumed initial imperfection, which reproduces softening during compression loading and reduced stiffness while the buckled bar straightens during tension loading. Hysteretic stress reduction and fracture were modeled using a damage model based on low-cycle fatigue. The analytical model was calibrated using published data from three experimental investigations of reinforcing steel bars subjected to monotonic and cyclic loading that exhibit buckling. For lap-spliced reinforcing steel bars, a strain decomposition approach was adopted based on the equilibrium of axial and shear bond stresses along the splice region. A constitutive material law for cyclic bond-slip behavior was developed by combining a confinement-sensitive envelope curve, a set of multi-linear unloading-reloading rules, and a hysteretic stress reduction factor. The constitutive bond-slip material was calibrated using experimental data of locally bonded steel bars subjected to monotonic and cyclic deformations. The use of the bond-slip constitutive law to model bond-slip of lap-spliced bars using the proposed strain decomposition approach was calibrated using published data from experimental investigations of starter bars embedded in reinforced concrete column blocks.

3 Modeling of Concrete Column Cross Sections

The nonlinear response of axially loaded RC columns to laterally imposed deformations is a phenomenon made complex by a number of factors. The interaction between cross-section response to axial load, bending moment, and shear force plays an important role. In addition, the geometry of a column, the proportioning of its core concrete, and the longitudinal and transverse reinforcement often define the force capacity and governing mode of failure. Moreover, the detailing of these materials affects the deterioration of a column's lateral load-carrying capacity with the increase in number and magnitude of deformation cycles, and often determines a column's ability to maintain its axial load-carrying capacity following the deterioration and loss of its lateral load-carrying capacity.

FE modeling of RC columns whose behavior is dominated by flexure-axial interaction using fiber-discretization of beam-column element cross sections has been successfully established. The theoretical formulation for finite elements using fiber-discretized cross sections (referred to hereafter as fiber elements) to represent the spread of plastic regions along the element length (referred to hereafter as distributed plasticity) can be reviewed in e.g., Spacone et al. (1996a,b). Fiber elements invoke displacement-based, force-based, or mixed-interpolation formulations for numerically integrating the strain energy over the FE length. They offer a practical method to include the effect of flexure-axial interaction without the computational cost of solid modeling and multi-dimensional material constitutive models. However, the fiber-discretized modeling of the cross-section response is independent of the element formulation being used, and in fact can be used in conjunction with lumped-plasticity elements such as beams with plastic hinges, as demonstrated in Mazzoni et al. (2004). The process of developing accurate fiber-discretization of a cross section depends on selecting an adequate mesh size and

accurate constitutive material models for the uniaxial response of individual fibers. Mesh selection has been extensively investigated in the literature, and with the abundance of uniaxial material models for reinforcing steel and concrete, there appears to be little room for improvement. However, this chapter introduces a fundamental improvement to the modeling process by combining the low computational cost of fiber elements together with confinement-sensitive constitutive concrete material and cross-section models.

Chapter 2 presented the modeling of the individual response of reinforcing steel. The modeling process accounted for two failure modes in non-ductile column design, namely the buckling of laterally restrained steel bars in compression and the failure of lap-spliced steel bars in tension. The analytical models in Chapter 2 explicitly account for the effect of lateral confinement whether supplied by internal ties or external retrofit measures. Both the confining stress and lateral stiffness supplied by transverse reinforcement were shown to be of importance. This chapter complements the previous one by introducing analytical models to compute the stress state in transverse reinforcement and include its effect on the individual cross-section fibers. First, a review of the available literature about incorporating the effect of transverse reinforcement on the lateral response of axially loaded columns is conducted. Next, a uniaxial material model and a cross-section model for the response of RC column cross sections subjected to the combined effect of axial force and bending moment are developed. Together these two models compute and explicitly account for the stress state and potential failure of transverse reinforcement based on their governing constitutive laws. These models are calibrated using comparisons with experimental results from Ahmad and Shah (1982), Lokuge et al. (2003), and Mosalam et al. (2007a,b). They can be used together with the material models developed in Chapter 2 to construct beam-column elements using distributed or lumped plasticity, following force-based, displacement-based, or mixed FE formulation. They can also be combined with the shear friction-based model developed in Elwood (2002)—and recently updated in Elwood and Moehle (2005)—to account for shear-axial interaction in shear-critical columns as discussed in Section 3.1.4.

3.1 REVIEW OF PUBLISHED LITERATURE

The literature reviewed in this chapter pertains to the role of RC in columns as follows:

1. Modeling of concrete behavior in tension
2. Modeling of confined (and unconfined) concrete behavior in compression
3. Modeling of transverse confinement
4. Modeling of shear-axial interaction

3.1.1 Modeling of Concrete Behavior in Tension

Concrete behavior in tension may seem of secondary importance to modeling of collapse. Nonetheless, the relatively low tensile stresses that develop in concrete cross sections may significantly influence the stiffness of a column and possibly its force capacity, and thus may affect the demands imposed on the column during a dynamic analysis up to collapse where it is known that the collapse phenomenon is path dependent (Powell 2005). It is widely believed that concrete displays a linear behavior when subjected to a uniaxial tensile stress until cracking occurs when the tensile strength is reached. After initial cracking, tensile stress can still be transferred across a crack face through intact regions (commonly referred to as "the process zone"), and surface friction and does not drop instantly to zero (Bazant and Oh 1983). As the crack length grows, the crack width increases, shifting the process zone further toward the crack tip and reducing the ability to transfer tensile stress. This process is known as tension softening and is reviewed in Bazant et al. (2004).

Several researchers conducted experimental tests on the monotonic tensile-softening behavior, e.g., Cornelissen et al. (1985), as well as on the cyclic behavior, e.g., Yankelevsky and Reinhardt (1989). Analytical models have been developed based on the basic properties of the concrete aggregates to determine the critical crack width at which the tensile stress capacity vanishes, as well as crack width values that affect the hysteretic behavior. A number of linear, multi-linear, and nonlinear models are reviewed in Van Mier (1997). A comparative study and a deterministic sensitivity analysis of several such models in the context of modeling bond failure due to concrete cover splitting is recently conducted in Talaat and Mosalam (2007). For the purpose of modeling the collapse of RC columns in this report, linear and multi-linear tensile-

softening models are used after preliminary calibration showed that little accuracy can be gained by using computationally more expensive nonlinear models.

3.1.2 Modeling of Confined Concrete Behavior in Compression

The effect of transverse reinforcement on the strength and the ductility of concrete in a RC column core is well-established, and there are several analytical models that attempt to incorporate this effect into the uniaxial concrete stress-strain behavior. A literature review of existing confined concrete stress-strain models can be found in Teng and Lam (2004) and Lokuge et al. (2005). These existing confined concrete models are classified by their analytical form into three categories: Models based on equations proposed in Sargin et al. (1971), such as El-Dash and Ahmad (1995) and Attard and Setunge (1996); models based on equations proposed in Park et al. (1972), such as Sheikh and Uzumeri (1982) and Saatcioglu and Razvi (1992); and models based on equations proposed in Popovics (1973), such as Mander et al. (1988) and Binici (2005). The third class of constitutive models have the advantage of using one continuous nonlinear function, suitable for numerical implementation, to describe both ascending and descending branches of the stress-strain curve in compression.

Earlier modeling attempts define the confinement in terms of the estimated lateral stress supplied by the transverse ties. These models include Mander et al. (1988) and Razvi and Saatcioglu (1999), which are originally developed to model transverse steel-confined concrete. Owing to the yielding property of steel, the confining stress can be satisfactorily estimated for the entire analysis duration without explicitly computing the dilation strain in the core concrete. However, Pantazopoulou (1995) demonstrates that the core dilation strain under axial load best describes the internal damage sustained by concrete and should be used instead to determine the confining stress. This is true, since the concrete is passively confined and the confining stresses are being developed as the reaction of the confining medium to the lateral expansion of the core. Dilation-based monotonic envelope models have been developed in Pantazopoulou (1995) and Saenz and Pantelides (2007), which are particularly useful in modeling the effect of externally applied FRP composite wraps commonly used in retrofitting seismically deficient columns. FRP composites generally exhibit an elastic-brittle behavior and lack the analytically convenient

yielding characteristic of confining steel reinforcement (ties, hoops, or spiral) or jackets. Another analytical model has been developed in Lokuge et al. (2004) and (2005) for cyclic and monotonic behavior of high strength concrete (HSC) under active (prescribed) and passive confinement, respectively. The model developed by Binici (2005) uses the dilation strain in concrete, the constitutive model of the confining medium, and mechanical compatibility of lateral strains to develop a confining stress-based material model for confined concrete. The models developed in Binici (2005) and Lokuge et al. (2004) are modified and used for modeling the uniaxial behavior of confined concrete in this report, as will be presented and discussed in the next section.

3.1.3 Modeling of Transverse Confinement

Constitutive models for the uniaxial behavior of confined concrete cannot be employed directly in a column cross section before estimating the magnitude and spatial distribution of confinement supplied by transverse reinforcement under the combined action of axial load and bending moment. Earlier models assume the effect of confinement to be uniform throughout the cross section and estimate the confining stress using the steel yield stress, the geometry and arrangement (spacing) of transverse reinforcement, and an efficiency factor tied to the geometric shape of the cross section (Chung et al. 2002; Mander et al. 1988; Saatcioglu and Razvi 1992). Even though this approach is strictly developed for steel-confined concrete, it has been used in several studies for modeling the confining effect of FRP composites (Xiao and Ma 1997).

The non-uniform distribution of confining stresses is studied in Mau et al. (1998) by means of linear-elastic FE solutions using solid elements. The results show that the confinement stresses vary significantly within the cross section and that the relationship between tie spacing and overall confinement efficiency is similar for circular and rectangular cross-section shapes. The use of solid modeling is computationally demanding for complex models involving extremely nonlinear behavior. There are a few studies available which attempted to model the non-uniform confinement effect within a RC cross section while avoiding solid modeling or resorting to heuristic approximations. A study by Parent and Labossiere (2000) includes the spatial distribution of confinement within a fiber element and relates the dilation strain of

individual fibers within the cross section to the computed axial strain at each fiber using equations proposed in Mirmiran and Shahawy (1997a,b). More recent studies of Binici and Mosalam (2007) and Mosalam et al. (2007b) describe a confining stress distribution model for FRP-confined cross sections using the equilibrium of bond stresses along the FRP-concrete interface. A comparison with experimental records of circumferential strains measured in FRP composites shows agreement with the analytical model. Moreover, computational simulations of several experiments of RC columns (see Chapter 5) suggest that the model performance is adequate for transverse steel-confined columns as well. A version of this latter model is implemented in this report, and hence its analytical formulation is presented and discussed in Section 3.3.

3.1.4 Modeling of Shear-Axial Interaction

In RC column with inadequate transverse reinforcement, shear failure can take place prior to flexural failure, resulting in a brittle mode of failure and a sudden reduction in lateral load-carrying capacity. In RC columns designed with adequate transverse reinforcement, shear strength should be sufficient for the column to develop its flexural strength (i.e., yielding of longitudinal reinforcement) before shear failure takes place, resulting in a ductile behavior afterwards. However, the yielding of longitudinal reinforcement and the subsequent increase in flexural crack widths with increasing drift demands at nearly constant flexural demands, reduce the cross section's ability to transfer shear stresses, and may ultimately lead to non-ductile shear failure. For shear-damaged columns, the loss of lateral stiffness leads to the inability to resist excessive lateral drift demands leading to axial collapse, i.e., loss of gravity load system, due to P-Δ effect.

Several researchers have proposed analytical models for predicting shear failure of columns. Some of these models are based on lateral displacement ductility, e.g., Priestley et al. (1994), Sezen (2002), and Sezen and Moehle (2004). However, ductility-based models have been criticized for being highly sensitive to inherent variability in shear strength. In contrast, models proposed in Pujol et al. (1999), (2000), and Pujol (2002) estimate the drift capacity at shear failure based on statistical data, Coulomb failure, and Coulomb failure with displacement

history, respectively. However, these models do not describe the column response after shear failure nor address the hysteretic behavior.

To address the issue of hysteretic behavior following shear failure, Ricles et al. (1998) uses an element model composed of a linear beam-column component which has flexural and shear nonlinear components lumped at both ends. This model predicts shear failure and accounts for post-failure stiffness and strength degradation, besides flexural inelasticity, using evolutionary yield surfaces. However, this model needs to be calibrated for each element and joint configuration independently.

The model proposed in Elwood (2002) empirically defines an expression for the lateral drift at shear failure, and a shear-friction-based expression for the lateral drift at subsequent axial failure. These expressions are included below for completeness.

$$\frac{\Delta_s}{L} = \frac{3}{100} + 4\rho'' - \frac{v}{6020\sqrt{f_c'}} - \frac{P}{40A_g f_c'} \geq \frac{1}{100} \qquad \text{[N, mm units]} \tag{3.1}$$

$$\frac{\Delta_a}{L} = \frac{4}{100}\frac{1+\tan^2\theta}{\tan\theta + P\left(s_t / A_{st} f_{st} d_c \tan\theta\right)}$$

where Δ is the lateral displacement, subscripts s and a refer to values at shear and the axial limit states, respectively, v and P are the applied shear stress and axial load, respectively, A_g is the gross cross-sectional area, f_c' is the 28-day concrete compressive strength of the standard cylinder, ρ'' is the transverse reinforcement ratio A_{st}/bs_t where b is the cross-section width or diameter, s_t, A_{st}, f_{st}, and d_c are the spacing, cross-sectional area (all branches), yield stress and core depth from centerline to centerline of transverse reinforcement, respectively, and $\theta = 65^o$ is assumed to be the orientation of the shear failure plane. Recent developments of this model in Elwood and Moehle (2005) correlate the angle θ to the axial load level and reduce the buckled longitudinal bars' axial capacity. However, the estimation of the buckled bar stress capacity is based on assuming no fracture in the transverse reinforcement and a corresponding buckling length between $0.5s_t$ and s_t ($0.8s_t$ is adopted based on statistical correlation). The ratio between this model's prediction of lateral drift values at axial collapse compared to results from 12 experiments reported in Lynn (2001) and Sezen (2002) are reported to have mean values

of 0.97 and 1.02, and coefficients of variations of 0.26 and 0.22, upon including or excluding the reduction in the buckled bar axial capacity, respectively.

Equations (3.1) are used to define failure surfaces (hereafter referred to as "limit curves") for two coupled nonlinear shear-axial springs added in series at the ends of a nonlinear beam-column FE component to create a compound element, as illustrated in Figure 3.1. The behavior of the compound element can be characterized using three or four main phases as identified in Figure 3.1, based on shear-axial damage progression. Phase 1 takes place prior to shear failure; the response of the springs is linear-elastic and mainly rigid unless significant shear flexibility in short members needs to be accounted for. The only possible source of nonlinearity in this phase is due to the beam-column component. Phase 2 starts when the computed lateral drift in the shear spring violates the shear force-lateral drift limit curve. The shear spring follows a multi-linear hysteretic behavior with symmetric backbone curves while the flexural beam-column component unloads as a result. Phase 3 is identified when the computed lateral drift in the shear spring violates the axial force-lateral drift limit curve. Perfectly brittle axial collapse of the column may be defined at this stage. Alternatively, an optional Phase 4 (indicated by lighter tone in Fig. 3.1) can be adopted, in which the axial spring follows a softening branch, while the shear spring reaches a residual force capacity. This latter phase has been observed to present computational convergence problems (Elwood 2004). This analytical model has been computationally implemented as a *LimitStateMaterial* component in the structural modeling software platform OpenSees (Elwood 2002). This model can receive more support from additional experimental data to calibrate the softening branch of the axial spring component, and a physics-based expression for the shear failure limit curve, since the empirical formula proposed in Elwood (2002) is derived from statistical analysis of tests that show a considerable amount of scatter. Moreover, the data used for calibration of the shear and axial limit curve equations are derived from column experiments conducted mostly under compressive axial loads and none under tensile loads—which may occur in columns of RC frames while resisting overturning moments. However, this model is both practical and intuitive, and has been adapted to model the axial collapse of shear-critical columns in Chapter 7.

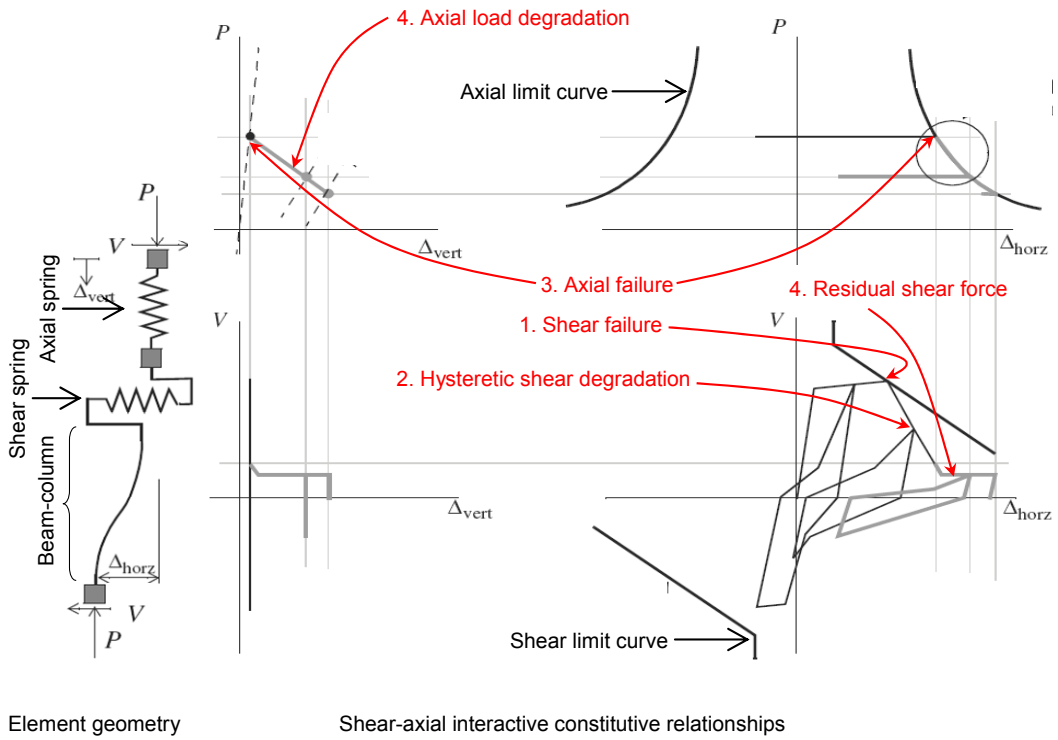

Fig. 3.1 Shear-axial limit-state material model developed in Elwood (2002).

3.2 ANALYTICAL MODEL FOR CONFINED CONCRETE MATERIAL

The proposed uniaxial material model for confined concrete behavior has been formulated from five main components. The first and second components are the monotonic envelope in compression and the compatibility of lateral strains, both assumed to follow the model first developed in Binici (2005). The third component is the hysteretic loading and unloading rules, modified from Lokuge et al. (2004). The fourth component is the hysteretic strength reduction of the monotonic envelope, assumed to depend on dissipated hysteretic energy. The fifth component is the behavior in tension, assumed to follow confinement-independent linear pre-cracking, softening, and unloading-reloading branches for simplicity. These five components are individually discussed in the following sections. The special case of unconfined (e.g., cover) concrete can also be modeled as a special case with confinement set to zero.

3.2.1 Monotonic Confined Concrete Envelope in Compression

The adopted confined concrete envelope model is shown in Figure 3.2 and has been developed and fully discussed in Binici (2005) and Binici and Mosalam (2007). The governing equations are being reproduced herein for convenience and completeness. The envelope model incorporates the confinement ratio $\phi = \sigma_3 / f_c'$ and a Leon-Pramono failure criterion (Pramono and William 1989) which depends on the fracture energy in compression to determine the axial stress σ_1 at the elastic stress limit $\sigma_{1,e}$, the peak stress $\sigma_{1,cc}$, and the residual stress at the end of the softening branch $\sigma_{1,r}$. Accordingly,

$$\sigma_1 = -f_c'\left(k_c\sqrt{c_c + m_c\phi} - (1-k_c)\phi^2 + \phi\right) \tag{3.2}$$

where k_c is a hardening parameter equal to 0.1, 1.0, and 1.0 for evaluating $\sigma_{1,e}$, $\sigma_{1,cc}$ and $\sigma_{1,r}$, respectively, and c_c is a softening parameter equal to 1.0, 1.0, and 0.0 for evaluating $\sigma_{1,e}$, $\sigma_{1,cc}$ and $\sigma_{1,r}$, respectively, and $m_c = \dfrac{f_c'^2 - f_t'^2}{f_c' f_t'}$, f_t' being the concrete uniaxial tensile strength.

The elastic strain limit $\varepsilon_{1,e}$ and the strain $\varepsilon_{1,cc}$ corresponding to peak stress are given by

$$\varepsilon_{1,e} = \frac{\sigma_{1,e}}{E_c} \tag{3.3}$$

$$\varepsilon_{1,cc} = 5\varepsilon_{1,c}\left(\frac{|\sigma_{1,cc}|}{f_c'} - 0.8\right) \tag{3.4}$$

where $\varepsilon_{1,c}$ is the axial strain corresponding to unconfined compressive strength f_c'.

The proposed envelope describes the axial stress-strain behavior of confined concrete in compression using three continuous branches: a linear elastic branch, a Popovics-type function for the hardening branch (Popovics 1973), and an exponential softening branch (Pivonka et al. 2000). This constitutive law is thus given by

$$\sigma_1 = \begin{cases} E_c \varepsilon_1 & \text{if } 0 \le -\varepsilon_1 \le -\varepsilon_{1,e} \\ \sigma_{1,e} + (\sigma_{1,cc} - \sigma_{1,e}) \left(\dfrac{\varepsilon_1 - \varepsilon_{1,e}}{\varepsilon_{1,cc} - \varepsilon_{1,e}} \right) \dfrac{r_c}{r_c - 1 + \left(\dfrac{\varepsilon_1 - \varepsilon_{1,e}}{\varepsilon_{1,cc} - \varepsilon_{1,e}} \right)^{r_c}} & \text{if } -\varepsilon_{1,e} \le -\varepsilon_1 \le -\varepsilon_{1,cc} \\ \sigma_{1,r} + (\sigma_{1,cc} - \sigma_{1,r}) \exp\left[-\left(\dfrac{\varepsilon_1 - \varepsilon_{1,cc}}{\alpha_{cr}} \right)^2 \right] & \text{if } -\varepsilon_{1,cc} \le -\varepsilon_1 \end{cases} \tag{3.5}$$

where ε_1 is the axial compressive strain (negative) and E_c is the initial modulus of elasticity of concrete. The material constant r_c is defined as

$$r_c = \frac{E_c}{E_c - E_{cs}} \quad \text{with} \quad E_{cs} = \frac{\sigma_{1,cc} - \sigma_{1,e}}{\varepsilon_{1,cc} - \varepsilon_{1,e}} \tag{3.6}$$

The parameter α_{cr} controls the shape of the softening branch, which is characterized by the continuity requirement at the peak stress. In addition, a condition is imposed that the area under the softening region is equal to the fracture energy in compression—a material property obtained from a uniaxial compression test—divided by the characteristic length of the specimen in the loading direction, G_{fc}/l_c. Accordingly, this confined concrete constitutive model includes a localization length (e.g., the gage length of the test specimen) over which average strain values are normalized. Referring to Figure 3.2:

$$\frac{G_{fc}}{l_c} = \int_{\varepsilon_{1,cc}}^{\infty} (\sigma_{1,cc} - \sigma_{1,r}) \exp\left[-\left(\frac{\varepsilon_1 - \varepsilon_{1,cc}}{\alpha_{cr}} \right)^2 \right] d\varepsilon_1 + \frac{(\sigma_{1,cc} - \sigma_{1,r})^2}{2E_c} \tag{3.7}$$

$$\alpha_{cr} = \frac{1}{\sqrt{\pi}(\sigma_{1,cc} - \sigma_{1,r})} \left(\frac{2G_{fc}}{l_c} - \frac{(\sigma_{1,cc} - \sigma_{1,r})^2}{E_c} \right) \tag{3.8}$$

3.2.2 Compatibility of Lateral Strains

Deformations in the transverse direction are computed using the secant strain ratio υ_s,

$$\upsilon_s = -\varepsilon_3/\varepsilon_1 = \upsilon_s(\varepsilon_1, \phi) \tag{3.9}$$

This ratio is confinement dependent, and follows a continuous function of ε_1 (Binici 2005). The lowest value of υ_s is equal to Poisson's ratio of concrete in the elastic region:

$$\upsilon_s\big|_{-\varepsilon_1<-\varepsilon_{1,e}} = \upsilon_o = 0.15 \sim 0.20 \tag{3.10}$$

up to a limiting value at large strains:

$$\upsilon_s\big|_{-\varepsilon_1>>-\varepsilon_{1,cc}} = \upsilon_l = 0.5 + (\phi + 0.85)^{-4} \tag{3.11}$$

based on fitting experimental data reported in Smith et al. (1989). This continuous function satisfies the assumption of no volumetric strain at the peak axial stress, in accordance with triaxial compression results reported in Imran and Pantazopoulou (2001):

$$\upsilon_s\big|_{\varepsilon_1=\varepsilon_{1,cc}} = \upsilon_p = 0.5 \tag{3.12}$$

and takes the form:

$$\upsilon_s\big|_{-\varepsilon_1\geq-\varepsilon_{1,e}} = \upsilon_l - (\upsilon_l - \upsilon_0)\exp\left[-\left(\frac{\varepsilon_1 - \varepsilon_{1,e}}{\Delta_c}\right)^2\right] \tag{3.13}$$

where

$$\Delta_c = \frac{\varepsilon_{1,cc} - \varepsilon_{1,e}}{\sqrt{-\log_e \beta_c}} \quad \text{with} \quad \beta_c = \frac{\upsilon_l - \upsilon_p}{\upsilon_l - \upsilon_0} \tag{3.14}$$

For a confined concrete cylinder or circular column, compatibility of lateral strains is enforced so that circumferential strains in the confining jacket and lateral strains in the neighboring concrete are equal at any imposed axial strain. This process is schematically illustrated in Figure 3.2, where the jacket strain and the confining stress provided by the jacket on the concrete cross section are computed by iteratively solving the following nonlinear equation:

$$\varepsilon_1 \upsilon_s(\varepsilon_1, \phi) + \varepsilon_3(\sigma_3) = 0 \tag{3.15}$$

where $\varepsilon_3(\sigma_3)$ is the circumferential strain demand in the jacket in order to result in the confining stress σ_3 according to the cross-section geometry and the constitutive material model of the jacket. In the case of a FRP or steel confining jacket, $\sigma_3 = \varepsilon_3 D_j$ in the elastic range and a

nearly constant value (e.g., zero for FRP and the yield stress for steel) afterwards. The parameter D_j is the effective jacket stiffness, given by

$$D_j = E_j t_j / R_c \tag{3.16}$$

where E_j is the modulus of elasticity of the jacket in the hoop direction, t_j is the thickness of the continuous jacket (or an equivalent value for discrete ties as defined in Equation (3.17)) and R_c is the radius of the concrete cylinder or circular column.

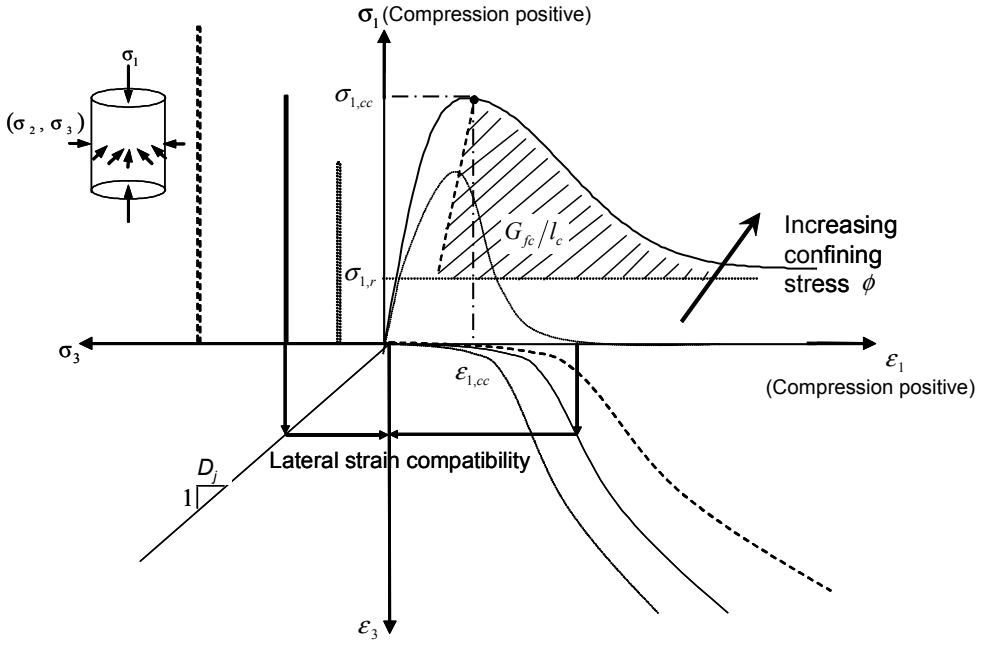

Fig. 3.2 Strain-compatible confined concrete envelope model (Binici 2005).

For reinforcing a steel-confined circular concrete column, Equation (3.16) is modified to account for the efficiency of discretely spaced transverse hoops or spiral along the length direction. In this case the equivalent jacket thickness to be used in Equation (3.16) is given by

$$t_j = \frac{A_{st}}{s_t}\left(1 - \sqrt{\frac{s_t}{1.25D_c}}\right) \quad \text{with} \quad s_t \le 1.25D_c \tag{3.17}$$

where A_{st} and s_t are the cross-sectional area and spacing, respectively, of the transverse reinforcement and D_c is the core diameter defined by the centerline of the hoop or the spiral. This relationship was deduced from observations made in Ahmad and Shah (1982) of negligible

confinement effect for spiral spacing $s_t > 1.25D_c$ (Binici 2005). The circumferential stress in the jacket can be scaled from Equation (3.16) as $\sigma_j = \sigma_3 t_j / R_c$. Equation (3.17) can be extended to RC columns of non-circular cross sections by introducing the well-known cross-section efficiency factors (Mander et al. 1988) to reflect the reduced confinement efficiency of non-circular sections.

3.2.3 Hysteretic Confined Concrete Behavior in Compression

The hysteretic material model for confined concrete has been modified from Lokuge et al. (2004). The key elements of the model are demonstrated graphically in Figure 3.3. The model postulates that the relationship between compressive stress and strain under prescribed confining stress is invariant in the principal shear space. This model is reproduced and presented in detail below, since certain modifications have been introduced for numerical consistency. It should be noted that the original hysteretic model in Lokuge et al. (2004) is developed for concrete specimens subjected to a constant prescribed confining stress. In the current study, this hysteretic model has been extended to variable confinement by computing σ_3 at each load step, using lateral strain compatibility between the concrete and the confining jacket (Eq. (3.15)) and the confining stress distribution profile (see Section 3.3).

The unloading curve is defined by the unloading point $(\varepsilon_{un}, \sigma_{un})$ and the plastic strain ε_{pl} . The latter is defined through the use of the strain ε_a at a surrogate point (point a in Fig. 3.3) as

$$\varepsilon_{i,pl} = \varepsilon_{i,un} - \frac{(\varepsilon_{i,un} - \varepsilon_{i,a})\sigma_{i,un}}{\sigma_{i,un} - E_c \varepsilon_{i,a}} \quad \text{for} \quad i = 1, 3 \tag{3.18}$$

where the subscript i refers to the axis direction, and

$$\varepsilon_{i,a} = 0.5 a_i \sqrt{\varepsilon_{i,un} \varepsilon_{i,cc}} \tag{3.19}$$

$$a_i = \min\left\{ \frac{4\varepsilon_{i,cc}}{\varepsilon_{i,cc} + \varepsilon_{i,un}} (-1)^{0.5(i+1)}, \frac{0.09\varepsilon_{i,un}}{\varepsilon_{i,cc}} (-1)^{0.5(i+1)} \right\} \tag{3.20}$$

where $\varepsilon_{i,cc}$ are the axial and transversal strain values corresponding to the peak compressive stress of the confined envelope according to Equations (3.4) and (3.12). Following the computation of plastic strain, the problem is transformed to the normalized principal shear space, where the principal shear stress τ and strain γ are given by

$$\tau = \frac{\sigma_1 - \sigma_3}{2}, \quad \gamma = \frac{\varepsilon_1 - \varepsilon_3}{2} \tag{3.21}$$

For the unloading curve, these principal shear stress and strain are normalized as follows:

$$\bar{\tau}_{un} = \frac{\tau - \tau_{pl}}{\tau_{un} - \tau_{pl}} \tag{3.22}$$

$$\bar{\gamma}_{un} = \frac{\gamma - \gamma_{pl}}{\gamma_{un} - \gamma_{pl}} \tag{3.23}$$

where τ_{un}, γ_{un}, τ_{pl}, and γ_{pl} correspond to $\sigma_{i,un}$, $\varepsilon_{i,un}$, $\sigma_{i,pl}$, and $\varepsilon_{i,pl}$, respectively. Note that $\sigma_{1,pl} = 0$ by definition and $\sigma_{3,pl} = \sigma(\varepsilon_{3,pl}) \geq 0$ according to the constitutive model of the confining medium, e.g., the jacket. The constitutive model for the unloading curve in the normalized principal shear space in Lokuge et al. (2004) is experimentally fitted to the following expression:

$$\bar{\tau}_{un} = 0.43\left(e^{1.2\bar{\gamma}_{un}} - 1\right) \tag{3.24}$$

The best-fit unloading correlation between normalized axial and lateral strains is given by

$$\bar{\varepsilon}_{3,un} = \left(\bar{\varepsilon}_{1,un}\right)^{1/p_c} \tag{3.25}$$

where p_c is a parameter controlling the width of the unloading-reloading loops and is fitted to $p_c = -0.0035 f_c' + 1.445$ [N, mm units] in Lokuge et al. (2004). The normalization of the axial and lateral strains follows the same manner as in Equation (3.23). In order to update the hysteretic material model to account for variable confinement, the value of ε_3 computed using Equation (3.25) is used to update the confining stress σ_3 according to the constitutive model of the confining jacket. This updated confining stress is then used in the transformation Equations (3.21).

The reloading curve follows a similar procedure to that of the unloading curve. It is defined by a reloading point $(\varepsilon_{ro}, \sigma_{ro})$ and a return point $(\varepsilon_{new} = \varepsilon_{un}, \sigma_{new})$ where

$$\sigma_{1,new} = \begin{cases} \sigma_{1,un} & \text{if } 0 \le -\varepsilon_{1,new} \le -\varepsilon_{1,el} \\ 0.92\sigma_{1,un} + 0.08\sigma_{1,ro} & \text{if } -\varepsilon_{1,cc} \le -\varepsilon_{1,new} \end{cases} \tag{3.26}$$

with parabolic transition in between, i.e., for $-\varepsilon_{1,e} < -\varepsilon_{1,new} < -\varepsilon_{1,cc}$. For the reloading curve, the stresses and strains in the principal shear space are normalized as follows:

$$\bar{\tau}_{re} = \frac{\tau - \tau_{ro}}{\tau_{new} - \tau_{ro}} \tag{3.27}$$

$$\bar{\gamma}_{re} = \frac{\gamma - \gamma_{ro}}{\gamma_{new} - \gamma_{ro}} \tag{3.28}$$

where τ_{new}, γ_{new}, τ_{ro} and γ_{ro} correspond to $\sigma_{i,new}$, $\varepsilon_{i,new}$, $\sigma_{i,ro}$ and $\varepsilon_{i,ro}$, respectively. The constitutive model for the reloading curve in the normalized principal shear space in Lokuge et al. (2004) is experimentally fitted to the following expression:

$$\bar{\tau}_{re} = \frac{1}{\log_e(2)} \log_e\left(\bar{\gamma}_{re} + 1\right) \tag{3.29}$$

The best-fit reloading correlation between normalized axial and lateral strains is given by

$$\bar{\varepsilon}_{3,re} = \left(\bar{\varepsilon}_{1,re}\right)^{p_c} \tag{3.30}$$

where p_c is the same parameter defined after Equation (3.23). Similar to the procedure discussed for the unloading curve, the confining stress σ_3 is updated according to the computed lateral strain ε_3 and the constitutive model for the confining jacket.

To return to the envelope, the material follows a parabolic transition curve that preserves derivative continuity at the end of the reloading curve. This transition curve is defined by the stress state at the return point $(\varepsilon_{new}, \sigma_{new})$, the ultimate strength of the confined envelope $\sigma_{1,cc}$, and the envelope stress at the reentry point $(\varepsilon_{re}, \sigma_{re})$ where

$$\varepsilon_{1,re} = \varepsilon_{1,un} + \left(\sigma_{1,un} - \sigma_{1,new}\right) \times \left(2 - \frac{\sigma_{1,cc}}{f_c'}\right) \Bigg/ \left(\frac{\sigma_{1,ro} - \sigma_{1,new}}{\varepsilon_{1,ro} - \varepsilon_{1,new}}\right) \tag{3.31}$$

and $\sigma_{1,re} = \sigma_1\left(\varepsilon_{1,re}\right)$ according to Equations (3.5). The ratio between axial and lateral strains along the transition curve is assumed to follow the secant strain ratio $\upsilon_s(\varepsilon_1, \phi)$ according to Equation (3.9). Accordingly,

$$\sigma_1 = \sigma_{1,new} + E_{new}\left(\varepsilon_1 - \varepsilon_{1,new}\right) - \left[E_{new}\left(\varepsilon_{1,re} - \varepsilon_{1,new}\right) - \left(\sigma_{1,re} - \sigma_{1,new}\right)\right] \times \left(\frac{\varepsilon_1 - \varepsilon_{1,new}}{\varepsilon_{1,re} - \varepsilon_{1,new}}\right)^2 \tag{3.32}$$

where $E_{new} = \partial\sigma_1 / \partial\varepsilon_1\big|_{\varepsilon_1 = \varepsilon_{1,new}}$ is the tangent stiffness modulus at the end of the reloading curve.

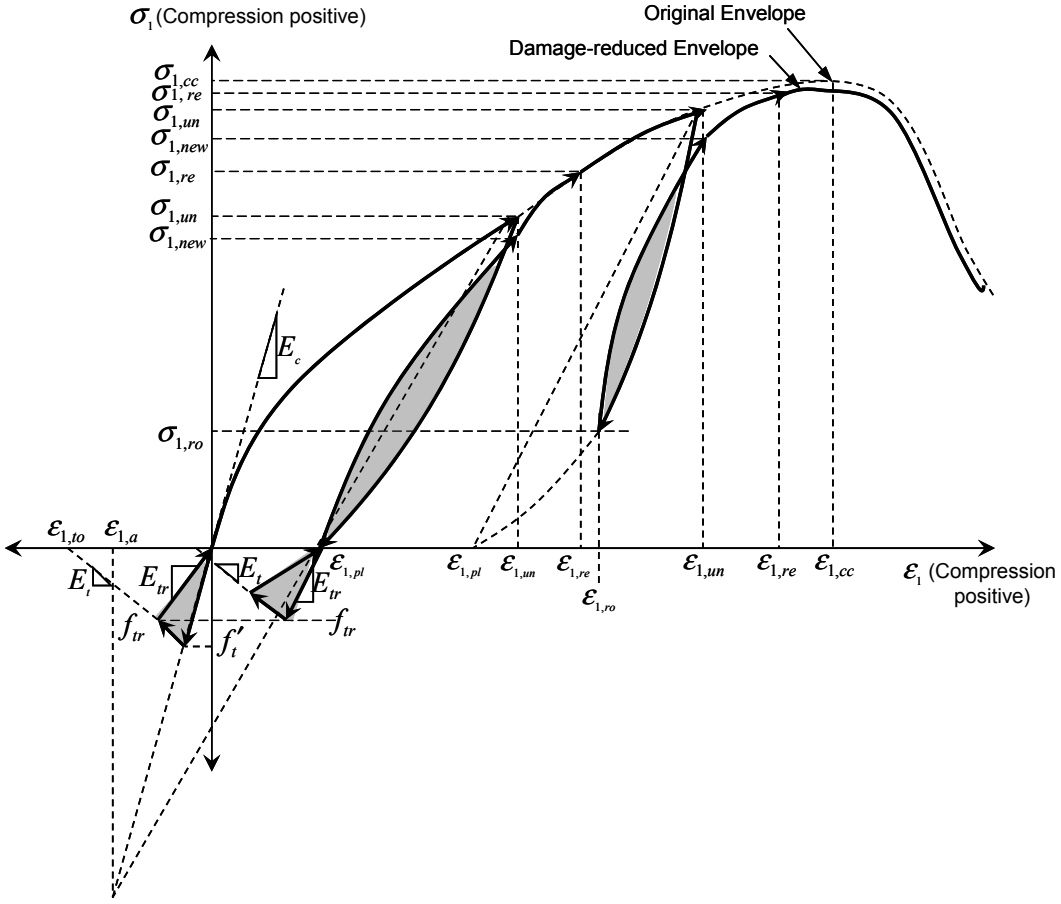

Fig. 3.3 Confined concrete hysteretic material model (with first cycle in tension).

3.2.4 Hysteretic Compressive Strength Degradation

To account for hysteretic strength degradation in compression, the stress computed from the monotonic confined envelope is reduced over successive loading cycles through multiplication by a reduction factor obtained from a hysteretic damage model. Several energy- and ductility-based damage models are present in the literature, e.g., Park and Ang (1985), whose parameters

can be calibrated using experimental data. In Lokuge et al. (2004) a simple factor is proposed based on the number of stress cycles as follows:

$$R_f(n) = 1 - n/N \tag{3.33}$$

where n is the current number of loading cycles and N (assumed 100) is the number of cycles to failure. In this study, the following alternative hysteretic energy-based reduction factor is formulated and calibrated to the experimental results reported in Lokuge et al. (2003):

$$R_f(n) = \left(\sum_{i=1}^{n-1} (U_{re} - U_{un})_i \Big/ G_{fc} \right)^{\alpha_e} \tag{3.34}$$

where $(U_{re} - U_{un})_i$ is the energy dissipated during the i^{th} unloading-reloading cycle (shaded in Fig. 3.3) and α_e is a model calibration parameter as discussed in Section 3.2.6. If cracking takes place during a tensile loading cycle, the energy dissipated therein is automatically included in Equation (3.34), which results in a corresponding reduction of the monotonic envelope curve in compression. Consequently, previously cracked concrete will exhibit lower peak strength in compression. The computation of the term $(U_{re} - U_{un})_i$ is simplified for numerical efficiency by assuming that the unloading and reentry stresses coincide. In addition to the stress reduction factor, the following maximum dilation-based damage index is defined:

$$D_f = \left(\max\{\varepsilon_3\} / \varepsilon_{3,\max} \right)^{\alpha_f} \tag{3.35}$$

where $\varepsilon_{3,\max}$ is the fracture or maximum estimated strain in the transverse reinforcement of the confining jacket before the loss of confinement and α_f is a model calibration parameter. Typically, $\alpha_f = 1$ would be assumed if this damage index is solely used to determine whether loss of confinement has occurred, which is the case in this report. α_f may be calibrated to other values using experimental data if it is desired that the damage index values correspond to intermediate visual characteristics of damage defined as milestones prior to loss of confinement. In that regard and from the functional form of the damage index defined in Equation (3.35), it represents the damage level in the confined concrete fibers by considering the amount of lateral expansion sustained in the material and comparing it to the expected maximum expansion allowed before disintegration takes place.

3.2.5 Monotonic and Hysteretic Concrete Behavior in Tension

The behavior in tension is assumed independent of the confining stress. Figure 3.3 illustrates the cyclic response path followed by the material in uniaxial tension. If tensile stress is detected during unloading, the material follows a linear-elastic response along the initial tangent modulus of concrete E_c up to the cracking stress f_t'. Subsequently, the material follows a linear tension softening modulus E_t. The strain corresponding to complete loss of tensile resistance $\varepsilon_{1,to}$ is determined from the tensile fracture energy G_{ft} that is assumed to be a known (i.e., measured) material property. If strain reversal takes place after partial tension softening to a stress $f_{tr} > 0$, the material unloads linearly toward the origin following a secant modulus. Upon reloading to compression from tension, cracks are assumed to fully close and the reloading point in compression is relocated at the plastic strain. Subsequent tensile response of a previously cracked material follows the current secant modulus E_{tr} up to the stress f_{tr} and then starts to soften with modulus E_t (i.e., E_t does not degrade hysteretically), and so on until total loss of tensile strength (i.e., complete dissipation of G_{ft}). The assumption of linear unloading-reloading of cracked concrete with no residual crack widths underestimates the hysteretic energy dissipated if several tension cycles of low amplitude were to take place at the same cracked concrete fiber. However, this limitation of the model is considered a valid approximation for the purpose of modeling gravity-load collapse, which typically takes place long after flexural cracking has taken place.

3.2.6 Parameter Calibration and Experimental Verification

In this section, the uniaxial material model for confined concrete developed in the present section is compared to the experimental results published in Ahmad and Shah (1982) and Lokuge et al. (2003) to assess its validity and calibrate the parameter α_e. The experiments reported in Ahmad and Shah (1982) include six concrete cylinders (75 × 150 mm) subjected to monotonic compression. Cylinder compressive strengths are 25 and 50 MPa. The cylinders are either unconfined or confined with spiral reinforcement placed flush with the concrete outer surface with no cover. Variable spiral spacing is investigated, with spiral yield strength of 414 MPa and

diameter of 3 mm. The concrete compressive fracture energy for these specimens is reported as estimated from the unconfined concrete response in Binici (2005). Note that the lower grade concrete has a slightly higher value despite the lower compressive strength due to higher ductility and less steep softening branch. Concrete tensile strength is not reported and is estimated as 2.5 and 5 N/mm^2, respectively. Figure 3.4 illustrates the comparison between the observed and estimated stress-strain responses. The analytical model slightly overestimates the peak stress and corresponding strain for the case of 12.5 mm spiral spacing. However, the model is successful in reproducing the profile of the hardening and softening branches and the residual strength as affected by lateral confinement. The aforementioned discrepancy may suggest that the expression used in Equation (3.17) may overestimate the efficiency of spiral reinforcement in cases of closely spaced spirals resulting in a small spacing-to-diameter ratio. In addition, the discrepancy may be partially due to the approximation involved in estimating the tensile strength (see the definition of m_c in Equation (3.2)).

The experiments reported in Lokuge et al. (2003) include 24 confined concrete cylinders (101.6 × 198 mm) subjected to cyclic compression. Concrete nominal strengths are 40, 60, 80, and 100 MPa. The cylinders are confined using a triaxial pressure apparatus with confining stress levels set to 4, 8, or 12 MPa. The measured response includes axial and lateral strains in the concrete cylinders, as well as axial stresses. The reported values of cylinder strength on the testing date are 43.6, 57.7, 83.0, and 105.9 MPa, respectively. Concrete fracture energy in compression and tension are estimated as $G_{fc} = 8.8\sqrt{f_c'}$ [N, mm units] and $G_{ft} = G_{fc}/250$ according to Mizuno et al. (1999) based on uniaxial load-test results. Tensile strength is estimated as $f_t' = 0.05 f_c' + 0.175\sqrt{f_c'}$ [N, mm units], which is adapted from Binici and Mosalam (2007). Figure 2.8a illustrates the comparison between the observed and predicted behavior for cylinders with medium concrete nominal strength (40–60 MPa). The analytical model's reproduction of the experimentally recorded behavior is satisfactory for all cases. Figure 2.8b illustrates the comparison between the observed and predicted behavior for cylinders with high concrete nominal strength (80–100 MPa). The analytical model's reproduction of the experimentally recorded behavior is satisfactory prior to the softening branch. It is less so in reproducing the subsequent brittle, rapid loss of strength and limited, rapid dilation. This

discrepancy can be observed in cylinders whose nominal compressive strength is 100 MPa. The experimental records for these tests show very few data points due to the highly brittle nature of the softening branch and the difficulty in controlling the experimental loading setup. Hence, this uniaxial material model is suitable for modeling the confined behavior of normal-to-medium strength concrete and may be inaccurate for modeling the complete stress-strain response in concrete of compressive strength larger than about 90 MPa. The minimum and maximum values of the parameter α_e used during the simulations for reproducing all 24 specimens reported in Lokuge et al. (2003) are 0.9 and 1.5, with mean and COV values of 1.175 and 0.201, respectively.

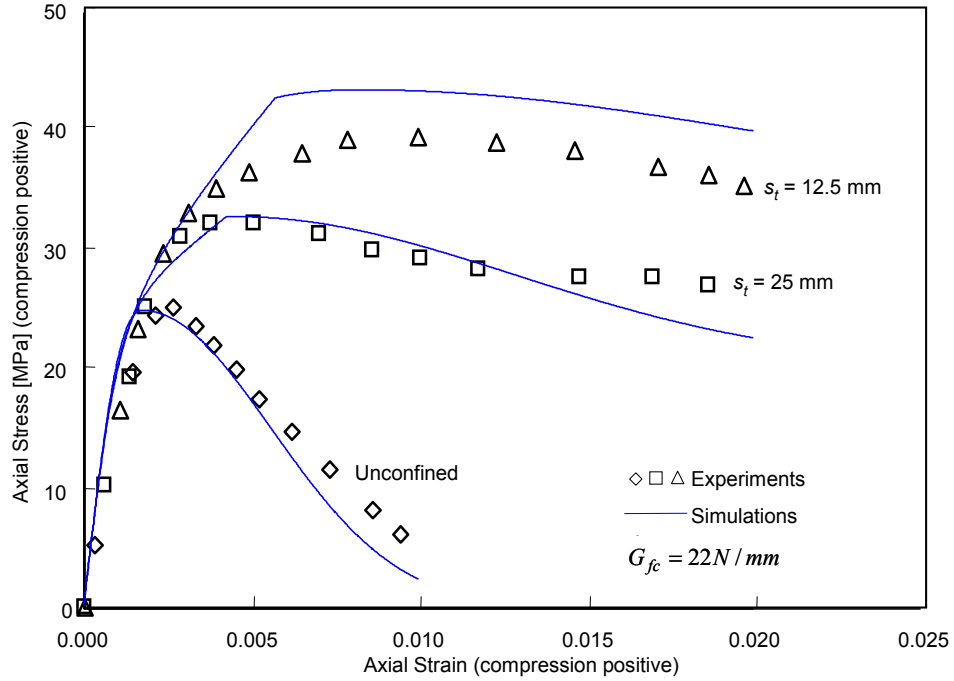

(a) Concrete grade = 25 MPa

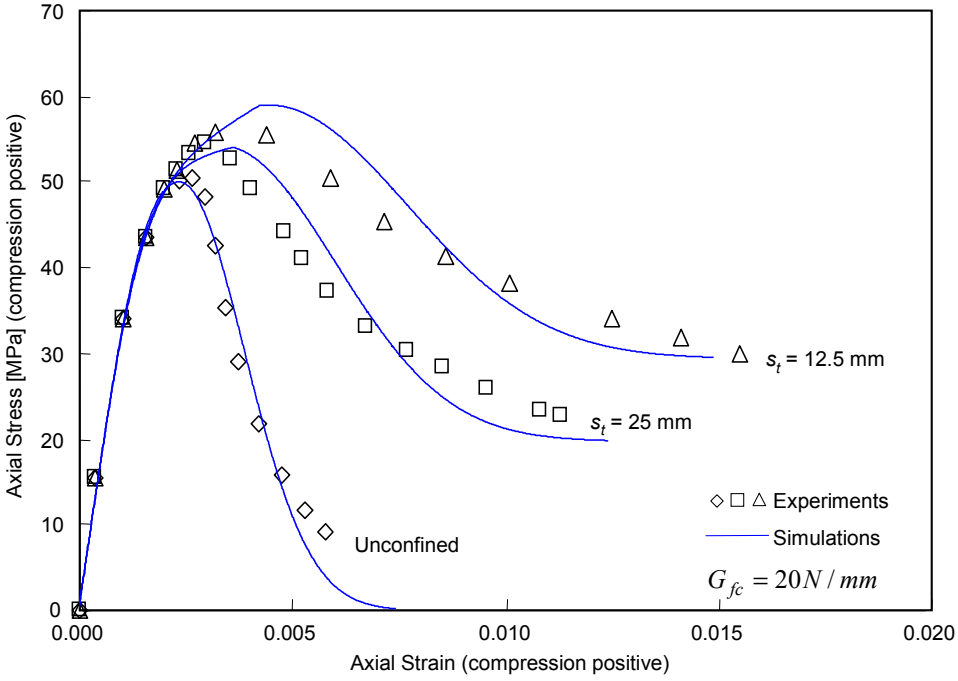

(b) Concrete grade = 50 MPa

Fig. 3.4 Model simulations of Ahmad and Shah (1982) confined concrete tests.

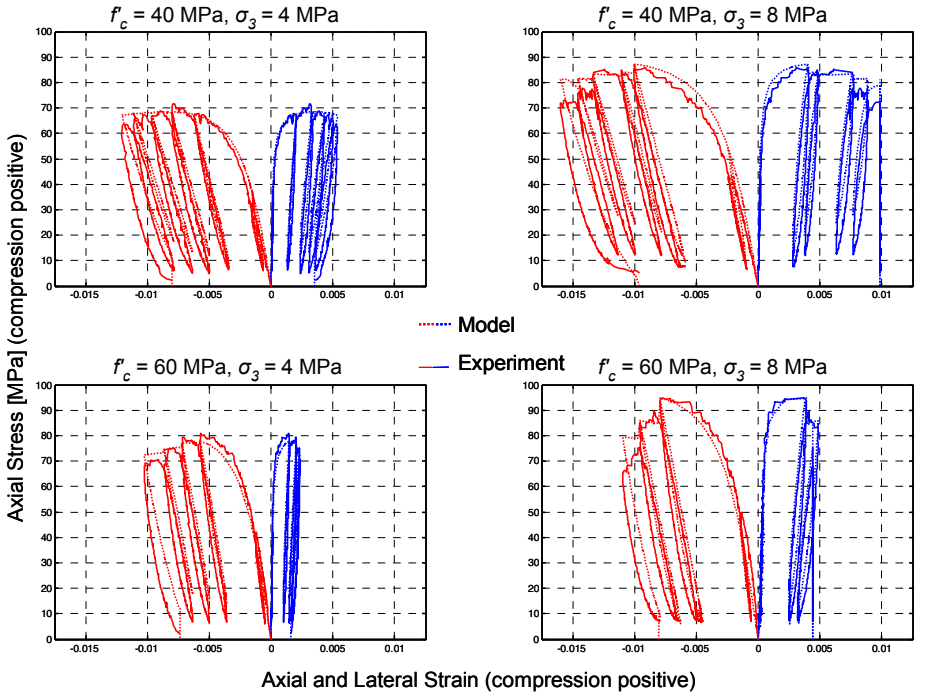

(a) Medium-strength concrete cylinders

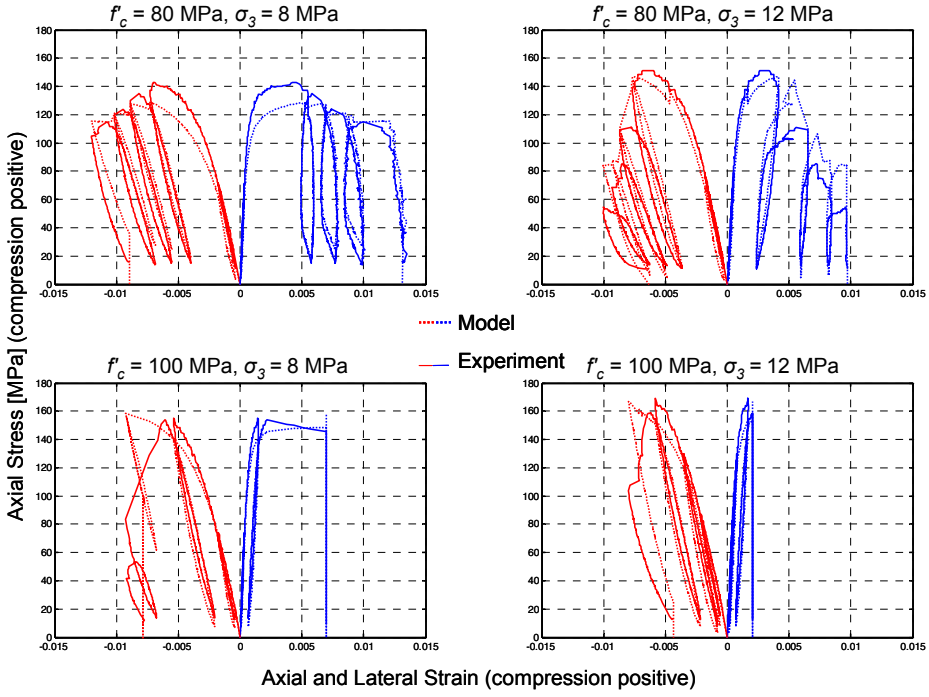

(b) High-strength concrete cylinders

Fig. 3.5 Model simulations of Lokuge et al. (2003) confined concrete tests.

3.3 ANALYTICAL MODEL FOR CONFINED CONCRETE CROSS SECTION

This section describes the development of the fiber-discretized cross-section model to be used in conjunction with the confined concrete uniaxial material model developed in Section 3.2. This cross-section model was originally developed in Binici and Mosalam (2007) for FRP-wrapped RC columns of circular cross-section geometry. The model is based on the equilibrium of interface shear stresses between a continuous FRP jacket and the concrete surface of a RC column cross section undergoing primarily flexural deformations. Columns with deficiency in shear capacity are outside the scope of the present model. This approach has been successfully extended for use with RC columns traditionally confined by transverse steel reinforcement using Equations (3.16) and (3.17). It can be readily extended to RC columns of non-circular cross sections by introducing the well-known cross-section efficiency factors (Mander et al. 1988) to reflect the reduced confinement efficiency of non-circular sections. The effect of stress concentration at the cross-section corners is not explicitly considered.

3.3.1 Bond-Based Model for Spatial Distribution of Confining Stress

Consider a circular RC cross section with radius R_c confined with a continuous jacket (e.g., FRP lamina) and subjected to the combined effect of axial force and bending moment (Fig. 3.6a). Following the classical beam theory, a linear axial strain distribution is assumed (Fig. 3.6b). In the compression zone, the jacket stress distribution—and, accordingly, the confining stress distribution—is expected to be non-uniform; the jacket stress reaches a maximum value $\sigma_{j,\max}$ at the extreme compression fiber and monotonically decreases to zero at the neutral axis location (Fig. 3.6e). In order to estimate this non-uniform confining stress distribution, the following four assumptions are made: (1) an elastic behavior is assumed to govern the relationship between stress and strain in both the jacket and the adhesive layer along the jacket-concrete interface; (2) the jacket and the adhesive are assumed thin compared to the concrete cross section, i.e., the column radius to the centerline of the jacket is approximately the same as the concrete column radius R_c; (3) the jacket and the adhesive can carry only axial and shear stresses, respectively; and (4) only shear deformation (i.e., no slip) takes place in the adhesive between the jacket and

the concrete cross section. Hence, considering the free-body diagram of the confining jacket in the compression zone (Fig. 3.6c), the equilibrium condition for an infinitesimal jacket sector of length ds along the arc surrounding the cross section (Fig. 3.6d) is given by

$$d\sigma_j \, t_j = \tau \, ds \tag{3.36}$$

where σ_j is the jacket stress, t_j is the jacket thickness, and τ is the interface shear stress. The assumed elastic material behavior of the adhesive and the jacket implies

$$\sigma_j = E_j \, du_j / ds \tag{3.37}$$

$$\tau = u_j \, G_a / t_a \tag{3.38}$$

where E_j is the modulus of elasticity of the jacket, u_j is the circumferential elongation of the jacket (equal to the shear deformation of the adhesive), G_a is the shear modulus of the adhesive, and t_a is the thickness of the adhesive. Differentiating Equation (3.38), combining with Equation (3.37), substituting in Equation (3.36) after differentiating it, and substituting for $ds = R_c d\theta$, one obtains the following governing differential equation:

$$d^2\sigma_j / d\theta^2 - A^2 \, \sigma_j = 0 \quad \text{with} \quad A^2 = \left(R_c^2 G_a\right) / \left(E_j t_j t_a\right) \tag{3.39}$$

where A is a non-dimensional bond parameter. The solution of Equation (3.39) after substituting for the stress boundary conditions $\sigma_j \big|_{\theta=0} = 0$ and $\sigma_j \big|_{\theta=\theta_c} = \sigma_{j,\max}$ (see Fig. 3.6c) is given by

$$\sigma_j = \sigma_{j,\max} \sinh(A\theta) / \sinh(A\theta_c) \tag{3.40}$$

where θ and θ_c are defined in Figure 3.6c.

For the cross section subjected to a combined axial force and bending moment (Fig. 3.6), the confining stress σ_3 is linearly related to the jacket stress σ_j as discussed in Section 3.2.2. The lateral strain compatibility is iteratively enforced for the extreme concrete fiber in compression, i.e., at $\theta = \theta_c$, using Equation (3.15). Once the maximum jacket stress $\sigma_{j,\max}$ is known, the jacket and confining stresses at any location along the perimeter can be computed using the expression in Equation (3.40). Concrete fibers in the interior of the compression zone are assumed subjected to confining stresses equal to those of the fiber adjacent to the jacket at

the same distance y_c from the neutral axis (2D idealization). This modeling approach incorporates the spatial variation in the confining stress distribution within the compression zone and is capable of monitoring the lateral dilation of concrete and accordingly the stress state in the confining jacket. This feature has several advantages besides estimating the confining stress at individual concrete fibers for use with the confined concrete material model developed in Section 3.2. For FRP-retrofitted RC columns, the jacket rupture, which generally dictates the failure of a retrofitted column, can be explicitly predicted by comparing the computed jacket strain $\varepsilon_j = du_j / ds$ with the FRP rupture strain ε_{rup}. For longitudinal steel bars laterally restrained by transverse reinforcement, the lateral tie or hoop stiffness can be readily estimated for use by the bar-buckling model developed in Section 2.2. In addition, the confining effect of both steel ties or hoops and FRP lamina on clamping lap-spliced steel bars can be evaluated according to the model developed in Section 2.3.

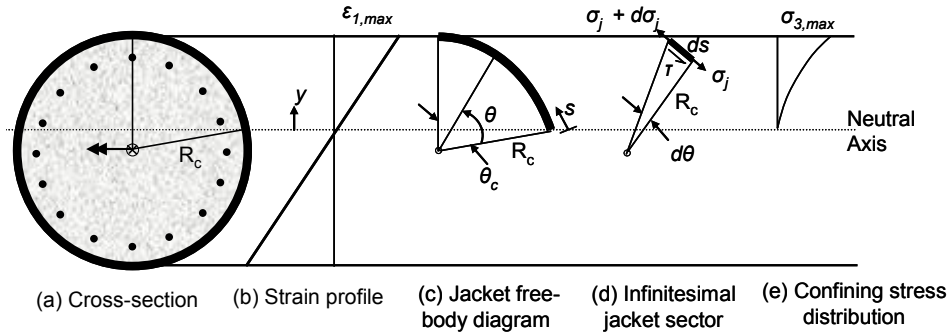

Fig. 3.6 Confining stress distribution on RC circular column cross section.

In practice, it is difficult to estimate with high precision some quantities such as the adhesive thickness and the shear modulus in order to compute the value of the bond parameter A. The effect of uncertainty in this parameter on the global response of FRP retrofitted RC columns was investigated in Binici and Mosalam (2007) using a deterministic sensitivity analysis tool known as the Tornado diagram (Lee and Mosalam 2005), where individual model parameters of uncertain values are ranked in a descending order of the resulting uncertainty in the response quantity estimated by the model. The effect of uncertainty in the parameter A on estimating the peak lateral force capacity of FRP-retrofitted columns subjected to monotonic lateral deformation was found to rank 11th out of 14 model parameters. The resulting uncertainty

in estimating the peak lateral force due to uncertainty in the parameter A was shown to be significantly less than the resulting uncertainty due to other factors such as the jacket's stiffness modulus, the concrete strength, and the applied axial load. For typical FRP-retrofitted columns, the value of the parameter A ranges from about 1 to 5 (Binici and Mosalam 2007; Mosalam et al. 2007b). Figure 3.7 illustrates the variation in the confining stress spatial distribution within this range. Observe that the confining stress distribution in Figure 3.7 resembles a power function of the relative distance from the neutral axis given by

$$\sigma_3/\sigma_{3,\max} \approx \left(y/R_c\right)^{p_s} \tag{3.41}$$

and can be approximated and input directly as such in order to minimize computation time and increase numerical efficiency. In the applications discussed in Section 5.1, the cross-section moment capacity exhibits a moderate sensitivity (10–15% reduction in maximum value under monotonic loading) in response to increasing the exponent p_s in the range of 0.5–4.0. Moreover, the curvature capacity exhibits less than 5% corresponding reduction in maximum values.

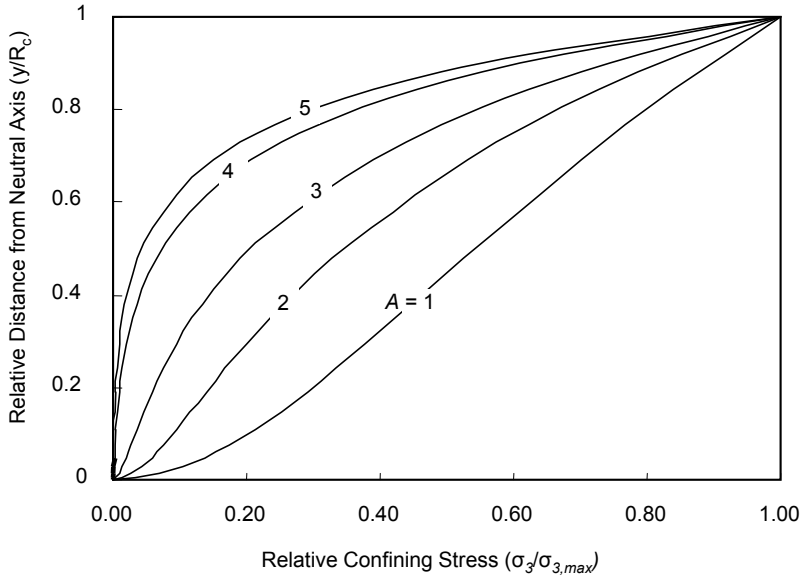

Fig. 3.7 Spatial distribution of confining stress for typical bond parameter values.

3.3.2 Aggregated Cross-Section Damage Indices

The material damage indices previously defined in Sections 2.2.5, 2.3.4, and 3.2.4 for the individual fibers constituting the discretized cross section are combined to define two aggregated damage indices. These damage indices, designated D_A and D_M, quantify the effect of material damage on the cross section's capacity to resist axial loads and bending moments, respectively. These aggregated damage indices are defined as follows:

$$D_A = 1 - \mathrm{I}_{conf}\left(1 - \sum_{\text{fibers}} \left(D_{fiber} A_{\text{fiber}} / A_{\text{cross-section}}\right)\right) \tag{3.42}$$

$$D_M = 1 - \mathrm{I}_{conf}\left(1 - \sum_{\text{fibers}} \left(D_{\text{fiber}} A_{\text{fiber}} h_{fiber}^2 / I_{\text{cross-section}}\right)\right) \tag{3.43}$$

where A refers to the transformed area, I to the transformed moment of inertia, and h to the distance between the fiber's center and the uncracked section centroid. Areas and inertias are transformed using the ratio between the initial stiffness moduli of the individual fiber materials to obtain a homogeneous section. D_{fiber} is the material-specific damage index previously defined for individual fibers. I_{conf} is an indicator variable for the loss of confinement whose value becomes 0 if transverse reinforcement fracture is detected and remains 1 otherwise. These damage indices are implicitly sensitive to the effect of confinement due to including the individual fiber responses according to their constitutive models, in addition to being explicitly sensitive to the confinement effect due to including the indicator variable I_{conf} of the confining medium (ties or FRP jacket), and are therefore suitable for use with both deficient and retrofitted RC columns. The performance of these damage indices in representing the cross section's damage state during an analysis is demonstrated in Chapter 5.

3.3.3 Experimental Verification and Parameter Calibration

In this section, the confining stress distribution model for RC cross sections developed in the present section is compared to results from an experimental program reported in Mosalam et al. (2007b). The experiments were designed specifically for the purpose of assessing the model validity and calibrating the exponent of the approximate confining stress distribution power

function. The experimental program was conducted at the Middle East Technical University (METU), Turkey. Four reduced-scale RC columns with identical dimensions and steel reinforcement were subjected to combined axial loads and bending moments. One of the columns is investigated in its as-built condition under constant axial load and monotonically increasing eccentricity, while the other three columns are strengthened by one layer of Carbon FRP (CFRP) laminate and subjected to monotonically increasing axial load at three different eccentricity levels (including concentric axial load, i.e., no eccentricity). Details of the experimental setup, specimen geometry, material properties, and loading regimes are discussed in Section 5.1, where they are used to assess the behavior of RC column models integrally formulated using the analytical component models developed in Chapters 2 and 3. In this section, only the results pertaining to the circumferential strain distribution in the confining jacket are discussed. CFRP jacket circumferential strains are measured and recorded during the experiments using electronic strain gages surface-mounted at four different locations around the cross sections at the mid-heights of the tested columns (see the insets in Fig. 3.8). The circumferential stresses in the jacket and the resulting confining stresses in the cross section are directly proportional to the circumferential strains, since the confining CFRP jacket used in the experiments exhibited a linear-elastic response until rupture.

Figure 3.8a illustrates the confining ratio computed at each of the four gage locations using the circumferential strains measured at successive load increments for specimen 3, plotted against the relative distance from the cross-section centroid (normalized by the cross-section radius). These data are reduced in Figure 3.8b, which illustrates the confining stress normalized by the maximum confining stress computed from the strain measurements at Gage 4. Superimposed on the experimental relationships is the estimated confining stress distribution according to Equation (3.40) using a bond parameter $A = 5$, as well as power-function approximations of Equation (3.40) using Equation (3.41) of the second ($p_s = 2$) and fourth ($p_s = 4$) orders.

It can be observed that the confining stress distribution has a nonlinear profile that exhibits a close agreement with the analytical confined cross-section model. Furthermore, the comparison suggests that the confining stress distribution can be well represented using a fourth-order power function for the present cross-section geometry. The normalized strain values

suggest that the neutral axis position lies above that of the cross-section centroid (assumed for simplicity in the predicted distribution plots shown in Fig. 3.8b) throughout most of the experiments (note the negative normalized circumferential strains at the location of Gage 1 in Fig. 3.8). Hence, an even closer agreement between the analytical and experimental results can be achieved using a more accurate determination of the neutral axis position. The compressive strains in the jacket correspond to adjacent concrete fibers being outside of the compression zone, whose axial response is not affected by the confining stress according to the constitutive concrete model in Section 3.2. It can also be observed that the normalization of the experimental data in Figure 3.8b results in the reversal of the order of symbols denoting the curvature levels from those shown in Figure 3.8a. This is due to the increase in lateral dilation strain and secant strain ratio v_s of the maximum compression fibers near Gage 4 (i.e., relative to the other fibers) due to the accumulation and localization of material damage with increased curvature levels. Hence, normalization of the measured circumferential strains by the measurement of Gage 4 results in smaller values of normalized strains at Gages 1, 2, and 3 at higher curvature levels.

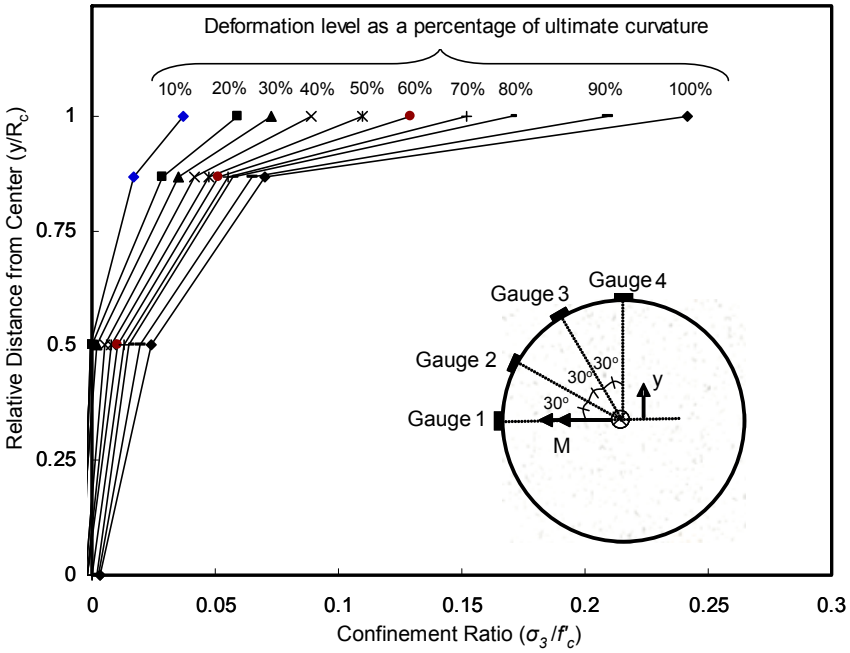

(a) Confinement ratios at gage locations

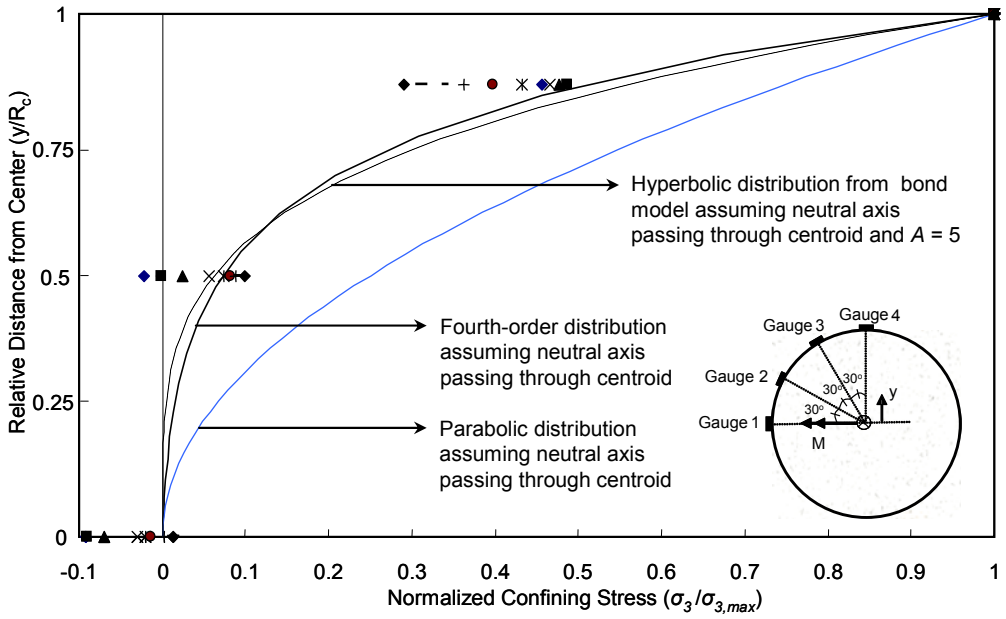

(b) Normalized confinement ratios at gage locations compared to model predictions

Fig. 3.8 Model simulations of jacket strains in Mosalam et al. (2007b) column tests.

3.4 SUMMARY

In this chapter, a brief review was conducted of existing analytical models for simulating RC column cross-section behavior leading to one of two distinct collapse modes, governed by shear-axial and flexure-axial interaction. An analytical material model was developed for the hysteretic behavior of confined and unconfined concrete. This material model enforces lateral strain compatibility between the confined concrete and the confining jacket (or transverse reinforcement) to determine the stress state in both materials at each load step. This confined concrete material model was calibrated using published data from experimental investigations of concrete cylinders subjected to monotonic and cyclic uniaxial compressive loading. Another analytical model was developed to describe the spatial distribution of confining stresses within a confined circular RC cross section subjected to combined axial and flexural loads. This model is based on the equilibrium of bond stresses between the RC cross-section perimeter and the confining jacket. A closed-form analytical expression for the confining stress distribution was derived and shown to be approximately equivalent to a power law. The cross-section confinement model exhibits good correlation with experimental measurements of circumferential strains from distributed strain gages on cross sections of RC columns retrofitted with FRP jackets and subjected to monotonic flexure-axial loading.

4 Object-Oriented Implementation of Proposed Component Models

The component models developed in Chapters 2 and 3 are implemented within OpenSees, an open-source FE modeling software developed using C++ programming language and object-oriented software architecture (Mazzoni et al. 2004; McKenna 1997). Object-oriented architecture offers more flexibility, more reusability of computer code, and greater accessibility for independent researchers to add to the code than is available in the more traditional procedure-oriented (PO) architecture. In PO architecture, a FE modeling software is based on hierarchical procedures that perform specific computations in a given order, e.g., stress-state determination, computation of tangent stiffness, and solution of the governing equations of motion. The resulting data structures are often tightly bound to each other and stored globally in the common memory available to the program. Any addition of new components such as element and material models must comply with the forms of the existing data structures to be able to communicate with the PO program. Such programs are often written to fit specific types of analysis or a certain class of solution methods. Extending an existing PO program by adding new solvers or solution methods is usually very difficult.

In contrast, object-oriented software architecture is based on a number of independent modules that are loosely linked to each other. Each module stores its data locally and defines its own procedures and methods (a "method" is equivalent to a "function"; a "function-call" is an invocation of a method within the C++ code). These modules can communicate and exchange information and commands across each other. The software's main code defines the interactive relationship between the separate modules only during the course of an analysis. This enables independent software developers and researchers to implement additional modules or submodules and link them to the main program without having to learn extensively about the

entire software architecture or being bound by a specific form of data structure. In addition, object-oriented software architecture offers independent researchers the ability to focus on making improvements in areas of their expertise, such as material and joint constitutive models, and then implement and test the new developments in the context of analyzing structural systems without having to write a FE code to do such things as meshing and performing time integration. In addition, existing modules can be modified and optimized to reflect improvements in available computing hardware and resources without having these modifications propagating throughout the entire software (Fenves et al. 2004).

In C++ terminology, such independent modules are implemented using "classes." A class represents a unit cell of an object-oriented program, which contains data and definitions of methods to manipulate these data, and has the ability to communicate with other classes. Most basically, a class provides: (a) the ability to construct instances of itself during runtime, often referred to as "objects" and (b) the method to destruct an object if commanded to do so. All objects that belong to the same class share the same functionality. Since classes are responsible for maintaining their data and for performing their own computations locally while providing information only about themselves when requested, internal data and procedures of a class are called "member variables" and "methods," respectively. In addition to providing functionality, each class provides an interface that lists the available member variables and methods through which the main program and other classes can communicate with it.

An important concept to object-oriented programming is that of inheritance, whereby new classes can be derived from existing "base" classes. Derived classes are sometimes referred to as "subclasses" apropos of the base class, and they possess the same functionality as the base class in addition to added properties. Consequently, classes representing high-level independent modules are implemented as "abstract classes," which serve mainly as a title under which several other subclasses can be derived while sharing a common set of basic features and methods. Typically, the methods of abstract classes are declared "virtual," supplying a default definition and leaving the flexibility to each subclass to implement its own version of the method. A method that is declared virtual in a base class and has no default definition is called "pure virtual" and must be implemented in all its subclasses. Hence, a base class representing a high-level independent module resembles the stem of a tree with many branches.

Another important concept of C++ programming is the use of "pointers." A pointer is an address in memory in which a variable is stored. This variable can be an object of a certain class or even simply a numerical value. This pointer can be used to pass messages to objects requesting that they perform certain methods or report the value of certain member variables.

In this chapter, an outline is given of the modular software architecture of OpenSees, with emphasis placed on defining the classes relevant to this report. In the same context, the new classes added to OpenSees are identified, as well as the class relationships and interdependency with the main program. Next, the details pertaining to the implementation of each new class are discussed. The discussion provides the class interface needed to communicate with the other classes and highlights the steps necessary to extend these classes in the future (e.g., by deriving subclasses). The discussion also addresses implementation details, adopted methods for the numerical computation of analytical expressions, and modifications made to the analytical formulae in order to overcome runtime difficulties such as convergence errors. In textual reference, references to classes or objects are italicized, while references to methods or member variables are boldfaced. Member methods are often mentioned without preceding them with the associated class. However, in situations where ambiguity may arise, the method is preceded by the class name with two colons separating them.

4.1 OVERVIEW OF OPENSEES MODELING PLATFORM

OpenSees is a software framework for modeling structural behavior using the FE method. OpenSees is being collaboratively developed by the Pacific Earthquake Engineering Research (PEER) Center for use in PBEE studies (Mazzoni et al. 2004). The high-level architecture of OpenSees was initially developed in McKenna (1997) and is presented in several publications, including Fenves et al. (2004). OpenSees is composed of a number of independent modules in addition to an application program interface (API). The API defines the relationship between the independent modules through a set of function-calls that solicit information from the modules and request that they perform specific tasks. The collection of modules and API can together construct a runtime application which represents a structural or geotechnical engineering problem subjected to a series of analyses. This application is constructed by reading an

instructions code written by the analyst that represents the geometry and materials of the problem, as well as the analysis parameters to be applied to it. In the case of OpenSees, this instructions code is input using the Tool command language (Tcl) (Welch et al. 2003) into the interpreter module of OpenSees. The advantages of giving analysts a programmable language for defining structural models and solution options include the ability to conduct parametric studies in batch mode and to communicate with graphical user interfaces (Fenves et al. 2004). Thus, the implementation of new classes into OpenSees includes writing interpreter entries to enable the analyst to construct corresponding objects during the analysis.

An illustration of four main OpenSees modules and the relationship between them is given in Figure 3.1, together with a conceptual representation of different OpenSees components and their interconnectivity. The most important module is the *Domain*, which maintains the information necessary to describe and represent the state of the FE model throughout the analysis. The *Domain* object is constructed using *ModelBuilder* subclasses, such as the one that interprets Tcl commands. The *Domain* class controls several *DomainComponent* subclasses (materials, elements, nodes, loads, etc.) to assemble the residual nodal force vector and stiffness matrix. The *Analysis* class is an abstract class that depends on the analyst's choice of *Integrator* class to define the time integration method, the *SystemOfEquations* class to describe the characteristics of the stiffness matrix, and the *ConvergenceTest* class to define the criteria for a converged load step, etc. The equilibrium equations are solved using the *Solver* class chosen by the analyst, while possibly taking advantage of several "Compute Technology" capabilities such as parallel computing. Requested quantities from the analysis can be stored and displayed using *Database* and *Visualization* modules, both implemented using *Recorder* classes.

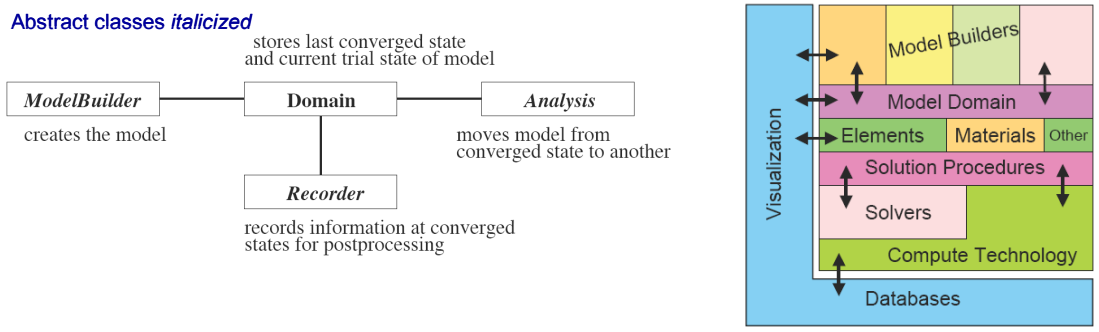

(a) Main high-level abstractions (b) Conceptual module layout

Fig. 4.1 High-level objects in OpenSees software framework (Fenves et al. 2004).

4.2 NEWLY IMPLEMENTED CLASSES IN OPENSEES

The component models developed and verified in Chapters 2 and 3 have been implemented using 14 new OpenSees classes. The new classes belong to the *Material* and *DamageModel* base classes. A partial OpenSees class map, illustrated in Figure 4.2, indicates the hierarchical relationship between the different classes. A triangle indicates an inheritance relationship and a circle indicates a "has-a" relationship where one class (the one farther from the circle) has exclusive access privileges to certain objects of the other class (the number of objects is indicated next to the circle). The abstract class *Material* is a subclass of the *DomainComponent* class. Two abstract subclasses of *Material* are extended in this report, namely *SectionForceDeformation* and, more extensively, *UniaxialMaterial*.

The *SectionForceDeformation* class provides abstraction for several derived classes representing cross-section response, such as *FiberSection2D* and *FiberSection3D*. This class has been extended by deriving *ConfinedFiberSec2D* and *ConfinedFiberSec3D* classes representing the 2D and 3D versions, respectively, of the confined concrete cross-section model developed in Section 3.3. These two classes are collectively referred to as *ConfinedFiberSec* hereafter when no distinction needs to be made. Each object of this new derived class constructs and typically controls one typically *UniaxialMaterial* object that represents the confining hoop or FRP jacket. *UniaxialMaterial* subclasses include material templates that can be calibrated to represent steel,

concrete, and other common building material behavior. In addition, each object of a *ConfinedFiberSec* class constructs and maintains control over a number of material fibers representing discretized core and cover concrete (the number of which depends on the analyst) and longitudinal steel which may be lap-spliced (the number of which depends on the number of continuous and spliced bars, if any). While any *UniaxialMaterial* objects can be used within a *ConfinedFiberSec*, ideally confinement-sensitive *UniaxialConfinedMaterial* objects (defined in the next paragraph) are used to benefit from the cross section's determination of the confining stress, which incurs an additional computational cost.

A new abstract class called *UniaxialConfinedMaterial* is added to *UniaxialMaterial* in order to provide abstraction for classes of materials used in uniaxial fibers whose stress-strain responses in the main axis direction are affected by their stress states in the transverse direction(s). Subclasses derived from this abstract class include *SteelRebar*, which represents the buckling-enabled steel bar model developed in Section 2.2; *LapSplice*, which represents the lap-spliced steel bar model developed in Section 2.3; and *ConfinedConcrete*, which represents the confined concrete material model developed in Section 3.2, in addition to an abstract *UniaxialConfinedCurve* class. Each object of the class *ConfinedConcrete* constructs and maintains control over an object of each of four new classes *BiniciEnvelope*, *LokugeUnloading*, *LokugeLoading*, and *ParabolicTransition*, in addition to one *DamageModel* subclass. The first four classes derive from the abstract class *UniaxialConfinedCurve* and represent the different confinement-sensitive branches describing the hysteretic behavior of the confined concrete material. This independent setup of material and hysteretic branches provides flexibility whereby any of these branch classes can be individually replaced by an alternate candidate branch class without rewriting the material class. Instead, the link to the corresponding branch in the *ConfinedConcrete* class can be modified to the new subclass of *UniaxialConfinedCurve* representing the candidate branch. Moreover, derived *UniaxialConfinedCurve* subclasses can serve independent of *ConfinedConcrete* to represent other *UniaxialConfinedMaterial* subclasses (e.g., the form of the Popovics-type curve in *BiniciEnvelope* class may be reused to model bond-slip behavior).

Each *UniaxialConfinedMaterial* object constructs and controls one *DamageModel* derived object. The role of these *DamageModel* derived objects is to track the structural damage

state sustained in the associated *UniaxialConfinedMaterial* object during the simulation and compute the hysteretic stress-reduction factors and damage indices defined in Chapters 2 and 3, which are later used in Chapter 6 to establish the component removal criteria. Four new *DamageModel* derived classes are implemented in this report: (1) *CoffinManson* evaluates the damage state based on plastic strain accumulation in steel bars, as defined in Section 2.2, (2) *MaxSlip* evaluates the damage state based on maximum slip displacement in lap-spliced bars, as defined in Section 2.3; (3) *DissipatedEnergy* evaluates the damage state based on the hysteretic energy dissipated in the confined concrete constitutive material model, as defined in Section 3.2; and (4) *MaxNumCycle* evaluates the damage state based on the damage factor proposed in Lokuge et al. (2004), which is also defined in Section 3.2.

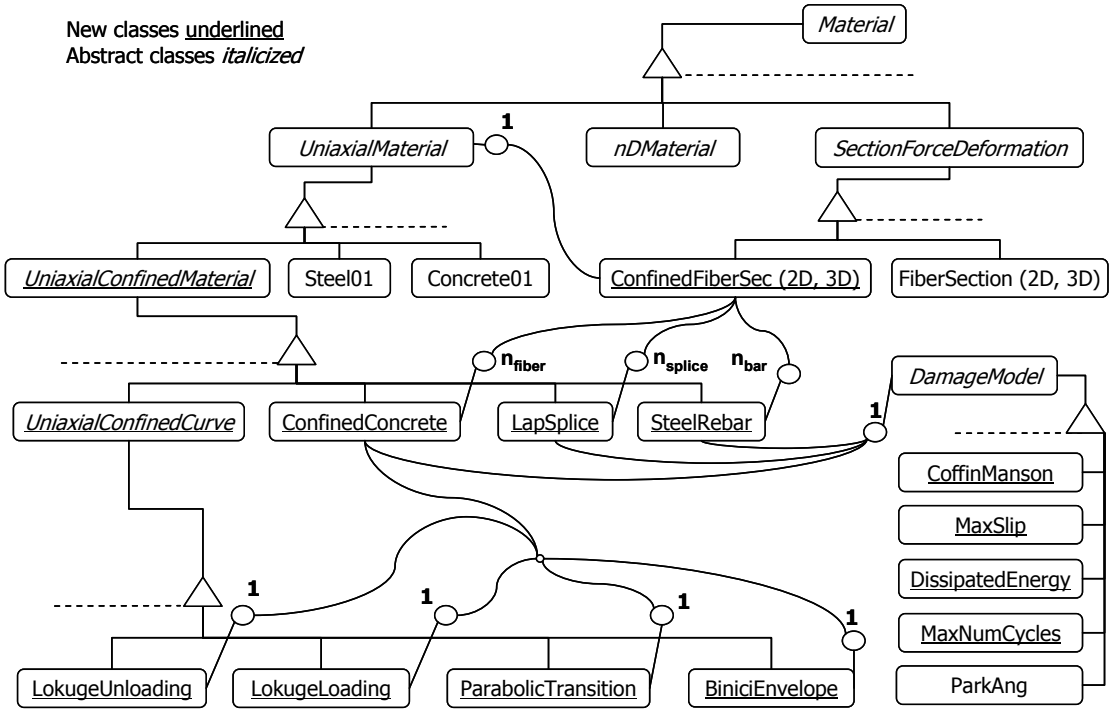

Fig. 4.2 Partial OpenSees class map showing newly implemented components.

4.3 IMPLEMENTATION OF *UNIAXIALCONFINEDMATERIAL* SUBCLASSES

UniaxialConfinedMaterial is a new abstract class that provides basic functionality to derived classes representing stress-strain response in the main axis direction of confinement-sensitive materials. This section provides the class interface and discusses the primary methods available to the base class. In addition, this section presents the derived classes that inherit from the base class to represent the analytical material models described in Chapters 2 and 3. Note that in displaying class interfaces, often only public members of a class (e.g., methods that can be invoked by other objects) are illustrated, while private members (e.g., variables and internal data structures) are not.

4.3.1 *UniaxialConfinedMaterial* Abstract Class

The class interface for *UniaxialConfinedMaterial* is illustrated in Figure 4.3. This is an abstract class that extends the abstractions provided in *UniaxialMaterial* in order to supply basic methods and member variables for derived classes representing confinement-sensitive uniaxial material behavior. Examples of additional member variables include quantities to describe confining stress and dilation strain values in the current and last converged load steps, and the secant ratio of lateral and axial strains. The additional methods are purely virtual (indicated by setting them equal to zero). They include three access methods to retrieve internal variables, in addition to one method to set the material stress state. This latter method, **setTrialState()** receives as arguments the strain and an optional strain rate similar to **UniaxialMaterial::setTrialStrain()**, in addition to an optional confining stress value and a pointer to a *UniaxialMaterial* object representing the hoop or jacket (typically supplied by the *ConfinedFiberSec* object). In the absence of the latter two arguments, the derived class should be equivalent to its base *UniaxialMaterial*. This is ensured in the implementation of the virtual **setTrialStrain()** method in the derived classes, which are discussed in the following sections.

```
class UniaxialConfinedMaterial : public UniaxialMaterial
{
public:
//    Constructor and destructor
      UniaxialConfinedMaterial (int tag, int classTag);
      virtual ~UniaxialConfinedMaterial();

//    Pure virtual methods inherited from base UniaxialMaterial class (not shown)

//    Main and access methods needed by confinement-sensitive subclasses
      virtual int setTrialStrain(double strain, double strainRate, double sig_3,
          UniaxialMaterial* theHoop = 0);
      virtual double getSig_3(void) = 0;
      virtual double getEps_3(void) = 0;
      virtual double getVs(void) = 0;
};
```

Fig. 4.3 Class interface for *UniaxialConfinedMaterial*.

4.3.2 *SteelRebar* Material Class

The class interface for *SteelRebarMaterial* is illustrated in Figure 4.4, where the suffix "Material" is dropped for brevity in previous and future references to the class. The constructor receives as arguments the material and geometry parameters and uses them to populate the member variables of the constructed objects. Several of these parameters have default values listed in Appendix A and need not be explicitly input. Most importantly, the constructor assigns to each object of class *SteelRebar* a previously defined *UniaxialMaterial* object to represent the mechanical stress-strain constitutive law for the steel bar material, whose pointer is the constructor argument **theRealBar.** The class input allows the analyst the option to specify a *UniaxialMaterial* object representing the transverse reinforcement, e.g., hoop, pointed to by **theDefaultHoop**. Alternatively such material can be specified in the definition of the *ConfinedFiberSec* object containing the *SteelRebar* objects, and later provided to these objects during runtime using the pointer **theHoop** in the function-call to **SteelRebar::setTrialStrain()**.

If a pointer to a hoop is provided using both methods, only the *UniaxialMaterial* object to which **theDefaultHoop** points is considered in computing the critical buckling stress. This setup can be used in modeling buckling in steel bars laterally supported by specially arranged transverse reinforcement. If neither pointer is provided, the hoop stiffness is ignored in computing the critical buckling stress and the buckling length is set by the analyst using the argument **spacing** in the constructor.

The method **setTrialState()** is overloaded to correspond with the purely virtual methods defined in the base classes *UniaxialMaterial* and *UniaxialConfinedMaterial*. An overloaded method is a method that has more than one definition depending on the number and types of arguments passed to it. The first definition corresponds to the case where the material object is being addressed as a *UnixaialMaterial* by existing OpenSees *SectionForceDeformation* or *Element* classes. In this case the call to the method is simply redirected to the second definition with the confinement information set to zero in the corresponding arguments. This second definition in turn invokes a number of methods to check the state of the steel bar with regards to yielding and buckling. If the bar is detected to have buckled, the strain decomposition approach discussed in Section 2.2 is enforced to compute the effective stress in the bar. This is performed using the built-in iterative method **secantSolver()** until the outcome of the **objective()** method, representing the compatibility of the total, the mechanical, and the buckling-induced strains, converges.

The method **checkYielding()** is used to redefine the boundary conditions on the buckling-prone steel bar once yielding is detected in order to capture the additional reduction in bar stiffness due to initial imperfection in the transition phase between yielding and the onset of buckling (see Section 2.2.3). The implementation allows the analyst to disable this extra accuracy in modeling (e.g., for the sake of better numerical robustness) so that the bar will follow its constitutive material law without stress decomposition after yielding until buckling is detected. If bar buckling had not been detected during a compression loading half-cycle, the method **setBucklingStress()** is used to compute the critical buckling stress for the current stress states in the bar and the transverse ties. This critical stress is then checked against the current stress in the bar using the method **checkBuckling()**. Once bar buckling is detected, the method **setBucklingStrain()** is called. This method redefines the boundary conditions controlling the

strain decomposition equation to reflect the stress state at the onset of buckling. In addition, this method sets a flag member variable **isBuckled** to indicate buckling, which is reset upon recovery of the buckling-induced strain.

The information necessary for keeping the damage state current is routinely passed on to the associated *DamageModel* object using the method **setDamage()** in the course of **setTrialStrain()**. Since the *DamageModel* objects typically associated with the *SteelRebar* class belong to the subclass *CoffinManson*, **setDamage()** is typically invoked upon strain reversal, which enables the computation of accumulated plastic strain (see Section 2.2.5). To preserve the continuity of the stress-strain response and the consistency of the computed tangent stiffness modulus, the corresponding stress-reduction factor is applied only upon stress reversal, using the method **updateDamage()**. The method **getDamage()** is an example of access methods used by other objects (e.g., *ConfinedFiberSec*) to query *SteelRebar* objects' information (e.g., damage index value).

```
class SteelRebarMaterial : public UniaxialConfinedMaterial
{
public:
//    Constructor and destructor
      SteelRebarMaterial(int tag, double eu, double ey, double barDiam,
          UniaxialMaterial* theRealBar, int redMode, double spacing, double beta,
          UniaxialMaterial* theDefaultHoop, double strainRecRatio, double
          maxLatStrain, double Nf, double mf, double af);
      ~SteelRebarMaterial();

//    Main methods to set stress state using strain decomposition
      int setTrialStrain(double strain, double strainRate = 0.0) {return setTrialStrain
          (strain, strainRate, 0, 0);};
      int setTrialStrain(double strain, double strainRate, double sig_3,
          UniaxialMaterial* theHoop = 0);
      double objective (double &aRealStrain);
      int secantSolver(double *x1, double *x2, double tol);

//    Methods to check yielding/buckling & define strain decomposition param's
      void checkYielding(double strain, double ey);
      int setBuckleStress(double strain, double springStiffness, double
          springSpacing, double A, double I, UniaxialMaterial* aRealMat);
      void checkBuckling(double strain, double springStiffness, double
          springSpacing, double A, double I);
      int setBuckleStrain (double &currentRealStrain);

//    Methods to communicate with associated DamageModel
      int setDamage(void);
      int updateDamage(void);

//    Access & pure virtual methods declared in base class (partial list)
      double getDamage(void);
};
```

Fig. 4.4 Class interface for *SteelRebar* material.

4.3.3 *LapSplice* Material Class

The class interface for *LapSpliceMaterial* is illustrated in Figure 4.5. The class interface is similar to that of *SteelRebar* illustrated in Figure 4.4. The constructor operates in a similar way, as well as the communication with the associated *DamageModel* object. In addition, the constructor allows the analyst the option to specify a null value for the argument **theRealBar**, pointing to the *UniaxialMaterial* object representing the bar material's mechanical stress-strain constitutive law. In this optional case, the constructed object will reproduce the behavior of the constitutive bond-slip law without considering strain decomposition with a bar material acting in parallel, which can be used for bond-slip model calibration purposes in the presence of such experimental observations. In contrast to class *SteelRebar*, the strain decomposition equation for class *LapSplice* is enforced at all times and not only when a critical (i.e., buckling) stress value has been violated (see Section 2.3). The method **setTrialState()** is overloaded in a manner similar to that of class *SteelRebar*. The built-in method **secantSolver()** enforces the convergence of the **objective()** method, which in *LapSplice* class represents the equilibrium between bond stress and total axial stress along the spliced bars.

The method **initiateEnvelope()** is used to include the effect of lateral confinement on the bond capacity. It is invoked only during the first function-call to **setTrialStrain()**. This is performed in order to allow for the possibility that the *UniaxialMaterial* object representing the transverse ties be supplied using the function-call by the associated *ConfinedFiberSec* object, instead of being specified at the object's construction using the constructor's pointer argument **theDefaultHoop**.

```
class LapSpliceMaterial : public UniaxialConfinedMaterial
{
public:
//    Constructor and destructor
      LapSpliceMaterial(int tag, double spliceLength, double eps_dl,
          UniaxialMaterial* theRealBar, double tao_or_fc, double barDiam, double
          r_not, UniaxialMaterial* theDefaultHoop, double u_max, double
          pinchRatio1, double pinchThresh,  double pinchStrain, double
          unloadMult, double u_ult, double exponent, double expn, double
          slipStrainMult, double alpha, double beta);
      ~LapSpliceMaterial();

//    Main methods to set stress state using strain decomposition
      int setTrialStrain(double strain, double strainRate, double sig_3 = 0,
          UniaxialMaterial* theHoop = 0);
      double objective (double &aRealStrain);
      int secantSolver(double *x1, double *x2, double tol);
      int initiateEnvelope(void);

//    Methods to communicate with associated DamageModel (not shown)
//    Access & pure virtual methods (not shown)
};
```

Fig. 4.5 Class interface for *LapSplice* material.

4.3.4 *ConfinedConcrete* Material Class

The class interface for *ConfinedConcreteMaterial* is illustrated in Figure 4.6, where the suffix Material is dropped for brevity in previous and future references to the class. The class interface designates as "friends" four *UniaxialConfinedCurve* subclasses representing the different branches of the hysteretic behavior. The mention of the suffix "Curve" in the subclass names is dropped for brevity in previous and future references and retained only in references to the base *UniaxialConfinedCurve* abstract class. Each *ConfinedConcrete* object owns one object of each derived subclass, and the friend designation allows such subclasses to access certain local

member variables of *ConfinedConcrete* objects at runtime. This accessibility is needed for the *UniaxialConfinedCurve* objects to update their state during the analysis and redefine their starting and ending points as explained in the next section. The implementation allows the analyst to specify a prescribed confining stress value, a *UniaxialMaterial* object representing the confining jacket (which can be alternately specified in the definition of the associated *ConfinedFiberSec* object), a combination of both, or neither. The constructor receives as arguments the material and damage model parameters and populates the corresponding member variables in the constructed objects.

The definition of **setTrialState()** depends on whether lateral strain compatibility is requested in the function-call to the method or not. If so, the confining stress argument **sig_3** in the function-call is null and is therefore computed using the pointer argument to the confining jacket **theHoop**. Otherwise, the confining stress value is passed on as an argument in the function-call and used directly in computing the axial stress. The method **setCyclicState()** is invoked when a change is detected in the hysteretic branch defining the material's current stress state (e.g., a reversal in strain increment) in order to identify which *UniaxialConfinedCurve* derived object to call. The method **addDefaultDamage()** is used if the analyst chooses to use the dissipated energy-based damage model defined in Section 3.2.4. However, any existing *DamageModel* object implemented in OpenSees can be constructed and linked to the current *ConfinedConcrete* object if its parameters are calibrated to the material properties. Several *DamageModel* classes have previously been implemented in OpenSees, e.g., Park and Ang (1985). The majority of these *DamageModel* classes are documented and discussed in Altoontash (2004).

The method **getTangent()** depends on the current hysteretic state of the object. According to the outcome of **setCyclicState(),** the corresponding *UniaxialConfinedCurve* derived object is responsible for computing and returning the tangent stiffness modulus. In the case that the derived object is of class *BiniciEnvelope*, the tangent can be computed only by using numerical differencing. Direct differentiation of stress-strain equations for class *BiniciEnvelope* is not feasible because of the equation's complex dependence on the confining stress. Evaluation of the tangent stiffness moduli is discussed in detail in Section 4.4.

The static class-wide dummy object **theShadowEnvelope** of class *BiniciEnvelope* is constructed so that all objects of class *ConfinedConcrete* should use it in order to compute virtual stress states needed for computing the tangent by numerical differencing without altering the stress state of their own associated *BiniciEnvelope* object. A "static" designation means that there is only one such dummy *BiniciEnvelope* object available and accessible for all *ConfinedConcrete* objects combined. Since the material objects are asked by the *Analysis* class to compute the tangent stiffness moduli one-at-a-time, the use of one class-wide dummy *BiniciEnvelope* object for this purpose shared by all *ConfinedConcrete* objects at runtime reduces the demand on computational memory.

The method **getDamage()** in turn queries the associated *DamageModel* object and retrieves the current information about the material's damage state. The information necessary for updating the damage state (as discussed in Section 4.6) is routinely passed during the analysis to the associated *DamageModel* object in the course of executing the method **setTrialStrain()**.

```
class ConfinedConcreteMaterial : public UniaxialConfinedMaterial
{
public:
    friend class BiniciEnvelopeCurve;
    friend class LokugeUnloadingCurve;
    friend class LokugeLoadingCurve;
    friend class ParabolicTransitionCurve;

//  Constructor and destructor
    ConfinedConcreteMaterial(int tag, double fcc, double ecc, double Ec, double
        f3u, double e3u, double ft, double et0, double vs, double lc, double Gf,
        double paramP, double paramC, double paramA, DamageModel*
        theDamageModel, int theDamageMode, double sig_3p, UniaxialMaterial*
        theDefaultHoop);
    ~ConfinedConcreteMaterial();

//  Main methods
    int setTrialStrain(double strain, double strainRate, double sig_3,
        UniaxialMaterial* theHoop = 0);
    void setCyclicState(int stateTag);
    int addDefaultDamage(int tag, double paramC);

//  Access, input-checking & pure-virtual methods from base class (partial list)
    double getTangent(void);
    double getDamage(void);

//  Class-wide dummy object for calculating tangent using differencing
    static BiniciEnvelopeMaterial theShadowEnvelope;
};
```

Fig. 4.6 Class interface for *ConfinedConcrete* material.

4.3.5 *UniaxialConfinedCurve* Abstract Class

The class interface for *UniaxialConfinedCurve* is illustrated in Figure 4.7. Being an abstract class, all of its member methods are designated virtual. No stand-alone objects of this class or its derived classes can be constructed through the interpreter, nor can any such object exist in the domain independent of a *UniaxialConfinedMaterial* object which is designated as the "parent" object. Hence, every object of the current class has as a member variable a pointer called **theParentMat**.

The method **setParent()** allows the assignment or reassignment of pointer member variable **theParentMat**. It is mainly used when constructing copies of the parent *UniaxialConfinedMaterial* object, e.g., during fiber-discretization, during which copies are also constructed of the associated *UniaxialConfinedCurve* objects. This method is then used to set the member variable **theParentMat** to point to the copied *UniaxialConfinedMaterial* object instead of the original one.

The method **updateAnchors()** is invoked in the parent *UniaxialConfinedMaterial* object once its stress state necessitates redefining the associated *UniaxialConfinedCurve* (e.g., upon reversal of loading direction). The method receives as arguments the vector **theMatData** of ordered material properties and the array **theParentMats** of pointers to objects of class *UniaxialMaterial*, which allows flexibility for *UniaxialConfinedCurve* subclasses derived in the future whose redefining stress state(s) may depend on one or more *Material* objects in the *Domain*. For the case of a *ConfinedConcrete* parent object, the array of pointers references the object and its associated *UniaxialConfinedCurve* derived objects. The stress states defining the beginning and end points of a derived object from class *UniaxialConfinedCurve* can be updated using this information and later retrieved using access methods whose definition depends on the derived class.

The method **setTrialStrain()** simply passes on the function-call made in the parent *UniaxialConfinedMaterial* object to the derived *UniaxialConfinedCurve* class. The methods **getStartStrain()** and **getEndSig_3()** are examples of the access methods used by other objects (e.g., the associated *ConfinedConcrete* object) to query derived objects of class *UniaxialConfinedCurve* for the stress states defining their start and end-points.

```
class UniaxialConfinedCurve : public UniaxialConfinedMaterial
{
public:
//    Constructor and destructor
      UniaxialConfinedCurve (int tag, int classTag);
      virtual ~UniaxialConfinedCurve();

//    Method to define the UniaxialConfinedMaterial that controls the curve
      virtual void setParent(UniaxialConfinedMaterial* aNewParent) = 0;

//    Methods to update & retrieve (partial list) stress states defining curve object
      virtual int updateAnchors(UniaxialMaterial** theParents, Vector theMatData)
          = 0;
      virtual double getStartStrain(void) = 0;
      virtual double getEndSig_3(void) = 0;

//    Main method to set the current stress state
      virtual int setTrialStrain(double strain, double strainRate, double sig_3,
          UniaxialMaterial* theHoop) = 0;

//    Access & virtual methods declared in base class (not shown)

protected:
      UniaxialConfinedMaterial* theParentMat;
};
```

Fig. 4.7 Class interface for *UniaxialConfinedCurve.*

4.3.6 *UniaxialConfinedCurve* Subclasses

Four classes are derived from the abstract *UniaxialConfinedCurve* as illustrated in Figure 4.2. These derived classes are *BiniciEnvelope*, *LokugeUnloading*, *LokugeLoading*, and *ParabolicTransition*. Aside from receiving the class-dependent curve parameters in order to populate the member variables, the four class interfaces are generally similar to that of base class *UniaxialConfinedCurve* and are not shown herein. Each derived class implements its methods to

correspond with its respective component of the confined concrete constitutive model discussed in Section 3.2, where the behavior in tension has been appended to *LokugeUnloading*. For all four derived classes, it should be noted that the implemented stress-strain relationships are setup to deal with compressive stresses and strains in the axial direction as possessing a positive algebraic sign. Hence, the function-call to their **setTrialStrain()** method within **theParentMat::setTrialStrain()** method reverses the algebraic signs of axial stress and strains arguments, while the corresponding access methods in the derived classes reverse the algebraic signs back when queried for these values. The significant additions to the class interface of *UniaxialConfinedCurve* are the methods added to enforce lateral strain compatibility. This latter step is performed mainly using a built-in **secantSolver()** method similar in construction to those defined in Sections 4.3.2–4.3.3, and an **objective()** method that represents lateral strain compatibility by checking the equilibrium of the resulting confining stresses in the core concrete and the confining jacket.

4.4 EVALUATION OF MATERIAL TANGENT STIFFNESS MODULI

All *UniaxialConfinedMaterial* derived classes implemented in the previous section are required by OpenSees architecture to define an access method that retrieves the *Material* object's tangent stiffness modulus at the stress state current during runtime. The numerical convergence of the FE model's *Solver* object requires accurate estimation of these tangent moduli. For *UniaxialConfinedMaterial*, an analytical evaluation of the tangent modulus may be difficult in certain cases due to the complex dependence of the stress-strain response on future confining stress values. In such cases, the tangent moduli have to be evaluated numerically. This section presents the analytical expressions used for evaluating the tangent modulus of each *UniaxialConfinedMaterial* derived class at every stress state where analytical evaluation is possible, and describes the numerical differencing approach used otherwise. In the following sections, the unknown tangent modulus is generically referred to as E in each respective class.

4.4.1 *SteelRebar* Material Class

The tangent stiffness modulus in a *SteelRebar* object is evaluated depending on its stress state. Three stress states are possible with respect to buckling: (1) a bar with no buckling-induced strain subjected to any strain increment, (2) a buckled bar subjected to a compressive strain increment, and (3) a buckled bar subjected to a tensile strain increment. In stress state (1), the tangent modulus is retrieved from the associated *UniaxialMaterial* object representing the bar's mechanical stress-strain constitutive law, as identified by the pointer member variable **theRealBar**. This "mechanical" stiffness modulus is referred to hereafter as E_m.

In stress states (2) and (3), the following derivation is developed with reference to the analytical stress-strain model described in Section 2.2. Recall that the general definition of the tangent stiffness modulus E at any stress state is given by

$$E = \frac{\partial \sigma}{\partial \varepsilon_t} = \frac{\partial \sigma}{\partial \varepsilon_s} \frac{\partial \varepsilon_s}{\partial \varepsilon_t} \tag{4.1}$$

using the well-established chain rule of differentiation. The first term in Equation (4.1) is equivalent to the mechanical stiffness modulus of **theRealBar** object, namely,

$$\frac{\partial \sigma}{\partial \varepsilon_s} = E_m \tag{4.2}$$

During stress state (2), the second term in Equation (4.1) corresponds to

$$\frac{\partial \varepsilon_s}{\partial \varepsilon_t} = 1 + \frac{\partial \varepsilon_{fi}^b}{\partial \varepsilon_t} - \frac{\partial \varepsilon_f^b}{\partial \varepsilon_t} = 1 - \frac{\partial \varepsilon_f^b}{\partial \varepsilon_t} \text{ since } \varepsilon_{fi}^b \text{ is constant} \tag{4.3}$$

$$\frac{\partial \varepsilon_f^b}{\partial \varepsilon_t} = \frac{\partial \varepsilon_r}{\partial \varepsilon_t} + \frac{\partial}{\partial \varepsilon_t} \frac{\varepsilon_b}{\left(1 - \alpha_{\Delta P}^b\right)^2} = \frac{2\varepsilon_b}{\left(1 - \alpha_{\Delta P}^b\right)^3} \frac{\partial \alpha_{\Delta P}^b}{\partial \varepsilon_t} \tag{4.4}$$

$$\frac{\partial \alpha_{\Delta P}^b}{\partial \varepsilon_t} = \frac{\partial}{\partial \varepsilon_t} \frac{\sigma - \sigma_b}{\sigma_{cr|\infty} - \sigma_b} = \frac{1}{\sigma_{cr|\infty} - \sigma_b} \frac{\partial \sigma}{\partial \varepsilon_t} = \frac{E}{\sigma_{cr|\infty} - \sigma_b} \tag{4.5}$$

After substitution, Equation (4.1) is re-written as

$$E = E_m \left(1 - \frac{2\varepsilon_b}{\left(1 - \alpha_{\Delta P}^b\right)^3 \left(\sigma_{cr|\infty} - \sigma_b\right)} E \right) \tag{4.6}$$

which can be solved to compute the tangent stiffness modulus in stress state (2)

$$E = E_m \left(1 + \frac{2\varepsilon_b E_m}{\left(1-\alpha_{\Delta P}^b\right)^3 \left(\sigma_{cr|\infty} - \sigma_b\right)} \right)^{-1} \tag{4.7}$$

During stress state (3) and according to Equation (2.34), the second term in (4.1) corresponds to

$$\frac{\partial \varepsilon_s}{\partial \varepsilon_t} \approx 1 - \eta_f \frac{\varepsilon_f}{\varepsilon_f^{un}} \tag{4.8}$$

Substitution in (4.1) yields the following tangent stiffness modulus in stress state (3):

$$E \approx E_m \left(1 - \eta_f \frac{\varepsilon_f}{\varepsilon_f^{un}} \right) \tag{4.9}$$

Note that if the method **checkYielding()** is enabled by the analyst, a potential stress state (4) may exist in which a yielding bar is subjected to a compressive strain increment prior to buckling. Referring to Section 2.2.3, stress state (4) is conceptually similar to stress state (2). Following Equations (2.28)–(4.7) while substituting superscript b by h and making necessary adjustments, the tangent stiffness modulus is derived for stress state (4) as follows:

$$E = E_m \left(1 + \frac{2\varepsilon_{fi}^h E_m}{\left(1-\alpha_{\Delta P}^h\right)^3 \left(\sigma_{cr}^h - \sigma_i^h\right)} \right)^{-1} \tag{4.10}$$

4.4.2 *LapSplice* Material Class

The tangent modulus in a *LapSplice* object is evaluated depending on the stress state in its associated bond-slip material model. Four stress states are possible: (1) loading along the envelope, (2) unloading, (3) pinching, and (4) reloading. It will be shown that the computation of tangent stiffness modulus for the latter three stress states follows the same approach. First, with reference to the lap-splice constitutive model described in Section 2.3, the following is true for the two serially linked materials:

$$\frac{1}{E} = \frac{\partial \varepsilon_t}{\partial \sigma_s} = \frac{\partial \varepsilon_s}{\partial \sigma_s} + \frac{\partial \varepsilon_{sl}}{\partial \sigma_s} = \frac{1}{E_m} + \frac{\partial u_s}{L_s \partial \sigma_s} \tag{4.11}$$

where E_m is the mechanical stiffness modulus (see Section 4.4.1). Invoking the equilibrium of bond and axial stresses (see Eq. (2.41)), one obtains

$$\frac{\partial \sigma_s}{\partial u_s} = \frac{\partial \sigma_s}{\partial \tau_m}\frac{\partial \tau_m}{\partial u_s} = 2\frac{(L_s - l_1)^2 + l_1^2}{d_b L_s} S \tag{4.12}$$

Substitution in Equation (4.11) yields the following tangent stiffness modulus:

$$E = E_m\left(1 + E_m \frac{0.5 d_b}{(L_s - l_1)^2 + l_1^2}\frac{1}{S}\right)^{-1} \tag{4.13}$$

The stiffness S of the bond-slip component (see Eq. (2.42)) during stress state (1) is defined as

$$S = \frac{\partial \tau_m}{\partial u_s} = \frac{\tau_{\max} r(r-1)\left(1 - \left(u_s / u_{s,\max}\right)^r\right)}{u_{s,\max}\left(r - 1 + \left(u_s / u_{s,\max}\right)^r\right)^2} \tag{4.14}$$

Therefore, for stress state (1), one obtains

$$E = E_m\left(1 + E_m \frac{0.5 d_b}{(L_s - l_1)^2 + l_1^2}\frac{u_{s,\max}\left(r - 1 + \left(u_s / u_{s,\max}\right)^r\right)^2}{\tau_{\max} r(r-1)\left(1 - \left(u_s / u_{s,\max}\right)^r\right)}\right)^{-1} \tag{4.15}$$

During stress states (2)–(4), the bond-slip material component exhibits a linear stiffness modulus S (where the omitted subscript and superscripts depend on the stress state, as defined in Section 2.3.3). Hence, substituting the proper S from Section 2.3.3 into the Equation (4.13), one obtains the corresponding tangent stiffness modulus for each stress state.

4.4.3 *ConfinedConcrete* Material Class

Evaluation of the tangent stiffness modulus of the *ConfinedConcrete* objects depends on the outcome of their respective **setCyclicState()** method and the corresponding *UniaxialConfinedCurve* derived object that fits the material's current stress state. The tangent stiffness modulus is computed differently in each *UniaxialConfinedCurve* subclass, as described in the next sections. The *ConfinedConcrete* object queries only the appropriate *UniaxialConfinedCurve* derived object for its current stiffness modulus.

4.4.4 *BiniciEnvelope* Curve Class

The tangent stiffness modulus for objects of class *BiniciEnvelope* cannot be evaluated analytically. This is due to the constitutive law's complex dependency on the confining stress. Moreover, the confining stress varies during the analysis based on the confining jacket's stress state, the applied cross-section forces, and the fiber location within the cross section. Therefore, the variation of this confining stress as a function of axial strain cannot be explicitly evaluated. Hence, the tangent stiffness modulus is computed using numerical differencing. Prior to failure of the confining jacket, a central difference is used. Hence, the previously discussed static object **ConfinedConcrete::theShadowEnvelope** is used to evaluate the virtual stress states $\{\sigma_1^+, \sigma_1^-\}$ at imaginary axial strain values $\{\varepsilon_1^+, \varepsilon_1^-\}$ infinitesimally incremented and decremented from the current axial strain ε_1. Meanwhile, virtually incremented and decremented confining stress values $\{\sigma_3^+, \sigma_3^-\}$ are computed and added to the virtual stress states being evaluated by adding infinitesimal values to the current confining stress σ_3. The values of these infinitesimal values are approximated based on the ratio of the confining stress increment $\Delta\sigma_3$ to axial strain increment $\Delta\varepsilon_1$ from the previous converged load step. Finally, the tangent stiffness modulus is approximated by

$$E = \frac{\delta\sigma_1}{\delta\varepsilon_1} = \frac{\sigma_1^+ - \sigma_1^-}{\varepsilon_1^+ - \varepsilon_1^-} \tag{4.16}$$

The static object is then reset so that another *BiniciEnvelope* object can use it. Upon failure of the confining jacket, the central difference approach outlined above becomes inaccurate due to the potentially brittle failure mode (especially in fibers with relatively high confinement ratios, ϕ, see Section 3.2.1). Hence, forward difference is used instead, whereby only one virtual stress state is evaluated and the tangent stiffness modulus is approximated by

$$E = \frac{\delta\sigma_1}{\delta\varepsilon_1} = \frac{\sigma_1^+ - \sigma_1}{\varepsilon_1^+ - \varepsilon_1} \tag{4.17}$$

4.4.5 *LokugeUnloading* Curve Class

In objects of class *LokugeUnloading,* the constitutive law's dependence on the variable confining stress is straightforward and differentiable. However, the variation in confining stress with axial strain is smooth but not necessarily explicitly computable. Hence, the tangent stiffness modulus for objects of class *LokugeUnloading* is evaluated based on the choice of the analyst. Three options exist: (1) using numerical differencing, (2) using closed-form differentiation while assuming the variation in confining stress, and (3) using closed-form differentiation while assuming fixed confining stress. In the third option, the variation in confining stress for individual fibers is disabled upon unloading and resumed upon returning to the envelope in order to enhance numerical robustness. The first option is implemented in a manner similar to *BiniciEnvelope* objects. The second and third options are simultaneously presented in the following paragraph.

With reference to Section 3.2.3:

$$E = \frac{\partial \sigma_1}{\partial \varepsilon_1} = \frac{\partial}{\partial \varepsilon_1}\left(2\tau + \sigma_3\right) \tag{4.18}$$

The first term in Equation (4.18) is expanded using the following series of chain-rule equations:

$$2\frac{\partial \tau}{\partial \varepsilon_1} = 2\left(\tau_{un} - \tau_{pl}\right)\frac{\partial \bar{\tau}_{un}}{\partial \varepsilon_1} = 2\left(\tau_{un} - \tau_{pl}\right)\frac{\partial}{\partial \varepsilon_1}0.43e^{1.2\bar{\gamma}_{un}} \tag{4.19}$$

$$\frac{\partial}{\partial \varepsilon_1}0.43e^{1.2\bar{\gamma}_{un}} = 0.516e^{1.2\bar{\gamma}_{un}}\frac{\partial}{\partial \varepsilon_1}\bar{\gamma}_{un} = \frac{0.516e^{1.2\bar{\gamma}_{un}}}{\gamma_{un} - \gamma_{pl}}\frac{\partial}{\partial \varepsilon_1}\frac{\varepsilon_1 - \varepsilon_3}{2} \tag{4.20}$$

$$\frac{\partial}{\partial \varepsilon_1}\frac{\varepsilon_1 - \varepsilon_3}{2} = 0.5 - 0.5\left(\varepsilon_{3,un} - \varepsilon_{3,pl}\right)\frac{\partial}{\partial \varepsilon_1}\bar{\varepsilon}_{3,un} \tag{4.21}$$

$$\frac{\partial}{\partial \varepsilon_1}\bar{\varepsilon}_{3,un} = \frac{1}{p_c}\bar{\varepsilon}_{1,un}^{(1/p_c - 1)}\frac{\partial}{\partial \varepsilon_1}\bar{\varepsilon}_{1,un} = \frac{1}{p_c}\frac{\bar{\varepsilon}_{1,un}^{(1/p_c - 1)}}{\varepsilon_{1,un} - \varepsilon_{1,pl}} \tag{4.22}$$

The second term in Equation (4.18) is evaluated assuming a linear jacket stiffness modulus D_j:

$$\frac{\partial \sigma_3}{\partial \varepsilon_1} = \frac{\partial \sigma_3}{\partial \varepsilon_3}\frac{\partial \varepsilon_3}{\partial \varepsilon_1} = D_j\frac{\partial \varepsilon_3}{\partial \varepsilon_1} = D_j\left(\varepsilon_{3,un} - \varepsilon_{3,pl}\right)\frac{\partial}{\partial \varepsilon_1}\bar{\varepsilon}_{3,un} = \frac{D_j}{p_c}\frac{\left(\varepsilon_{3,un} - \varepsilon_{3,pl}\right)\bar{\varepsilon}_{1,un}^{(1/p_c - 1)}}{\varepsilon_{1,un} - \varepsilon_{1,pl}} \tag{4.23}$$

Substituting through and adding all terms, the tangent stiffness modulus is expressed as

$$E = 0.516e^{1.2\bar{\gamma}_{un}} \frac{\tau_{un} - \tau_{pl}}{\gamma_{un} - \gamma_{pl}} \left(1 - \frac{1}{p_c} \frac{\varepsilon_{3,un} - \varepsilon_{3,pl}}{\varepsilon_{1,un} - \varepsilon_{1,pl}} \bar{\varepsilon}_{1,un}^{(1/p_c - 1)} \right) + \frac{D_j}{p_c} \frac{\left(\varepsilon_{3,un} - \varepsilon_{3,pl} \right)}{\varepsilon_{1,un} - \varepsilon_{1,pl}} \bar{\varepsilon}_{1,un}^{(1/p_c - 1)} \tag{4.24}$$

where the last term is only valid in option (2) and becomes zero in option (3) above.

4.4.6 *LokugeLoading* Curve Class

Similar to objects of class *LokugeUnloading*, the analyst has the choice between using numerical differencing or closed-form differentiation (either with assumed or disabled confining stress variation) for class *LokugeLoading*. Following a similar derivation to that presented in the previous section, Equation (4.20) is replaced by

$$\frac{\partial}{\partial \varepsilon_1} \frac{1}{\log_e(2)} \log_e\left(\bar{\gamma}_{re} + 1 \right) = \frac{1.443}{\left(\gamma_{new} - \gamma_{ro} \right)\left(\bar{\gamma}_{re} + 1 \right)} \frac{\partial}{\partial \varepsilon_1} \frac{\varepsilon_1 - \varepsilon_3}{2} \tag{4.25}$$

The tangent stiffness modulus is therefore expressed as

$$E = \frac{1.443}{\left(\bar{\gamma}_{re} + 1 \right)} \frac{\tau_{new} - \tau_{ro}}{\gamma_{new} - \gamma_{ro}} \left(1 - p_c \frac{\varepsilon_{3,new} - \varepsilon_{3,ro}}{\varepsilon_{1,new} - \varepsilon_{1,ro}} \bar{\varepsilon}_{1,re}^{(p_c - 1)} \right) + D_j p_c \frac{\left(\varepsilon_{3,new} - \varepsilon_{3,ro} \right)}{\varepsilon_{1,new} - \varepsilon_{1,ro}} \bar{\varepsilon}_{1,re}^{(p_c - 1)} \tag{4.26}$$

where as for *LokugeUnloading*, the last term in Equation (4.26) is non-zero if the confining stress variation is enabled, otherwise it is set to zero.

4.4.7 *ParabolicTransition* Curve Class

The axial stress-strain relationship in objects of class *ParabolicTransition* does not depend on the confining stress. Unlike other *UniaxialConfinedCurve* derived classes, only the stress-state points defining the start and end points of this curve depend on the confining stress. With reference to Section 3.2.3, the tangent stiffness modulus is evaluated explicitly as follows:

$$E = \frac{\partial \sigma_1}{\partial \varepsilon_1} = E_{new} - 2\left[E_{new}\left(\varepsilon_{1,re} - \varepsilon_{1,new} \right) - \left(\sigma_{1,re} - \sigma_{1,new} \right) \right] \times \frac{\varepsilon_1 - \varepsilon_{1,new}}{\left(\varepsilon_{1,re} - \varepsilon_{1,new} \right)^2} \tag{4.27}$$

4.5 IMPLEMENTATION OF *SECTIONFORCEDEFORMATION* SUBCLASSES

The use of the newly developed *UniaxialConfinedMaterial* derived classes to model the flexural response of fiber-discretized cross sections is accomplished through constructing corresponding *Fiber* objects within a *ConfinedFiberSec2D* or a *ConfinedFiberSec3D* class, both subclasses of *SectionForceDeformation*. The analyst input for either *ConfinedFiberSec* class is essentially the same. The dimensionality of the class is decided by the geometry of the structural model. For the purposes of this report, only *ConfinedFiberSec2D* is fully implemented. The full implementation of *ConfinedFiberSec3D* involves the numerical solution of a planar geometry problem to determine the spatial orientation of the neutral axis during runtime and its normal distance from individual fibers. Since no *ConfiendFiberSec3D* objects are utilized in this report, C++ implementation of this numerical solution has not been completely carried out and this implementation is considered out of the scope of this report.

The class interface for *ConfinedFiberSec2D* is illustrated in Figure 4.8, which is modified from the class interface for class *FiberSection2D*. Accordingly, additional arguments are received by the constructor to populate member variables of constructed objects by a pointer **theHoop** to a *UniaxialMaterial* object representing the transverse reinforcement or confining jacket, an integer **confTag** representing the power p_s of the confining stress distribution function (see Section 3.3), and the strain value **e3Limit** corresponding to failure in the confining jacket and subsequent loss of confinement. The method **setTrialSectionDeformation()** conducts a preliminary scan of all *Fiber* objects representing core concrete to identify the one with maximum compressive strain. Core *Fiber* objects in a cross section must share the same material tag as the first *Fiber* object to be defined by the analyst for the discretized cross section (using the Tcl interface). Next, the *Fiber* object's method **ConfinedConcrete::setTrialStrain()** is invoked with a null confining stress argument in order to enforce lateral strain compatibility as discussed in Section 4.3.4. Once the stress state in **theHoop** object is set and the maximum confining stress is determined, Equation (3.41) is used to compute the confining stress at each fiber location. *Fiber* objects representing the cover concrete are assigned no confining stress. The individual *Fiber* objects' **setTrialStrain()** and **getDamage()** methods are then invoked. The *Fiber* objects' stresses and stiffness moduli are retrieved and assembled in the established fiber-

section procedure (Spacone et al. 1996a,b) to compute the *ConfinedFiberSec2D* object's stiffness matrix and resisting-force vector. Moreover, the *Fiber* objects' retrieved damage indices are assembled to create the cross-section damage indices defined in Section 3.3.2. The access method **getSecDamage()** retrieves the 2×1 vector of cross-section damage indices D_A and D_M.

It should be noted that each *Fiber* object may belong to any *UniaxialMaterial* subclass and not necessarily possess the extra functionality of *UniaxialConfinedMaterial* subclasses. Hence, the *ConfinedFiberSec* object must verify that each *Fiber* object corresponds to a subclass of *UniaxialConfinedMaterial*. If not, no attempt to exchange confinement-related or damage-related information should be made in order to avoid a possible runtime segmentation fault in the case that the corresponding access methods were not properly implemented in the non-*UniaxialConfinedMaterial Fiber* objects. This can be achieved by checking the class tag of each *Fiber* object (the class tag is unique to each class and is defined in its OpensSees implementation) and checking it against a list of *UniaxialConfinedMaterial* derived class tags. However, this approach is impractical as it requires constant updating of the list to reflect additional subclasses of *UniaxialConfinedMaterial* that may be added in the future. Hence, the verification is instead conducted using "dynamic casting," whereby each *Fiber* object is first assumed to belong to a *UnixialConfinedMaterial* subclass, and a pointer to it is "cast" (or re-declared) during runtime to the base class *UnixialConfinedMaterial*. According to standard C++ rules, if the assumption is valid (i.e., the dynamic casting is successful), this process results in a value for the newly declared pointer that belongs to the base class. However, if the assumption is not valid (i.e., the dynamic casting fails), the newly declared pointer value is null. This type of casting is called "dynamic" because it takes place during runtime and is not checked for validity by the C++ compiler beforehand.

```
class ConfinedFiberSec2D : public SectionForceDeformation
{
public:
//  Constructor and destructor
    ConfinedFiberSec2D(int tag, int numFibers, Fiber **fibers, UniaxialMaterial*
        theHoop, int confTag, double e3Limit);
    ~ConfinedFiberSec2D();

//  Main methods
    int setTrialSectionDeformation(const Vector &deforms);

//  Access & pure virtual methods declared in base class (partial list)
    Vector getSecDamage(void)
};
```

Fig. 4.8 Class interface for *ConfinedFiberSec2D.*

4.6 IMPLEMENTATION OF *DAMAGEMODEL* SUBCLASSES

Four new derived classes are added to the abstract class *DamageModel*, as illustrated in Figure 4.2. Similar to *UniaxialMaterial*, *DamageModel* is a *DomainComponent* subclass. An object of class *DamageModel* can be associated with any *DomainComponent* object that controls it to monitor damage propagation within itself. The associated *DomainComponent* objects are usually of class *Material* or *Element*. The class interface and functionality of the four derived classes are similar and therefore only that for class *DissipatedEnergy* is illustrated in Figure 4.9. The class configuration is relatively simple. The constructor populates the object with the relevant parameters—in this case the energy capacity **Etot** and an exponent **CPow**. When the main method **setTrial()** is invoked, it receives as arguments numerical values representing the current stress state of the associated *DomainComponent* object. These arguments typically contain information about the force (stress), deformation (strain), and stiffness modulus in the associated *DomainComponent* object. This information is used to incrementally update the *DamageModel* object's member variable which stores the value of the corresponding damage index. It is up to

the *DomainComponent* object to decide when to send its updated stress-state information to its associated *DamageModel* object. For example, the method **DissipatedEnergy::setTrial()** is only called within a *ConfinedConcrete* object if its stress state corresponds to either the unloading or reloading branch. Hence, only the hysteretic energy dissipated between these two branches (i.e., not the envelope or transition branch) enters the computation; see shaded areas in Figure 3.3. Similarly the method **CoffinManson::setTrial()** is called only within a *SteelRebar* object upon strain reversal to record the accumulation of plastic strain.

```
class DissipatedEnergy : public DamageModel
{
public:
//   Constructor and destructor
     DissipatedEnergy(int tag, double Etot, double Cpow);
     ~DissipatedEnergy();

//   Main method to set the current damage-sate
     int setTrial(Vector trialVector);

//   Access and pure virtual methods declared in base class (not shown)
};
```

Fig. 4.9 Class interface for *DissipatedEnergy* damage model.

5 Simulations of Experimentally Tested Deficient RC Columns

In this chapter, the material and cross-section models, which have been developed and individually calibrated in the previous chapters, are combined to develop computational models of RC columns using the OpenSees computational platform. The column models are used to simulate the experimentally observed behavior of deficient RC columns previously investigated under extreme deformation demands. The selected suite of investigated RC columns includes specimens tested in their as-built condition or after retrofitting by FRP jackets, and subjected to load-tests whose results represent monotonic or hysteretic behavior. The results from four experimental programs are used in this study, according to the following designations and characteristics:

1. Experimental Program A (Mosalam et al. 2007a,b): Monotonic behavior of as-built and FRP-retrofitted RC columns with inadequate core confinement.
2. Experimental Program B (Sheikh and Yau 2002): Hysteretic behavior of FRP-retrofitted RC columns with inadequate core confinement.
3. Experimental Program C (Xiao and Ma 1997): Hysteretic behavior of as-built and FRP-retrofitted RC columns with deficient lap-splices.
4. Experimental Program D (Henry 1998): Hysteretic behavior of as-built RC columns exhibiting longitudinal bar buckling and reinforcement fracture.

The column specimens investigated in this chapter all exhibit a collapse mode dominated by flexure-axial interaction and are modeled using the aggregation of material and cross-section models developed in this report. A schematic representation of the lumped-plasticity beam-column FE model used in the simulations and a typical discretization of the cross section

representing flexure-axial interaction in its plastic hinge region are illustrated in Figure 5.1. It is out of the scope of this report to calibrate the analytical model developed in Elwood (2002) to simulate the effect of shear-axial interaction and its *LimitState* implementation in OpenSees. This model has not been developed in this report and has been repeatedly calibrated by the model developers (Elwood 2002; Elwood and Moehle 2005). However, this model is used in the present report to account for the shear-axial collapse mode for RC columns and to formulate element removal criteria as discussed and implemented in Chapter 6. In addition, this model is used in Chapter 7 to demonstrate the process of progressive seismic collapse on two structures using the methodology developed in this report.

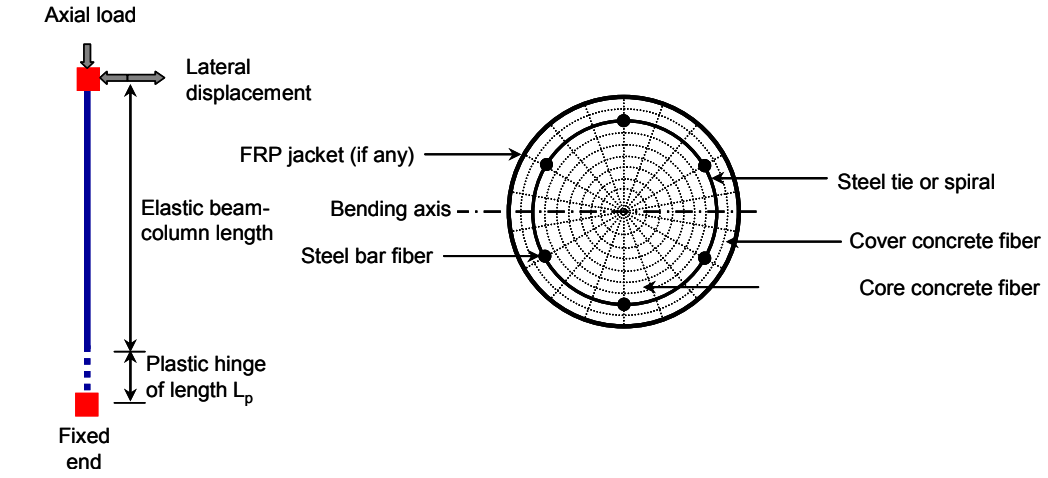

(a) Beam-column FE (b) Cross-section discretization

Fig. 5.1 Typical details of FE model used in simulating deficient RC columns.

5.1 EXPERIMENTAL PROGRAM A

Experimental program A was designed specifically for the purposes of this study. It has been conducted at the Middle East Technical University (METU), Turkey, and first reported in Mosalam et al. (2007b). Four RC columns of circular cross section and identical dimensions and steel reinforcement are subjected to combined axial loads and bending moments. One of the columns is investigated in its as-built condition under fixed axial load and monotonically increasing eccentricity, while the other three columns are strengthened by one layer of CFRP composite and subjected to monotonically increasing axial load at three different eccentricity

levels. FRP jacket strain records from program A were used to evaluate the analytical cross-section confinement model in Chapter 3. For completeness, the details of this experimental program are herein presented.

5.1.1 Specimen Geometry and Test Setup

All four specimens have the dimensions and longitudinal reinforcement illustrated in Figure 3.1. The total height of each specimen is 1000 mm. The middle 400 mm constitute the test region, having a diameter of 200 mm. The two column heads of each specimen are designed to mount the loading assembly and transfer the eccentric load to the column without sustaining damage outside the test region. For this purpose, three bolt holes in each were been formed during casting using steel pipes. Longitudinal reinforcement consists of six deformed bars of 10 mm diameter, continuous along the specimen length and uniformly distributed around the perimeter. The target concrete cover is 6 mm, yet this small cover could not be guaranteed because of difficulties in construction. Hence, a value of 10 mm is calibrated using the bending moment capacity of the as-built specimen and used in all the simulations. Within the test region, undeformed 4 mm diameter spirals with a pitch of 120 mm are used. In the transition and end zones, 6 mm diameter circular hoops with a spacing of 30 mm are used to safeguard against the possibility of failure outside the test region. The column heads are additionally confined by U-shaped deformed bars of 8 mm diameter. Prior to FRP application, all column surfaces are air-blown. Epoxy-impregnated FRP is then wrapped around the columns, with a 150 mm overlap length maintained for anchorage. Additional FRP patches are placed in the transition zones so that premature failure outside the test region is eliminated.

A steel reaction frame is used in the experiments as illustrated in Figure 5.3. Roller supports are placed at the ends of the specimen to eliminate moment restraint. A steel cable is passed vertically between the two (top and bottom) steel channel sections and fixed with chucks at top and bottom. A hydraulic jack is used to stress the cable against a steel plate in order to apply the eccentric axial load. The location of the steel plate along the channel sections is manipulated to provide the target eccentricity. Another hydraulic jack is placed directly on top of the column. Both hydraulic jacks are used to execute the load control scheme of specimen 1,

which is investigated in its as-built condition. Specimen 1 is subjected to monotonically increasing eccentricity while continuously adjusting the load in both hydraulic jacks as explained in Figure 5.3 so that their total force remains constant at 120 kN (approximately 44% of the nominal axial force capacity $P_o = 0.85 f_c' A_g + \sigma_y A_s$ with $A_g = \pi(100)^2$ mm^2 and $A_s = 6\pi(5)^2$ mm^2). Specimens 2 and 3 are investigated after being FRP-retrofitted by subjecting them to monotonically increasing axial load under constant eccentricities of 290 mm and 175 mm, respectively, where only the hydraulic jack connected to the steel cable is activated. Specimen 4 is investigated after being FRP-retrofitted by subjecting it to monotonically increasing concentric axial load, where only the hydraulic jack placed on top of the column is activated. Linear-variable displacement transducers (LVDTs) are used to measure the deformations of the column along the compression and tension sides of the test specimens over the length of the test region. Using these displacement measurements, a gage length of 400 mm, and the normal distance between the LVDTs, curvatures (for specimens 1, 2, and 3) and average axial strains (for specimen 4) are computed. In addition to LVDTs, electrical strain gages are mounted on the FRP composite to measure the circumferential strains for specimens 3 and 4. For specimen 4, additional strain gages are used to measure local axial strains and verify the calculated average strains from the measurements of the LVDTs. Lateral displacements of the column specimens along their heights were not measured, which would have made it possible to update the computed bending moments by including geometric P-Δ effects.

Material properties for concrete, reinforcing steel, and FRP composites are listed in Table 2.1. The target compressive strength is 10 MPa for all specimens. Manufacturer's data for individual FRP fibers list a thickness of 0.165 mm, rupture strain of 0.015, and modulus of elasticity of 230 GPa. After epoxy impregnation, the FRP composite has a thickness of about 1 mm and a modulus of elasticity of 61 GPa, obtained from CFRP test coupons.

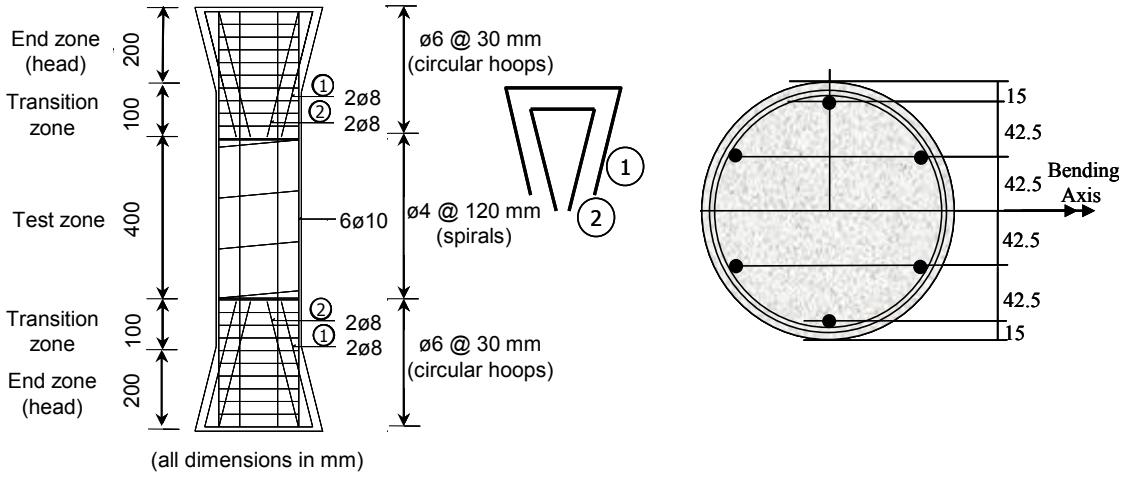

(a) Elevation and reinforcement arrangement (b) Cross-section details

Fig. 5.2 Specimen geometry and reinforcement for program A.

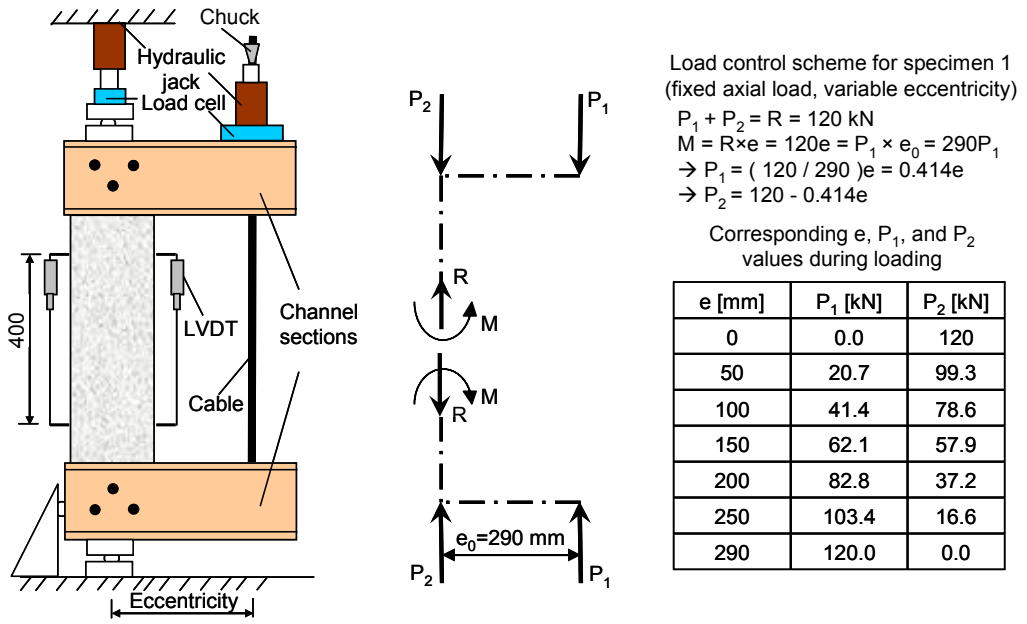

Load control scheme for specimen 1
(fixed axial load, variable eccentricity)

$P_1 + P_2 = R = 120$ kN

$M = R \times e = 120e = P_1 \times e_0 = 290P_1$

$\rightarrow P_1 = (120 / 290)e = 0.414e$

$\rightarrow P_2 = 120 - 0.414e$

Corresponding e, P_1, and P_2 values during loading

e [mm]	P_1 [kN]	P_2 [kN]
0	0.0	120
50	20.7	99.3
100	41.4	78.6
150	62.1	57.9
200	82.8	37.2
250	103.4	16.6
290	120.0	0.0

(a) Loading frame (b) Free-body diagram (c) Load-eccentricity history

Fig. 5.3 Specimen setup and loading scheme for program A.

Table 5.1 Material properties for program A.

Material property	Value
f_c' [MPa]	8.7*, 8.9**, 9.4***
Concrete cover [mm]	10
Longitudinal steel σ_y [MPa]	260
Transverse steel σ_y [MPa]	400
Longitudinal steel ratio [%]	1.50
Transverse steel ratio [%]	0.22
E_{FRP} [GPa]	61
ε_{rup}	0.015

* Specimen 1 ** Specimens 2 and 3 *** Specimen 4

5.1.2 Computational Modeling of Test Specimens

Computational simulation of experimental program A is conducted on the cross-section moment-curvature level within the 400 mm test region. The cross-section confinement model and the confined concrete material model developed in Chapter 3 are used to model the column concrete cross section. The concrete cross section is fiber-discretized using 24 uniform-thickness layers along the radial direction within the core region and 6 layers within the cover region. Each such layer is segmented into 18 circumferential sectors, each encircling a $20°$ central angle (see Fig. 5.1b). Since there is neither lap-splices nor reported bar buckling (except for specimen 1), longitudinal steel bars are modeled using the material model in Menegotto and Pinto (1973). The confining effect of transverse spirals in the test zone is secondary, since they are made insufficient by design, and hence are modeled assuming a simple bilinear material model until yielding and then fracture. FRP composites are modeled using an elastic-brittle material model. The equivalent FRP jacket stiffness is computed taking into account the overlap of FRP application in the circumferential direction along the column length. This results in an equivalent FRP thickness uniformly increased by 24%. Four structural models are then constructed of zero-

length finite elements incorporating the constructed cross sections and subjected to the axial load and curvature histories recorded in the test zone.

The confined concrete material model requires information about the damage localization length, fracture energies, and tensile strength, of which little data are directly available from the experiments. The localization length l_c is assumed equal to the product of the plastic hinge length and the weight of the integration point under consideration (1.0 for the zero-length element used in this study), as suggested in Coleman and Spacone (2001), in addition to a factor $\gamma_l \leq 1$. The factor γ_l represents the extent of the damaged compression zone within the cross section, since the localization length l_c of the confined concrete material model is pertinent only to the compressive fracture energy G_{fc}. The plastic hinge length is assumed to spread over the 400 mm test region due to the near-constant bending moment demand (with the exception of the geometric nonlinearity effect) and the experimentally observed spread of damage over the entire test region. The factor γ_l is negatively correlated to the axial load eccentricity level and is calibrated in this study using the post-peak response of the column specimens. In program A, $\gamma_l = 1.00$ for all specimens except specimen 2 which is subjected to relatively high axial load eccentricity and hence $\gamma_l = 0.50$ is chosen for it. Concrete compressive and tensile fracture energies $G_{fc} = 8.8\sqrt{f'_c}$ [N, mm units] and $G_{ft} = G_{fc}/250$ were adopted from Mizuno et al. (1999) based on uniaxial compression tests. Concrete tensile strength is assumed to be $f'_t = 0.35\sqrt{f'_c}$ [N, mm units].

5.1.3 Comparison of Observed and Simulated Behavior

Specimen 1 is experimentally observed to fail at low curvature ductility due to cover spalling followed by buckling of longitudinal reinforcing bars. Specimens 2 and 3 sustain very high curvature ductilities, and exhibit a spread of several observable flexural cracks spaced at approximately 100 mm before the FRP jackets rupture. All FRP-strengthened columns are experimentally observed to fail as a result of FRP jacket rupture in a sudden and explosive

manner accompanied by a loud popping sound. Photographs of tested specimens are shown in Figure 5.4.

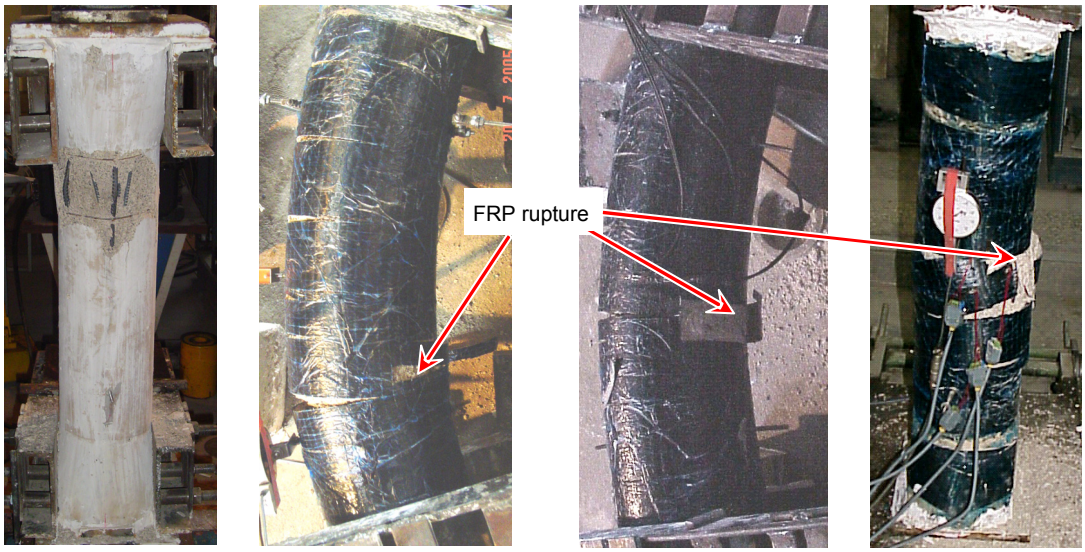

Fig. 5.4 Photographs of tested specimens from program A.

The measured and simulated moment-curvature results for specimens 1, 2, and 3 are compared in Figure 5.5a. Specimen 1 is experimentally observed to sustain a maximum bending moment of approximately 14.5 kNm at a curvature of 95 rad/km, exhibit brief hardening, and then soften rapidly to 9 kNm at a curvature of 225 rad/km. The computationally simulated response exhibits a close agreement to the experimental behavior at early stages of loading. Near the maximum bending moment, the simulated behavior exhibits slightly higher stiffness, reaching a maximum moment capacity of 14.6 kNm at a curvature of 70 rad/km, and softens afterwards. The simulated softening is only slightly less brittle than that observed, and the moment capacity reduces to 9.25 kNm at a curvature of 225 rad/km where the simulation is manually terminated after reaching the maximum experimentally recorded value.

Specimens 2 and 3 (Fig. 5.5a) sustain maximum bending moments of 15.3 and 17.3 kNm, at corresponding curvatures of 1180 and 1040 rad/km, respectively. The increase in curvature ductility over specimen 1 due to retrofitting by FRP is evident. Specimen 2 exhibits lower stiffness than specimen 3 due to the larger imposed eccentricity. Simulations predict the

maximum moment capacity of specimens 2 and 3 to be 15.8 and 17.7 kNm, respectively, which are approximately equal to the experimentally observed values. However, the corresponding curvatures are predicted to be only 1000 and 960 rad/km, respectively. This may be attributed to the uncertainty in the estimated material properties and imperfect geometrical parameters that are difficult to control, e.g., FRP jacket thickness and concrete cover, especially when such a reduced specimen scale is involved. The increase in simulated stiffness may be attributed to the fact that the experimentally recorded bending moments are computed simply by multiplying axial loads by load eccentricity and are not amplified for geometric nonlinearity (P-Δ effect), which can be judged from Figure 5.4 to have been present. This discrepancy is more observable in specimen 2, since the imposed eccentricity is higher and hence the additional bending moment due to P-Δ effect is larger. It should be noted that the simplifying assumption of completely brittle failure of FRP and the subsequent complete loss of confinement effect in the cross section prevents the model from computationally reproducing the descending branch of the moment-curvature response after FRP rupture. However, in seismic applications, this descending branch will rapidly lead to collapse of the retrofitted column due to dynamic P-Δ effects (Gupta and Krawinkler 2000) and its exact shape is of little interest to the present study. Instead of the descending branch, a sudden drop in moment capacity occurs, after which the moment capacity is controlled by the residual strength of core concrete (with confinement removed) and strain-hardening of longitudinal steel bars (bar buckling and fracture prior to FRP rupture were not experimentally observed or computationally simulated).

The axial load-average strain response of specimen 4, subjected to concentric axial loading, is presented in Figure 5.5b. The longitudinal strains are computed using measurements from LVDTs and electrical strain gages, while the circumferential strains are measured using electrical strain gages located around the cross section. Despite the axi-symmetric nature of the loading setup, the plots reveal differences that sometimes exceed 20% among the local strain gage measurements in the longitudinal direction, and larger differences between them and the averaged measurements of the LVDTs. It is thus believed that the applied axial load was not perfectly concentric and that slight eccentricities resulted from inadvertent moment restraint and friction at the specimen heads. For all longitudinal strain measurements, the experimental response is approximately linear up to an axial load value of approximately 440 kN and then

exhibits linear hardening up to failure, which occurs suddenly due to FRP jacket rupture at an axial load value of 770 kN. The LVDTs-measured longitudinal strain is -0.0175 at failure. The electrical strain gages reached their maximum strain of -0.01 and failed at an axial load of 725 kN. At FRP jacket rupture, the circumferential strains in the FRP jacket are not uniform; the minimum and maximum are approximately 0.0052 and 0.0085, respectively. These values are lower than the 0.015 rupture strain of the FRP test coupons. Several researchers have previously reported that FRP-confined concrete cylinders tested experimentally under concentric loads were observed to fail at measured dilation strains lower than those corresponding to FRP rupture (Ilki and Kumbasar 2003; Mirmiran and Shahawy 1997a,b). This phenomenon is attributed to the internal friction between FRP jackets and dilating concrete, the multi-axial stress state in FRP jackets due to axial shortening of concrete, the stress concentration in FRP jackets induced by local crushing of concrete, and the difference in geometry between circular jackets and flat test coupons. The studies reported in Mirmiran and Shahawy (1997a,b) and Saenz and Pantelides (2007) observe that the reduction in concrete dilation capacity from FRP rupture strain is an increasing function of the confining FRP jacket stiffness (e.g., number of layers).

The computationally simulated response of specimen 4 is presented in Figure 5.5b for two cases. The fist simulation represents a perfectly concentric axial load. The second simulation represents an imperfectly concentric axial load, whereby an assumed “accidental” eccentricity of 15 mm (i.e., 7.5% of the column diameter) is imposed. In the first simulation, the bilinear axial load-longitudinal strain behavior observed in the experiment is successfully reproduced except for a relatively high early stiffness as previously discussed, and is afterwards bounded by the measurements obtained from the LVDTs and electrical strain gages. The longitudinal strain is estimated to be -0.01 at an axial load level of 710 kN, exhibiting a close match to local strain measurements. The circumferential strain is estimated to be 0.005 at an axial load level of 790 kN, which is approximately equal to the minimum experimentally observed value. However, the FRP jacket rupture strain of 0.015 is not detected. This is attributed to the uncertainty in load eccentricity, amplified by the reduced scale of the test specimen. While not significantly affecting the early global stiffness or the measured average deformation quantities, a small eccentricity or moment restraint at the ends could significantly reduce the axial load capacity and result in early failure due to non-uniform distribution of strains in the brittle FRP jacket. The

potential extent of this effect is demonstrated by the results of the second simulation illustrated in Figure 5.5b. For an accidental eccentricity equal to 7.5% of the column diameter, the initial stiffness is barely reduced, and the axial load-longitudinal strain response remains bounded by the experimental observations. However, the maximum circumferential strain in the FRP jacket increases rapidly, and rupture is detected, i.e., circumferential strain of 0.015, at an axial load level of 795 kN. Note that according to the spatial distribution of confining stresses (see Section 3.3), the maximum circumferential strain in the FRP jacket for eccentric loading is significantly larger than values measured elsewhere and from the average value.

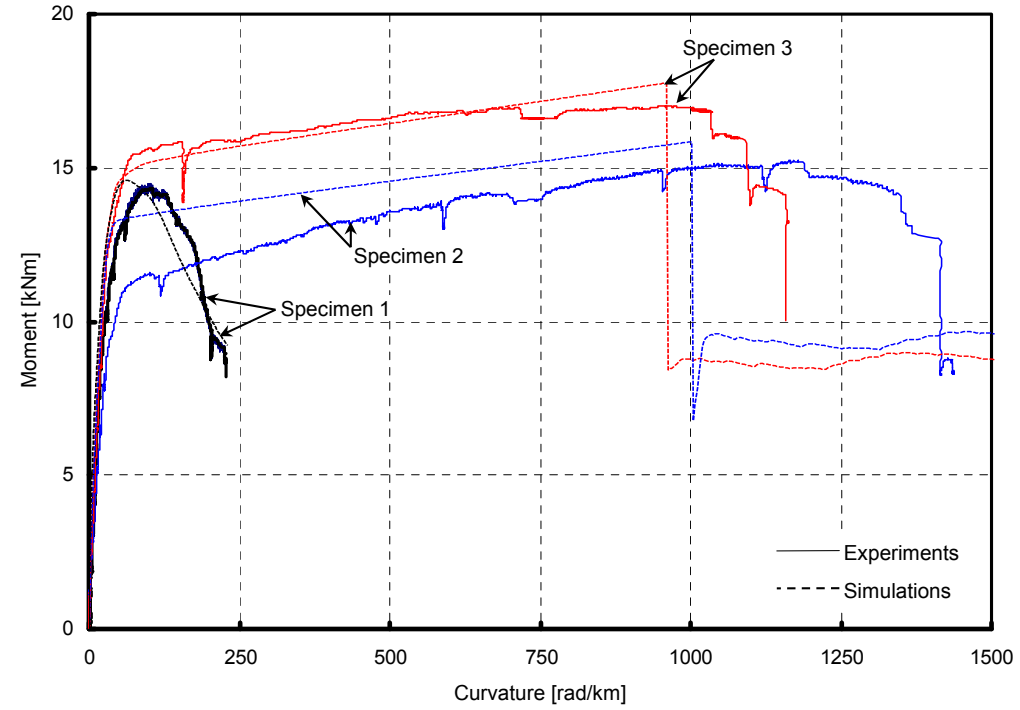

(a) Specimens 1, 2, and 3

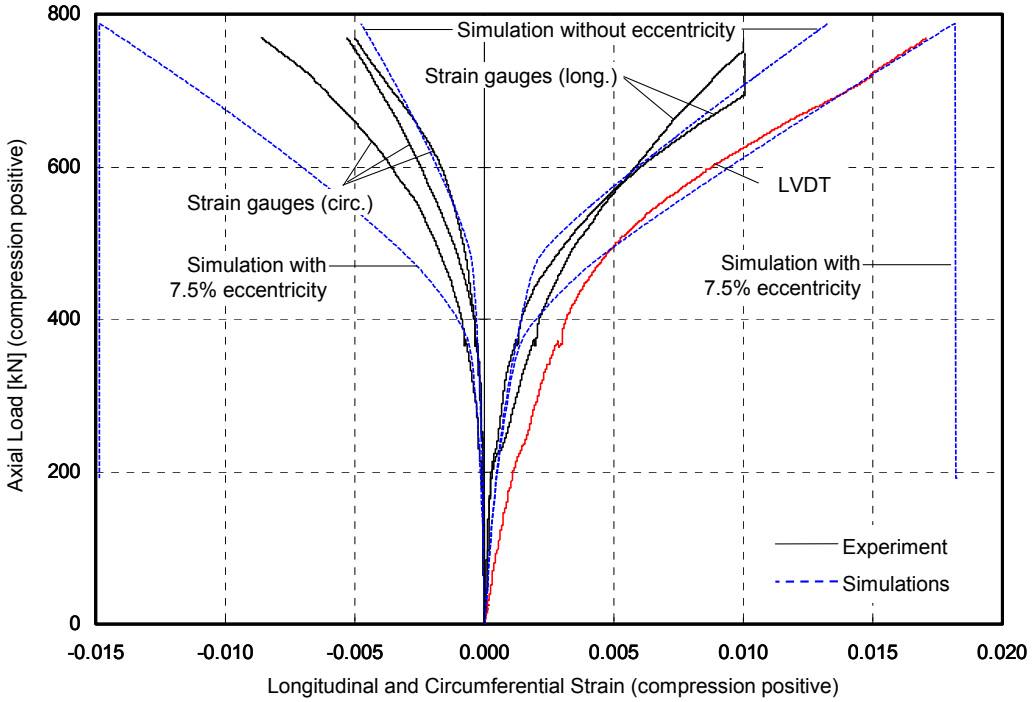

(b) Specimen 4

Fig. 5.5 Simulated and experimental program A column load-deformation results.

5.2 EXPERIMENTAL PROGRAM B

Experimental program B uses experimental data that have been reported in Sheikh and Yau (2002). Twelve RC columns of circular cross section are subjected to constant axial load and increasing cycles of symmetric lateral deformation in a single-curvature setup. The objective of the experiments is to assess and compare the improved capacity and ductility of RC columns retrofitted or repaired using different configurations of FRP composites during seismic events. Experimental program B consists of four column specimens reported in Sheikh and Yau (2002).

5.2.1 Description and Computational Modeling of Test Specimens

All column specimens investigated in Sheikh and Yau (2002) have identical dimensions and steel reinforcement as illustrated in Figure 5.6a. Each column is 356 mm in diameter and 1470 mm in length, in addition to a column stub of 510×760×810 mm dimensions. The column longitudinal reinforcement consists of 6 steel bars of 25 mm diameter distributed uniformly around the cross section. The transverse reinforcement consists of 9 mm spirals pitched at 300 mm in the column's designated plastic hinge region (within 800 mm of the face of the stub), and 200 mm otherwise. The stub region is well reinforced to eliminate the possibility of failure outside the plastic hinge region. Four column specimens are investigated, using two different levels of applied axial load (relative to the axial load capacity P_o) and two different types of FRP retrofit (carbon (CFRP) and glass (GFRP)). Material properties are listed in Table 5.2. The deformation profile of the concrete core on both sides of the column is measured using LVDTs and later post-processed to compute curvature values. The transverse displacements measured at six locations along the column length. In addition, strain gages are mounted on longitudinal and transverse steel reinforcement at the stub face and within the plastic hinge region. The test setup is illustrated in Figure 5.6b. Specimen designation is as follows:

1. ST2NT: 54% P_o axial load and two layers of 1.25 mm-thick (each) GFRP retrofit
2. ST3NT: 54% P_o axial load and one layer of 1.0 mm-thick CFRP retrofit
3. ST4NT: 27% P_o axial load and one layer of 0.5 mm-thick CFRP retrofit
4. ST5NT: 27% P_o axial load and one layer of 1.25 mm-thick GFRP retrofit

Similar to program A, computational simulation of program B is conducted on the cross-section moment-curvature level within the plastic hinge region. With reference to Section 5.1.2, 18 and 8 uniform-thickness layers are used to discretize the cross section within the core and cover regions, respectively (see Fig. 5.1b). Each such layer is segmented into 18 circumferential sectors, each encircling a $20°$ central angle. The effective jacket thickness is uniformly increased by 8% to account for the overlap length of FRP application in the circumferential direction along the column length. Based on statistical correlation and regression analysis of surveyed data from column experiments, the following expression for the plastic hinge length is suggested in Lu et al. (2005), modified from Priestley and Park (1987):

$$L_p = 0.077\,L_c + 8.16\,d_b \tag{5.1}$$

where L_c is the length between the column's contra-flexure points and d_b is the longitudinal steel bar diameter. The localization length γ_l factor is chosen as 1.0, 1.0, 0.25, and 0.25 for specimens ST2NT, ST3NT, ST4NT, and ST5NT, respectively. As in program A, the smaller value of γ_l for the latter specimens is attributed to the fact that these two specimens are subjected to relatively high axial load eccentricity compared to the other two specimens.

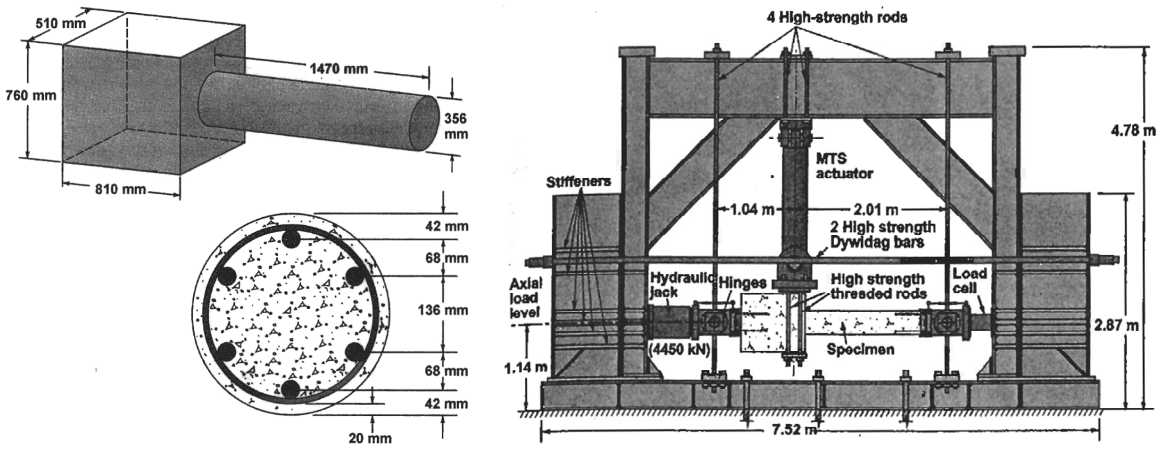

(a) Geometry and reinforcement (b) Test setup

Figure 5.6 Specimen details and setup for program B.

Table 5.2 Material properties for program B.

Material property	Value
f_c' [MPa]	40.4*, 44.8**, 40.8***
Concrete cover [mm]	20
Longitudinal steel σ_y [MPa]	500
Transverse steel σ_y [MPa]	520
Longitudinal steel ratio [%]	3.00
Transverse steel ratio [%]	0.30
E_{FRP} † [GPa]	68±, 21.2±±
ε_{rup} †	0.014±, 0.020±±

* ST2NT and ST3NT ** ST4NT *** ST5NT ± CFRP ±± GFRP

† Computed from stress-strain plots reported in Sheikh and Yau (2002)

5.2.2 Comparison of Observed and Simulated Behavior

The failure of all specimens is preceded by delamination of FRP wraps during the cycle in which concrete was crushed beyond its peak strength and started softening. This experimentally observed delamination spread over a length of 200 to 400 mm prior to FRP rupture. The delamination may have altered the confining stress spatial distribution within the cross section due to incomplete strain compatibility between concrete and FRP in the softening region. However, an investigative analysis conducted under the extreme assumption of uniform confining stress distribution for all simulated specimens resulted in only a 10–15% change in the computed bending moment capacities and less than 3% change in the predicted curvature ductility values. Specimen ST3NT has sustained some crushing damage in the concrete outside of the FRP-wrapped region. Hence, the FRP wraps for the later specimens in the experimental program are extended along the entirety of the column length (Sheikh and Yau 2002).

The experimentally observed and computationally simulated moment-curvature responses of specimen ST2NT are illustrated in Figure 2.8a. An excellent agreement in moment capacity and stiffness is observed as well as in moment values in the positive curvature direction.

However, the moment values in the negative curvature direction are relatively overestimated. This may be attributed to the decreased efficiency of the FRP wrapping in the reverse deformation cycle due to the spread of FRP delamination caused in the forward deformation cycle. Hence, the difference between computationally simulated and experimentally observed moment response during the negative curvature cycles increases at larger curvatures. Most importantly, the curvature level at FRP rupture is predicted with excellent accuracy. Detection of FRP jacket rupture during the simulation results in sudden loss of strength, whereas the experimentally observed loss of strength due to the initiation of FRP jacket rupture is less brittle than the computational simulation. This is due to the elastic-brittle FRP material model and the subsequent complete loss of confining stresses in the entire cross section upon reaching the rupture strain at any point along the FRP jacket. It is known that physical damage in the test specimens must spread over some length of FRP wrapping before causing complete loss of confinement. The simulated response after detecting FRP jacket rupture is less brittle for specimens ST4NT and ST5NT (Fig. 5.8) than that for specimens ST2NT and ST3NT (Fig. 2.8) due to the thickness of FRP and applied axial load being relatively lower, and therefore the amount of confinement lost and the size of the affected compression zone are relatively smaller.

The experimentally observed and computationally simulated moment-curvature responses of specimen ST3NT are illustrated in Figure 2.8b. Similar to specimen ST2NT, an excellent match is observed in the bending moment capacity and values in the positive curvature direction. The sudden softening experimentally observed just prior to FRP rupture is attributed to crushing damage observed during the experiment to the unwrapped concrete outside the designated plastic hinge region (Sheikh and Yau 2002), which is not computationally modeled. The experimentally observed and computationally simulated moment-curvature responses of specimen ST4NT are illustrated in Figure 5.8a. In spite of lower predicted hysteretic energy dissipation than experimentally observed, FRP rupture is predicted during the -150 rad/km deformation cycle shortly after its initiation has been experimentally observed. This may be due to the ability to experimentally observe the initiation of rupture in a few FRP strands in the non-homogeneous material prior to its spread to cause explosive failure (especially under relatively low axial load of specimen ST4NT). The experimentally observed and computationally simulated moment-curvature responses of specimen ST5NT are illustrated in Figure 5.8b. An

excellent agreement is observed in moment capacity, positive moment values, and post-rupture behavior. FRP rupture is predicted near the end of a positive curvature cycle of 150 rad/km magnitude, while it is experimentally observed during the subsequent negative deformation cycle.

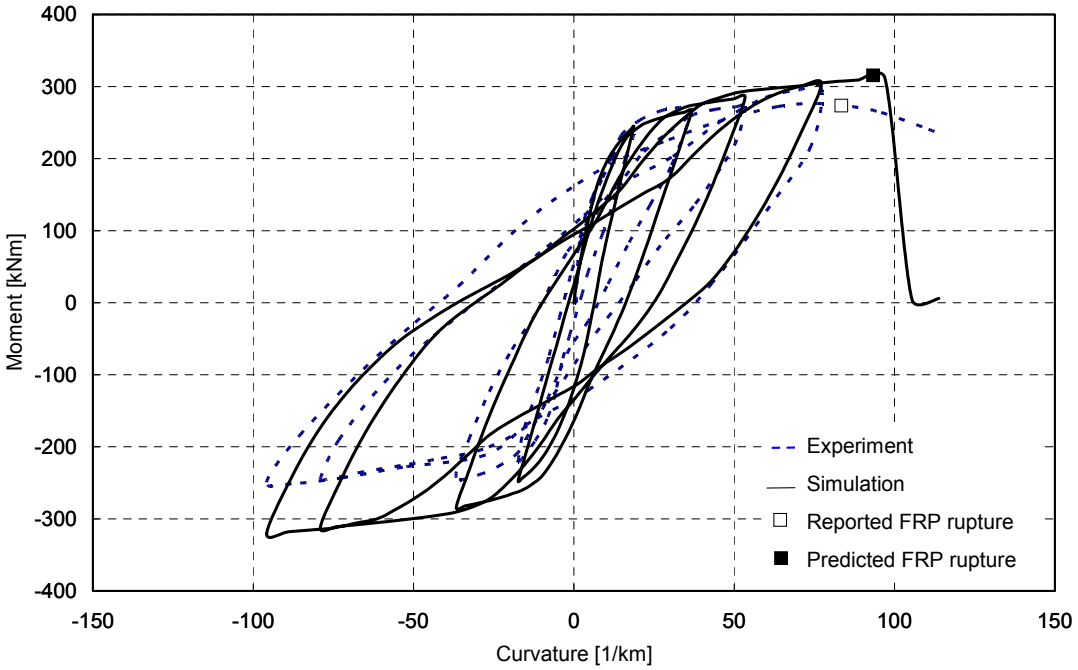

(a) Specimen ST2NT

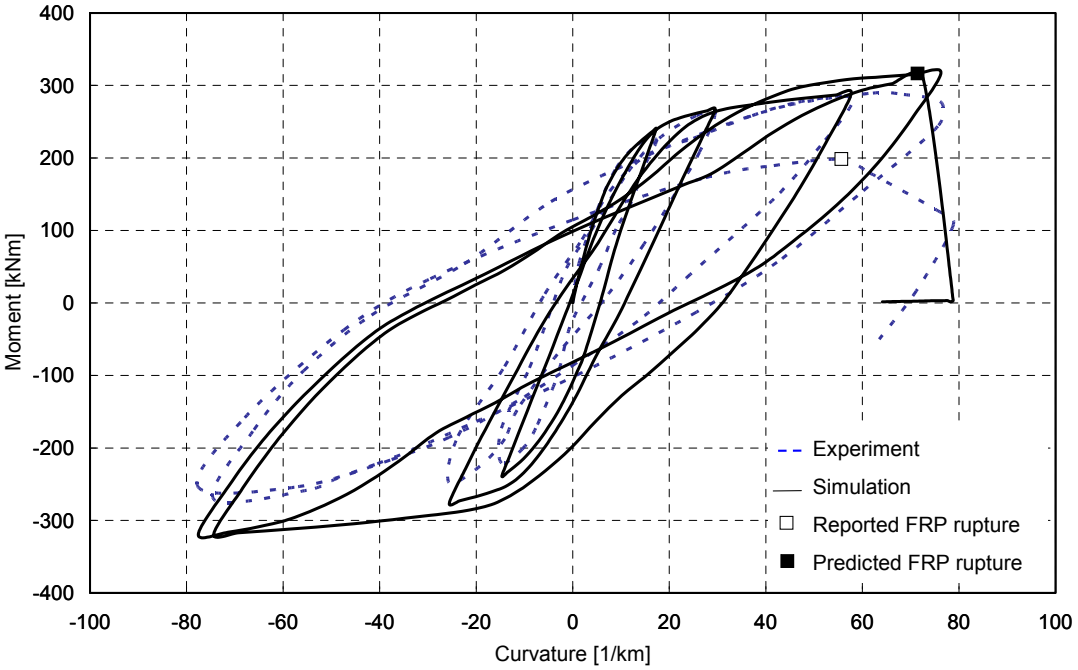

(b) Specimen ST3NT

Fig. 5.7 Simulated and experimental program B results: high axial load columns.

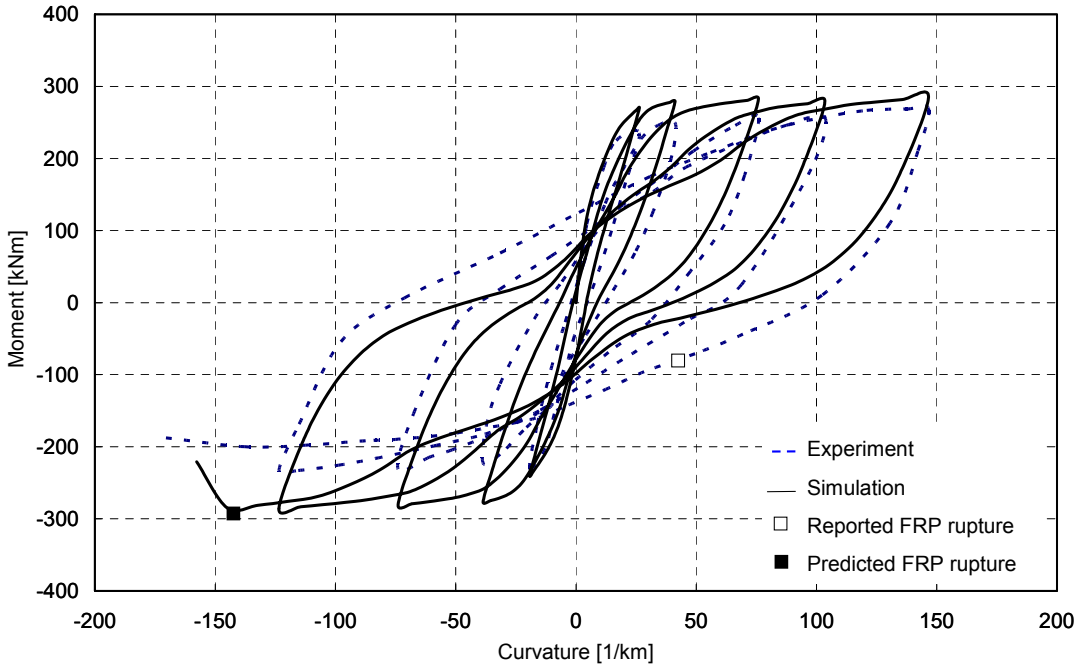

(a) Specimen ST4NT

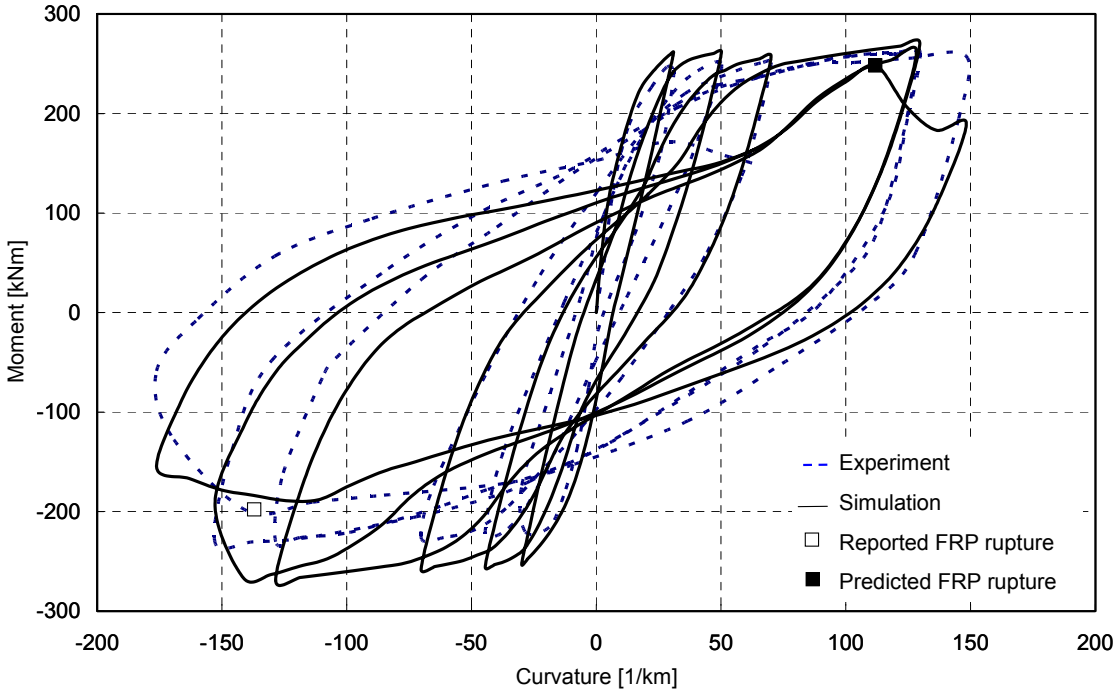

(b) Specimen ST5NT

Fig. 5.8 Simulated and experimental program B results: low axial load columns.

5.3 EXPERIMENTAL PROGRAM C

Experimental program C uses experimental data that have been reported in Xiao and Ma (1997). Three half-scale RC bridge columns of circular cross section are subjected to constant axial load and increasing cycles of symmetric lateral deformation in a single-curvature setup. The objective of the experiments is to establish the behavior of RC bridge columns designed with longitudinal reinforcing steel lap-splice deficiency and to assess and compare the improvement in lateral load-carrying capacity and displacement ductility after being retrofitted or repaired using layers of FRP composites (GFRP composites are used). Both retrofitted and repaired columns exhibit increased load-carrying capacity and displacement ductility. Program C consists of one as-built and two retrofitted column experiments (no repaired columns) from Xiao and Ma (1997).

5.3.1 Description and Computational Modeling of Test Specimens

All column specimens investigated in Xiao and Ma (1997) have identical dimensions and steel reinforcement as illustrated in Figure 5.9a. Each column is 610 mm in diameter and 2642 mm in length, in addition to a RC footing of 432 mm thickness. Column longitudinal reinforcement consists of 20 steel bars of 19 mm diameter distributed uniformly around the circular cross section. The bars are lap-spliced to 20 starter bars of the same diameter anchored in the RC footing and extending to a length of 381 mm upward. Transverse reinforcement consists of 6.4 mm hoops spaced at 127 mm along the entire column length. The RC footing is reinforced by a mesh of steel bars placed in the top and bottom layers, as well as X-shaped bars beneath the column joint to eliminate the possibility of failure outside the column (see Fig. 5.9a). Material properties are listed in Table 5.3 as reported in Xiao and Ma (1997). A fixed axial load of 712 kN (5% P_o) is applied using two high-strength steel rods post-tensioned against a hydraulic jack on top of the column (see Fig. 5.9b). Symmetric lateral displacements cycles of increasing amplitude are then applied using a displacement-controlled actuator, with three repetitions at each displacement level. The applied lateral load is measured using a cylindrical load cell, as well as the lateral displacement applied at the column tip. In addition, electrical strain gages are mounted on the FRP composite jacket to measure the circumferential strain. Specimen designation is as follows:

1. C1A0: As-built
2. C2R4: Four layers of 3.2 mm-thick GFRP each over a 610 mm length
3. C3R5: Five layers of 3.2 mm-thick GFRP each over a 1220 mm length

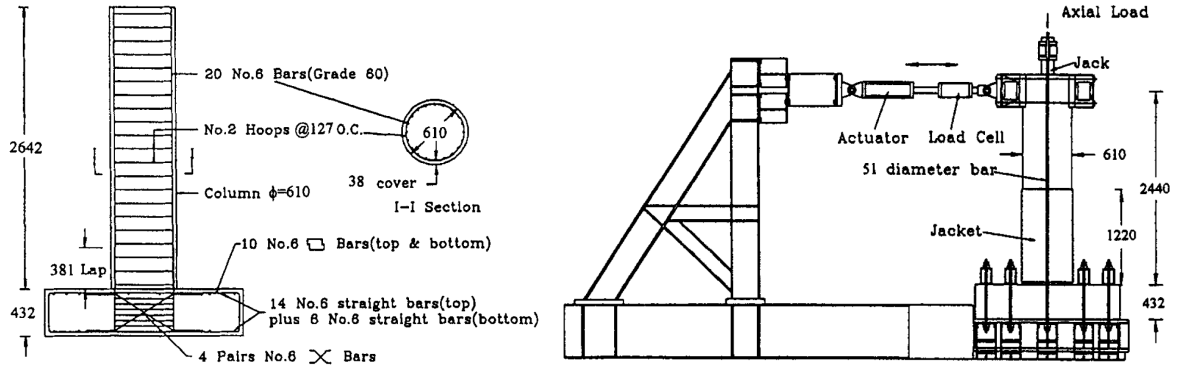

(a) Geometry and reinforcement (b) Test setup

Fig. 5.9 Specimen details and setup for program C.

Unlike programs A and B, a computational simulation of program C is conducted on the column's lateral load-displacement level. Each structural model consists of a force-based lumped-plasticity beam-column element (see Fig. 5.1a), which is documented in detail under the "BeamWithHinges" section in Mazzoni et al. (2004). Given the experimental axial load-application setup, the element stiffness matrix is configured to exclude P-Δ effects because the direction of the applied load (through post-tensioned rods) nearly follows the orientation of the column axis. However, a preliminary investigation suggested that this step has a minor effect on the simulation results due to the relatively low level of axial load. The end plastic hinges are defined using the confined cross-section model developed in Chapter 3 to account for flexure-axial interaction. With reference to Section 5.1.2, 24 and 8 uniform-thickness layers are used to discretize the cross section within the core and cover regions, respectively (see Fig. 5.1b). Each such layer is segmented into 18 circumferential sectors, each encircling a 20° central angle. The fibers representing the core and cover concrete are modeled using the uniaxial concrete material model developed in Chapter 3. In the as-built column C1A0, the core concrete fibers are confined with the spiral reinforcement, whereas the cover concrete fibers are not. In the retrofitted column specimens C2R4 and C3R5, all concrete fibers are confined with the much

stiffer—and stronger—FRP jacket and the confining effect of the spiral is ignored for simplicity. The fibers representing the steel bars are modeled using the lap-splice uniaxial material model developed in Chapter 2, with the material model in Menegotto and Pinto (1973) representing the mechanical stress-strain constitutive relationship of the bars. For reasons of numerical stability, FRP composites are modeled using a bilinear uniaxial material model with a steep softening branch (10 times the elastic stiffness) to avoid discontinuity in their stress-strain response if they were modeled as elastic-brittle. The plastic hinge length is estimated using Equation (2.1). The beam-column element exhibits elastic behavior between the two end hinges. The flexibility of the elastic segment of the column between plastic hinges is computed using a calibrated value of half of the concrete elastic modulus to account for the effect of flexural cracking. Moreover, due to the cantilever loading setup, the behavior of the plastic hinge at the loaded end remains approximately within the linear range. The localization length factor γ_l is chosen as 1.0 for all columns. The constructed structural models are subjected to the imposed axial load and then to simulated pushover by monotonically increasing the imposed lateral deformation at the column tip.

Table 5.3 Material properties for program C.

Material property	Value
f_c' [MPa]	44.8
σ_y [MPa]	462
Concrete cover [mm]	38
Longitudinal steel ratio [%]	2.00
Transverse steel ratio [%]	0.20
E_{FRP} [GPa]	48.3
ε_{rup}	0.0114

5.3.2 Comparison of Observed and Simulated Behavior

Specimen C1A0 (as-built) is reported in Xiao and Ma (1997) to have developed its first longitudinal crack, indicative of the initiation of lap-splice failure, at a lateral displacement of 13 mm. The maximum lateral load recorded at this lateral displacement is approximately 230 kN without exhibiting significant signs of steel bar yielding. The response is asymmetric, with lateral load capacity in the negative direction exhibiting larger values. Vertical cracks have spread within the lap-splice region after one displacement cycle at 41 mm. At 61 mm displacement, the lateral load capacity reaches 115 kN (50% of its maximum value) and the experiment is terminated. The failure of this specimen is experimentally observed to have been brittle with no significant ductility. Specimens C2R4 and C3R5 (FRP-retrofitted) are reported not to have exhibited any delamination or rupture in the FRP composites. However, fine horizontal cracks are observed during later displacement cycles. These specimens develop a maximum lateral load of approximately 290 and 330 kN, respectively. Both specimens exhibit signs of steel bar yielding at a lateral load value of approximately 230 kN, and thenceforth maintain a ductile behavior until the lap-splices are observed to fail at FRP circumferential strains of 0.0010 to 0.0015. The reduction in lateral load capacity following lap-splice failure is gradual and can be characterized as ductile in comparison to the brittle failure mode of the as-built Specimen C1A0. Both retrofitted specimens exhibit an asymmetric lateral load-displacement behavior, in which lateral load capacity in the negative direction exhibits larger values. The experiments are terminated at a lateral displacement level of 130 mm, at which the lateral load capacity is reduced to approximately 190 and 225 kN (66% and 68% of lateral load capacity), for specimens C2R4 and C3R5, respectively (Xiao and Ma 1997).

The experimentally observed and computationally simulated lateral load-displacement responses of specimen C1A0 under cyclic and monotonic loading, respectively, are illustrated in Figure 5.10. An excellent agreement in lateral load capacity and stiffness is observed. The estimated lateral load capacity is bounded between the experimentally observed values in the positive and negative directions, and the corresponding lateral displacement at the initiation of lap-splice failure is slightly underestimated but still in close agreement with the experimentally observed values. The computational simulation successfully reproduces the brittle behavior following lap-splice failure, indicated by a sudden drop followed by rapid reduction in lateral

load capacity. The slope of the softening branch and the lateral load capacity at the maximum displacement are both estimated in close agreement with the envelope of the experimentally observed response.

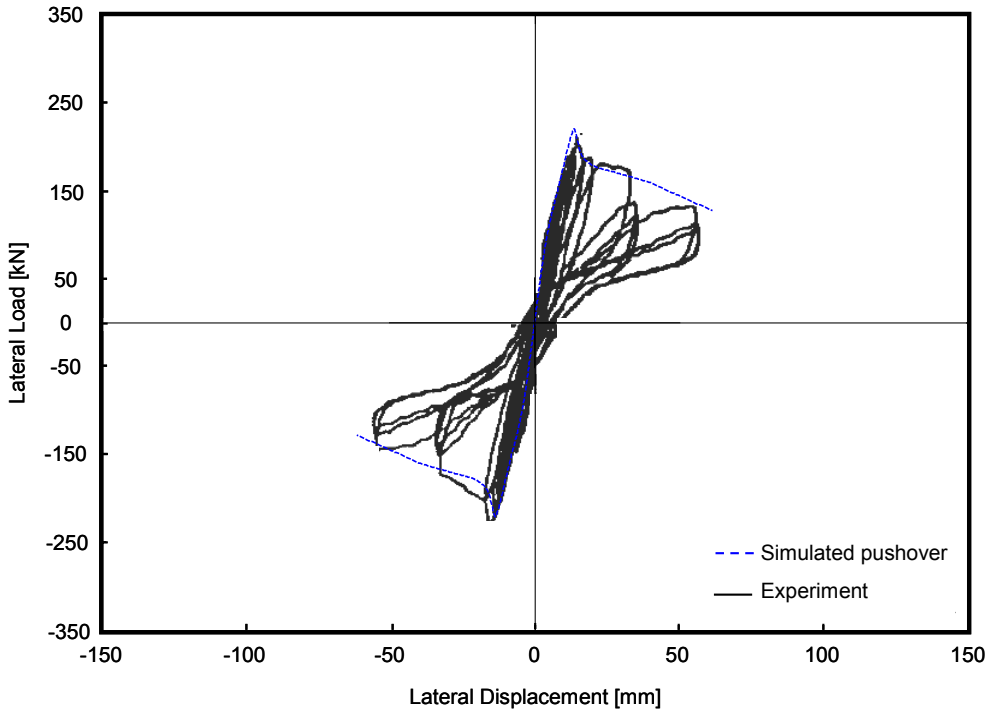

Fig. 5.10 Simulated and experimental program C results: as-built column.

The experimentally observed and computationally simulated lateral load-displacement responses of specimen C2R4 under cyclic and monotonic loading, respectively, are illustrated in Figure 5.11a. Similar plots for specimen C3R5 are illustrated in Figure 5.11b. A close agreement in lateral load capacity and lateral stiffness is observed, especially in the negative displacement direction. It is believed that the softer response in the positive direction is due to hysteretic degradation due to previous loading in the negative direction, which is not represented in the pushover analysis. The lateral load corresponding to yielding in longitudinal reinforcement is accurately predicted, whereas the corresponding displacement is slightly underestimated for both specimens. The hardening response until lap-splice failure and the subsequent reduction in lateral load capacity are successfully reproduced. The displacement level corresponding to initiation of lap-splice failure is slightly underestimated for specimen C2R4. The underestimation of

displacements at longitudinal bar yielding and lap-splice failure may be attributed to the uncertainty in estimating the plastic hinge length. It has been suggested in Priestley and Seible (1991) that FRP-wrapped column cross section may be able to spread the localization of structural damage along a greater length than as-built columns. A larger plastic hinge length prior to lap-splice failure (due to the stabilizing effect of FRP retrofit) when multiplied by the critical cross-section curvature value (e.g., corresponding to yielding of longitudinal reinforcement), will result in larger corresponding base rotation and hence in larger lateral displacement. In addition, the hysteretic damage accumulated in the column during earlier loading cycles may have resulted in larger flexibility in the cyclic experiments than the simulated pushover results. Nevertheless, simulations for both specimens C2R4 and C3R5 successfully predict the failure mechanism and the relatively gradual loss of lateral strength following lap-splice failure. In addition, lateral load capacity at the maximum displacement is reasonably predicted, considering that the experimental values are further reduced due to unaccounted-for hysteretic damage.

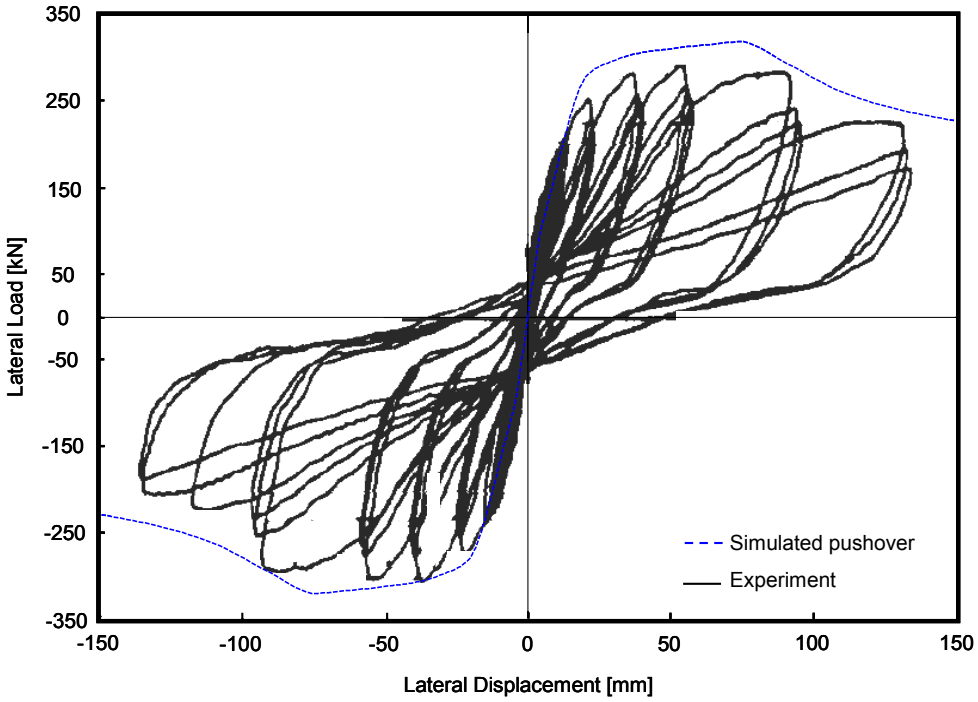

(a) Specimen C2R4

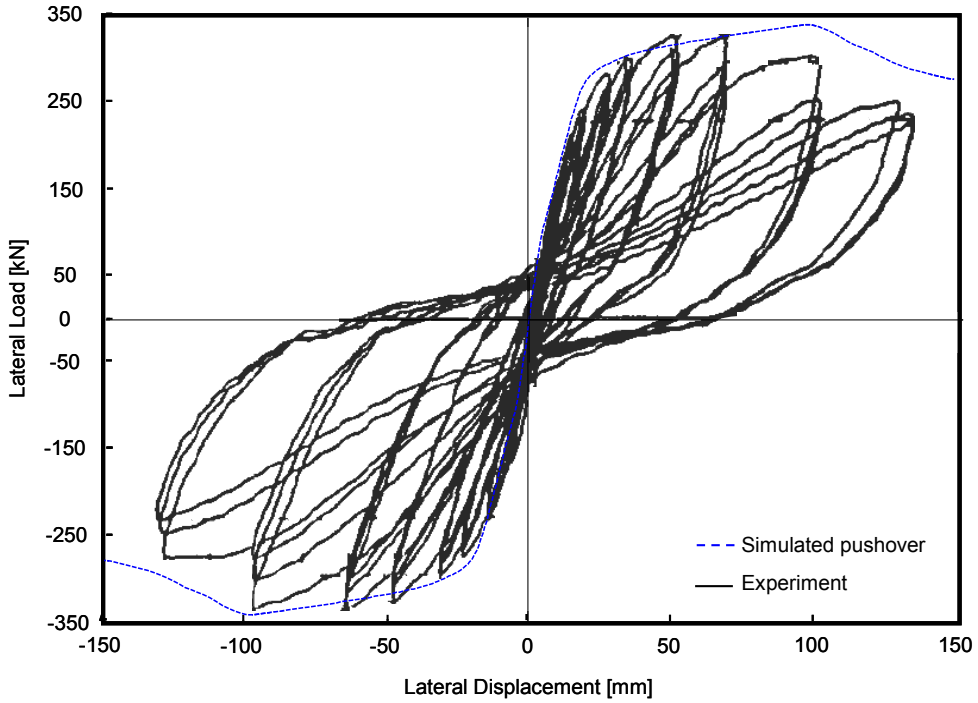

(b) Specimen C3R5

Fig. 5.11 Simulated and experimental program C results: retrofitted columns.

5.4 EXPERIMENTAL PROGRAM D

Experimental program D uses experimental data that have been reported in Henry (1998). Two one-third scale RC bridge columns of circular cross section are subjected to constant axial load and increasing cycles of symmetric lateral deformations in a single-curvature setup. The objective of the experiments is to establish the behavior and usable ductility limit of RC bridge columns susceptible to longitudinal steel bar buckling. Both columns are investigated in their as-built configuration without retrofit. The investigated parameters are the amount of transverse reinforcement and the level of applied axial load.

5.4.1 Description and Computational Modeling of Test Specimens

Both column specimens investigated in Henry (1998) have identical dimensions and longitudinal reinforcement as illustrated in Figure 5.12. Each column is 610 mm in diameter and 2440 mm in length, in addition to a RC anchor block of approximately 730 mm thickness. Column longitudinal reinforcement consists of 22 steel bars of 16 mm diameter distributed uniformly around the circular cross section and anchored by extending them inside the anchor block, while their ends are terminated with 90° bents. Transverse reinforcement consists of 6.4 mm spirals pitched at a spacing prescribed for each specimen along the entire column. Material properties are listed in Table 5.3. The experimental setup is similar to that shown in Figure 5.9b. A fixed axial load is applied on each specimen using two steel rods post-tensioned against a steel beam positioned at the top of the column. The axial load-application setup is such that the load follows the orientation of the column axis and hence excludes P-Δ effects. Symmetric cycles of increasing amplitude of lateral displacements are then applied using a displacement-controlled actuator, with three repetitions at each displacement level. The lateral displacement and the applied lateral load at the column tip are measured. The deformation profile of the concrete core on both sides of the column is also measured using LVDTs and later post-processed to compute curvature values. The axial strain at seven locations along three longitudinal bars (two located on opposite sides of the cross section, farthest from the neutral axis, and one located halfway between them, i.e., near to the neutral axis) is recorded using electrical strain gages. The

circumferential strain farthest from the neutral axis is measured for all spirals within 255 mm of the column base. Specimen designation is as follows:

1. 415P: Axial load = 1310 kN (20% $f_c'A_g$); transverse spiral pitch = 32 mm
2. 415S: Axial load = 655 kN (10% $f_c'A_g$); transverse spiral pitch = 64 mm

Similar to program C, computational simulation of program D is conducted on the column's lateral load-displacement level. Similar to Section 5.3.1, each structural model consists of a force-based lumped-plasticity beam-column element (Mazzoni et al. 2004). No P-Δ effect is included in the stiffness matrix. The end plastic hinges are defined using the confined cross-section model developed in Chapter 3, with 18 and 2 uniform-thickness layers being used to discretize the cross section within the core and cover regions, respectively (see Fig. 5.1b). Each such layer is segmented into 18 circumferential sectors, each encircling a $20°$ central angle. The fibers representing the core and cover concrete are modeled using the uniaxial concrete material model developed in Chapter 3. The core concrete fibers are confined with the spiral reinforcement while the cover concrete fibers are not. The fibers representing the steel bars are modeled using the buckling-enabled steel bar uniaxial material model developed in Chapter 2, with the material model in Menegotto and Pinto (1973) representing the bars' mechanical stress-strain constitutive relationship.

The plastic hinge length is adopted from the measured lengths over which longitudinal reinforcement is recorded to have yielded. These lengths are reported in Henry (1998) to be 765 and 612 mm for specimens 415P and 415S, respectively, which are approximately 2.0 and 1.6 times the values predicted by Equation (2.1). The flexibility of the elastic segment of the column between plastic hinges is computed using half of the concrete elastic modulus to account for the effect of flexural cracking. Similar to the FE models of program C columns, the behavior of the plastic hinge at the loaded end remains approximately within the linear range due to the cantilever loading setup. The localization length factor γ_l is chosen as 0.3 and 0.2 for specimens 415P and 415S, respectively (specimen 415P is subjected to twice the axial load and hence to a lower eccentricity level given the comparable values of the experimentally observed bending moment capacities for both specimens). The constructed structural models are subjected to the imposed axial load and then to simulated pushover by monotonically increasing the imposed

lateral deformation at the column tip. For comparison and assessment of model performance, a second set of pushover analyses is constructed using the same structural models while disabling the buckling feature of the longitudinal steel bars.

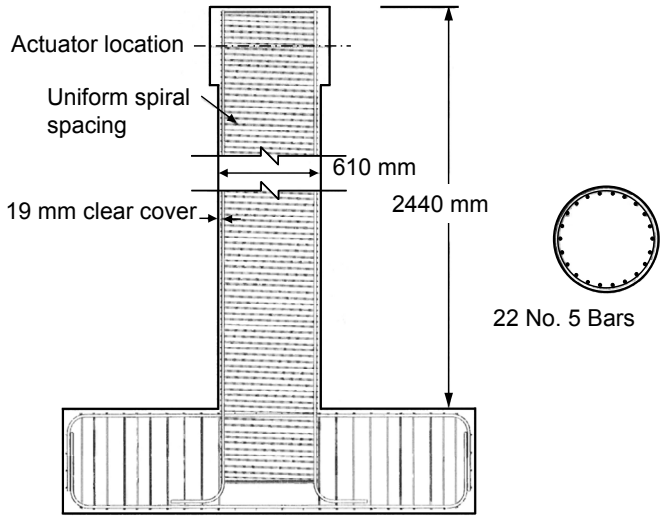

Fig. 5.12 Specimen details for program D.

Table 5.4 Material properties for program D.

Material property	Value
f_c' [MPa]	37.2
f_t' [MPa]	3.2
Concrete cover [mm]	19
Longitudinal steel σ_y [MPa]	462
Transverse steel σ_y [MPa]	607
Transverse steel σ_u [MPa]	897
E_s [GPa]	210
E_{sh} (assumed)	2% E_s
Longitudinal steel ratio [%]	1.5
Transverse steel ratio [%]	0.66*, 0.33**

* 415P ** 415S

5.4.2 Comparison of Observed and Simulated Behavior

The experimentally observed behavior and failure modes of both column specimens are similar. Specimen 415P exhibits yielding in longitudinal steel at a lateral load of approximately 235 kN and a displacement of 28 mm. Subsequent hardening leads to a maximum lateral load of approximately 335 kN at a displacement of 125 mm. During the second displacement cycle at 125 mm level, one longitudinal steel bar is observed to buckle, followed by fracture in two spirals on one side of the column. During the first displacement cycle at the maximum level of 175 mm, spirals are observed to fracture on both sides of the column. During the subsequent displacement cycles at the 175 mm level, severe damage and disintegration are observed in the core concrete due to loss of confinement, and several longitudinal bars are observed to fracture.

Specimen 415S follows a similar path, but exhibits lower lateral load capacity values due to the reduced levels of confinement and axial load. The lateral force corresponding to yielding in longitudinal steel is approximately 220 kN at a displacement of 23 mm. The maximum lateral load capacity is approximately 305 kN at a displacement of 125 mm. During the first displacement cycle at 125 mm level, several longitudinal steel bars are observed to buckle on both sides of the column. Bar buckling is observed to span multiple spirals, which shortly afterward start to fracture. During the maximum displacement level of 175 mm, the test is stopped due to the severe reduction of the column stiffness as a result of the disintegration of the concrete core in the area where the spirals have fractured. No longitudinal bars are reported to have fractured in specimen 415S (Henry 1998).

The experimentally observed and computationally simulated lateral load-displacement responses of specimen 415P under cyclic and monotonic loading, respectively, are illustrated in Figure 5.13a. The simulated pushover, with or without bar buckling, estimates yielding in the first longitudinal steel bar at a lateral load of 223 kN and a displacement of 18 mm. With bar buckling enabled, the maximum lateral load capacity is estimated to be 302 kN at a displacement of 98 mm. Subsequently, the lateral load capacity exhibits slight softening that can be idealized as almost perfectly plastic. The first bar buckling is estimated to occur at a displacement of 134 mm, and subsequently the lateral load capacity exhibits an observable reduction. At a lateral displacement of 168 mm, the onset of fracture is estimated in the spirals after reaching the

ultimate tensile stress capacity σ_u. A severe reduction in the lateral load capacity ensues due to loss of confinement to the concrete core. With bar buckling disabled, no fracture in the spirals or brittle reduction in lateral load is predicted. Note that the experimentally simulated response exhibits higher stiffness in the early phase of loading, i.e., prior to yielding in longitudinal reinforcement, than the experimentally observed response. This may be attributed to the effect of cyclic loading on the bar-slip at the foundation (which is not modeled) and the opening and closing of flexural and shrinkage cracks.

Similar results and comparisons for specimen 415S are illustrated in Figure 5.13b. The simulated pushover estimates yielding in the first longitudinal steel bar at a lateral load of 187 and a displacement of 15 mm. With bar buckling enabled, the maximum lateral load capacity is estimated to be 261 kN at a displacement of 83 mm. The lateral load capacity subsequently exhibits slight softening. The first bar buckling is estimated to occur at a displacement of 134 mm, subsequently the lateral load capacity exhibits a significant and rapid reduction. At a lateral displacement of 151 mm, the onset of fracture is estimated in the spirals and the lateral load capacity is further reduced. With bar buckling disabled, no fracture in the spirals or brittle reduction in lateral load is predicted.

It should be noted that the effect of bar buckling on increasing the strain demand and subsequent fracture of spirals is not explicitly accounted for in the confined concrete cross section and buckling-enabled steel bar models. However, such effect is observed indirectly due to the interaction between the resulting overload in concrete fibers (due to buckling and subsequent softening of adjacent bar), the increased lateral dilation of the cross section, and the lateral strain compatibility in the confining spirals, as estimated by means of the developed confined concrete constitutive and cross-section models in Chapter 3.

There is an observed difference between the predicted loss of lateral load following bar buckling and spiral fracture in each specimen. In specimen 415P, the column cross section is well confined. Hence, the extent of bar buckling when it occurs (the rate of subsequent softening in the bar) is limited due to the close spacing of the spirals laterally stiffening the bar (see Section 2.2). In addition, the closely spaced spirals result in well-confined core concrete fibers capable of carrying relatively high stresses (see Section 3.2). Moreover, due to the subsequent softening of the buckled bar being relatively limited, the resulting overstress in neighboring

fibers is limited and so is the number of additional bars that buckle as a result. Hence, the resulting reduction in lateral load after bar buckling is limited relative to the simulation with bar buckling disabled. However, upon the fracture of spirals, the resulting loss of confinement and axial strength of the core concrete and steel bars, in addition to the relatively high axial load, lead to the predicted sharp reduction in lateral load capacity. In contrast, the column cross section is lightly confined in specimen 415S. Hence, the extent and the number of bars buckling due to the subsequent overstress are more significant relative to specimen 415P. Hence, the subsequent reduction in lateral load after bar buckling is more significant. The widely spaced spirals offer little confinement to the core concrete fibers and steel bars. Upon the fracture of spirals, the resulting loss of axial strength in the concrete fibers is not severe. This, in addition to the relatively low axial load, leads to a predicted reduction in lateral load capacity significantly less brittle than that of specimen 415P.

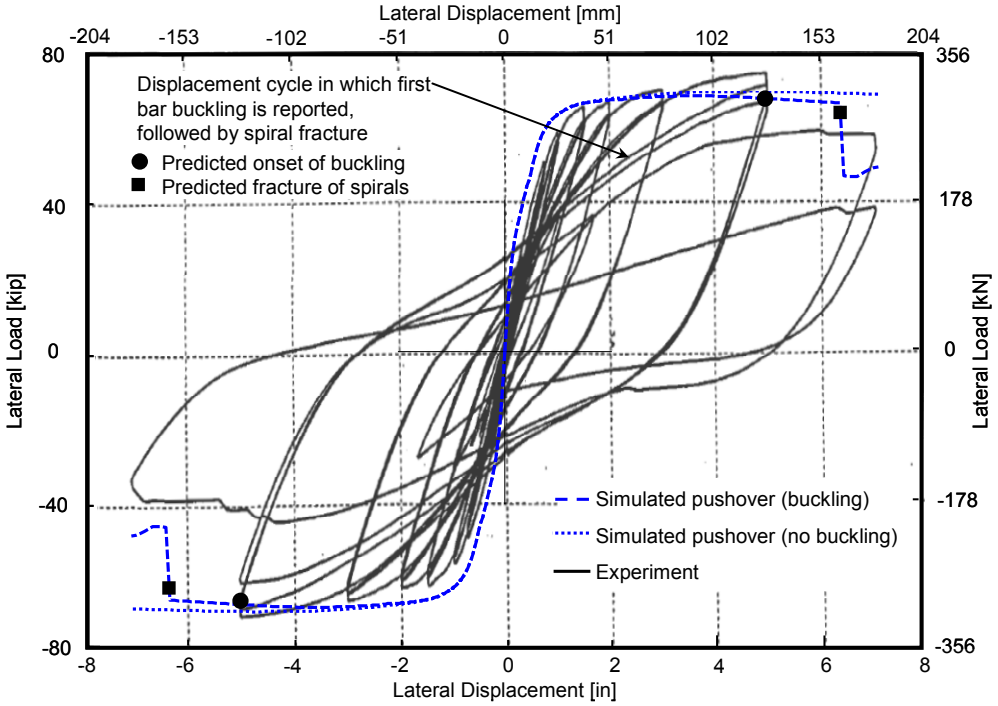

(a) Specimen 415P

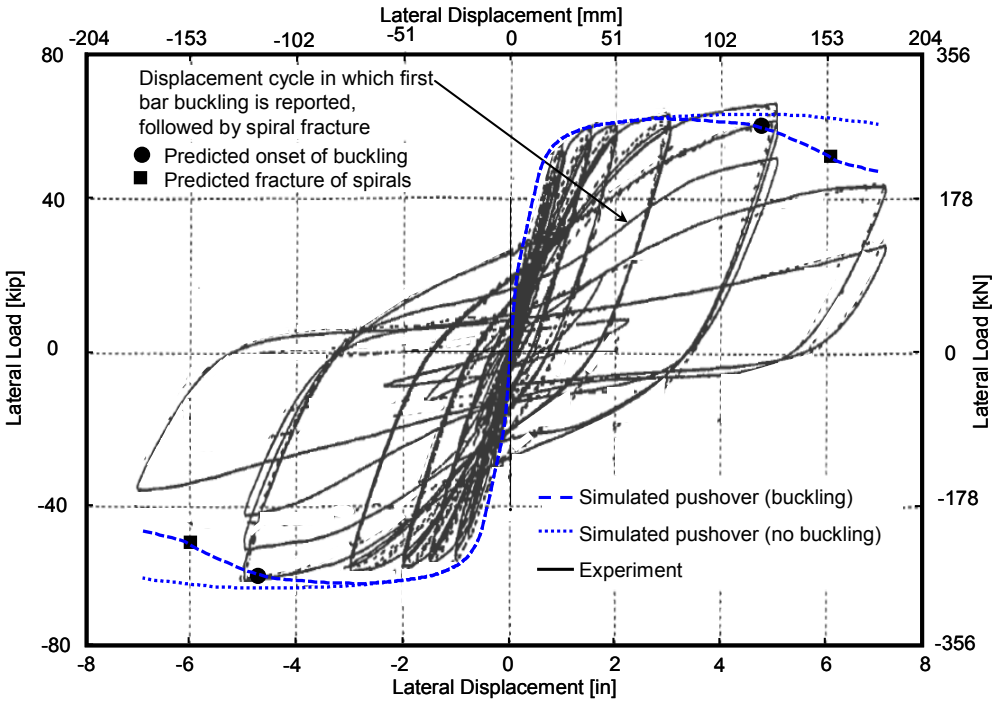

(b) Specimen 415S

Fig. 5.13 Simulated and experimental program D column load-deformation results.

5.4.3 Demonstration of Cross-Section Damage Indices

For the simulated pushover test specimens discussed in Section 5.4.2, the progression of damage is predicted using the cross-section damage indices developed in Section 3.3. Figure 5.14a illustrates the values of the damage index D_A, representing the deterioration in cross-section axial load capacity, for increasing lateral displacements in specimens 415P and 415S. For comparison, the values of D_A are plotted as obtained from the pushover simulations conducted with and without bar-buckling enabled. In both cases, the increase in D_A values in both specimens exhibits a logarithmic trend with lateral displacements (the relationship is approximately linear when plotted in log-log space). With bar buckling enabled, D_A values increase asymptotically until the fracture strain is reached in the transverse spirals, after which they increase to 1.0 according to the definition of D_A. Moreover, D_A values are consistently higher in specimen 415S than specimen 415P, which corresponds with the widely spaced spirals in specimen 415S. Consequently, higher axial strains are experienced in the concrete and longitudinal steel fibers, which result in faster accumulation of damage. The disabling of bar buckling does not result in significant discrepancies in the corresponding D_A values prior to fracture of the spirals. Since fracture in the spirals was not predicted in the simulations with bar buckling disabled, the corresponding D_A values continue to increase monotonically until they reach a maximum of 0.74 and 0.80 for specimens 415P and 415S, respectively.

Figure 5.14b illustrates the values of the damage index D_M in both specimens, representing the deterioration in the cross-section bending moment capacity with increasing lateral displacements. Similar to Figure 5.14a, plotted D_M values are obtained from the pushover simulations conducted with and without bar-buckling enabled. In both specimens, the increase in D_M values exhibits an approximately bilinear trend with lateral displacements. With bar buckling enabled, D_M values increases steadily (at an increasing rate) until the predicted fracture of the transverse spirals, after which they increase to 1.0. Similar to that observed in D_A, D_M values are consistently higher in specimen 415S than specimen 415P. This observation is attributed to the same reasons, in addition to the curvature values along the critical cross sections of specimen 415S being larger than those of specimen 415P for the same lateral displacement

values, due to the smaller observed plastic hinge length in specimen 415S. Accordingly, the division of plastic rotation (approximately equal values for both specimens at the same lateral displacement levels) by a smaller plastic hinge length results in larger curvature values for specimen 415S. The discrepancy in plastic hinge lengths may in turn be attributed to the higher confinement of specimen 415P, the resulting relatively lower dilation strains in the core concrete, and the relatively more limited extent of cover spalling and bar buckling. The disabling of bar buckling results in more significant discrepancies in the corresponding D_M values than previously observed in D_A values prior to the fracture of the spirals. Moreover, the discrepancy is larger in specimen 415S than in specimen 415P due to the larger extent of bar buckling prior to fracture of the spirals, as previously discussed in Section 5.4.2. In the absence of predicted fracture in the spirals due to the disabling of bar buckling, the evolution of the corresponding D_M values continues monotonically until they reach a maximum of 0.8 and 0.83 for specimens 415P and 415S, respectively.

It is observed that D_A values computed with buckling disabled are slightly larger than the corresponding values computed with buckling enabled for lateral displacement values higher than those corresponding to maximum lateral load capacities in both column specimens. However, an opposite behavior is observed for D_M values. Since the value of the latter assigns a relatively larger weight to damage sustained in the fibers farthest from the cross-section centroid according to its definition (see Section 3.3), it is clear that the occurrence of bar buckling results in higher strain demands on these extreme fibers and hence reduces more rapidly the bending moment-carrying capacity of the cross section. The opposite effect on the axial load-carrying capacity is not entirely clear, yet may be attributed to a relative relief of the inner core fibers due to the increased strain values at the extreme fibers and the resulting outward shift of the cross section's neutral axis. Consequently, the compressive strains and the corresponding lateral dilation in these inner core concrete fibers may decrease, and so may their corresponding material damage index value D_f (see Section 3.2.4).

The performance of the proposed damage indices is illustrated to satisfactorily represent the progression of damage in the investigated RC column cross sections. Their prediction of the collapse limit state is consistent with the lateral displacement levels reported in Henry (1998) to

cause instability leading to terminating the experiments. If bar buckling is prevented, the damage indices predict that very limited reserve capacity is left in the investigated columns. Based on comparing the observed trends of D_A and D_M with bar buckling prevented, the loss of the bending moment-carrying capacity will always take place before the loss of the gravity load-carrying capacity for these column specimens.

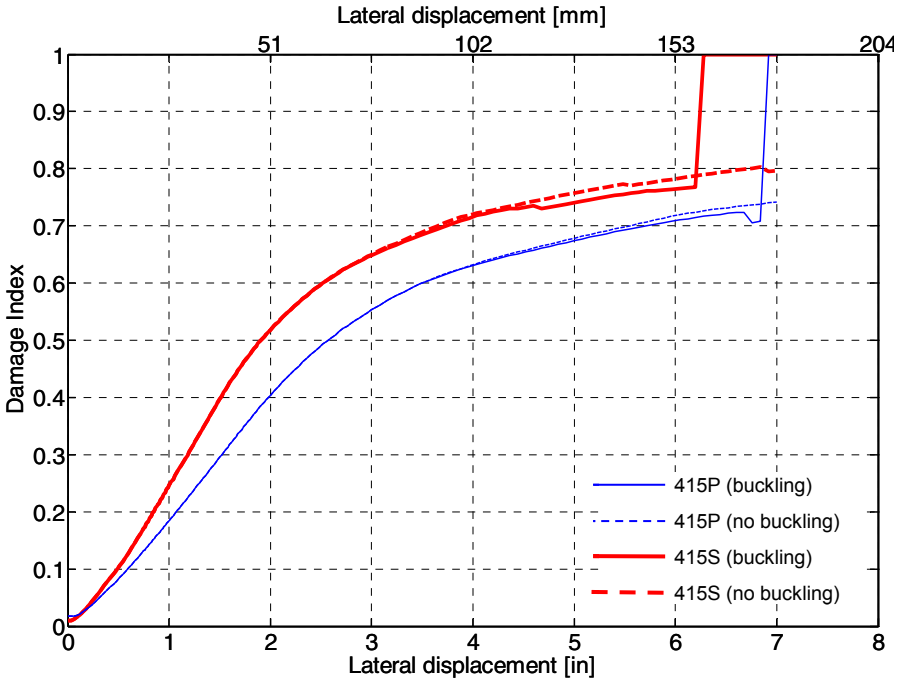

(a) Axial damage index D_A

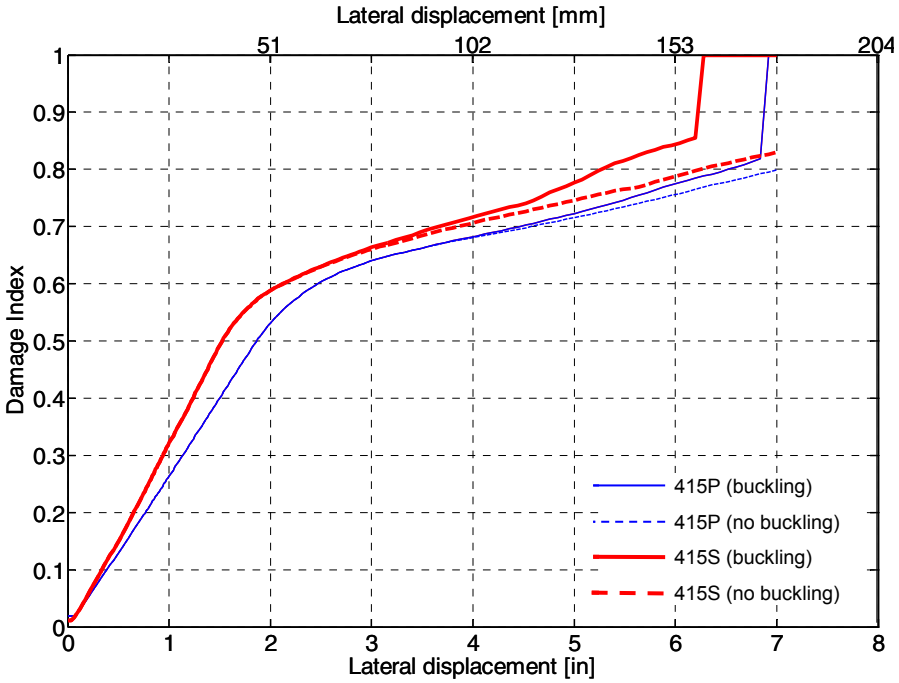

(b) Flexural damage index D_M

Fig. 5.14 Computed cross-section damage indices during column push-over simulations for test specimens of program D.

5.5 SUMMARY AND COMPARISONS

In this chapter, RC column specimens from four experimental programs were modeled using the material and cross-section component models developed and implemented in Chapters 2–4. These columns represented a number of seismic deficiencies common to the non-ductile detailing of older RC construction for columns whose collapse is controlled by flexure-axial interaction. The range of deficient column behavior examined in the experimental programs included the failure of confining transverse reinforcement and external jackets, the loss of confinement to the concrete core, the failure of lap-splices, and the buckling of longitudinal bars, in addition to the fracture of internal transverse reinforcement and rupture of external FRP composites commonly used as a retrofit measure for existing non-ductile details. The examined RC columns contained seismically deficient as-built as well as FRP-retrofitted specimens, examined under applied axial load and applied monotonic or cyclic lateral displacement history. Computational simulations of the column experiments were performed on the level of the cross-section moment-curvature response and the column lateral load-displacement response. Several structural models were developed using the OpenSees structural modeling platform in accordance with the documented geometry, the material properties, and the boundary conditions of the specimens in each experimental program. The OpenSees simulations utilized the component models developed in Chapters 2 and 3 to represent the flexure-axial behavior of RC column cross sections.

The results from the simulations exhibited the ability to predict with good to excellent accuracy the behavior of seismically deficient as-built columns, including their lateral load capacities, the deformation levels at the initiation of failure in non-ductile details, and the resulting global modes of collapse reflected by the brittleness of the post-failure response. In addition, these simulations were able to account for the effects of retrofitting using FRP composites and estimate the resulting improvements in the lateral load capacity and the ductility. Most important, the simulations successfully identified fracture in the transverse steel reinforcement and rupture in the CFRP and GFRP composites used as retrofitting jackets, which typically define the ends of their usable range of application. Finally, the relationship between the lateral displacement and the cross-section damage indices developed in Section 3.3 was evaluated for two investigated column specimens exhibiting longitudinal bar buckling and

subsequent loss of core concrete confinement due to the fracture of transverse reinforcement. The correlations between the computed damage indices and the observed damage progression and collapse limit states in the investigated column specimens exhibited the expected trends.

The comparison between force and deformation quantities corresponding to the yield, the ultimate response, and the residual capacity for specimens subjected to lateral loading is summarized in Table 5.5, Table 5.6, and Table 5.7, respectively. Some of the experimental quantities are approximated from the graphical plots of the experimentally observed response and are not reported in the source data. The error in estimating both the yield moment and the corresponding curvature in at least one loading direction is less than or equal to 10% in all but one experimental program. The error in estimating the maximum moment in all programs in at least one loading direction is less than or equal to 10%; however, there is more discrepancy in estimating the corresponding curvature. The error in estimating the residual moment in all programs in at least one loading direction is less than or equal to 15%. These estimates are considered within acceptable engineering accuracy and confirm the soundness of the component models developed in Chapters 2 and 3 and implemented in Chapter 4 of this report, and their ability to predict flexure-axial collapse of RC columns within a progressive collapse simulation.

Table 5.5 Comparison of experimental and simulated yield force and corresponding deformation quantities for column specimens of programs A–D.

Specimen	Yield moment [kNm]			Curvature [rad/km]		
Program A	Experiment	Simulation	% Error*	Experiment	Simulation	% Error*
1	13.5	14.3	5.9	60.0	49.0	18.3
2	11.8	13.0	10.1	55.0	42.0	23.6
3	15.5	14.7	5.2	75.0	63.0	16.0
Program B	Experiment	Simulation	% Error*	Experiment	Simulation	% Error*
ST2NT	245 -220	245 -246	0.0 11.8	18.6 -17.4	18.7 -17.2	0.5 1.1
ST3NT	219 -200	222 -201	1.4 0.5	13.5 -10.3	13.0 -8.3	3.7 19.4
ST4NT	223 -202	251 -205	12.5 1.5	14.8 -12.9	20.0 -12.0	35.1 7.0
ST5NT	200 -216	223 -226	11.5 4.6	15.5 -18.9	17.3 -20.1	11.6 6.3
	Yield lateral load [kN]			Lateral displacement [mm]		
Program C	Experiment	Simulation	% Error*	Experiment	Simulation	% Error*
C1A0**	NA	NA	NA	NA	NA	NA
C2R4	230 -230	±268	16.5 16.5	19.0 -18.5	±20.7	8.9 11.9
C3R5	230 -230	±271	17.8 17.8	18.0 -16.5	±19.1	6.1 15.8
Program D	Experiment	Simulation	% Error*	Experiment	Simulation	% Error*
415P	225 -209	±223	0.8 6.7	20.0 -18.5	±18.0	5.0 2.7
415S	200 -190	±187	6.5 1.6	18.0 -16.0	±15.0	16.7 6.3

* Computed relative to experimental quantities

** Column reinforcement did not yield (NA = not applicable).

Values denoted by "±" refer to two simulations conducted under monotonic loading.

Table 5.6 Comparison of experimental and simulated maximum force and corresponding deformation quantities for column specimens of programs A–D.

Specimen	Maximum moment [kNm]			Curvature [rad/km]		
Program A	Experiment	Simulation	% Error*	Experiment	Simulation	% Error*
1	14.5	14.6	0.7	95	70	26.3
2	15.3	15.8	3.3	1180	1000	15.3
3	17.3	17.7	2.3	1040	960	7.7
Program B	Experiment	Simulation	% Error*	Experiment	Simulation	% Error*
ST2NT	297 -249	313 -320	5.4 28.5	77.2 -95.8	97.0 -95.8	25.6 0.0**
ST3NT	292 -271	318 -319	8.9 17.7	69.6 -74.4	76.3 -74.4	9.6 0.0**
ST4NT	285 -233	285 -286	0.0 22.7	147.0 -123.0	147.0 -123.0	0.0** 0.0**
ST5NT	262 -230	270 -266	4.3 15.7	130.0 -153.0	130.0 -141.0	0.0** 7.9
	Maximum lateral load [kN]			Lateral displacement [mm]		
Program C	Experiment	Simulation	% Error*	Experiment	Simulation	% Error*
C1A0	220 -230	±224	1.8 2.6	12.0 -13.0	±11.9	0.8 8.5
C2R4	275 -290	±314	14.2 8.3	55~94 -55~-94	±74	NA***
C3R5	330 -340	±345	4.5 1.5	62~97 -62~97	±98.2	NA***
Program D	Experiment	Simulation	% Error*	Experiment	Simulation	% Error*
415P	335 -315	±302	9.9 4.1	127.5 -127.7	±98	23.1 34.9
415S	285 -265	±261	8.4 1.5	127.5 -127.5	±83	34.9 34.9

* Computed relative to experimental quantities

** Validity of comparison questionable because curvature values coincide with point of load reversal; see Figures 2.8 and 5.8.

*** Experimental quantities valid for comparison cannot be determined with certainty due to cyclic loading; see Figure 5.11.

Values denoted by "±" refer to two simulations conducted under monotonic loading.

Table 5.7 Comparison of experimental and simulated residual force and corresponding deformation quantities for column specimens of programs A–D.

Specimen	Residual moment [kNm]			Curvature [rad/km]		
Program A	Experiment	Simulation	% Error*	Experiment	Simulation	% Error*
1	9.0	9.25	2.8	225	225	NA**
2	NA (Behavior too brittle)			NA		
3						
Program B	Experiment	Simulation	% Error*	Experiment	Simulation	% Error*
ST2NT	NA (Behavior too brittle)			NA		
ST3NT						
ST4NT	NA -188	NA -221	NA 17.6	NA -170.0	NA -158.0	NA**
ST5NT	149 NA	165 NA	10.7 NA	64.5 NA	65.0 NA	NA**
	Residual lateral load*** [kN]			Lateral displacement [mm]		
Program C	Experiment	Simulation	% Error*	Experiment	Simulation	% Error*
C1A0	140 -140	±137	2.1 -2.1	61 -61	±65	NA**
C2R4	225 -205	±225	0.0 9.8	130 -130	±150	NA**
C3R5	255 -275	±281	10.1 2.2	130 -130	±150	NA**
Program D	Experiment	Simulation	% Error*	Experiment	Simulation	% Error*
415P	245 -170	±209	14.7 22.9	178.5 -178.5	±178.5	NA**
415S	190 -160	±202	6.3 26.2	178.5 -178.5	±178.5	NA**

* Computed relative to experimental quantities

** Comparison invalid because maximum deformation quantities are pre-determined.

*** Experimental quantities are estimated from the envelope of the hysteretic response.

Values denoted by "±" refer to two simulations conducted under monotonic loading.

6 Simulated Element Removal of Collapsed RC Members

This chapter discusses the analytical and computational details of removing elements representing RC members that have collapsed during an ongoing FE simulation. First, a review of previously published literature involving the collapse of structural elements and element removal during progressive collapse simulation is conducted to some degree of detail since this field of research is relatively new. The following discussion introduces the mechanics of removing a collapsed element from the structural system. The principles of dynamic equilibrium are used to characterize how this removal affects the kinematics of the damaged structural system, the resulting dynamic redistribution of forces, and the corresponding updates to the FE model's geometry, the boundary conditions, and the numerical solution procedure. The steps for automated element removal of collapsed elements are then formalized into a logical algorithm. This algorithm is implemented into a new class of OpenSees that enables runtime evaluation and monitoring of element removal criteria and updates the *Domain* object to reflect the removal of the collapsed elements. Concurrent updates to the *Analysis* objects are discussed in the same context. Next, a benchmark problem representing an idealized structural system is presented to verify the implementation of the element removal algorithm and demonstrate its robustness. The discussion is concluded by introducing the criteria adopted in this report to identify RC column collapse. These criteria are based on the damage indices defined in Section 3.3 for RC columns whose collapse is dominated by flexure-axial interaction, and on the axial load-drift capacity model (Elwood 2002) for RC columns whose collapse is dominated by shear-axial interaction. The discussion extends the interpretation of these criteria to apply to RC beams as well, which is utilized in the progressive collapse simulations presented in Chapter 7. Moreover, treatment of the potential collision between removed elements and the remaining intact part of the structure is

briefly addressed and further details are given in Appendix B. However, the implementation of a computational algorithm to identify contact and collision within a general structural model geometry is outside the scope of this report. It is believed that the full treatment of the collision phenomena within the progressive collapse of RC frame structures subjected to earthquake loading is of limited practical purposes and therefore is marginally addressed in this report for completeness.

6.1 REVIEW OF PUBLISHED LITERATURE ON ELEMENT REMOVAL

Progressive collapse assessment using nonlinear time-history FE simulation is an approach recently gaining popularity over traditional methods based on alternate-path analysis and redundancy-detailing. Examples of these traditional methods include applications for decommissioned RC structures (Virdi and Beshara 1992), existing RC building structures (Gilmour and Virdi 1998; Krauthammer et al. 2002), existing and retrofitted steel frame structures (Houghton and Karns 2002), retrofitted building structures (Crawford 2002), multi-span bridges (Starossek 1999, 2006), and probabilistic evaluation methods (Ellingwood 2006). To the best of the authors' knowledge, there is very limited literature on this developing field of research. Very few experimental investigations have been conducted on reduced-scale RC frames that are redundant enough to experience progressive collapse, with seismically deficient RC columns designed to lose axial load-carrying capacity. These studies include Kim and Kabeyasawa (2004), Wu et al. (2006), and Ghannoum (2007). Experimental data collected from these studies are intended to establish the behavior of RC systems after the loss of one or more load-carrying columns. However, the collapse modes observed in these studies remain limited, and difficult to generalize to cases involving disconnection and subsequent collision by collapsed elements.

A recent analytical study reported in Grierson et al. (2005a,b) describes an analytical approach to use post-yield strength and stiffness degradation in order to conduct a quasi-static progressive failure analysis. Another analytical study reported in Kaewkulchai and Williamson (2004) defines a macro-level damage index to predict collapse of yielding beam-column elements based on maximum element deformations and accumulated plastic energy. Upon

reaching a threshold value (e.g., one) of the damage index, the collapsed element is removed from the structural system. External nodal forces are then applied at the end-nodes using a step function for the duration of the subsequent load step, to represent the effect of the redistributed internal forces from the collapsed element. This approach is valid for simulating quasi-static behavior but is sensitive to the choice of time step (i.e., time step size) during a dynamic simulation and may not be accurately representative of the stored energy imparted into the damaged structure due to the release of internal forces from the collapsed element. In the approach presented in Kaewkulchai and Williamson (2004), the downward motion of the collapsed element is virtually tracked using a condensation method that avoids redefining the unknown degrees of freedom (DOFs) and reassembling the stiffness matrix's connectivity relationships to reflect the splitting of one node into two. Assuming that the equations of the Newmark's β-method (Newmark 1959) describe well the relationship between kinematic quantities, the equations of motion for the collapsed element are uncoupled from those of the damaged structural system. Hence, the DOFs at the removed element's separated node(s) are analytically computed from the state of the damaged structural system after each converged time step following element removal. This DOF condensation approach is extended in Kaewkulchai and Williamson (2006) to include a simplified approach to account for impact on the structure by a collapsed element, based on assumptions of a low-velocity impact by a perfectly plastic (undeformable) mass on a relatively stationary damaged structure which results in negligible local deformations at the impact location. The resulting impact force is assumed to have a negligible duration and result in immediate change of nodal velocity at the point of impact based on the mass and velocity of the impacting collapsed element.

The consideration of locally released internal energy due to element collapse has been presented in a previous study by Pretlove et al. (1991). This study uses an energy balance approach to argue that the portion of strain energy stored in the structure and released upon the brittle collapse of a structural element will excite transient vibrations in the damaged structure. The study concludes that a quasi-static equilibrium-based assessment of the resulting force demands in structural elements is unconservative in assessing the potential for progressive failure. A case study is presented in Pretlove et al. (1991) of two stacked masses supported by two brittle tension-only wires of which one wire prematurely fails. With regards to the ratios of

wire cross-section areas and tensile strengths, a significant region is demonstrated where "static" safety overlaps with "dynamic" progressive failure. Another case study is presented in Pretlove et al. (1991) of a rigid circular wheel frame spoked with brittle pre-tensioned radial wires of which one wire prematurely fails. A significant discrepancy is again demonstrated in the level of pre-tension load that leads to progressive failure when quasi-static and dynamic analyses were singly adopted to compute force redistribution. These case-study demonstrations were conducted under the simplifying assumption of no distributed mass, plasticity, structural damping, or buckling taking place in the structural system and its elements (Pretlove et al. 1991). A similar study is reported in Ramsden (1987) on progressive failure analysis of undamped multiple degree-of-freedom (MDOF) truss structural systems with lumped masses, demonstrating similar conclusions.

An analytical formulation to assess the effect of brittle element collapse on large-scale progressive collapse alternate to that of Kaewkulchai and Williamson (2004) is developed in Powell (2005). This formulation uses an energy balance method to characterize the displacement demand of a structural system immediately following the removal of a gravity load-carrying column. The damaged structural system is assumed to undergo maximum deformations that dissipate an amount of energy in each element equivalent to that dissipated assuming linear-elastic element behavior over twice the deformations necessary to reach its new equilibrium state (under quasi-static loading conditions and given the damaged structural system's updated geometry). According to this formulation, progressive collapse will be arrested if the load-carrying capacity of the structural elements can withstand twice the additional redistributed load, computed using quasi-static analysis of the damaged structure. The progressive collapse will propagate if the structural load carrying-capacity cannot withstand one time the additional redistributed load. In between these two limits, the survival of the damaged structure is dictated by the ductility capacity of its structural elements and their ability to sustain the maximum deformation demands. The analytical formulation in Powell (2005) ignores the portion of locally released energy dissipated by viscous damping in the system. In justification of that Powell (2005) argues that the imposed displacement demands on the damaged structural system due to element collapse resemble a pulse of relatively short duration. This, in addition to computing the element deformation demands assuming that energy dissipation takes place only through

inelastic behavior of the damaged structural system, should make the approximation both valid and conservative. In addition, Powell (2005) characterizes the kinematic state of the damaged structural system at the onset of column gravity-load collapse using nodal displacements only. Hence, the analysis approach in Powell (2005) computes the deformation demands required to reach the new equilibrium state without considering the complete kinematic boundary conditions of the structural system (i.e., nodal velocities and accelerations) at the time of element removal. These quantities may result in amplifying the actual deformation demands on some structural elements and in reducing them on others.

The study reported in Pretlove et al. (1991) also investigates the effect of uncertainty in spoke wire load-carrying capacity represented by the observed standard deviation in measured load-carrying capacity values. The experimental, the computational (i.e., Monte-Carlo simulation), as well as the analytical (i.e., using an assumed jointly normal distribution of spoke wire load-carrying capacity) responses to intentionally cutting one spoke wire is deemed to result in progressive failure if at least one more wire fractures, and to result in survival otherwise. Experiments and computations are conducted in accordance with both quasi-static and dynamic response conditions. The outcome of this study is fragility curves representing the conditional probability of survival given the pre-tension load ratio to the mean wire capacity. These fragility curves conclusively demonstrate the discrepancy between the outcomes of quasi-static and dynamic behavior, and the close agreement between experimental, computational, and analytical predictions.

Two recent analytical studies in Haselton and Deierlein (2005) and Zareian and Krawinkler (2007) include the effect of uncertainty on simulated progressive collapse assessment of MDOF structural systems representing building structures. The uncertainty in the exciting ground motion is handled through the application of the incremental dynamic analysis (IDA) technique (Vamvatsikos and Cornell 2002, 2004) using multiple scaled ground motion records in the context of PEER's PBEE methodology (Porter 2003). The effect of uncertainty in the ground motion is quantified using fragility curves of conditional collapse probability given some intensity measure of the ground motion (typically, the 5%-damped spectral acceleration of the equivalent single degree-of-freedom (SDOF) oscillator representing the structural system's fundamental period, $S_a(T_1, 5\%)$). However, these two studies employ for the definition of

collapse a side-sway mechanism of the gravity load-bearing columns within an entire story, and thus assume ductile detailing in compliance with current building codes' seismic provisions and do not explicitly conduct any removal of elements during the simulation.

6.2 MECHANICS OF ELEMENT REMOVAL

Consider the dynamic equilibrium of the internal node illustrated in Figure 6.1a. At time t during the simulation, two beam elements $B1$ and $B2$ and two column elements $C1$ and $C2$ are attached to the node. Generally, externally applied nodal forces may be applied directly at the node. However, for clarity of illustration, the free-body diagram of an interior node with no externally applied nodal forces is shown. The present discussion can be generalized to the case of externally applied nodal forces as long as these forces are prescribed a priori throughout the analysis duration and are not conditioned on the connectivity of structural elements attached to the node. The subscripted symbols F and M refer respectively to the resisting forces (both axial and shear forces) and bending moments from the attached elements, where the subscripts denote the element designation. The node has a lumped translational mass m and rotational mass moment of inertia I. The dynamic equilibrium is satisfied by the inertial forces ma_x, ma_y, and $I\alpha$ acting on the node, where a_x and a_y refer to the translational accelerations in the x and y directions and α refers to the rotational acceleration in the $x-y$ plane, respectively, in addition to any externally applied nodal forces.

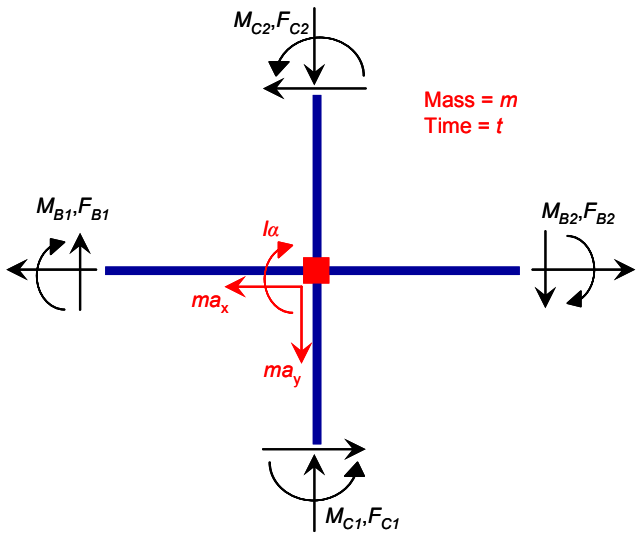

(a) Before element removal

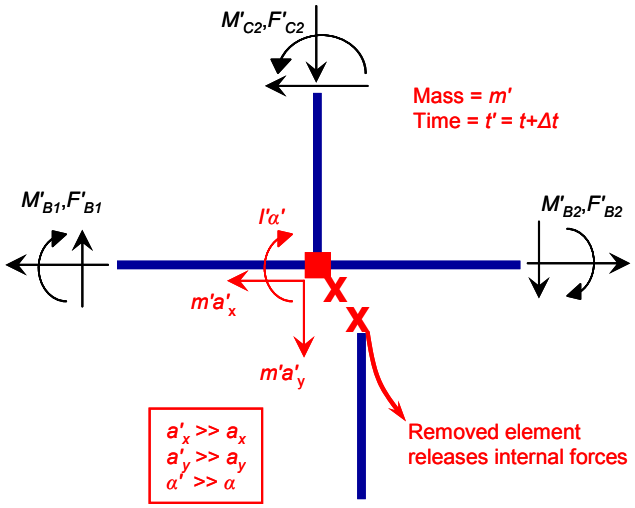

(b) After element removal

Fig. 6.1 Dynamic equilibrium of a node connected to a collapsed element.

At time t, the lower column element $C1$ is assumed to lose its axial load-carrying capacity and collapse in a brittle manner. Element $C1$ is abruptly removed from the computational model of the structural system at the new time $t' = t + \Delta t$ where Δt is the prescribed time step. The free-body diagram of the same node after removal of element $C1$ is illustrated in Figure 6.1b, where the nodal masses and accelerations are updated to m', I', a'_x,

a'_y, and α', respectively. In practical applications, the majority of the lumped nodal masses are derived from the floor system, and the contribution by individual columns is negligible. Hence, the updated masses m' and I' may not be significantly different from the original masses m and I.

The dynamic equilibrium of the node under resisting and inertial forces can be expressed by

$$\vec{P}_{ex} + \sum \begin{Bmatrix} F_x \\ F_y \\ M \end{Bmatrix} - \begin{Bmatrix} ma_x \\ ma_y \\ I\alpha \end{Bmatrix} = \vec{P}_{ex} + \sum \begin{Bmatrix} F'_x \\ F'_y \\ M' \end{Bmatrix} - \begin{Bmatrix} m'a'_x \\ m'a'_y \\ I'\alpha' \end{Bmatrix} \tag{6.1}$$

where $\vec{P}_{ex}$ is the vector of externally applied nodal loads, subscripts x and y denote the principal directions of a Cartesian coordinate system, and the summation is conducted for the still-attached elements. Upon abrupt element collapse and removal, this dynamic equilibrium is disturbed by the sudden release of internal forces from element $C1$ and must be restored before the solution can be continued for the following time steps. This can only be achieved through a corresponding change in the externally applied nodal forces (if any), the resisting forces from the still-attached elements, the inertial forces, or a combination thereof. Since the externally applied forces $\vec{P}_{ex}$ are defined and applied directly on the node throughout the analysis, they are not affected by the removal of a collapsed element. The resisting forces in the still-attached elements (F' and M') can only change as a result of updated element deformations, which require a change in relative displacements (and possibly velocities) between the elements' respective end-nodes. These nodal displacements and velocities can be updated only as a result of updating the nodal velocities and accelerations, and requires a period of time. On the other hand, the inertial forces are directly related to the nodal accelerations. Such nodal accelerations need to change in order to update the nodal velocities and, subsequently, displacements, in order for the damaged structural system to reach a new equilibrium state. In order to satisfy dynamic equilibrium at time t' after the abrupt release of resisting forces from element $C1$, a corresponding abrupt change in accelerations a'_x, a'_y, and α' must take place. Since the still-attached elements' end-nodes other than their shared node are under dynamic equilibrium themselves, this abrupt change is first localized at the shared node at time t'.

In the following time steps, the abrupt change in nodal accelerations initiates a case of transient loading superposed on the damaged structural system, whereby the resulting changes in nodal velocities and displacements lead to an updated set of resisting (and inertia) forces that propagate outward through the still-attached elements into neighboring nodes in the damaged structural system. These updated nodal forces must satisfy dynamic equilibrium of their respective DOFs during every time step as well, which results in updated inertial forces and, consequently, updated nodal accelerations. This process will continue to propagate throughout the damaged structural system according to its element connectivity until updated nodal displacements (and velocities), corresponding to a new equilibrium state, are reached.

It is not sufficient for progressive collapse assessment to estimate the resisting element forces in the damaged structural system based on its quasi-static response to the new equilibrium state, which is typically performed by superposing the released internal forces from the collapsed element as externally applied loads on the affected node(s). This insufficiency is due to the fact that the nodal velocities of the damaged structural model, upon reaching the new equilibrium state, will result in overshooting the corresponding displacements. This will in turn overload (increase) the deformation demand in the structural elements. Hence, in the absence of structural damping and external excitation (e.g., earthquake), a case of free-vibration of the damaged structural system will ensue, in which the initial transient phase is followed by a steady-state phase oscillating about the new equilibrium state. The resulting overload may lead to the collapse of additional structural elements, which are otherwise "safe" in the new equilibrium state according to quasi-static analysis. The arguments presented thus far in this section agree with Pretlove et al. (1991), albeit derived from a dynamic equilibrium approach, instead of an energy balance approach.

If further element collapse takes place, a second transient phase is excited in the damaged structural model before it reaches another new equilibrium state and starts oscillating about it. As a result, additional elements may collapse due to overload. This process of dynamic force redistribution continues until either (a) the damaged structural system reaches an equilibrium state about which it can safely oscillate and the progression of element collapse is arrested, (b) the damaged structural system undergoes overall gravity-load collapse, or (c) the damaged structural system experiences partial large-scale collapse within sections of it which are

nevertheless compartmentalized while the rest of the structural system survives to a new equilibrium state. In the latter case, the structural system will probably need to be evacuated and demolished later, yet the prospect of maintaining life safety is enhanced compared to overall gravity-load collapse.

In the presence of external excitation (e.g., earthquake), the transient excitation due to the collapse of an element is superposed on the input ground motion. During computational simulation, the time step of the input ground motion is typically larger than that necessary to accurately reproduce the transient effect resulting from the removal of a structural element. Particularly, because this transient behavior may trigger local axial vibrations in stiff structural elements whose natural period of vibration may be significantly short. Hence, in order to accurately represent the dynamic load redistribution, shorter time steps are typically needed immediately after element removal, during which the input ground motion record may be interpolated. An adaptive time-stepping scheme can be used to enable a computationally efficient solution.

The interaction between structural damping (i.e., viscous and material damping) and the transient vibration resulting from abrupt element removal is an interesting phenomenon to explore. However, little literature exists on experimental or analytical treatments of this subject. Hence, classical viscous damping is assumed to change only as a result of the changes in the natural vibration periods of the intact structure upon removal of a collapsed FE. Nevertheless, additional material damping will be experienced due to energy dissipation through the combination of amplified element deformation during the transient phase and element inelasticity.

Traditionally, the more conventional approaches to conducting progressive failure analysis involved multiplying the stiffness of a collapsed FE by a small multiplier in order to eliminate its contribution to the properties of the structural model while avoiding the computationally inefficient process of redefining the structural model's DOFs and the stiffness matrix connectivity during an ongoing simulation. The advantages of explicitly removing a collapsed FE instead of assigning a low stiffness to it are threefold. First, it avoids numerical problems associated with ill-conditioned stiffness matrices. Second, suddenly releasing the internal forces from the removed FE and enforcing dynamic equilibrium at the end-nodes

enables the computation of the resulting increase in nodal accelerations. This leads to including the damaged structural model's complete kinematic state at the time of FE removal in estimating the subsequent transient response and in determining if the structure can successfully redistribute the forces from the removed FE and oscillate safely about its new equilibrium position. Third, the motion of the collapsed FE can be tracked relative to the intact damaged structural model to estimate the time and kinematics at subsequent collision, if any, between the removed FE and the intact damaged structure. The kinematics of the separated nodes being known, this tracking can be conducted using a rigid-body analysis of the removed FE (if separation has taken place at both FE end-nodes) or the condensation approach developed in Kaewkulchai and Williamson (2004) (if separation has taken place at only one FE end-node). Thus, no redefinition of DOFs or stiffness matrix assembly of the damaged structural system is required. If subsequent collision with the intact damaged structure is detected, an analytical approach based on the assumption of "soft-impact" by an elastic (deformable) mass can be followed to characterize the physics and duration of impact following such collision and to compute the impact-induced forces and redistribution of masses resulting from this collision (Zineddin and Krauthammer 2007). This approach is based on the assumption of relatively negligible relative displacement during the impact duration between the impacting collapsed FE and the impacted intact damaged structural system at the contact location, in addition to low-velocity impact which precludes the possibility of punching or penetration (Schonberg et al. 1987). The simplified approach pursued for modeling element collision in the progressive collapse applications presented in this report is explained in detail in Appendix B.

6.3 DESIGN OF ELEMENT REMOVAL ALGORITHM

This section formalizes into a logical algorithm the steps required to implement automated removal of collapsed elements from a FE structural model during the course of an ongoing OpenSees simulation, as illustrated in Figure 6.2. After each converged analysis step, each *Element* object is checked for possible violation of its respective removal criteria, which are presented in Section 6.6. A violation of any criterion triggers the activation of the element

removal algorithm on the violating *Element* object (see Fig. 1.2). The algorithm is split into two main sets of procedures.

The first set of procedures includes checking if the removal of the collapsed *Element* object will result in leaving any "dangling" nodes or "floating" elements behind, as illustrated in Figure 6.3. A dangling node is a *Node* object that will have no connectivity within the *Domain* if all its attached elements were to collapse and be removed during the simulation. Floating elements are *Element* objects that are connected to themselves but are completely disconnected from the rest of the damaged structural model and are unsupported against rigid body motion. An example of such floating elements are the *Element* objects that represent the interior of a collapsed column meshed by multiple beam-column finite elements, of which the *Element* objects representing the column ends are likely to violate their removal criteria (and thus get removed) first during a seismic event. The existence of either dangling nodes or floating elements will cause the *Analysis* object to permanently fail due to structural instability and lack of equilibrium (unless the *Solver* object can handle rigid-body motion). Hence, the removal algorithm identifies and removes such nodes and elements from the damaged structural model as well. Moreover, the successful removal of an *Element* object requires the identification and deletion of all its associated distributed forces from the load patterns existing in the *Domain*. Similarly, the removal of *Node* objects requires the identification and deletion of all its externally applied forces, imposed displacements, and fixed-point constraints (i.e., support fixities). Finally, this first set of procedures is concluded by updating the nodal masses lumped at the removed *Element* object's end-nodes which are not left dangling. This is conducted by subtracting from the associated nodal masses the product of multiplying the removed *Element* object's distributed mass (if defined) by an appropriate ratio (e.g., one half in the case of prismatic two-node beam-column and truss elements) of its length. This set of procedures has been fully implemented within the source-code of OpenSees, as detailed in Section 6.4.

The second set of procedures involves the tracking of the removed *Element* object's motion after separation. Without adding an explicit node to the damaged structural model, the kinematics of the separated end-node(s) in the removed *Element* object at the time of separation are identified from the last converged dynamic equilibrium state of the structural model. These kinematics represent the initial conditions for the free-falling motion of the collapsed element.

This motion can then be tracked using the condensation approach proposed in Kaewkulchai and Williamson (2006) or the assumption of rigid-body motion of the element under the effect of its own gravity load (Appendix B). At the end of each subsequent converged time step, the position of the collapsed element, separated from one end or both ends, is compared with the state of the damaged structural model to determine when collision takes place. At the time of collision, the kinematics of both the impacting element and the damaged (impacted) structural system can be determined, most importantly the relative impact velocity. The impact force, duration, temporal variation of force over duration, and additional mass imparted from the impacting element at the impact location are computed and superposed on the damaged structural system during the subsequent time steps. This second set of procedures has not been fully implemented into the source-code of OpenSees. It is conducted in this report by conducting the necessary computations using the general-purpose software MATLAB (MATLAB 2007), and transferring the results through the Tcl language used by the analyst to build and perform OpenSees simulations.

After completing both sets of procedures, the algorithm updates the state of the damaged structural system to include the updated masses, the geometry, and the impact forces (if applicable). The updating of the mass and stiffness matrices will result in updating the damping matrices as well if stiffness and/or mass-proportional damping is used. Since numerical convergence may face difficulties following such extreme events, especially in softening structural systems, the solution parameters may need to be updated. This is conducted by iteratively switching solver type (Newton-Raphson, Modified Newton-Raphson, etc.), convergence criteria (displacement norm, energy norm, etc.), and other options (e.g., time-step size) of the *Analysis* object, so that an ultimate failure to converge would be more likely to take place only if the damaged structural system has reached complete collapse (corresponding to global instability).

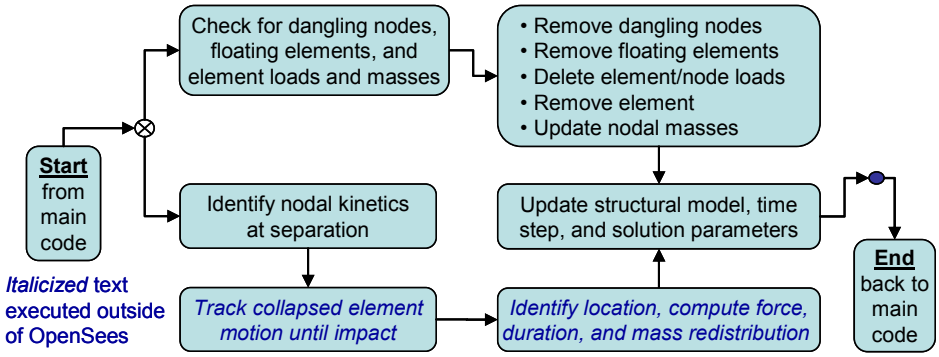

Fig. 6.2 Automatic element removal algorithm.

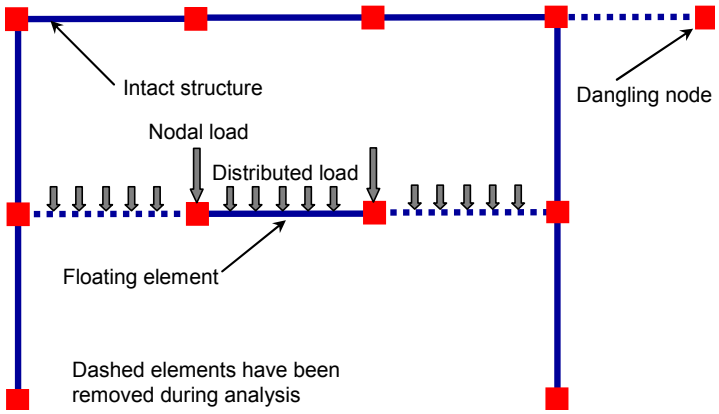

Fig. 6.3 Elements, nodes, and loads requiring removal due to element removal.

6.4 IMPLEMENTATION OF ELEMENT REMOVAL ALGORITHM

The implementation of the automatic element removal algorithm discussed in the previous section is carried out as a new class in the software platform OpenSees. The new class is declared a subclass of the abstract class *Recorder* (see Section 4.1). This declaration is made in order to take advantage of the existing inter-class interaction in OpenSees. According to the API main program, which specifies the relationship between the high-level classes representing OpenSees modules, all *Recorder* objects are called and ordered to execute their main method **record()** after each and every converged load step in the *Domain* object. In addition, all *Recorder* classes have access to the *Domain* object in order to extract the information they are

requested to record from the associated nodes, elements, materials, etc. This information is specified in the constructor method arguments at each *Recorder* object's instantiation (i.e., creation) during runtime.

The new *Recorder* derived class is called *RemoveRecorder*, whose class interface is illustrated in Figure 6.4. The constructor of the class receives as arguments a number of *ID* arrays that identify several *DomainComponent* objects to monitor, in addition to the *Vector* object **remCriteria** of threshold values representing element removal criteria. Moreover, in accordance with all *Recorder* classes, the constructor arguments include a pointer to the *Domain* object and the flag **echoTimeFlag** set by the analyst to indicate whether or not to print the current time at each recording time-step **deltat** in the output file **filename**. Two types of *RemoveRecorder* objects can be constructed according to the analyst's specification. The object type is specified by the type of input *ID* objects to the constructor and determines the definition of the main method **record()**.

The first type of *RemoveRecorder* objects is associated with an array of *Element* objects, represented by the constructor argument **eleIDs**. These *Element* objects are deemed vulnerable to collapse and subsequent removal by the analyst (e.g., all elements). Accompanying this is an optional array **secIDs**, which identifies the components (e.g., cross sections) within the *Element* objects (if any) where the element removal criteria are checked. In the current implementation, a total of six removal criteria are defined on the element and component (cross-section) levels. These removal criteria are discussed in Section 6.6. Another optional argument to this type of *RemoveRecorder* objects is an array of *Element* object identifiers **slaveEleIDs.** These are the *Element* objects that will become floating elements within the *Domain* object once all the *Element* objects specified in the **eleIDs** argument have collapsed and been removed by the *RemoveRecorder* object.

The second type of *RemoveRecorder* objects is associated with a *Node* object represented by the constructor argument **nodeID**. This is a *Node* object that will become a dangling node within the *Domain* if all its attached elements were to collapse during the simulation. This second type of *RemoveRecorder* objects requires an array of attached *Element* objects identified by the constructor argument **eleIDs**. This requires that all attached *Element* objects have been deemed vulnerable by the analyst and assigned removal criteria within previously defined

RemoveRecorder objects of the first type. Since it is unlikely that two *Node* objects will have the same connectivity to *Element* objects, each *RemoveRecorder* object of the second type is associated with only one *Node* object. It is impractical for large structural models to require the analyst to identify and list all nodes that may potentially become dangling during the course of a simulation. Therefore, future development of the *RemoveRecorder* class should eliminate this need by identifying a method to efficiently and reliably check the connectivity of all *Node* objects attached to a collapsed *Element* object and identify the ones that are attached to no other *Element* objects in the *Domain* object. This method was not implemented in the current version of class *RemoveRecorder* due to a limitation in the existing data structures of OpenSees, whereby *Element* objects store the identities of their associated *Node* objects, whereas *Node* objects do not store the identities of their attached *Element* objects. This means that the full automation of dangling node removal in the current version of OpenSees will require a search through all *Element* objects in the *Domain* upon the removal of any one *Element* object in order to check the connectivity of its associated *Node* objects, which is computationally impractical.

The definition of the main method **record()** depends on the type of the *RemoveRecorder* object. In objects of the first type, this method scans the *Element* objects identified in the constructor argument **eleIDs** and retrieves the information characterizing their respective damages-states. If the removal criteria are identified on a component level, the *DomainComponent* objects identified in the constructor argument **secIDs** are scanned and the values of their respective damage-state information retrieved from each *Element* object. Next, these values are compared to the corresponding threshold values defined in the constructor argument **remCriteria** (a threshold value of zero signifies that the corresponding removal criterion is disabled and is to be ignored during the execution of the method). If one active removal criterion is violated, the corresponding *Element* object is eliminated (removed) from the *Domain* by invoking the method **elimElem()**. However, the *Element* object is not destroyed or deleted from the program memory. It is only reset to its initial state by invoking its member method **revertToStart()**. The primary reason for eliminating the collapsed *Element* object from the *Domain* while not destroying it is that there may be other objects in the OpenSees program (e.g., other *Recorder* objects) associated with the collapsed *Element* object through pointers. Having not been informed of the *Element* object's destruction, these associated objects would try

to invoke methods on the non-existent *Element* object, causing a fatal runtime error. However, by resetting the collapsed *Element* object any element information "recorded" after its removal can be clearly identified and filtered-out during post-processing.

The retrieval of the elements' damage information is achieved through the extension of existing *Element* classes to include a new method **getRemCriteria()**. This method is declared virtual in the abstract base class *Element*, and then implemented individually for the derived *Element* classes which may be removed during an analysis. Currently supported *Element* classes include beam-column elements whose cross section is fiber-discretized using *ConfinedFiberSec* objects (both lumped and distributed plasticity, see Sections 3.3 and 4.5); zero-length elements whose constitutive law is defined using members of class *LimitState* (see Section 3.1), which represent the shear-axial coupled zero-length elements developed in Elwood (2002); and brittle truss elements (see Section 6.5). If all the *Element* objects identified in **eleIDs** are removed, the method **record()** invokes the method **elimSlaves()**, which in turn invokes the methods **elimElem()** and **elimNode()** on all the *Element* objects identified in **slaveEleIDs** and their associated *Node* objects, respectively. The methods **elimElem()** and **elimNode()** remove an *Element* and a *Node* object, respectively, from the *Domain* while resetting them to their initial states, in accordance with the first set of procedures discussed in the previous section.

In *RemoveRecorder* objects of the second type, the method **record()** compares the list of attached *Element* objects identified in **eleIDs** with the list **remEles** of *Element* objects already removed by all *RemoveRecorder* objects during the simulation up to the last converged time step. If all the attached *Element* objects have already been removed, the method **elimNode()** is invoked on the *Node* object identified by **nodeID**.

The identity and pointers to all *Element* and *Node* objects removed from the *Domain* by an object of class *RemoveRecorder* are stored in class-wide static arrays, as well as the number of *RemoveRecorder* objects currently existing in the *Domain*. Accordingly, when the destructor method of an object of class *RemoveRecorder* is invoked, the object first checks to see if it is the last *RemoveRecorder* object in the *Domain* and, if so, destroys all previously removed *Element* and *Node* objects in order to clear up the program memory. This step is significant in parametric or other multiple-run studies (e.g., IDA), where a large number of simulations is scheduled to run in batch mode, and the accumulation of memory leaks due to *DomainComponent* objects not

explicitly destroyed can negatively affect the computational efficiency. An optional log file **filename** may be constructed by the *RemoveRecorder* class and used by the method **record()** to indicate which *DomainComponent* objects were removed during the simulation, at what time and for what reason (i.e., which removal criterion was violated). This optional log file is closed by the last *RemoveRecorder* object to be destroyed. The method **restart()** is used to restore to the *Domain* object the previously removed components for subsequently scheduled simulations, e.g., in a parametric study.

The modification of the analysis time step (and possibly *Analysis* object options) following element removal is left flexible to the analyst's preference. Since Tcl is a script language, it offers the advantage of defining within the input to OpenSees interpreter a procedure for adaptive time-stepping and iterative solver modification (Mazzoni et al. 2004). One such procedure has been developed and used in the progressive collapse applications presented in this report (see Chapter 7).

```
class RemoveRecorder: public Recorder
{
public:
//   Constructor and destructor
     RemoveRecorder(int &nodeID, ID &eleIDs, ID &secIDs, ID &slaveEleIDs, const
          Vector remCriteria, Domain &theDomainPtr, bool echoTimeFlag, double
          deltat, const char* filename);
     ~RemoveRecorder();

//   Main method invoked by the Domain after a converged load step
     int record(int commitTag, double timeStamp);

//   Internal methods used by the class to check and remove components
     int checkEleRemoval(Element* theEle, int &theComponent, Vector Criteria);
     int elimElem(int theDeadEleTag, double timeStamp = 0);
     int elimNode(int theDeadNodeTag, double timeStamp = 0);
     int elimSlaves(double timeStamp = 0);

//   Static class-wide lists of removed components to be destructed after analysis
     static int numRecs, int numRemEles, numRemNodes;
     static Vector remEleList, Vector remNodeList;
     static Element** remEles;
     static Node** remNodes;

//   Access & pure virtual methods declared in base class (partial list)
     int restart();
};
```

Fig. 6.4 Class interface for *RemoveRecorder.*

6.5 VERIFICATION OF ELEMENT REMOVAL ALGORITHM

In this section, the OpenSees implementation of the element removal procedure developed and automated in Sections 6.2–6.4 is verified using a benchmark problem representing an idealized structural system subjected to earthquake excitation. The benchmark structural system is constructed specifically for the purpose of this validation. It consists of trussed cantilever beams of different lengths, positioned on top of each other. The behavior of two truss members within the structural system is allowed to alternate between being brittle or ductile in order to create four case-studies demonstrating the path-dependency of the progressive collapse process. Non-complex element removal criteria are adopted in order to make the analysis of the results more straightforward and exclusively relevant to the element removal procedure. Similarly, no viscous damping is considered. The structural system is subjected to its own gravity loads, in addition to an input excitation, Figure 6.5, applied in the vertical direction at all supports, i.e., nodes 1, 2, 4, 5, and 12. This excitation is scaled to peak ground acceleration (PGA) of 1.04g from ground motion acceleration recorded during the 1994 Northridge earthquake (Tarzana station, 90° direction). Given the small size of this computational model, adaptive time stepping is not deemed to save significant computational time. Hence, a fixed analysis time step of 0.005 sec is chosen.

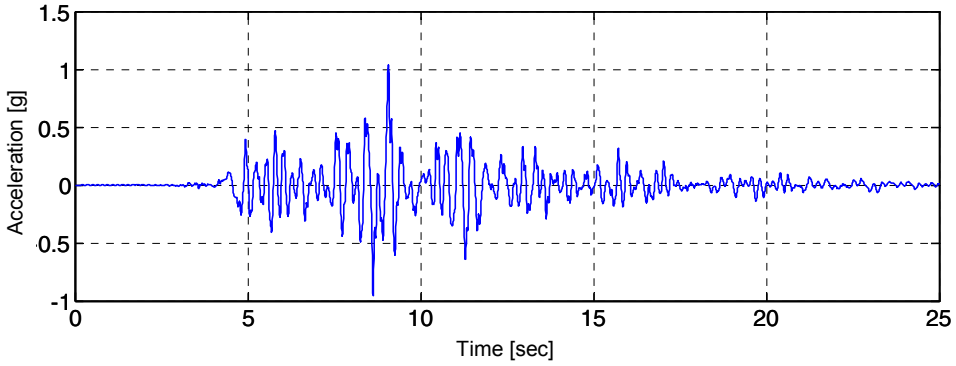

Fig. 6.5 Input ground acceleration record for benchmark problem.

6.5.1 System Properties of Benchmark Problem

The geometry and FE model idealization of the benchmark problem is illustrated in Figure 6.6. Circled numbers denote structural elements, while uncircled numbers denote nodes. All dimensions shown are in meters. The structural system consists of two independent cantilever-like canopies. Each canopy consists of one horizontal elastic beam supported by two inclined truss members. The beams are assumed to exhibit linear-elastic behavior and are modeled using elastic beam-column elements. The truss members are modeled using truss elements that exhibit a linear elastic behavior prior to reaching an axial load magnitude of F_y. Subsequently, they exhibit either a brittle or a perfectly plastic behavior, as discussed in Section 6.5.2. Nonlinear geometry and large-deformation effects are included in the FE model by employing a co-rotational formulation for the geometric transformation equations which relate element quantities (e.g., orientation, resisting forces, stiffness, etc) to global coordinates. This formulation updates the local coordinate systems of individual finite elements during the analysis and uses the updated coordinate system to compute the current element length and include geometric stiffness terms (Crisfield 1990; Crisfield and Moita 1996). The mass is lumped at the nodes as listed in Table 6.1. The properties of area for each element are listed in Table 2.2. Note that nodal gravity loads associated with these lumped masses are included in the simulation before the application of the seismic support excitation.

Table 6.1 Lumped masses at unrestrained nodes of benchmark problem.

Node	1	6,7	8	9–11
Mass [ton]	10	4	6	4

Table 6.2 Element properties of benchmark problem.

Element	EA [kN]	EI [kNm^2]	F_y [kN]
1	2,000	3,000	100
2	100,000	5,000	∞ (Elastic)
3	1,000	1,000	50
4–9	100,000	10,000	∞ (Elastic)
10,11	3,000	5,000	150

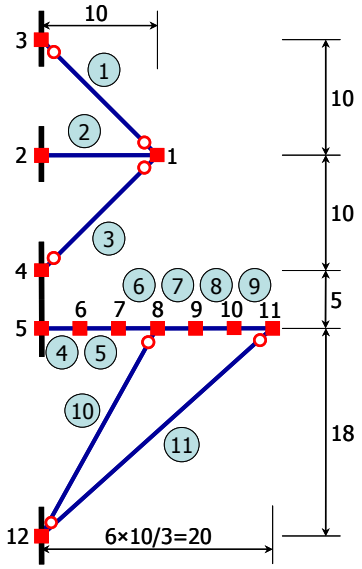

Fig. 6.6 Geometry and FE model of benchmark problem (dimensions in meters).

6.5.2 Progressive Collapse Case-Studies

By selecting combinations of the ultimate ductility limits for the truss elements used in constructing the FE model, four case-studies are investigated. Accordingly, in each case study, some of the truss elements fail in a ductile manner, and others fail in a brittle manner. This is performed in order to explore the path-dependent nature of the progressive collapse process and the sensitivity of the developed element removal procedure to this process. Prior to reaching their ultimate ductility limits, ductile truss elements are assumed to exhibit a perfectly plastic behavior

after yielding, linear-elastic unloading, and equal magnitudes of yield force in compression and tension. These elements are assumed to collapse upon reaching their ultimate ductility limits. The designation of the case-studies and the corresponding ultimate ductility limits for the truss elements are listed in Table 6.3.

Table 6.3 Ultimate truss element ductility limits for benchmark problem.

Truss element	1,11	3	10
Case 1	5	5	5
Case 2	5	5	1
Case 3	5	1	5
Case 4	5	1	1

It is further assumed that collapsed truss elements separate from the structural system at the location of their connection with the beam elements. Accordingly, the collapse of truss element 3 will cause it to fall and collide with the lower canopy. Given the undeformed configuration and geometry, the collision should take place approximately at node 9 (slightly to the right). For simplicity of the analysis, the collision is assumed to take place exactly at node 9, which implies an assumption of 0.1 m axial shortening in the collapsed truss element. As a result of the collision, the impacting truss element is assumed to deform in a flexural mode along its length, simply supported at nodes 4 and 9. The energy of the impact is assumed to be dissipated during one half-cycle of such flexural deformation, after which it rapidly decays (e.g., due to friction). After this half-cycle, truss element 3 is assumed to apply no additional impact forces at nodes 4 and 9 and remain passively supported prior to collapse of the lower canopy. The effect of the impact force on the collapse potential of the lower canopy is thus investigated. In the case-study simulations involving collapse of truss element 3, the time and duration of collision and the resulting impact force are computed and added as a time-varying externally applied load at node 9. The computation of these quantities is discussed in detail in Appendix B. In addition to impact, such collision will result in additional mass at noted 9. It is assumed that the collapsed truss elements contribute 2 tons of the mass lumped at each of their end-nodes. Hence, the

collision with (or the loss of) a collapsed element at any node results in updating its assigned lumped mass and gravity loads by adding (or subtracting) 2 tons.

6.5.3 Results and Discussion

All simulations were successfully conducted without exhibiting numerical convergence problems. Cases 1 and 2 result in similar responses where no element collapse is observed in either case. In the upper canopy, truss elements 1 and 3 exhibit brief yielding inducing a maximum ductility demand of 1.17 and 1.11, respectively, but their ultimate ductility capacity of 5.0 is not reached. The absolute force magnitude-axial strain responses of these two truss elements for Cases 1 and 2, normalized using their respective values at yield, are illustrated in Figure 6.7a. In the lower canopy, truss elements 10 and 11 exhibited linear-elastic behavior.

Case 3 results in partial collapse of the upper canopy. Truss element 3 reaches its ultimate ductility limit of 1.0 after 8.875 sec and subsequently collapses onto the lower canopy. As a result, the maximum ductility demand on truss element 1 increases to 2.1 but does not reach 5.0, and the upper canopy exhibits no further collapse progression. Since the upper canopy's response is not affected by whether truss members in the lower canopy are ductile or brittle, it exhibits the same response in Case 4. The absolute force magnitude-axial strain responses of the two truss elements 1 and 3 for Cases 3 and 4, normalized using their respective values at yield, are illustrated in Figure 6.7b. Figure 6.7c illustrates the time history of the normalized axial forces in truss elements 1 and 3 for all four cases. The time-history response for truss element 3 is identical for all cases prior to reaching its ultimate ductility limit in Cases 3 and 4, after which the response is discontinued for these two cases (at 8.875 sec). The response for truss element 1 is identical for all cases prior to 8.875 sec. Subsequent response exhibits higher average force values in Cases 3 and 4 than Cases 1 and 2, and longer periods of yielding before the damaged upper canopy starts to oscillate about a new equilibrium state. The collapse of truss element 3 results in a significant permanent displacement in the vertical direction at node 1, as illustrated in Figure 6.8a. The nodal displacements are normalized using their respective values due to the action of gravity load only, before the application of earthquake excitation.

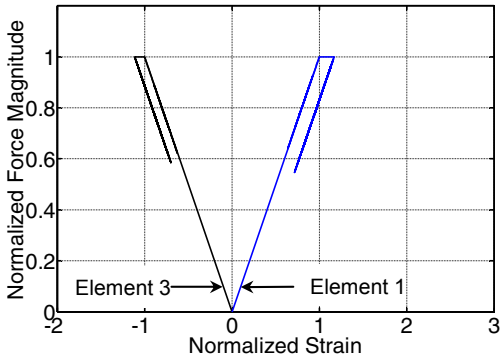

(a) Normalized force-deformation for Cases 1 and 2 (brittle truss element 3)

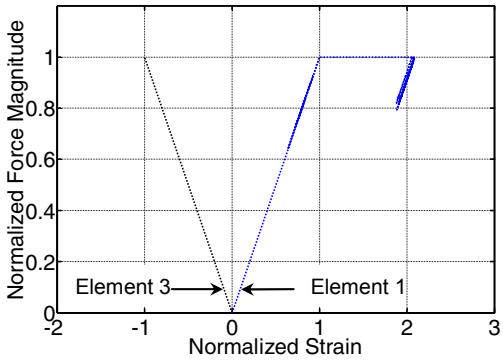

(b) Normalized force-deformation for Cases 3 and 4 (ductile truss element 3)

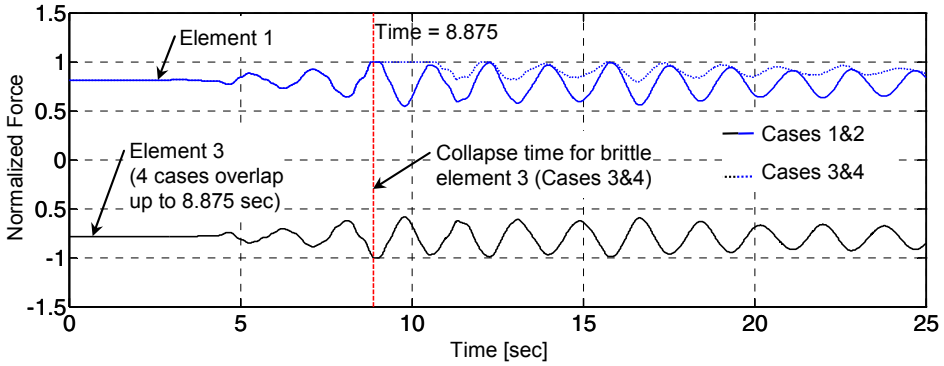

(c) Normalized force time-histories

Fig. 6.7 Simulated response of elements 1 and 3 for benchmark problem.

In the lower canopy, collapsed truss element 3 collides with node 9 at 11.260 sec. The resulting impact load results in reaching the yield force of truss elements 10 and 11. Subsequently, in Case 3, the ductility capacity of truss elements 10 and 11 is sufficient to prevent the progression of collapse to the lower canopy. The lower canopy reaches a new equilibrium state and starts oscillating about it while supporting additional load and mass from the partially collapsed upper canopy. In Case 4, truss element 10 reaches its ultimate ductility capacity of 1.0 at 12.370 sec and collapses. Before the lower canopy could safely reach a new equilibrium state, truss element 11 reaches its ultimate ductility limit of 5.0 and collapses at 14.07 sec, leading to complete collapse of the lower canopy. The vertical displacement time-histories (normalized by

the displacement due to gravity load application) at nodes 8, 9, and 11 are illustrated in Figure 6.8b–d, respectively.

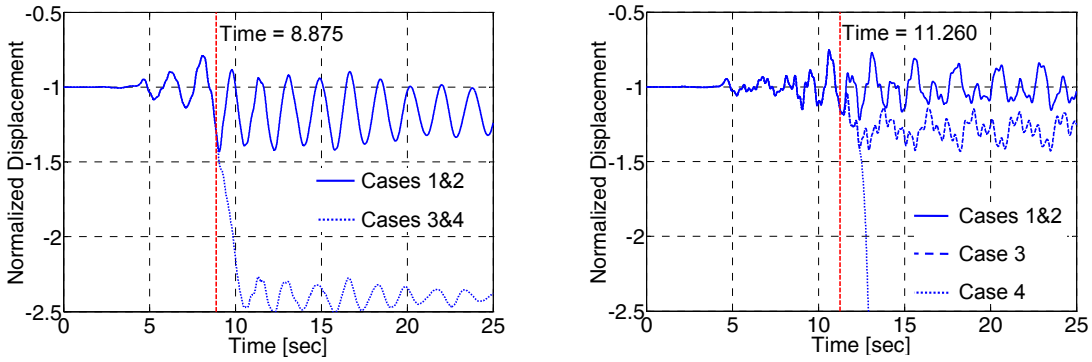

(a) Node 1

(b) Node 8

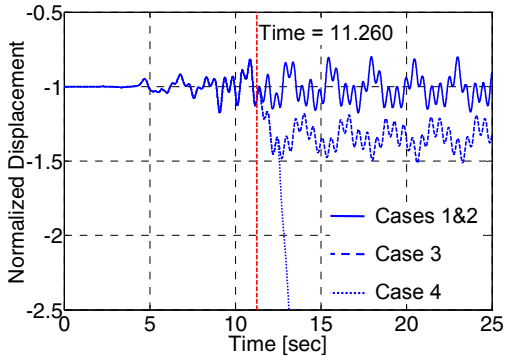

(c) Node 9

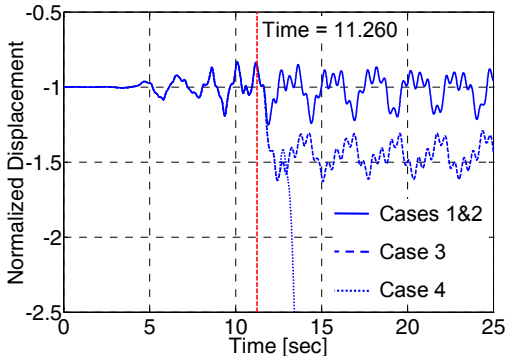

(d) Node 11

Fig. 6.8 Simulated nodal displacement time-histories for benchmark problem.

The ability of the implemented element removal procedure to update the structural system during the course of an ongoing simulation, in order to conduct progressive collapse analysis, is established. In addition, the four case-studies considered in the benchmark example explore the sensitivity of the progressive collapse process to the choice of criteria for truss element collapse (ductility capacity), which in turn results in different times and sequences of collapse for individual elements. The results of this exploration are summarized by comparing the corresponding maximum ductility demand on each truss element (Fig. 6.9), as well as the simulated deformed shapes and collapse progression of the case-studies (Figs. 6.10–6.12).

Figure 6.9 compares the maximum ductility demands imposed on each truss element during each case-study simulation and lends insight to the sensitivity of the outcome and extent of the benchmark system collapse to its constituent element properties. For the cases involving truss elements 1, 3, and 11 having an ultimate ductility capacity larger than 1.17, the maximum ductility demand on truss element 10 never reaches 1.0 and the structural system survives the earthquake. However, if the ductility capacity of truss element 3 is reduced to 1.0 (i.e., by 14.5%), the maximum ductility demand on truss element 1 nearly doubles, and the upper canopy of the structural system avoids complete collapse only if the corresponding ductility capacity of element 1 is greater than 2.1. Meanwhile, the maximum ductility demands on both lower canopy truss elements 10 and 11 exceed 1.0. If both have a ductility capacity larger than 1.31, the lower canopy does not collapse. However, if the ductility capacity of truss element 10 is reduced to 1.0 (i.e., by 23.6%) and it collapses, the lower canopy completely collapses as truss element 11 cannot sustain the resulting overload even at a ductility capacity equal to 5.0.

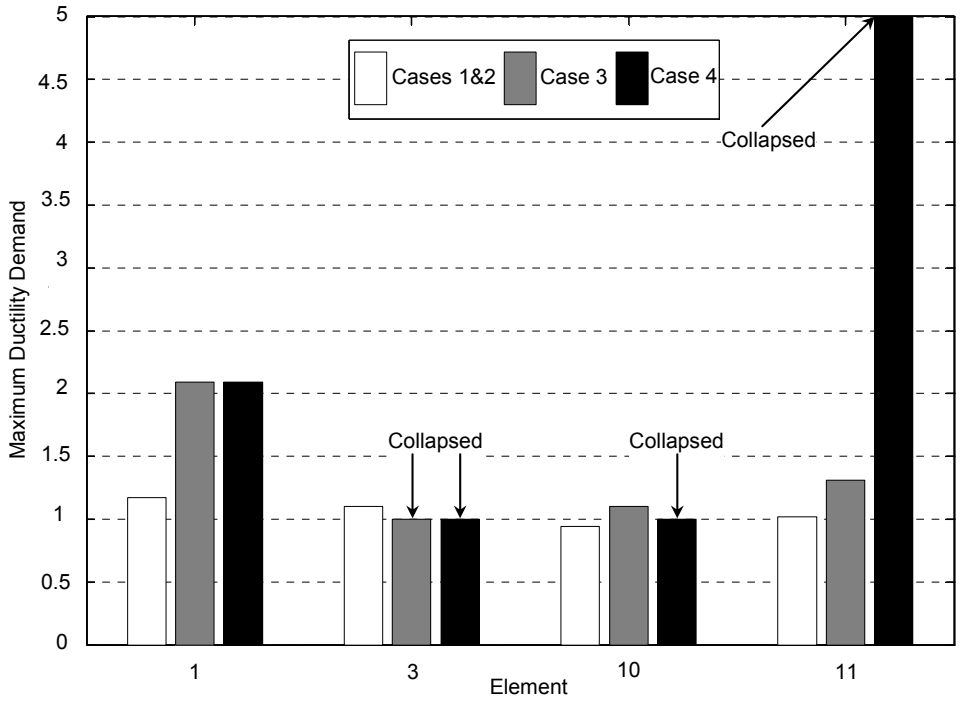

Fig. 6.9 Simulated maximum element ductility demands for benchmark problem.

The deformed shapes and collapse progression resulting from the simulation of Cases 1 and 2, Case 3, and Case 4, are illustrated in Figure 6.10, Figure 6.11, and Figure 6.12, respectively (displacement amplification factor = 1). The simulated deformed shapes of the structural system are compared at 9.5, 11.5, and 14.5 sec, following main element collapse events in individual case studies. Note that the deformed shapes of beam-column elements are plotted without accounting for the rotation at their end-nodes but rather simply by a straight line connecting the two end-nodes. Cases 1 and 2 exhibit no collapse at all, despite the presence of a brittle truss element in the lower canopy for Case 2. Case 3 results in partial collapse of the upper canopy due to a brittle truss element. However, the collapse gets arrested and contained in both the upper and lower canopies without propagating further due to the ductility capacity of the remaining truss elements. Case 4 results in partial collapse of the upper canopy which still gets contained there as well. However, the lower canopy suffers from complete collapse due to the presence of one brittle truss element and despite the ductility capacity of the remaining truss element. The case-study simulations demonstrate the sensitivity in the occurrence and extent of progressive collapse predicted by the element removal procedure to the structural model parameters (i.e., element removal criteria). Given this sensitivity, it is recommended that simulation-based progressive collapse assessment be conducted in a probabilistic framework and using statistical methods of evaluation. This is explored in the demonstration applications developed in Chapter 7.

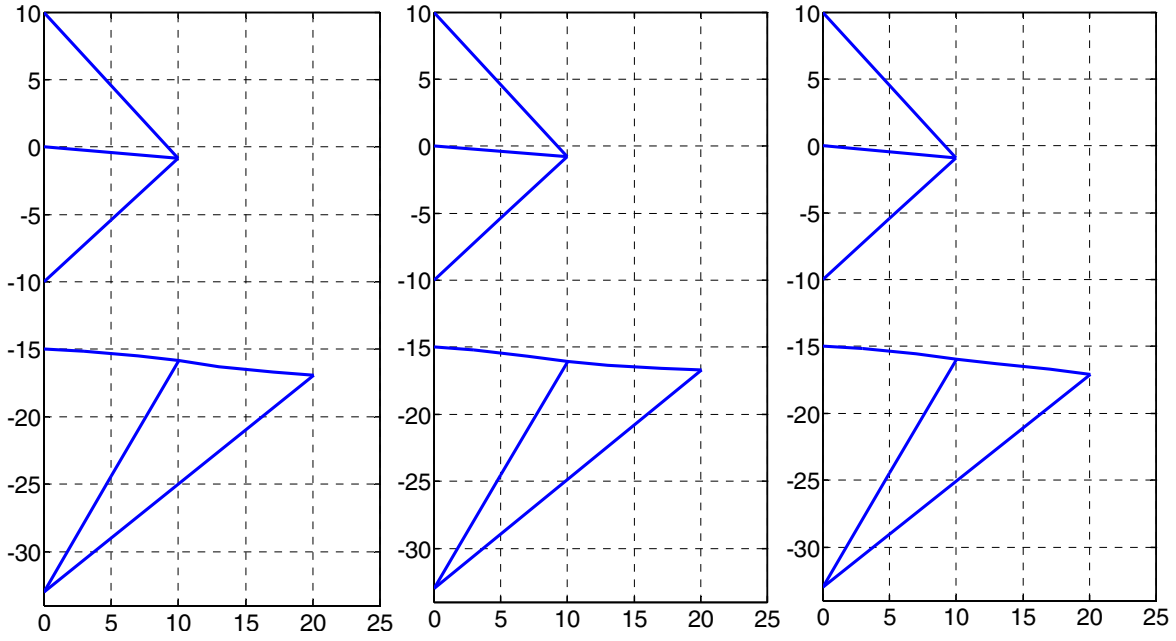

(a) Time = 9.5 sec (b) Time = 11.5 sec (c) Time = 14.5 sec

Fig. 6.10 Snapshots of benchmark structural model deformed shape (Cases 1 and 2).

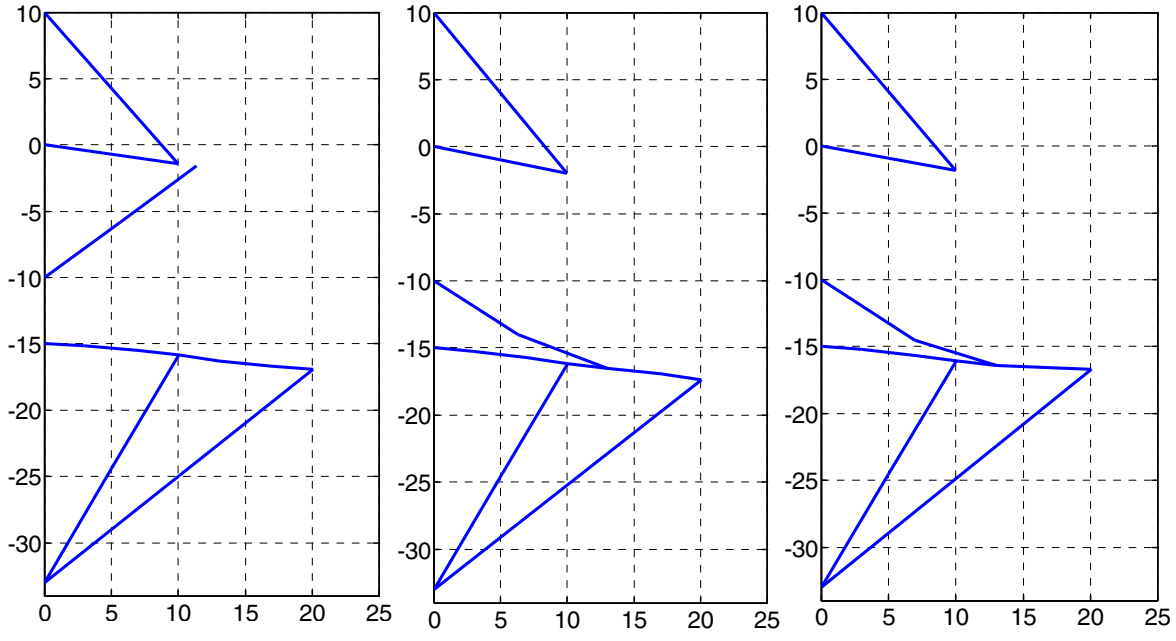

(a) Time = 9.5 sec (b) Time = 11.5 sec (c) Time = 14.5 sec

Fig. 6.11 Snapshots of benchmark structural model deformed shape (Case 3).

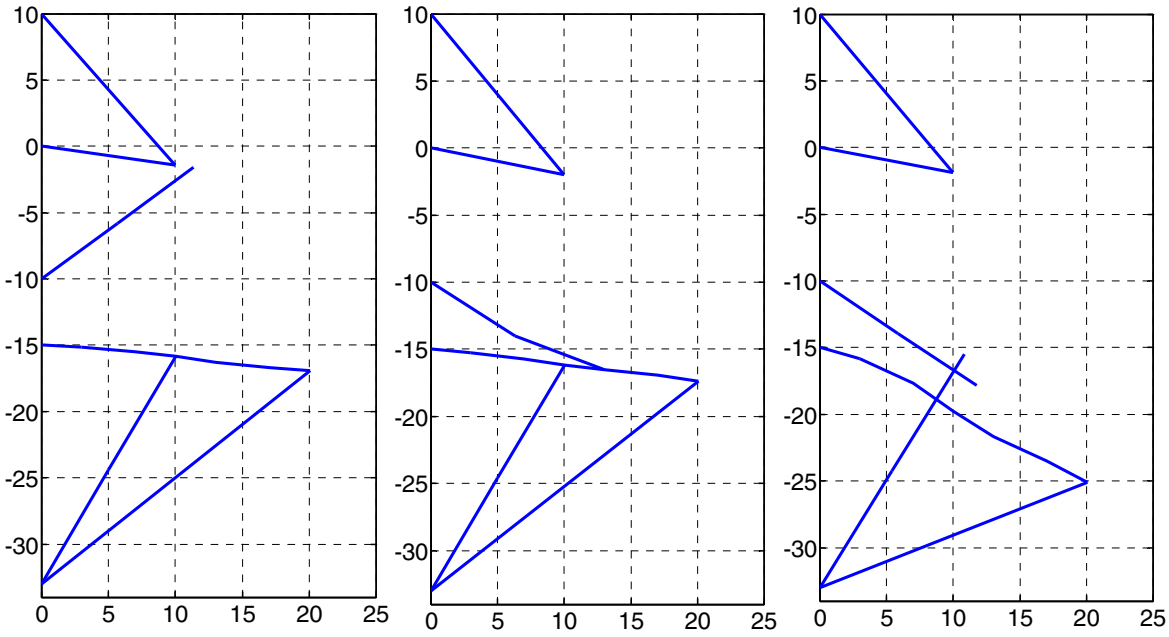

(a) Time = 9.5 sec (b) Time = 11.5 sec (c) Time = 14.5 sec

Fig. 6.12 Snapshots of benchmark structural model deformed shape (Case 4).

6.6 CRITERIA FOR ELEMENT REMOVAL

In the present report, two sets of element removal criteria are defined for two different modes of failure in seismically deficient and retrofitted RC columns. Moreover, these removal criteria, developed primarily for RC columns, are re-interpreted in order to be used as removal criteria for RC beams as well. In addition, a set of removal criteria based on maximum axial deformation is defined for truss members for use in constructing the benchmark problem discussed in the previous section. These criteria are explained in the following sections, with reference to OpenSees *Element* classes in which they are implemented. It is worth repeating that it is up to the analyst to decide which removal criteria to activate during the simulation. However, if an activated removal criterion is violated, the resulting criterion-dependent update to the structural system follows the courses defined in the following sections.

6.6.1 Removal Criteria for RC Beam-Columns due to Flexure-Axial Interaction

Two element removal criteria correspond to violating pre-set threshold values of damage indices reflecting the structural integrity of individual cross sections along the column length. Two damage indices have been defined in Section 3.3 for evaluating the damage state of confined RC cross sections. These damage indices are based on evaluating calibrated material-level damage indices for the constituent fibers and aggregating them over the cross section to minimize the arbitrariness in calibration. One of these damage indices, D_A, represents the degradation in the axial load-carrying capacity of the cross section. The other damages index, D_M, represents the degradation in the bending moment-carrying capacity of the cross section. These damage indices are currently implemented for *SectionForceDeformation* (hereafter referred to as *Section* for brevity) subclasses *ConfinedFiberSec* only.

When the value of D_A reaches its pre-defined threshold value, the associated *Section* object is considered to have lost its axial load-carrying capacity. As a result, the *Element* object that contains this *Section* object is removed from the *Domain* as previously discussed in Sections 6.2–6.4. This threshold value is defined by the analyst when constructing the corresponding *RemoveRecorder* object. In this report, this threshold value is suggested as

$$D_A = 1 \tag{6.2}$$

As a future extension, it is proposed that a threshold value that reflects the level of axial load P/P_o applied on the column can be developed, where P is the axial load in the RC column and P_o is the nominal cross-section axial force capacity under concentric compression.

When the value of D_M reaches its pre-defined threshold value, the associated *Section* object is considered to have lost its bending moment-carrying capacity. The consequences of reaching this threshold value depend on the function of the associated beam-column *Element* object in the structural system. In *Element* objects representing RC beams (i.e., horizontal structural members subjected to primarily bending moments and relatively low axial loads), reaching this threshold constitutes collapse and the *Element* object is removed from the *Domain* object as previously discussed in Sections 6.2–6.4. In *Element* objects representing RC columns (i.e., vertical structural members subjected to significant axial loads), the *Element* object is

redefined to release the rotational stiffness of its end-nodes. Subsequently, this *Element* object functions as a strut member supporting only the axial load after its end moments are released, until subsequent loss of the axial load-carrying capacity. In the applications conducted in this report, this latter model of collapse was not encountered in elements representing RC columns and thus the automation of this end moment-releasing procedure has not been fully implementation into OpenSees. In this report, this threshold value is suggested as

$$D_M = 1 \tag{6.3}$$

A relationship dependent on the nominal moment capacity is not proposed, since it is well-established that the loss of flexural capacity is controlled by the degree of deformation ductility and not the moment capacity, and that the moment capacity can continue to diminish while not being completely lost up to deformation levels much larger than those corresponding to any nominal cross-section moment capacity.

Several OpenSees *Element* classes are currently supporting the removal criteria discussed in the present section. These classes include force- and displacement-based distributed plasticity fiber elements, as well as force-based lumped plasticity beam-column elements, whose plastic hinge regions are defined using fiber-discretized *ConfinedFiberSec* objects.

6.6.2 Removal Criteria for RC Beam-Columns due to Shear-Axial Interaction

Two element removal criteria correspond to violating the limit curve equations corresponding to the drift-capacity model developed in Elwood (2002) (see Section 3.1). Recall that shear-axial coupled zero-length *Element* objects are constructed, and connected in series to a beam-column *Element* object in order to construct a compound beam-column element. When the axial limit curve is reached (Eq. 3.1) in the *LimitState* object defining the constitutive law of the coupled zero-length *Element* objects, this *LimitState* object is removed from the *Domain* object as previously discussed in Sections 6.2–6.4. Consequently, the connectivity between the associated beam-column *Element* object with the structural system is severed at one end-node. Optionally, when the shear limit curve is reached (Eq. 3.1) in the *LimitState* object, the consequences of reaching this shear limit curve in beam-column *Element* objects representing RC beams constitute collapse and the *LimitState* object is removed from the *Domain*, severing the

associated beam-column *Element* object's connectivity to the structural model. Hence, shear-damaged RC columns are allowed to maintain their axial load until they reach the axial load-lateral drift capacity limit state, while shear-damaged RC beams can be made to collapse in a brittle manner in the absence of a compressive axial force that prevents the shear cracks from propagating.

OpenSees *Element* classes which currently support these removal criteria include zero-length elements whose constitutive law is defined using *LimitState* classes. These zero-length elements can be connected to all inelastic as well as elastic beam-column elements in OpenSees to model their shear-axial interaction behavior (Elwood 2002).

6.6.3 Removal Criteria for Truss Members

Two element removal criteria correspond to violating maximum (positive) or minimum (negative) axial deformation values. When the axial deformation (related to the computed axial strain in the *UniaxialMaterial* object associated with the *Element* object representing the truss member) reaches one of the maximum or minimum threshold values defined by the analyst, the *Element* object is removed from the *Domain*, as previously discussed in Sections 6.2–6.4. The choice of these threshold values enables modeling both brittle and ductile truss member behavior prior to collapse.

OpenSees *Element* classes that currently support these removal criteria include truss elements following linear and nonlinear geometry. The constitutive behavior of these elements is defined using either a single *UniaxialMaterial* object or a pre-defined *Section* object, typically of the *FiberSection* or *ConfinedFiberSec* subclasses to take advantage of fiber discretization.

6.7 SUMMARY

In this chapter, a detailed survey of the limited literature on progressive collapse simulation was conducted. Previous analytical formulations to account for the removal of a load-carrying structural element from a structural model during an ongoing simulation were presented. These formulations utilized force equilibrium, DOF condensation, or energy balance approaches to

account for dynamic load redistribution from collapsed finite elements, and the resulting impact from collision between the collapsed element and the damaged structure.

An analytical formulation was developed based on the dynamic equilibrium of forces to account for abrupt element removal and to simulate the dynamic redistribution of forces using the resulting transient change in structural system kinematics. The analytical formulation was complemented by discussion of the resulting effects on the numerical behavior and potential changes to the numerical solution procedure of the dynamic equilibrium equations. This analytical procedure was formalized into a logical algorithm that separately accounts for collapsed element removal and for potential collision. The majority of the algorithm was implemented and compiled as a new class within the software platform OpenSees. The remaining components of the algorithm were implemented using the programmable input language (Tcl) which is used to construct simulation applications for OpenSees. This dual implementation approach automates the critical parts of the progressive collapse analysis yet provides the analyst enough flexibility to set removal-dependent solution parameters at runtime (e.g., adaptive time-stepping).

The implemented algorithm was computationally verified using a benchmark structural system of trussed cantilever beams. Four case-study simulations of the benchmark structural system highlighted the sensitivity of the progressive collapse process to the uncertainty in structural system parameters, represented by the chosen threshold values for element removal criteria. These criteria reflected the effect of ductile versus brittle detailing of structural members and joints, as well as uncertainty in the material properties used (and hence, while not explicitly investigated, applied loads). Given the observed results, it is recommended that this sensitivity be evaluated beforehand for the unknown structural system parameters and reduced by conducting progressive collapse simulations using statistical evaluation methods within a probabilistic framework. The chapter was concluded by introducing the element removal criteria used for determining mode-dependent (shear or flexure) axial-load collapse in seismically deficient and retrofitted RC columns, RC beams, as well as in brittle and ductile truss members.

7 Progressive Collapse Simulation: Applications to RC Structures

In this chapter, two test-bed structural systems are constructed and presented. Each test-bed structural system consists of RC moment-resisting frames, infilled with URM wall(s) in one or more bays. Hence, both test-bed structural systems are examples of RC frame/URM wall construction. In addition, the columns of the RC frames contain seismically deficient reinforcement details. These two test-bed structural systems are a one-story multi-frame building and a five-story multi-bay frame building. The test-bed structural systems are used to conduct three application studies of progressive collapse assessment using the methodology, structural component models, and element removal algorithm developed and implemented in the previous chapters of this report, hereafter collectively referred to as the computational developments. These three applications studies are designated as follows:

1. Application A: Deterministic progressive collapse simulation of a one-story RC frame/URM wall system;
2. Application B: Sensitivity analysis of progressive collapse in a five-story RC frame/URM wall system;
3. Application C: Probabilistic progressive collapse assessment of a one-story RC frame/URM wall system.

The objective of application A is to investigate the performance of aggregating the aforementioned computational developments in modeling progressive structural collapse in a moderately complex structural system, which includes URM wall-RC frame interaction and seismically deficient RC column details leading to multiple modes of gravity-load collapse (i.e., flexure-axial and shear-axial). The one-story structural system is selected for two reasons: (a) to take advantage of existing experimental data from a similar physical model previously subjected

to shake-table seismic excitation at the University of California, Berkeley, and (b) to render the analysis of the results more transparent by considering a single DOF in the lateral direction and thus excluding the dynamic effects of higher modes of vibration. Application A compares the simulated dynamic response and mechanism of progressive collapse in the structural system to two intensity levels of the same ground motion (i.e., acceleration) record.

The objectives of application B are to simulate the progressive collapse response of a more complex multi-story structural system located at a given geographic location during a specified seismic event, and to investigate the sensitivity of the global response variables to assumed uncertainties in selected system parameters, e.g., material properties, and in ground motion intensity measures, e.g., spectral acceleration, representing an uncertain seismic hazard level. The progressive collapse response of the test-bed structural system is first investigated using a set of reference uncertain parameter values to establish a reference set of simulated response variables, e.g., the time at incipient collapse. Next, a parametric study is performed to conduct a deterministic sensitivity analysis.

The objective of application C is to investigate the effect of uncertain measures of ground motion intensity, e.g., PGA, and characteristics, e.g., orientation, on the probability of predicting progressive collapse in the one-story structural system defined in application A. An empirical probability of collapse is defined and utilized to construct fragility curves representing four limit states of structural collapse, namely in-plane and out-of-plane collapse in the URM wall, and partial and complete gravity-load collapse of the structural system. The fragility curves represent the conditional probability of reaching the corresponding limit state, during simulations using ground motions of random characteristics, given the uncertain measure of ground motion intensity at a specific hazard level. The hazard level is defined by the probability of the associated intensity measure being exceeded at the building site location in a 50-year period. Fourteen ground motion records from the same seismic event are utilized in application C. These are selected in order to reflect the uncertainty in ground motion characteristics due to site location and building orientation, i.e., intra-event variability..

In all three applications A, B, and C, a building site location is assumed in Los Angeles County at a latitude and longitude of 34.3 and -118.5, respectively. The selection of the building site is discussed in Section 7.3.

7.1 APPLICATION A: DETERMINISTIC PROGRESSIVE COLLAPSE SIMULATION OF ONE-STORY RC FRAME/URM WALL SYSTEM

A one-story, seismically detailed structure consisting of three moment-resisting RC frames of identical dimensions and reinforcement, placed parallel to each other and connected by a RC slab and transverse RC beams, was previously constructed and subjected to predetermined ground motion records of increasing intensity using a shake- table. The middle RC frame was infilled with a URM wall prior to testing. The objective of the experiment was to establish the structural contribution and interaction of "non-structural" URM walls in structural systems where the RC frames have been designed to single-handedly resist the lateral loads during seismic events, and to calibrate a SAT model for representing the behavior of URM walls in RC frames. Another important objective of the experimental study was the assessment of lateral force distribution among the two bare RC frames and the infilled RC frame and the redistribution of the lateral force upon the damage and eventual collapse of the URM wall. Complete details of this experimental study are documented in Hashemi and Mosalam (2007).

In the next section, the geometry, material properties, and relevant details of the physical model are presented. Next, a FE computational model of the physical model described in Hashemi and Mosalam (2007) is constructed and calibrated using data from the shake-table experiments. Subsequently, the FE model is artificially modified to introduce seismically deficient reinforcement details in the RC columns. This modified FE model represents the test-bed structural system used in application A. The test-bed structural system is subjected to scaled ground motion records (N-component) from Lamont 375 station, of the moment magnitude $M_w = 7.2$ earthquake that struck Düzce, Turkey, in November, 12, 1999. For two different intensity levels, the collapse sequence and mechanisms are identified. In addition, time-history results representing the simulated dynamic behavior in terms of lateral displacement, base-shear force, and fundamental period of vibration are presented and discussed.

7.1.1 Details of Shake-Table Test-Structure and Experimental Observations

Figure 7.1a illustrates the physical model of the one-story structural system investigated in Hashemi and Mosalam (2007). The structural system consists of three one-bay moment-resisting

RC frames arranged in parallel to resist the lateral loads, and infilled with URM wall in the middle frame. URM Infill walls are more commonly located on the perimeter of a building, but in Hashemi and Mosalam (2007), the URM infill wall is situated in the center due to concerns about the shake-table capacity and the undesirable torsional mode of deformation in the test structure resulting from possible non-simultaneous failure of perimeter walls. The dimensions used in the physical model represent a 75%-sclae of typical dimensions due to the limitation of the shake-table size. Accordingly, the three RC frames are 4115 mm wide and 3219 mm high, arranged at 1830 mm spacing. The columns are square in cross section with 305 mm side width, eight 19 mm diameter longitudinal steel bars, and four branches of 10 mm diameter ties at 95 mm spacing over 610 mm from the faces of the joints and 152 mm spacing elsewhere. One concentric unbonded longitudinal steel rod of 32 mm diameter was installed along each column prior to casting. Prior to shake-table testing, these unbonded steel rods were each post-tensioned to apply an axial force of 290 kN and 145 kN on individual columns of the infilled and bare RC frames, respectively. The longitudinal beams are 267 mm wide and 343 mm deep with three 19 mm diameter steel bars on each side and 10 mm diameter closed stirrups at 70 mm spacing over 711 mm from the face of the beam-column joint and 203 mm spacing elsewhere. The middle frame is infilled with a URM wall 102 mm thick. Four transverse beams connecting the frame corners are 229 mm wide and 305 mm deep with two 19 mm diameter steel bars on each side and 10 mm diameter closed stirrups at 305 mm spacing. The three frames are connected at the top by a RC slab 95 mm thick, reinforced by a double-layer mesh of 10 mm diameter steel bars with 305 mm spacing. The slab extends outside the perimeter beams by 229 mm in each direction.

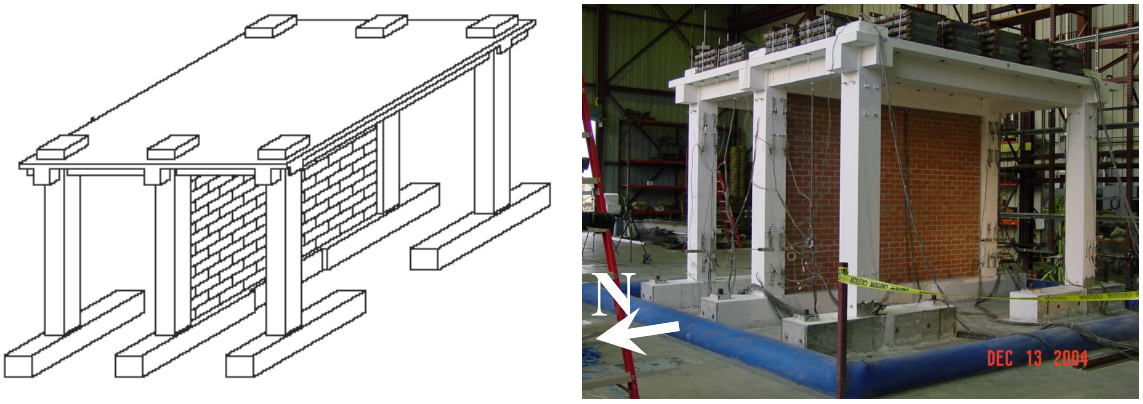

(a) 3D layout (b) Shake-table setup

Fig. 7.1 Shake-table test structure geometry and setup (Hashemi 2007).

The dimensions and reinforcement of structural members of the physical model are summarized in Table 7.1. The nominal yield stress of the 19-mm bars is 458 MPa. The specified 28-day compressive strength of the standard concrete cylinder is 31 MPa, and the split-tension strength is 3.0 MPa. The masonry wall is made of clay bricks with modular size of 102×203×68 mm, whose average 28-day compressive strength of the standard masonry prism is 17 MPa. The average shear strength for constructed masonry panels 102-mm thick is 1.81 MPa. Material properties are summarized in Table 7.2. Additional lead weights totaling 320.0 kN were uniformly distributed on the RC slab. Figure 7.1b presents a photograph of the test structure prior to shake-table testing. The physical model was experimentally tested under unidirectional seismic excitation in the north direction as indicated by the arrow labeled "N" in Figure 7.1b.

Table 7.1 Geometry and details of shake-table test structure (Hashemi 2007).

Structural member	Dimensions [mm]	Main reinforcement	Transverse reinforcement (closed stirrups)
Slab	95	10-mm bars @305 mm t&b*	Not applicable
Column	305×305	8 19-mm bars 32-mm post-tensioned rod	10-mm @ 95 mm over 610 mm from column face, then @152 mm
Longitudinal beam	267×343	3 19-mm bars t&b*	10-mm @ 70 mm over 711 mm from column face, then @203 mm
Transverse beam	229×305	2 19-mm bars t&b*	10-mm @ 305 mm
Footing	457×356	4 22-mm bars t&b*	10-mm @ 102 mm
URM wall	102	Not applicable	Not applicable

* top and bottom

Table 7.2 Material properties of shake-table test structure (Hashemi 2007).

Material property	Value
Concrete f_c' [MPa]	31.0
Concrete f_t' [MPa]	3.0
Concrete cover [mm]	15
Steel σ_y [MPa]	459
Steel σ_u [MPa]	600
Steel E_s [GPa]	210
Steel E_{sh} (assumed)	1.0% E_s

Figure 7.2 demonstrates the instrumentation used to measure the quantities representing the global response of the test structure. Eleven accelerometers were used to measure the acceleration response of the slab (7 longitudinal, 3 transversal, and one vertical). Three additional accelerometers (longitudinal, transversal, vertical) were installed at the base of the URM wall. Eight displacement transducers were used to measure the displacement of the roof slab (five transducers) and the shake table (three transducers) relative to the stationary ground. Another eight transducers were used to measure the relative in-plane displacements within the

roof slab. In addition to global response measurements, 75 displacement transducers (measuring diagonal wall and frame deformations, gap opening and sliding between the URM wall and the adjacent frame, and average curvature profile along column lengths) and 78 strain gages (installed on embedded reinforcing steel bars) were monitored in every shake-table experiment.

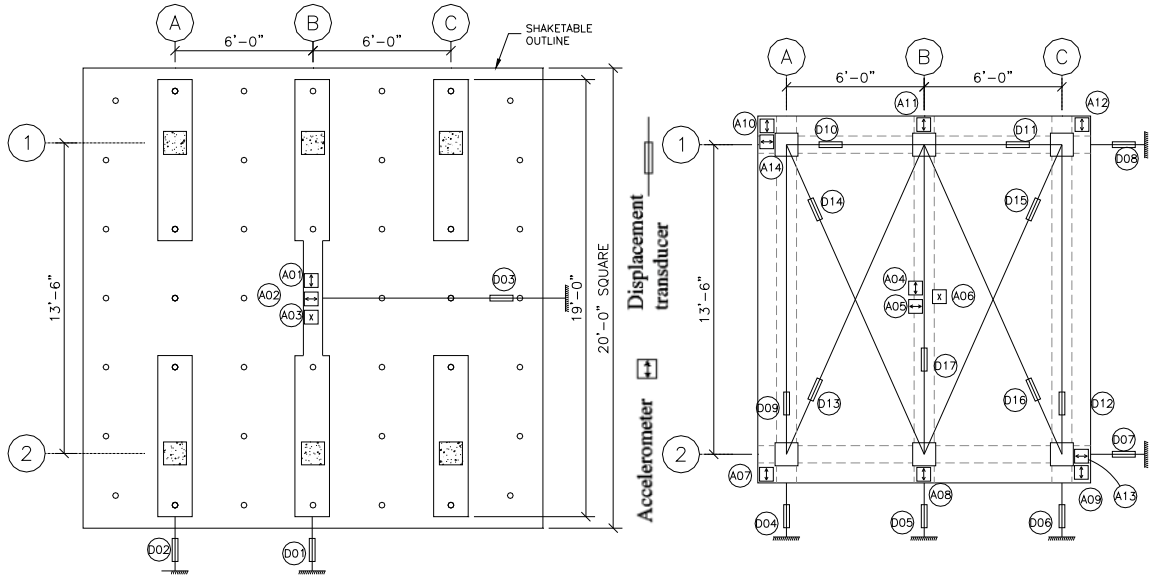

(b) Foundation plan (b) Roof plan

Fig. 7.2 Shake-table test structure instrumentation (Hashemi 2007).

The test structure was subjected to scaled ground motion records from Loma Prieta (1989), Northridge (1994) and Düzce (1999) earthquakes. The record intensities were scaled to represent decreasing probabilities of being exceeded in 50 years. The higher scale factors were limited by the shake-table capacity. The peak ground acceleration ranged within the experimental program from 0.27g to 1.93g. The behavior of the test structure exhibited an initial stiff response, which was expected due to the presence of the URM wall. At low excitation levels, the initial lateral stiffness was approximately 70 kN/mm, the fundamental vibration period was 0.135 sec, and the energy-equivalent damping ratio was approximately 4.3%. With the increase of the ground motion scale and damage to the URM wall, the stiffness decreased, while the fundamental vibration period and the damping ratio increased. The URM wall ultimately collapsed due to corner crushing of individual bricks and inclined cracks advancing from the corners inwards (at 45° to 60° from the vertical axis). Upon URM wall collapse, flexural cracks

had started to appear at the beam-column joints, lateral stiffness had decreased to approximately 30 kN/mm, while the fundamental vibration period and the damping ratio increased to approximately 0.180 sec and 11%, respectively. During the shake-table application of the ground motion level corresponding to complete disintegration and subsequent removal of the URM wall, these values have reached approximately 10 kN/mm, 0.400 sec, and 13%, respectively.

One major concern of the structural system investigated in Hashemi and Mosalam (2007) was the behavior of the test structure following failure in the stiff URM wall. The failure of the URM wall at the corners due to crushing of the URM and the resulting redistribution of horizontal forces to columns of the infilled RC frame in a short transfer length created a short-column situation which is vulnerable to shear failure if inadequate transverse reinforcement was provided in the RC columns. In the experimental study, the columns of the infilled RC frame showed higher levels of distress than the columns of the bare frames but continued to perform mainly in a flexural mode without exhibiting signs of shear failure. After URM wall removal, significant flexural cracks spread along most of the column lengths, and the lateral stiffness of the structural system decreased significantly, but the columns maintained their vertical load-carrying capacity, and finally the test had to be stopped due to excessive damage at the column-footing joints.

7.1.2 Construction and Calibration of FE Model for Shake-Table Test Structure

A FE model is constructed using OpenSees and calibrated to match the dynamic behavior of the shake-table test structure. An idealized FE model outline in Figure 7.3 presents an overview of the model designations for referencing during further discussion of member numerical idealization in the following paragraph. The FE model consists of displacement-based beam-column elements with fiber-discretized cross sections to represent the RC frame members C1 through C6 and B1 through B3. The URM wall is idealized using two struts S1 and S2, which are modeled using compression-only truss elements. Elastic truss elements (shown in dashed lines in Fig. 7.3) are used to model the in-plane behavior of the RC slab. Coupled springs (not shown) at the base of the infilled frame's columns C3 and C4 are used to model shear-axial interaction. Elastic beam-column elements are used to model beams B4–B7.

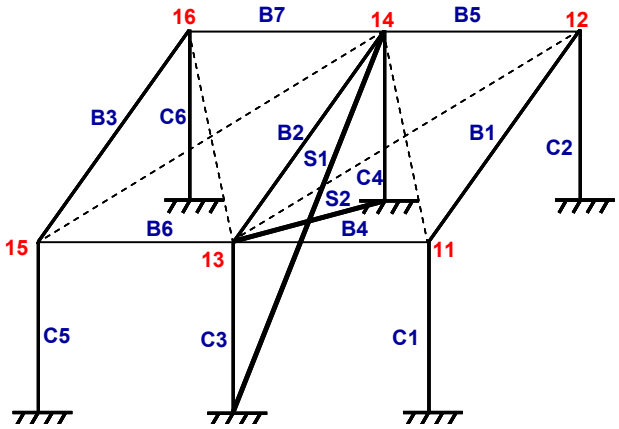

Fig. 7.3 FE model abstraction of shake-table test structure.

The element meshing of the bare RC frame C1-B1-C2 is illustrated in Figure 7.4. Nodes 1 and 2 are restrained from all translations and rotations. All beam-column elements use displacement-based distributed plasticity formulation with fiber-discretized cross sections (Filippou and Fenves 2004). The beam-column elements used to represent the plastic hinge zones of columns C1 and C2, namely elements 111, 113, 121, and 123 in Figure 7.4, have a length of 366 mm each (Eq. 5.1). Two Gauss numerical integration points are used along the length of each of these elements. With reference to Chapter 4, the cross section of these elements is discretized using *ConfinedFiberSec2D* with a grid of 10×10 *ConfinedConcrete* layers of fibers for the core concrete and 2 extra layers of fibers in each direction for the cover concrete (with confining stress set to zero for the latter fibers). The longitudinal steel is modeled using buckling-enabled *SteelRebar* fibers with bar mechanical stress-strain relationship according to Menegotto and Pinto (1973). The transverse reinforcement is modeled using a bilinear material model. A confinement efficiency factor of 0.75 is estimated according to Mander et al. (1988) for the square shape of the cross section with four stirrup branches (one square tie and one diamond tie) relative to the circular shape. The beam-column elements at the interior of the columns, namely elements 112 and 122, are modeled using nine Gauss numerical integration points each and cross-section discretization identical to that of their neighboring elements representing the plastic hinge zones. However, since experimental observations showed no damage or tie fracture taking place in the RC frames away from the column ends, the steel bars are assigned the

material model from Menegotto and Pinto (1973) with bar buckling disabled for computational efficiency. Similarly, a constant confining stress equal to that computed assuming yielding of the transverse ties is preset and applied to the core concrete fibers.

The beam-column elements used to represent the plastic hinge zones of beam B2, namely elements 101 and 103 in Figure 7.4, have a length of 303 mm each (Eq. 5.1). Two Gauss numerical integration points are used along the length of each of these elements. Along with element 102, the cross sections of elements 101 and 103 are discretized using a layered mesh of 5×10 *ConfinedConcrete* fibers for the core concrete (10 layers parallel to the bending axis) and one extra layer of fibers in each direction for the cover concrete. According to the recommendations of ACI (2002), a 1030-mm effective width of the RC slab was considered in resisting compressive stresses and meshed using one layer of *ConfinedConcrete* fibers with confining stress set to zero. Since no damage or stirrup fracture is experimentally observed in the beams, the confining stress for the core fibers is estimated assuming yielding of the transverse stirrups and preset during the analysis. The meshing of the other bare frame, C5-B3-C6, is similar to the present frame. In the other bare frame, columns C1 and C2 are replaced by C5 and C6, and the last and second digits in the respective node and element numbers shown in Figure 7.4 are changed from 1 and 2 to 5 and 6, respectively. Similarly, beam B1 is replaced by B3, and node numbers 101 and 102 are changed to 107 and 108, while element numbers 101, 102, and 103 are changed to 107, 108, and 109, respectively.

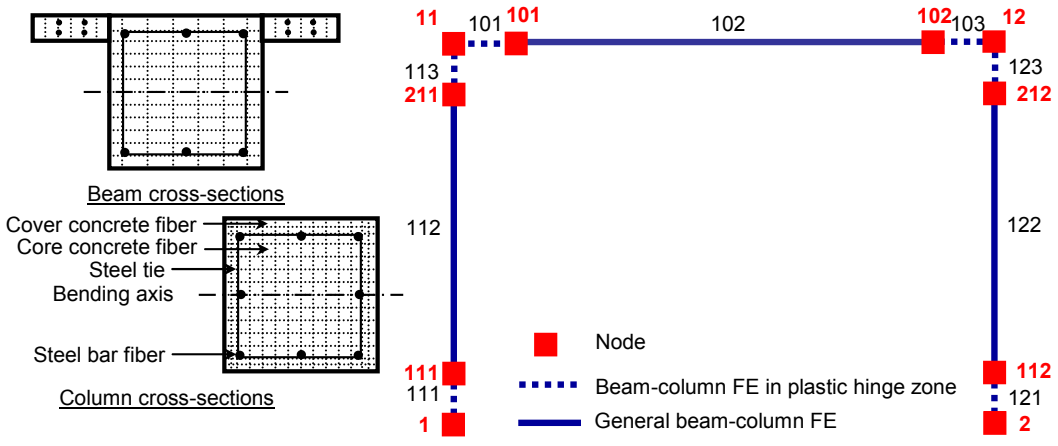

Fig. 7.4 FE mesh of one-story test-bed structure (bare frame).

The element meshing of the URM-infilled frame C3-B2-C4 is illustrated in Figure 7.5. Nodes 3 and 4 are restrained from all translations and rotations. Nodes 30 and 40, located at the same respective locations of nodes 3 and 4, are plotted separately for clarity. The elements and nodes corresponding to those of the bare frame are similar to those described in the previous two paragraphs. The URM wall is modeled using the two truss elements 1003 and 1004 to represent the struts S1 and S2 idealized in Figure 7.3. The axial force-deformation behavior of these truss elements is represented by *Concrete01*, a concrete-like material in OpenSees (Mazzoni et al. 2004) with a parabolic pre-peak behavior in compression, linear post-peak behavior, and no tensile capacity, as illustrated in Figure 7.5. The parameters for this stress-strain curve were calibrated in Hashemi and Mosalam (2006) from experimentally measured material properties and are reported as $\varepsilon_{mo} = 0.0028$, $\varepsilon_{mu} = 0.0042$, $f_{mo} = 17$ MPa, and $f_{mu} = 2$ MPa, corresponding to a strut member area of 223 mm^2. The zero-length elements 130 and 140 representing shear-axial interaction in the potential short columns forming as a result of URM wall partial collapse are constructed using *LimitState* material (Elwood 2002) to define shear and axial limit surfaces (see Section 3.1).

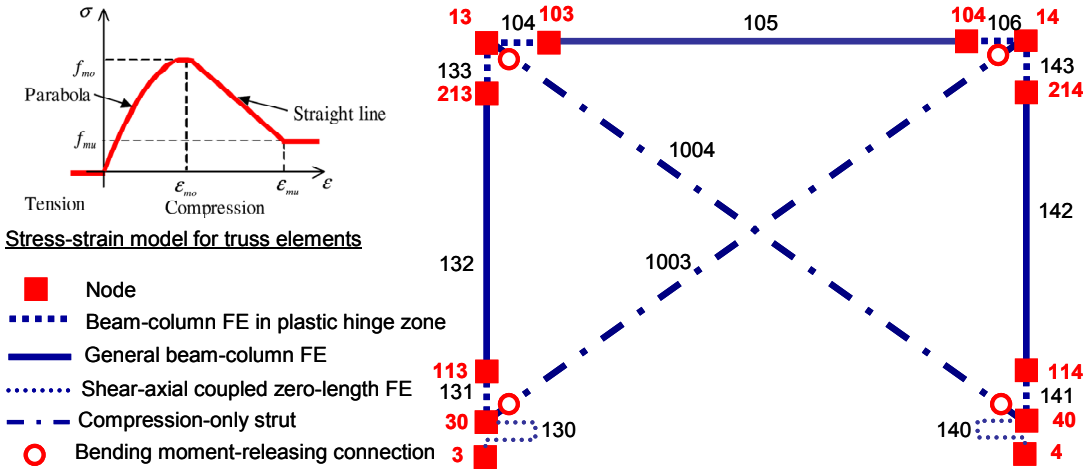

Fig. 7.5 FE mesh of the one-story test-bed structure (infilled frame).

The transverse beams B4 through B7 and the RC slab connecting the top of the three frames were not observed to exhibit significant signs of damage besides flexural cracking during the shake-table tests. Therefore, the flexural stiffness is modeled using elastic beam-column elements connecting nodes 11 to 13, 13 to 15, 12 to 14, and 14 to 16 (see Fig. 7.3). The flexural stiffness of these beam-column elements is computed assuming a 1000-mm effective width of the slab contributing to the beam cross section with 0.7 times the uncracked concrete Young's modulus of elasticity (ACI 2002). Note that the aspect ratio of the RC slab is 2.25:1 which means that its vertical loads will be transferred in a one-way path perpendicular to the RC frame orientation. The in-plane stiffness of the RC slab is modeled using elastic truss elements connecting nodes 11 to 14, 12 to 13, 13 to 16, and 14 to 15 (see Fig. 7.3). During the shake-table experiments, the vertical loads on the RC slab remain approximately constant, while the in-plane shear forces change as a result of the applied lateral loads due to the shake-table acceleration and the different stiffness between the bare and infilled RC frames. The in-plane stiffness of the RC slab is computed as a shear panel deforming under applied shear forces and used to calibrate the equivalent truss elements. The in-plane shear stiffness is observed in Hashemi and Mosalam (2007) to remain approximately constant throughout the shake-table experiments, and can be estimated from the published results as equal to 406.0 kN/mm. Assuming linear geometric transformation of displacement and force components in the plane of the RC slab leads to equivalent truss elements of stiffness 243.15 kN/m each.

The post-tensioning loads on the columns are applied as external nodal forces at nodes 11 through 16. Each frame is assumed to be responsible for a tributary area of the RC slab gravity load equal to one half of the RC frame spacing on each side, with the infilled frame carrying twice as much gravity load as the bare RC frames. The distributed masses and gravity loads from the structural elements are lumped at their end-nodes. Co-rotational geometric transformation is used for all elements (Crisfield 1990). The numerical time integration is performed using the Newmark β-method assuming constant acceleration during each time step (Newmark 1959). Based on snap-back test results in Hashemi and Mosalam (2007), a stiffness-proportional viscous damping ratio $\zeta = 0.045$ is assumed to exist in the fundamental mode of vibration (Chopra 2001). The stiffness matrix considered in computing the damping matrix is computed as the mean of the initial stiffness matrix and that of the last converged analysis step. The reason for

selecting this is to avoid rapid numerical reduction in viscous damping with the spread of structural damage and the corresponding decrease of global stiffness.

The FE model's estimation of the fundamental vibration period is 0.121 sec, compared to an experimentally recorded value of 0.135 sec. This 10.4% difference can be attributed to the development of shrinkage cracks in the test structure that are absent from the FE model. However, the FE model reasonably reproduces the force-displacement time histories of the test structure at levels of ground motion up to and including collapse of the URM wall. Example results from the model calibration study are demonstrated in Figure 7.6. The input ground motion used for exciting the shake-table test structure was recorded during the 1994 Northridge earthquake (Tarzana station in the 90° direction) and scaled to PGA = 0.61g. The ground motion record used as input in the FE simulation is the output (i.e., filtered) acceleration signal from the shake table as measured by the built-in accelerometers in the driving actuators instead of the input command signal to the shake table, and is illustrated in Figure 7.6a. The experimentally observed and computationally simulated displacement time-histories of the roof, measured at the middle frame in the shaking direction, are compared in Figure 7.6b. It can be observed that the FE model results demonstrate general agreement with the experimental results, while underestimating the maximum displacement response (5.26 mm simulated compared to 6.56 mm observed, i.e., 19.8% error) and generally exhibiting smaller displacement magnitudes. This discrepancy is attributed to the tensile strength assigned to the concrete material model, and its effect on the initial stiffness of the FE model during the simulation, as compared to the test structure that had already been partially cracked due to shrinkage and more importantly previous shaking conducted on it before this level of shaking of PGA = 0.61g

To investigate the role of concrete tensile strength, the FE simulations are repeated with the concrete tensile strength ignored, hypothetically assuming fully cracked cross sections prior to shake-table testing. The computationally simulated (with concrete tensile strength set to zero) and experimentally observed displacement time-histories of the roof are compared in Figure 7.6c. It can be observed that ignoring the tensile strength of concrete leads to an improved estimate of the maximum lateral displacement (5.89 mm simulated compared to 6.56 mm observed, i.e., 10.2% error) and a closer agreement in displacement values during the early interval of the dynamic response before the PGA has been reached (i.e., at time values smaller

than 8 sec), which suggests that some cracking had pre-existed in the physical model due to prior shake-table tests performed at lower seismic intensity levels. However, ignoring the tensile strength of concrete results in overestimating the lateral displacement magnitude in the rest of the record after the PGA has been reached (i.e., at time values larger than 8 sec), since the absence of tensile strength results in less dissipation of hysteretic energy through inelasticity (i.e., material damping). Such hysteretic energy dissipation would have been caused by the advancement of cracks and subsequent softening in previously uncracked concrete fibers due to the stronger shaking and higher deformation demands experienced during the present—higher—seismic intensity level.

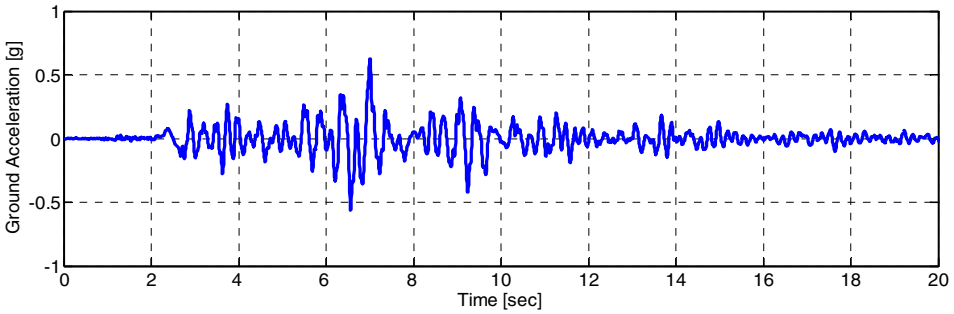

(a) Input (filtered) ground motion scaled from Northridge earthquake (Tarzana station, 90° direction, PGA = 0.61g)

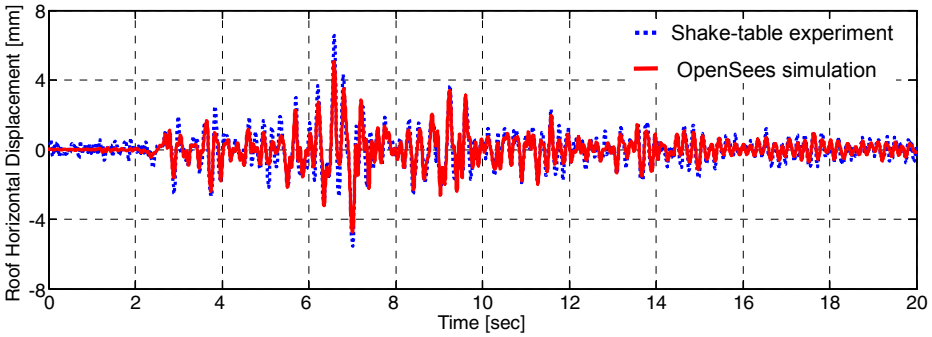

(b) Roof displacement history with concrete tensile strength included in FE model

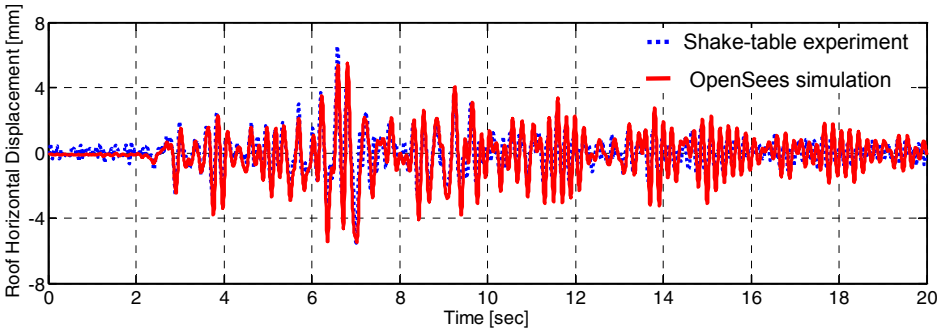

(c) Roof displacement history with concrete tensile strength ignored in FE model

Fig. 7.6 Simulated and experimental test data of shake-table test structure.

7.1.3 Modified FE Model for One-Story Test-Bed Structural System

After calibration, the FE model of the shake-table test structure is artificially weakened by introducing seismically deficient details in individual RC columns where plastic hinges are expected to form. The transverse tie spacing is increased to 150 mm, which is half the least column dimension, the maximum value allowed by the ACI building code used in 1960s' construction (ACI 1963). This increased transverse tie spacing makes the longitudinal bars more susceptible to bar buckling. In addition, it makes columns C3 and C4 more susceptible to the formation of a short-column mechanism following URM wall partial collapse, leading to shear failure and subsequent collapse in a shear-axial mode. Lap-splices are inserted at the column-footing level of columns C5 and C6 in order to observe the resulting difference in RC frame response and prevent simultaneous (non-progressive) collapse of the otherwise-symmetric bare frames. The length of the lap-splice is 20 times the bar diameter which meets the minimum requirements of 1960's construction (ACI 1963) and is deemed inadequate according to current standards (ICC 2003). In the applications presented in this chapter, the strut elements representing the URM wall are assumed to collapse in a brittle manner and are removed upon softening to $0.75 f_{mo}$, representing a case of brittle URM wall collapse.

Preliminary analysis indicated that columns C3 and C4 are likely the first columns to axially collapse—almost simultaneously—and therefore the transverse beams B4–B7 will experience large deformations as a result of the axial load from the collapsed columns being redistributed to the intact four corner columns C1, C2, C5, and C6. It is likely that these beams will be subjected to excessive transverse (vertical) displacements leading to crushing of concrete in compression and subsequent loss of bending moment capacity. However, due to the continuity of the longitudinal steel bars along the full length of these beams, they will subsequently act as catenaries supporting the vertical load through the action of inclined resisting axial forces in a manner similar to inclined cables until the longitudinal steel fractures. In addition, the catenary beams' capacity to support vertical loads will exhibit a hardening response with the increase of transverse displacement due to the increase in inclination angle and thus become more capable of carrying higher vertical component of the resisting axial force.

In order to model the effect of the large-displacement behavior of beams B4 through B7 as discussed above, an independent FE simulation has been conducted separately of the modified FE model. The geometric setup of the latter FE simulation is illustrated for beams B4 and B6 in Figure 7.7a, which shows a side view of the modified FE model with the elements and nodes representing the model after column C3 has been removed. A monotonic downward displacement is imposed at node 13. Beams B4 and B6 are modeled using a total of 12 displacement-based fiber-discretized beam-column elements with five Gauss integration points each. The cross-section discretization is similar to that of the beam cross section illustrated in Figure 7.4. Co-rotational geometric transformation is used. The reinforcing steel fracture strain is assumed equal to 0.130 as a typical value, since it was not reported in Hashemi and Mosalam (2007). The simulation is performed under displacement control to compute the relationship between the downward displacement at node 13 and the vertical reaction at node 1 which represents one half of the applied vertical load required at node 13.

This relationship as predicted by the OpenSees simulation is illustrated in Figure 7.7b. The simulated response reaches the moment capacity at a vertical reaction force of 244.5 kN and a displacement of 22.25 mm, and softens due to crushing of RC fibers (exhibiting a brief numerical irregularity) to a vertical reaction of 164.5 kN at a displacement of 36.6 mm, and then starts to exhibit hardening at an increasing rate through catenary action as the inclination angle increases nonlinearly with the downward displacement until fracture is predicted in the longitudinal steel at a vertical reaction of 449.8 kN and a displacement of 486.2 mm. In order to be used with the modified FE model described earlier in this section, this relationship is idealized by a multi-linear envelope defined by the force coordinates of 245 kN, 150 kN, and 450 kN at the corresponding displacement coordinates of 20 mm, 45 mm, and 490 mm.

Four nonlinear spring elements are used to represent the idealized envelope in Figure 7.7b. Each of these nonlinear spring elements is then defined to describe the relationship between the vertical DOFs at the end-nodes of each transverse beam B4 through B7 and attached to each beam's end-node nearest to nodes 13 and 14. Prior to removal of column C3 (or C4), the behavior of these nonlinear springs is in the linear-elastic range (i.e., downward displacement less than 20 mm). Following the removal of column C3 (or C4), no significant load reversal is expected in these nonlinear springs due to the vertical load they are required to transfer to the

intact columns. Momentary load-reversal, if any, follows the initial stiffness. Reaching a downward displacement of 490 mm constitutes the element removal criterion for these nonlinear springs. The transverse beams are considered axially rigid perpendicular to the RC frames, since only a two-dimensional excitation of the FE model is conducted (in-plane with the RC frames).

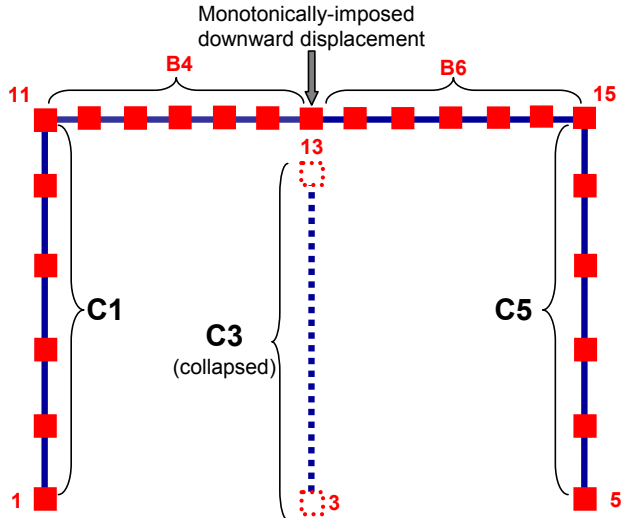

(a) Problem setup and boundary conditions

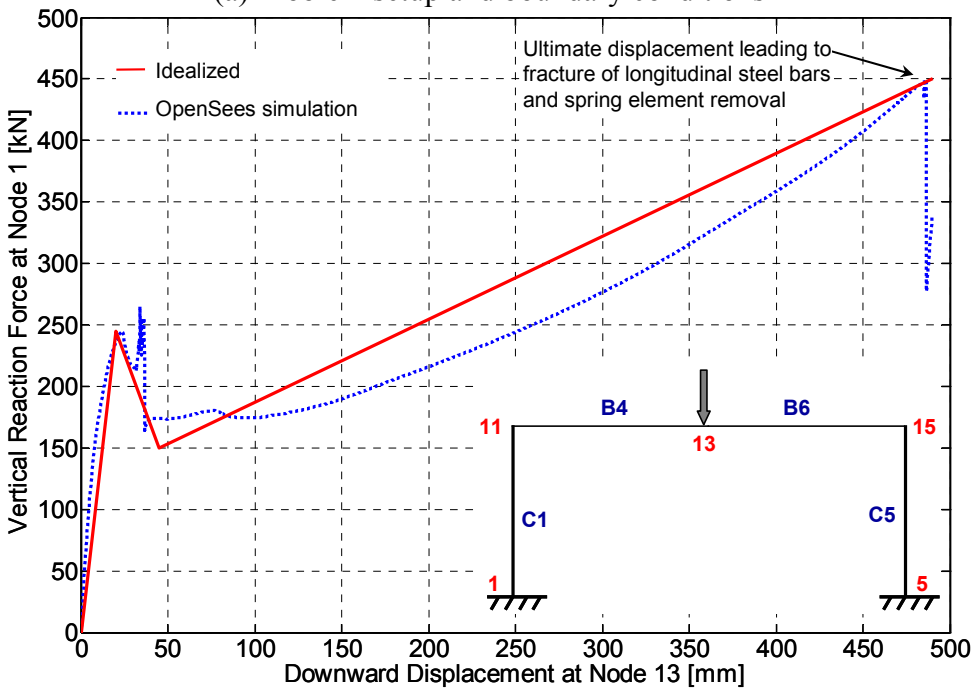

(b) Simulated and idealized force-displacement response

Fig. 7.7 OpenSees simulation of large-displacement response in transverse beams.

7.1.4 Ground Motion Selection and Scaling

The ground motions recorded during the Düzce (1999) earthquake are characterized by two intervals of high-amplitude shaking. Therefore, a structural system that has been badly damaged during the first interval of high-amplitude shaking may as a result completely collapse during the second interval of high-amplitude shaking. The ground motion record illustrated in Figure 7.8, which has been used in the shale-table experiments after filtering of the Lamont station record in the north direction, has a scaled PGA of 1.26g. It is used as the reference ground motion record and scaled for conducting the deterministic progressive collapse simulations of application A. Scaling of the ground motion record is conducted by matching the elastic 5%-damped spectral acceleration of the scaled record at the fundamental period of vibration (hereafter referred to by $S_a(T_1,5\%)$) to a spectral acceleration value of 3.39g. This value is computed from the uniform probabilistic hazard curves published by the U.S. Geological Survey (USGS 2002), and corresponds to 2% probability of being exceeded in 50 years (hereafter referred to as 2/50 hazard level) at the chosen location of the building site. This hazard level corresponds to the maximum considered earthquake (MCE) for the design of new structures, with an estimated return period (RP) of 2475 years, according to the National Earthquake Hazard Reduction Program guidelines (NEHRP 2001). In addition to the 2/50 hazard level, one other simulation was conducted for the FE model subjected to a "rare" event of twice the scale factor, i.e., $S_a(T_1,5\%) =$ 6.78g (corresponding to a hazard level between 1/250 and 1/500). The specifics of site location selection are discussed in detail in Section 7.3.

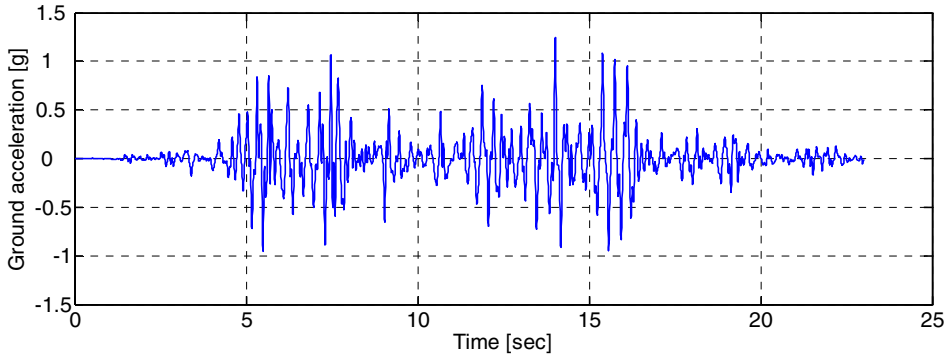

Fig. 7.8 Reference ground motion record used in application A.

7.1.5 Results and Discussion

Three time-history plots representing the simulated global response of the FE model for the case of $S_a(T_1,5\%) = 3.39$g are illustrated in Figure 7.9 during the time interval involving high-amplitude shaking. Figure 7.9a illustrates the horizontal displacement time history at node 14 at the intersection of column C4 and beams B2, B5, and B7, with the significant events leading to collapse as indicated. Complete collapse and onset of free-fall takes place after approximately 16.30 sec. It is initiated by the loss of capacity of the URM wall, corresponding to compression failure in struts S1 and then S2, at 5.17 and 5.33 sec, respectively. Following the removal of strut S1, the resulting increase in the shear force demand on the columns of the infilled frame, i.e., C3 and C4, results in shear failure in elements 130 and 140 (see Fig. 7.5), respectively. Concurrently, the increase in lateral deformation demands on columns C5 and C6 results in the initiation of lap-splice failure. The first indication of bar buckling is estimated at 5.59 sec in column C2. The damaged FE model survives the first interval of high-amplitude shaking and continues to support its gravity load while exhibiting lateral strength degradation. However, the damaged FE model does not survive the second interval of high-amplitude shaking. At approximately 15.70 and 16.00 sec, column C2 and then column C6 suffer from fracture of the transverse ties and loss of confinement. These successive failures and subsequent FE removals result in disproportionate axial load redistribution to shear-damaged column C4, which promptly collapses due to reaching the axial force-lateral drift limit curve of the zero-length element 140. With all columns on one side of the structure removed, a side-sway global collapse mechanism takes place. The remaining columns, C3, C1, and C5 soon collapse in sequence. The mode, sequence, and time of FE collapse are summarized in Table 7.3.

Figure 7.9b illustrates the vertical displacement time history at nodes 12, 14, and 16 (nodes 14 and 16 almost overlap due to the near-simultaneous removal of columns C4 and C6). The vertical displacement starts to exhibit disproportional increase once the column supporting the corresponding node is removed at the times indicated in Figure 7.9a, and ultimately exhibits unrestrained increase indicative of free-fall. Figure 7.9c illustrates the total base shear force time history. A maximum base shear force of 776 kN is recorded shortly before the ultimate collapse of the URM wall (strut S2), and strength degradation follows. At approximately 15.5 sec, a base

shear force of 610 kN is recorded. This places a significant lateral force demand on the columns of the RC frames which are already severely damaged and therefore start to collapse on one side of the structural system. This successive column collapse triggers excessive accelerations in the RC slab and initiates the side-sway mechanism from which the structural system does not recover.

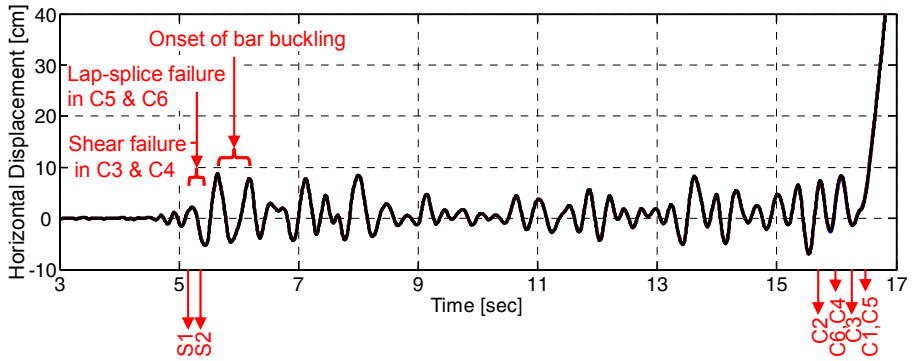

(a) Horizontal displacement at node 14

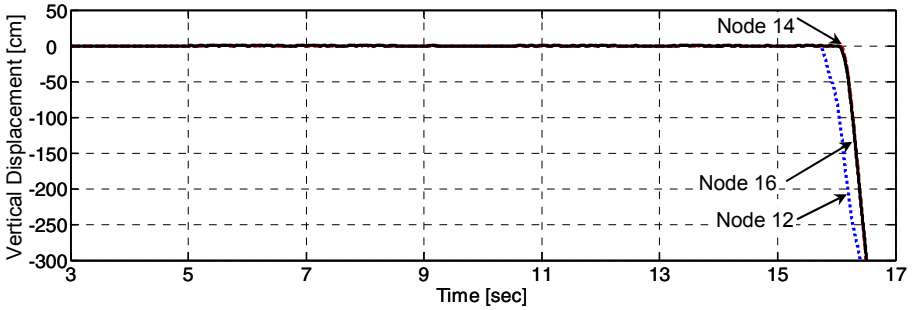

(b) Vertical displacements

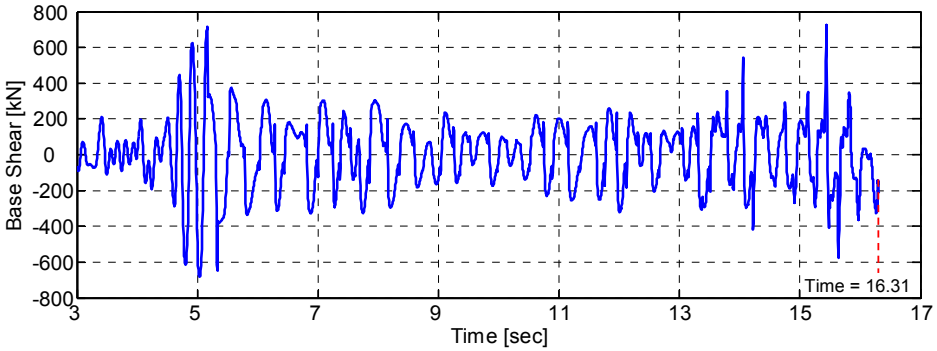

(c) Total base shear force

Fig. 7.9 Partial simulated time-history results for $S_a(T_1,5\%) = 3.39$g.

Table 7.3 Simulated sequence of structural system collapse for $S_a(T_1,5\%) = 3.39$g.

Collapse mode	Wall strut		Confinement loss		Shear-Axial		Confinement loss	
Collapsed FE	S1	S2	C2	C6	C4	C3	C1	C5
Time [sec]	5.170	5.330	15.715	16.041	16.067	16.276	16.285	16.310

In the case of $S_a(T_1,5\%) = 6.78$g, the simulated events leading to initiation of collapse are similar to those of the previous case, namely the collapse and removal of the wall struts followed by the onset of shear failure in the RC columns of the middle frame. However, the eventual sequence of FE collapse and resulting global collapse mechanism are different. As a result of the higher intensity, the FE model does not survive the first interval of high-amplitude shaking and completely collapses in less than 7.00 sec.

Figure 7.10a illustrates the horizontal displacement time history at nodes 11, 13, and 15 starting from shortly before the initiation of URM wall collapse until complete collapse for $S_a(T_1,5\%) = 6.78$g. The three plots are nearly coincidental for the three nodes prior to collapse and removal of three columns and remain close afterwards. This suggests that the membrane action of the RC slab—even though its shear rigidity is modeled—results in the structure behaving essentially as a SDOF plane frame prior to the removal of the vertical load-carrying RC columns. The progression of collapse in the structure is initiated by the loss of capacity of the URM wall indicated by compression failure in strut S1 at 4.75 sec, followed by shear failure in the columns of the middle frame (i.e., C3 and C4). The compressive failure of strut S2 takes place shortly afterwards at 4.80 sec, followed by lap-splice failure in columns C5 and C6. At 5.20 sec, the first bar buckling is detected in column C2 and then C1. At 6.14 sec, shear-damaged columns C3 and C4 collapse due to excessive lateral displacement demands resulting in the loss of axial load capacity (i.e., reaching the axial force-lateral drift limit curve) in zero-length elements 130 and 140, respectively. The increases in axial force and lateral displacement demands result in severe buckling in the longitudinal bars and complete loss of bond in lap-splices before the remaining columns successively collapse due to fracture of the transverse ties and loss of confinement. The mode, sequence, and time of FE member collapse and subsequent removal are summarized in Table 7.4.

Figure 7.10b illustrates the time-history response of the vertical displacement in nodes 11, 13, and 15. The effect of including the catenary action of the transverse beams is evident after the collapse and removal of column C3. Node 13 starts to move downwards, yet at a slower rate than that of free-fall due to the axial load being transferred to columns C1 and C5 through beams B4 and B6, respectively. Only after the removal of column C1, the downward motion of node 13 becomes unrestrained. Figure 7.10c illustrates the total base shear force time history. A maximum base shear force of 781 kN is experienced shortly before the ultimate collapse of the URM wall (strut S2).

The progression of damage in the FE model can be monitored using the change in its dynamic properties and linked to major events of individual FE collapse and removal. The fundamental period of vibration based on the eigen solution of the tangent stiffness matrix is selected as a global measure of dynamic properties since it captures the abrupt changes in stiffness caused by element removal. Figure 7.11 illustrates the evolution of the simulated fundamental period of vibration in the case of $S_a(T_1,5\%) = 6.78\text{g}$ for the time range corresponding to Figure 7.10. This plot has been smoothed using a running-mean averaging procedure with a window size of 0.20 sec (MATLAB 2007) in order to eliminate imaginary values computed during times when the structure is exhibiting softening behavior and the global tangent stiffness matrix is not positive-definite; hence the length of the record is slightly shortened due to the averaging procedure.

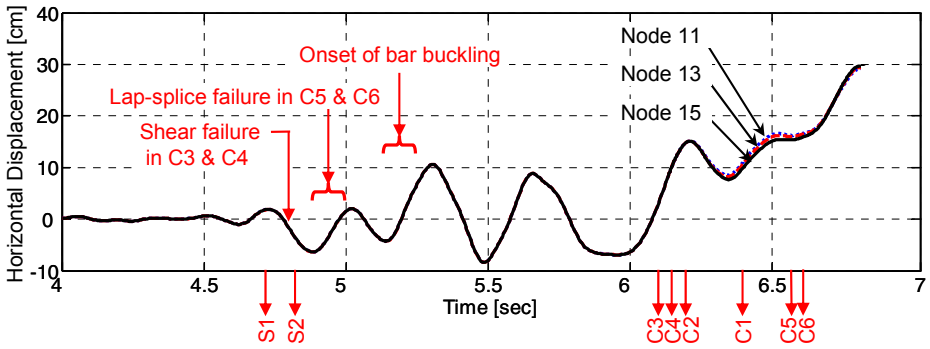

(a) Horizontal displacement

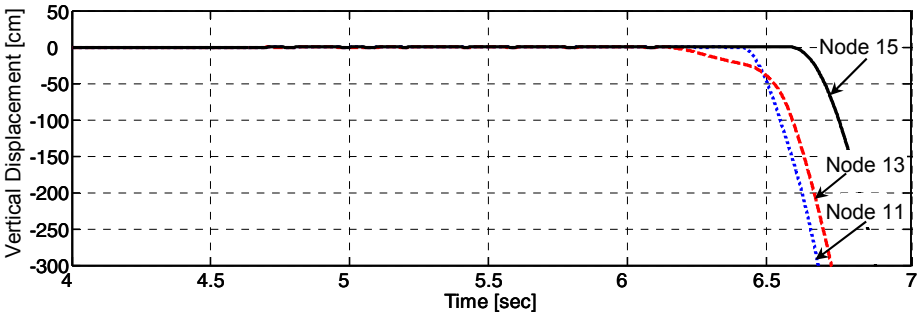

(b) Vertical displacement

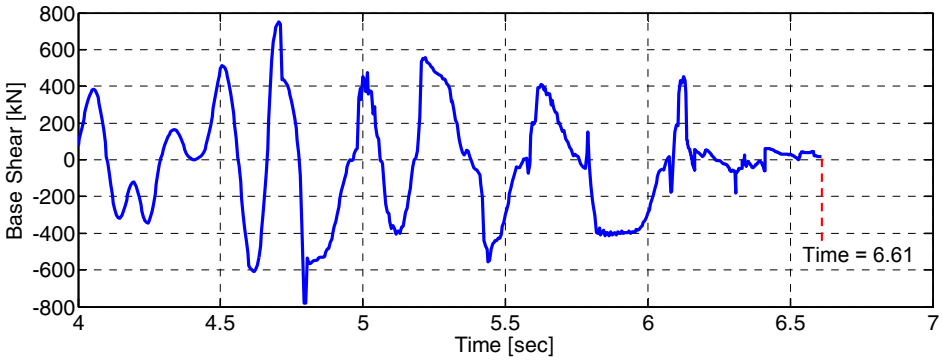

(c) Total base shear force

Fig. 7.10 Partial simulated time-history results for $S_a(T_1,5\%) = 6.78$g.

Table 7.4 Simulated sequence of structural system collapse for $S_a(T_1,5\%) = 6.78$g.

Collapse mode	Wall strut		Shear-Axial		Confinement loss			
Collapsed FE	S1	S2	C3	C14	C2	C1	C5	C6
Time [sec]	4.750	4.800	6.135	6.138	6.165	6.411	6.583	6.610

The initial fundamental period is 0.121 sec, and starts to increase with the spread of damage to the URM wall until it reaches 0.35 sec by the time the URM wall collapses. The fundamental period continues to increase afterwards due to shear failure in the columns of the infilled frame. A brief stability in the fundamental period is followed by an increase up to 0.90 sec during the time intervals in which lap-splice failure and bar buckling start to take place. Afterwards, the fundamental period momentarily stabilizes and then starts to decrease due to the closure of cracks and increased column stiffness during an interval of relatively low-amplitude shaking.

Following the collapse of column C3, the fundamental period starts to increase and is further amplified by the collapse of columns C4 and C2 to 2.70 sec. The fundamental period then decreases momentarily due to the change in the direction of shaking before increasing at the collapse of column C1 to 2.75 sec, and then momentarily decreases again. Since the damage induced in each side of the column face is dependent on the loading direction, the lateral stiffness of a column severely damaged in one direction can be momentarily higher during unloading in the opposite direction and the global stiffness matrix is therefore stiffer during intervals of displacement reversal. On the contrary, the abrupt removal of a column and removing its contribution to the stiffness matrix during a displacement cycle results in a sudden decrease in global stiffness and a corresponding increase in the fundamental period. However, the large "spike" in value is unrealistic as will be discussed in Section 7.2.5. Following the almost-simultaneous removal of the remaining two columns (i.e., C5 and C6), the stiffness matrix becomes singular and the fundamental period increases indefinitely.

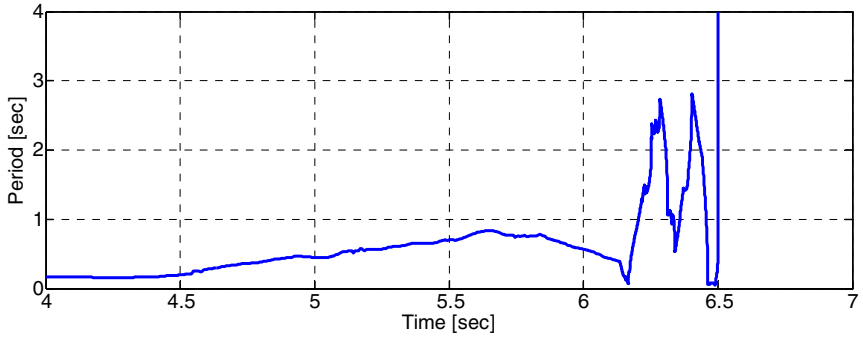

Fig. 7.11 Simulated evolution of fundamental vibration period ($S_a(T_1,5\%)=$ 6.78g).

Figure 7.12 graphically compares the two different global collapse mechanisms experienced for the two levels of earthquake intensity discussed above, namely $S_a(T_1,5\%) = 3.39$g and 6.78g. For each case, the original geometry of the FE model is plotted as well as the deformed geometry (without displacement amplification) at a time step during the analysis in which only three RC columns are intact. After collapse of the URM wall, the simulation results illustrated in Figure 7.12a indicate initial gravity-load collapse of two corner columns followed by one intermediate column on the same side of the structural system, while the RC slab behaves as a rigid diaphragm. The structural system will eventually collapse in a lateral side-sway mode which coincides with the direction of shaking in the plane of the URM wall, with significant debris expected to spread on one side outside the structure. In contrast, following URM wall collapse, the simulation results depicted in Figure 7.12b indicate initial gravity-load collapse of two interior columns, causing flexural failure in the RC slab along its major bending axis above the collapsed URM wall. The structural system will eventually collapse by caving inwards, with the outer frames and the RC slab folding toward the inner frame. Consequently, most of the debris is expected to fall within the footprint of the structure and not to spread outside it.

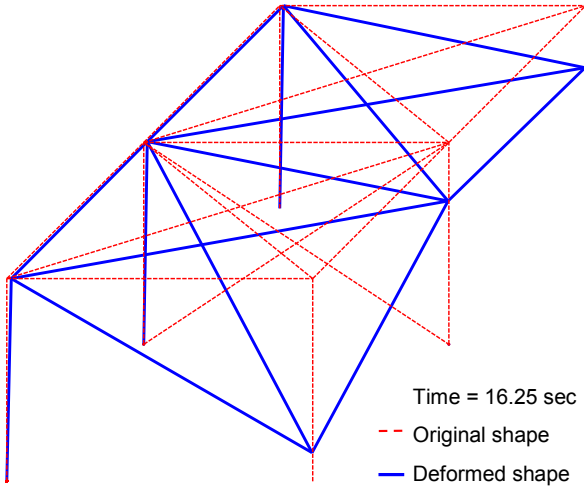

(a) $S_a(T_1,5\%) = 3.39\text{g}$

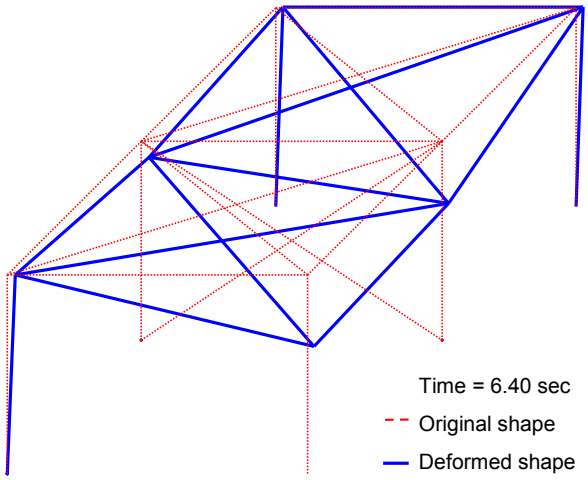

(b) $S_a(T_1,5\%) = 6.78\text{g}$

Fig. 7.12 Comparison of global collapse mechanisms resulting from different ground motion intensity levels of Düzce 1999 earthquake.

7.2 APPLICATION B: SENSITIVITY ANALYSIS OF PROGRESSIVE COLLAPSE IN FIVE-STORY RC FRAME/URM WALL SYSTEM

A five-story RC frame/URM wall structural system is adopted as a test-bed for application B in order to investigate the progressive collapse behavior of multi-story structural systems. The five-story structural system is designed to include seismically deficient RC column details, similar to

those investigated in application A. As a result of the relatively stiff URM wall and the seismically deficient column details, the collapse of the URM wall in any given story and the subsequent increased force and deformation demands on the RC columns are expected to significantly change the dynamic characteristics and modal properties of the structural system. The resulting localization of further damage and deformation in the story with collapsed URM wall may result in a soft-story collapse mechanism if the RC columns of this story cannot maintain their gravity load-carrying capacity under such increased lateral deformation demands.

The progressive collapse response is thus dependent on the stiffness of the URM wall, the mass and gravity loads of each story, the amount of damping in the structural system (which plays a role in determining the maximum deformation demands and the effect of higher modes of vibration), in addition to the intensity of the earthquake, all of which are uncertain random variables. The simulated collapse progression and its effect on the dynamic properties of the test-bed structural system of application B subjected to a MCE ground motion record are first investigated. Two simulated response variables, namely the maximum story drifts and the time at incipient collapse, are defined and discussed. In addition, the change in modal vibration periods with the progression of collapse in the structure is also investigated. Finally, the influence and relative importance of uncertain parameters defining the aforementioned random variables are assessed using the Tornado diagram analysis, a deterministic method for the analysis of sensitivity in the simulated response variables to an estimated range of variation in the individual (i.e., assumed uncorrelated) uncertain parameters.

7.2.1 Five-Story Test-Bed Structural System

The test-bed structural system adopted for application B is a three-bay five-story planar RC frame infilled with a URM wall in the middle bay of each story. This planar structural system is assumed to represent a uniform module of a typical building structure constructed in the 1960s. The RC frames and URM wall of the reference structural system are similar in dimensions and reinforcement to those of the one-story structural system investigated in application A, except where mentioned in this section. The spacing between the individual plane frames in the building structure is assumed to be 3500 mm, since the frame spacing of 1830 mm adopted in Hashemi

(2007) was imposed by the floor area of the shake table available. The design dead and live loads on each floor, including the roof for simplicity, are adopted from Hashemi (2007) and rounded to 5.5 kPa and 2.5 kPa, respectively.

The dimensions and steel reinforcement of the RC frame and URM wall members were described in Section 7.1.1. In accordance with the design recommendations for 1960s construction (ACI 1963), the spacing between the transverse ties is increased to 150 mm as discussed in Section 7.1.3. Moreover, a lap-splice in the longitudinal reinforcement is inserted above the floor level of each column in the second and fourth floors. As discussed in Section 7.1.3, the length of this lap-splice is taken according to ACI (1963) as equal to 20 times the longitudinal bar diameter.

7.2.2 FE Model of Five-Story Test-Bed Structural System

The geometry of the FE model representing the five-story test-bed structural system for application B is illustrated in Figure 7.13. This model consists of displacement-based beam-column elements to represent the RC frame members, compression-only diagonal truss elements to represent the URM walls, and coupled shear-axial zero-length elements at the bases of the columns of the intermediate bay which are susceptible to shear failure following the partial collapse of the URM wall in each story. Frame members are referred to by the letter C for columns and B for beams, followed by the floor and bay numbers. Struts representing the diagonals of a URM wall bay are referred to by the letter "S," followed by the floor and the bay number at the lower node. The coupled zero-length elements are shown only at the foundation level (nodes 3 and 4) for clarity of illustration. Meshing of the FE model and fiber-discretization of the beam-column element cross sections have been previously discussed in Sections 7.1.2 and 7.1.3.

Nodes 1 through 4 are fully restrained from all translations and rotations. Masses and gravity loads are lumped at the nodes. Co-rotational geometric transformation is used for all elements (Crisfield 1990). Material properties used in the FE model were previously listed in Table 7.2. The FE model has simulated vibration periods of 0.446, 0.146, 0.086, 0.081, and 0.064 sec for the first five modes of free vibration. Rayleigh viscous damping is assumed, with a

damping ratio of $\zeta = 0.05$ (see Section 7.2.4) for the first and third modes of vibration by combining mass- and stiffness-proportional damping (Chopra 2001). Hence, the respective multipliers of the mass and stiffness matrices are found to be 0.807 Hz and 0.834 kHz^{-1}, respectively.

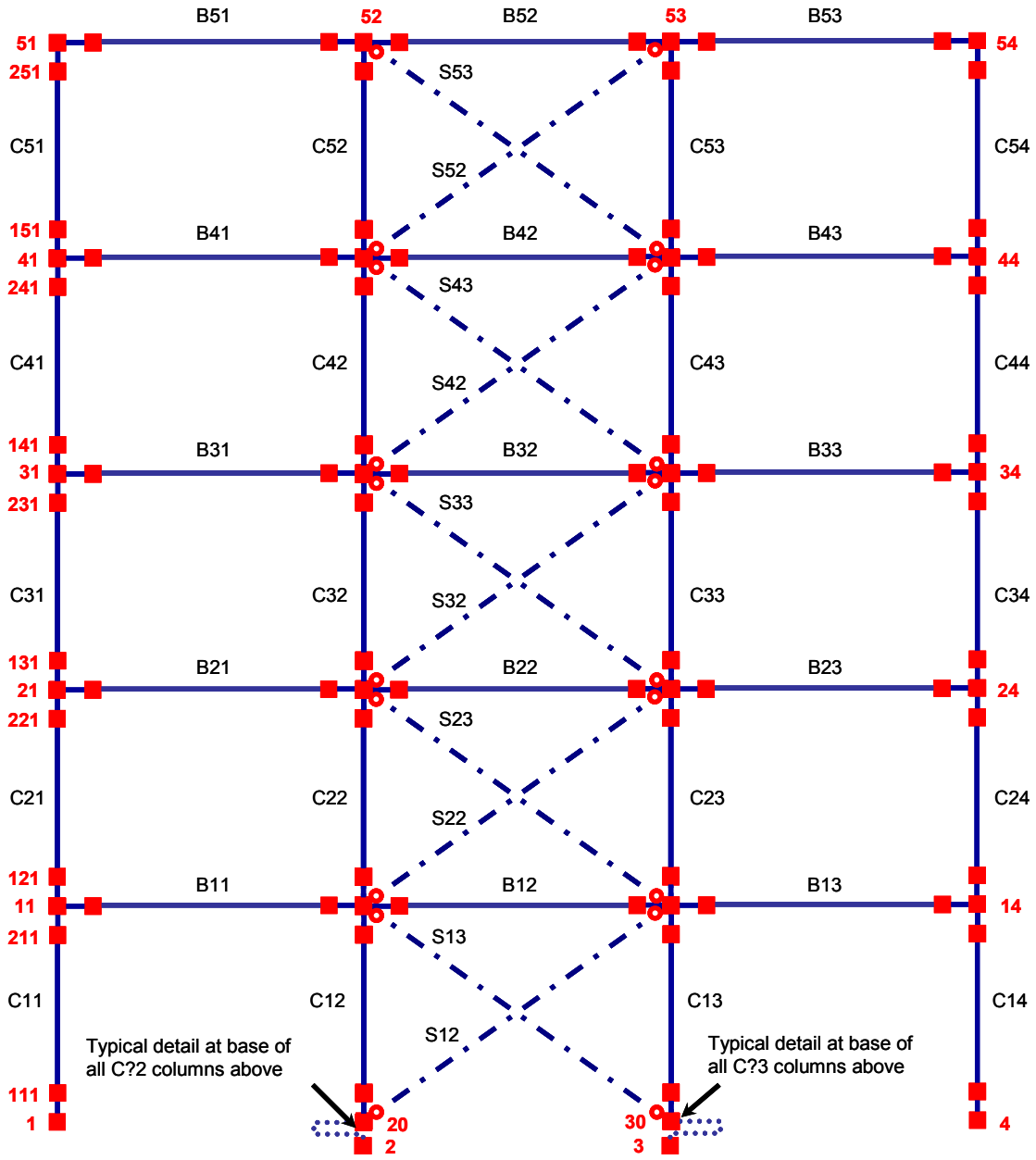

Fig. 7.13 FE model of five-story test-bed structural system.

7.2.3 Reference Ground Motion Record and Hazard Level

The filtered ground motion record that corresponds to the Düzce (1999) earthquake as previously defined in application A is adopted as the reference ground motion record for application B as well. This ground motion record has been discussed in Section 7.1.4 and shown in Figure 7.8. The MCE hazard level of 2/50 is selected as a reference hazard level for application B.

Scaling of the ground motion is conducted taking into consideration the significant changes that take place in the test-bed structural system's stiffness and dynamic characteristics as a result of collapse in the URM wall panels. The simulated fundamental vibration period increases from 0.446 to 0.591 sec upon elimination of the strut elements in the first story, which have been observed during preliminary simulations on the FE model to be the first structural elements to collapse. Hence, an elastic 5%-damped first-mode spectral acceleration of the FE model is computed as an average of the spectral acceleration values for the indicated range of vibration periods. This average value is denoted by $S_a(\overline{T}_1,5\%)$ and is found equal to 1.038g. The elastic pseudo-acceleration response spectrum and the averaging process are illustrated in Figure 7.14. The ground motion record is scaled so that the value of $S_a(\overline{T}_1,5\%)$ for the scaled record would match the target design value corresponding to the reference hazard level at the selected building site location (USGS 2002). This target spectral acceleration value is computed for the average first-mode vibration period to be 2.493g.

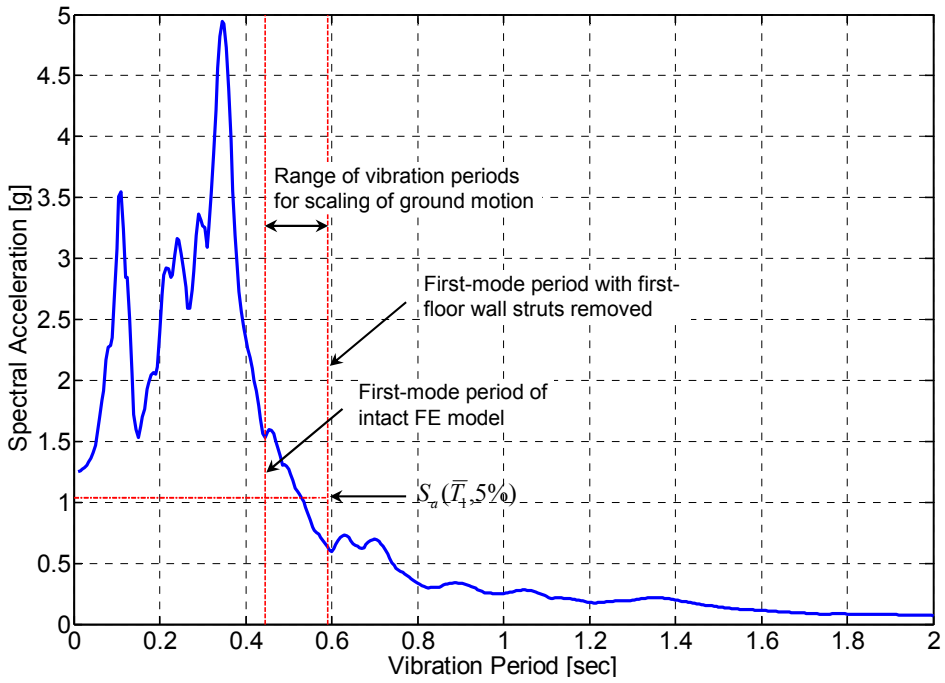

Fig. 7.14 Elastic 5%-damped response spectrum used in application B.

7.2.4 Modeling Uncertainty in Parameters for Deterministic Sensitivity Study

The effect of uncertainty in the system parameters is investigated and compared to the effect of uncertainty in the earthquake hazard level to determine their relative importance. This comparison is conducted using the Tornado diagram analysis, a deterministic method developed to numerically determine the sensitivity in a simulated response quantity of interest to uncertainty in input parameter values. Using this method, the relative importance of accounting for uncertainty in the input parameters with respect to the resulting accuracy and reliability of the simulated output is established. In this method, a reference point is initially set by computing the simulated response quantity using a set of reference values (e.g., the estimated mean values) of the uncertain input parameters. Next, these input parameters, assumed uncorrelated, are individually varied within a given range of uncertain values typically parameterized by their COV. The resulting changes in magnitude of the simulated response quantity are computed, compared, and sorted across the different parameters. These magnitudes are hereafter referred to as "swings" and are adopted as a sensitivity measure. A graphic comparison of the computed

swings is used to establish the relative importance of the input parameters. A larger swing indicates a higher relative importance for the associated input parameter and, consequently, a larger influence for the uncertainty associated with the input parameter in determining the outcome of the simulation. An extensive review of the Tornado diagram method can be found in Lee and Mosalam (2005), and applications of this method similar to the present study can be found in Binici and Mosalam (2007) and Talaat and Mosalam (2007).

For the test-bed structural system defined in application B, the simulated maximum first-story drift and time at incipient collapse are defined as the output quantities of interest. The uncertain parameters investigated in this application are the mass (i.e., gravity load on the structural system) the stiffness of the URM wall, the viscous damping ratio, and the seismic hazard level determining the intensity of the ground motion. The reference gravity load on the building is related to the expected occupancy of the structure and is taken as equal to the seismic design recommendations of the full dead load in addition to a live load factor LL = 0.25, i.e., one quarter of the design live load for gravity (NEHRP 2001). The maximum gravity load is assumed to correspond to a case of full occupancy and full live load (LL = 1.00), while the minimum gravity load on the building is assumed to correspond to a case of no occupancy and no live load (LL = 0.0).

The uncertain stiffness of the URM wall is calculated by considering the uncertain maximum strength of the diagonal struts f_{mo} (see Section 7.1.2) and a deterministic corresponding strain $\varepsilon_{mo} = 0.0028$. Hence, the initial stiffness of the URM wall, $E_{mi} = 2 f_{mo} / \varepsilon_{mo}$, has the same distribution as f_{mo}. The non-negative f_{mo} is assumed to have a lognormal distribution. The sample mean and COV of f_{mo} are estimated in Hashemi (2007) from experimental material tests to be 17.0 MPa and 0.10, and taken as estimates of the population median (which is more robust and more typically used than the mean for lognormal distribution) and COV, respectively. The reference value of f_{mo} is taken equal to the estimated mean value. The mean, maximum and minimum values of f_{mo} are computed taking into consideration the estimated level of uncertainty (represented by the COV value) and an assumed confidence interval. Since the uncertain gravity load is varied over the range from no occupancy to full occupancy (i.e., corresponding to a near-certain confidence interval), the uncertain stiffness of

the URM wall is assumed to vary over a confidence interval of 0.997, in order to establish a common ground for comparing the resulting sensitivity. According to the lognormal distribution, these values are computed as follows (Ang and Tang 1975):

$$\hat{\bar{f}}_{mo} = \hat{f}_{mo(0.5)}\sqrt{1+\hat{\delta}^2} \tag{7.1}$$

$$f_{mo}^{\max} = \hat{f}_{mo(0.5)}\exp\left[3\left(\ln\left(1+\hat{\delta}^2\right)\right)^{0.5}\right] \tag{7.2}$$

$$f_{mo}^{\min} = \hat{f}_{mo(0.5)}\exp\left[-3\left(\ln\left(1+\hat{\delta}^2\right)\right)^{0.5}\right] \tag{7.3}$$

where $\hat{\bar{f}}_{mo}$, $\hat{f}_{mo(0.5)}$, and $\hat{\delta}$ are the estimated mean, median, and COV, respectively.

Similar to the URM wall stiffness, the viscous damping ratio is treated as a random variable with a lognormal distribution. Preliminarily, a median value of $\zeta_{0.5} = 0.045$ is adopted in accordance with application A (see Section 7.1) and a relatively large COV of 0.4 is preliminarily assumed to represent the uncertainty corresponding to typical structural engineering applications. Following the example of Equations (7.1)–(7.3), mean, maximum, and minimum values of 0.0487, 0.1019, and 0.0199, respectively, are computed for a 0.997 confidence interval. Since viscous damping is often subjectively estimated in dynamic structural analysis at rounded percentage values, the reference (mean), maximum, and minimum values used in the Tornado diagram analysis are shifted to 0.05, 0.10, and 0.02, respectively, which coincides with the practical range typically used in structural engineering analyses, thus approximately fitting the arbitrarily estimated COV value of 0.4.

The reference seismic hazard level is set to the 2/50 MCE level (NEHRP 2001). The sensitivity of the collapse response is investigated between the hazard levels of 1/50 and 3/50. The values of the corresponding elastic spectral accelerations are listed along with the uncertain system parameter ranges in Table 7.5. The structural system and FE model corresponding to the reference set of parameter values are hereafter referred to as the reference structural system and reference FE model, respectively.

Table 7.5 Statistics of uncertain system parameters in Tornado diagram analysis.

Parameter	Distribution	Reference	COV	Minimum	Maximum
E_{mi} [GPa]	Lognormal	6.07	0.1	4.46	8.14
ζ [%]	Lognormal	5.0	0.4	2.0	10.0
LL [%]	NA*	25.0	NA*	0.0	100.0
$S_a(\overline{T}_1,5\%)$ [g] (Hazard level)	NA*	2.493 2/50	NA*	2.205 3/50	2.915 1/50

* Not Applicable

7.2.5 Progressive Collapse Response of Reference Five-Story Structural System

The simulated response of the reference five-story structural system eventually exhibits global collapse due to the formation of a soft first-story mechanism. The diagonal struts representing the URM wall in the first-story collapse and are removed at 5.061 and 5.581 sec for struts S12 and S13, respectively. The removal of the diagonal struts results in shear failure in the first-story columns C12 and C13. At 7.761 sec, column C13 loses its gravity load-carrying capacity due to shear-axial interaction and is removed from the FE model, closely followed by the removal of column C12 at 7.826 sec. The removal of these two columns results in beams B11, B12, and B13 acting as catenaries and therefore causing both remaining columns of the first story (i.e., C11 and C14) to drift laterally inwards. The increase in first-story lateral drift results in severe bar buckling and ultimately collapse of column C11 due to fracture of the transverse ties at 7.891 sec. The structural system starts to undergo almost-rigid body rotation at the connection with its one remaining column in the first story, i.e., C14, until the imposed curvature on the column cross section results in its flexure-axial collapse due to transverse tie fracture at 8.229 sec. The structure then undergoes unrestrained free-fall. It should be noted that the formation of the soft-story mechanism after the removal of the two columns C12 and C13 results in excessive lap-splice slip in the second-story column C21, which ultimately collapses at 7.690 sec. The resulting redistribution of forces contributes to the collapse of the lower-story column C11 taking place before column C14. The times corresponding to individual FE removal are indicated on the

story drift time-history plots in Figure 7.15. The sequence, mode, and time of FE collapse are summarized in Table 7.6.

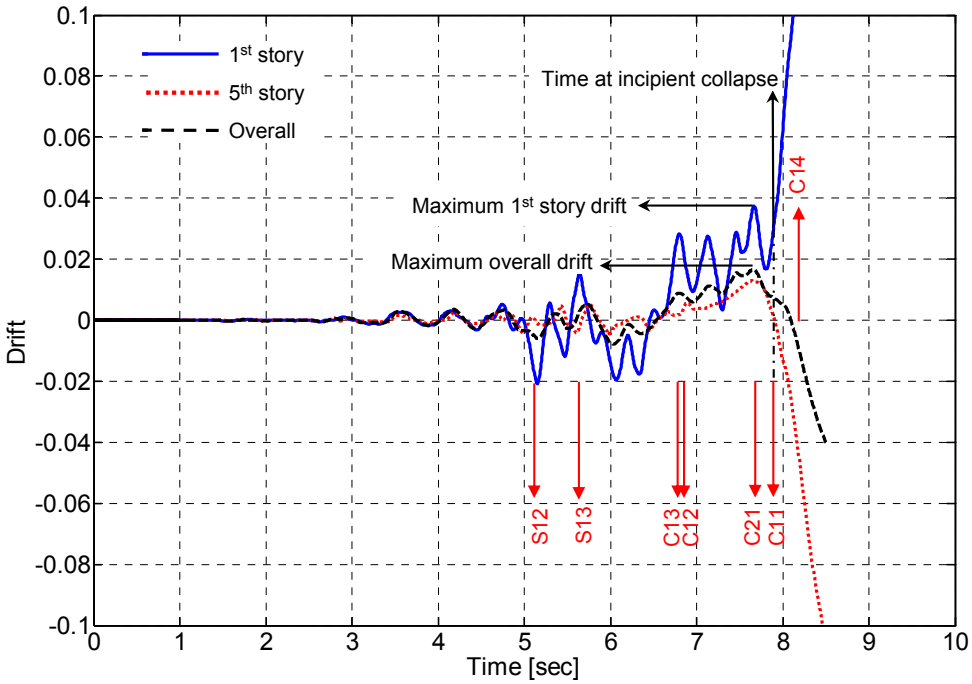

Fig. 7.15 Simulated drift time-histories of reference five-story structural system.

Table 7.6 Simulated sequence of collapse for reference five-story structural system.

Collapse mode	Wall strut		Shear-Axial		Confinement loss		
Collapsed FE	S12	S13	C13	C12	C21	C11	C14
Time [sec]	5.061	5.581	6.761	6.826	7.690	7.891	8.229

The effect of progressive collapse on the simulated structural system response can be demonstrated by interpreting the time-history responses of story drifts illustrated in Figure 7.15. The story drift is defined as the average drift ratio (i.e., difference in lateral displacements normalized by story height) calculated from the four pairs of nodes located at the top and bottom ends of each column (e.g., node pairs (11, 1), (12, 2), (13, 3), and (14, 4) for the first-story drift; see Fig. 7.13). The story drifts are plotted for the first and fifth stories, as well as the overall drift

computed at the roof relative to the ground floor. The times corresponding to FE removal are also indicated in Figure 7.15. The story drift time-histories for the first and fifth story before removal of the diagonal strut S12 are similar to each other and to the overall drift. This indicates that the dynamic response is dominated by the first mode of vibration, which is in accordance with modal analysis results of another five-story structural system modeled in Hashemi (2007) with similarity in general characteristics to this reference five-story structural system.

After removal of the first story diagonal struts, the first-story drift increases disproportionately compared to the fifth-story drift as the first mode shape changes due to the localization of damage in the weakened first story and as the participation of higher modes of vibration potentially increases. This leads to shear failure in columns C12 and C13 and the initiation of the soft-story mechanism due to localization of further deformation in the weakened first story. This is indicated by the increase in magnitude and the permanent positive shift in the first-story drift values. The maximum first-story drift value prior to collapse is 0.037 at 7.687 sec. During the same time interval, the fifth-story and overall drifts increase to maximum values of 0.013 and 0.017, respectively. The subsequent removal of column C21 and then C11 on one side of the FE model results in a collapse mode in which the structural system undergoes nearly rigid-body rotation about the first-story top end of column C14 (i.e., node 14) before its removal (see Fig. 7.18c). Hence, the first-story drift values start to exhibit unrestrained increase in the positive direction, while the fifth-story and overall drifts exhibit unrestrained increase in the negative direction. The time at incipient collapse is defined as the time at which unrestrained increase in inter-story drift is initiated, as illustrated in Figure 7.15. Accordingly, the maximum "meaningful" drift values are only defined for the time period preceding incipient collapse, which takes place at 7.891 sec, coincidental with the removal of column C11.

The effect of collapse progression on the dynamic properties of the structural system, as represented by the simulated periods of vibration for the first four modes, is demonstrated in Figure 7.16. The fifth vibration period is not illustrated because it does not exhibit different behavior from the first four and cannot be included in the same page without severely reducing the scale of the plots. These plots have been smoothed using a running-mean averaging procedure with a window size of 0.20 sec as previously discussed in Section 7.1; hence the length of the record is slightly shortened due to the averaging procedure. As stated earlier, the

initial periods of vibration are, respectively, 0.446, 0.146, 0.086, and 0.081 sec, and start to increase with the spread of damage to the URM walls. At approximately 5.05 sec, when the diagonal strut S12 reaches its compressive strength and starts to exhibit softening, the vibration periods have elongated by a factor ranging from 1.9 to 2.8 where these elongated periods are 0.991, 0.405, 0.240, and 0.150 sec. The subsequent softening response results in a momentary decrease in the simulated period for the first and second modes until strut S12 is removed, which results in an observed sudden increase in all four vibration periods to 1.351, 0.751, 3.376, and 0.360 sec. The spikes observed in the simulated vibration periods at the time of element removal, especially that of the third vibration mode, are interpreted as a numerical indication of the abrupt change in the mathematical model representing the structural system and not a quantitative measure of the actual period of vibration as would be measured by a snap-back test, which may be better estimated by the average increase in vibration period following the spike. Only the first-mode vibration period continues to steadily increase afterwards with the localization of damage in columns of the first story and reaches 2.210 sec after removing strut S13 at approximately 5.60 sec, whereas the second mode vibration period only exhibits a modest change to a value of 0.489 sec.

The removals of shear-damaged columns C12 and C13 at approximately 6.80 sec result in sudden increases (i.e., spikes) in all four vibration periods. The magnitude and immediacy of these increases are consistently descending from the first mode to the fourth. These increases indicate a major change in the properties of the structural system that corresponds with the formation of a soft first-story mechanism. Subsequently, the simulated period of the first vibration mode exhibits a spike at 7.14 sec before decreasing rapidly to zero at 7.54 sec. This is an indication of a non-positive definite stiffness matrix. The implication of this observation is that the structural system, if subjected to quasi-static lateral force distribution (i.e., pushover) consistent with its first mode of vibration at its current state, will exhibit a softening lateral load-displacement response.

Subsequent to the sudden increase (i.e., spike) at 6.95 sec, the second vibration period exhibits other spikes at 7.68 sec, corresponding to the collapse and removal of column C21, and at 7.89 sec, corresponding to the collapse and removal of column C11 and the initiation of the aforementioned rigid-body rotation mechanism of incipient collapse. In between the spikes, the

second vibration period exhibits smaller values with an increasing trend. At 8.00 sec, the simulated second period of vibration undergoes a sudden drop to zero, indicating that the quasi-static lateral load-displacement response (i.e., pushover) of the second vibration mode is exhibiting softening as well.

Subsequent to the sudden increase (i.e., spike) at 7.08 sec, the third vibration period exhibits other spikes at 7.72, corresponding to the collapse and removal of column C21, and at 7.88 sec, corresponding to the removal of column C11 and the initiation of the aforementioned rigid-body rotation mechanism of incipient collapse. In between the spikes, the third vibration period exhibits a nearly constant trend oscillating around a period of approximately 2.250 sec. At 7.89 sec, the simulated third period of vibration undergoes a sudden drop to zero, indicating that the quasi-static lateral load-displacement response (i.e., pushover) of the third vibration mode is exhibiting softening as well.

In contrast to the lower vibration modes, the fourth mode vibration period reaches a maximum value of 3.361 sec at the initiation of incipient collapse but does not drop all the way to zero. Ultimately, after the removal of column C14, the last column connecting the structure to the ground, the stiffness matrix becomes singular and all the simulated vibration periods, including the fourth, increase indefinitely.

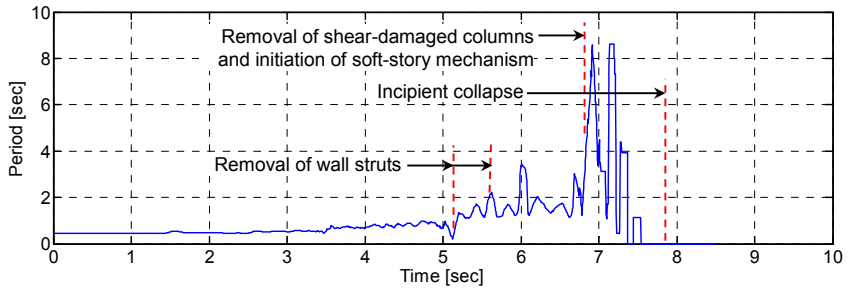

(a) First mode of vibration

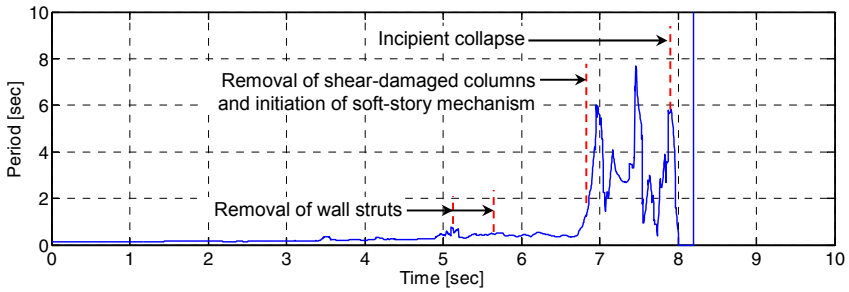

(b) Second mode of vibration

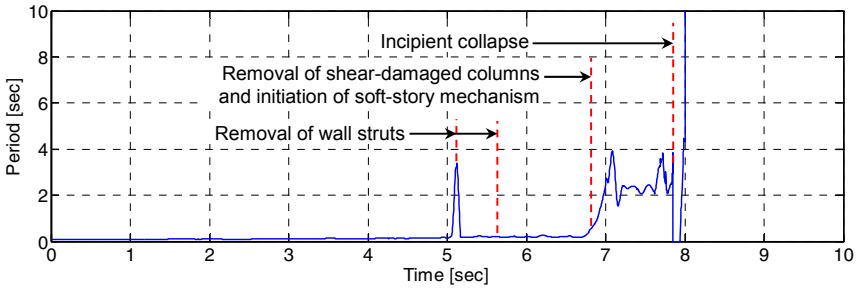

(c) Third mode of vibration

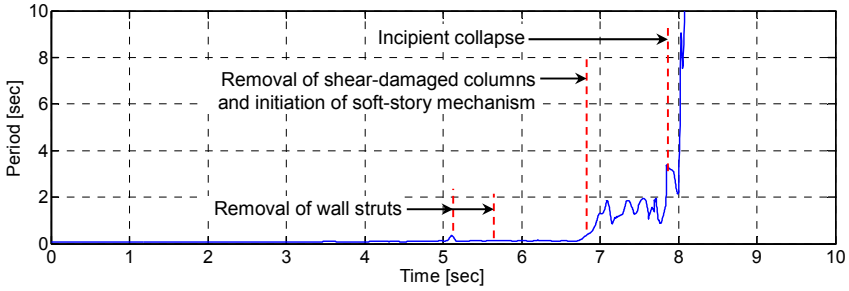

(d) Fourth mode of vibration

Fig. 7.16 Simulated evolution of vibration periods in reference five-story FE model.

The evolution of vibration periods suggests that FE collapse events excite temporary participations from several higher vibration modes and shift their corresponding mode-shapes and vibration periods. However, the subsequent dynamic response is dominated by the first vibration mode which continues to accumulate damage, evidenced by a steady increase in its vibration period. Subsequent FE collapse events again momentarily shift all vibration periods. After the first vibration mode reaches a state where it exhibits softening and loss of quasi-static stability (i.e., non positive-definite stiffness matrix), the second mode seems to dominate the dynamic response by exhibiting a positive trend with time in its vibration period between the spikes corresponding to the FE removal times, while higher mode periods, e.g., the third mode, oscillate about nearly constant shifted values in between the spikes. It is believed that this domination of the dynamic response by the lowest stable vibration mode is a result of the explicit FE removal procedure being used which creates a vibration mode for the damaged structural system significantly less-stiff (and thus more dominant) than the remaining higher vibration modes, especially after the localization of damage and the majority of subsequent element collapse events in the first story.

Figures 7.17 and 7.18 demonstrate the progression of collapse in the reference structural system during the simulation through snapshots of the deformed FE model geometry at time intervals corresponding to significant changes in the model. For simplicity of the demonstration, the deformed geometry is approximated by connecting the nodes at the ends of the beam and column members while ignoring the intermediate nodes, and using straight lines instead of the actual deformed shapes of the FE elements.

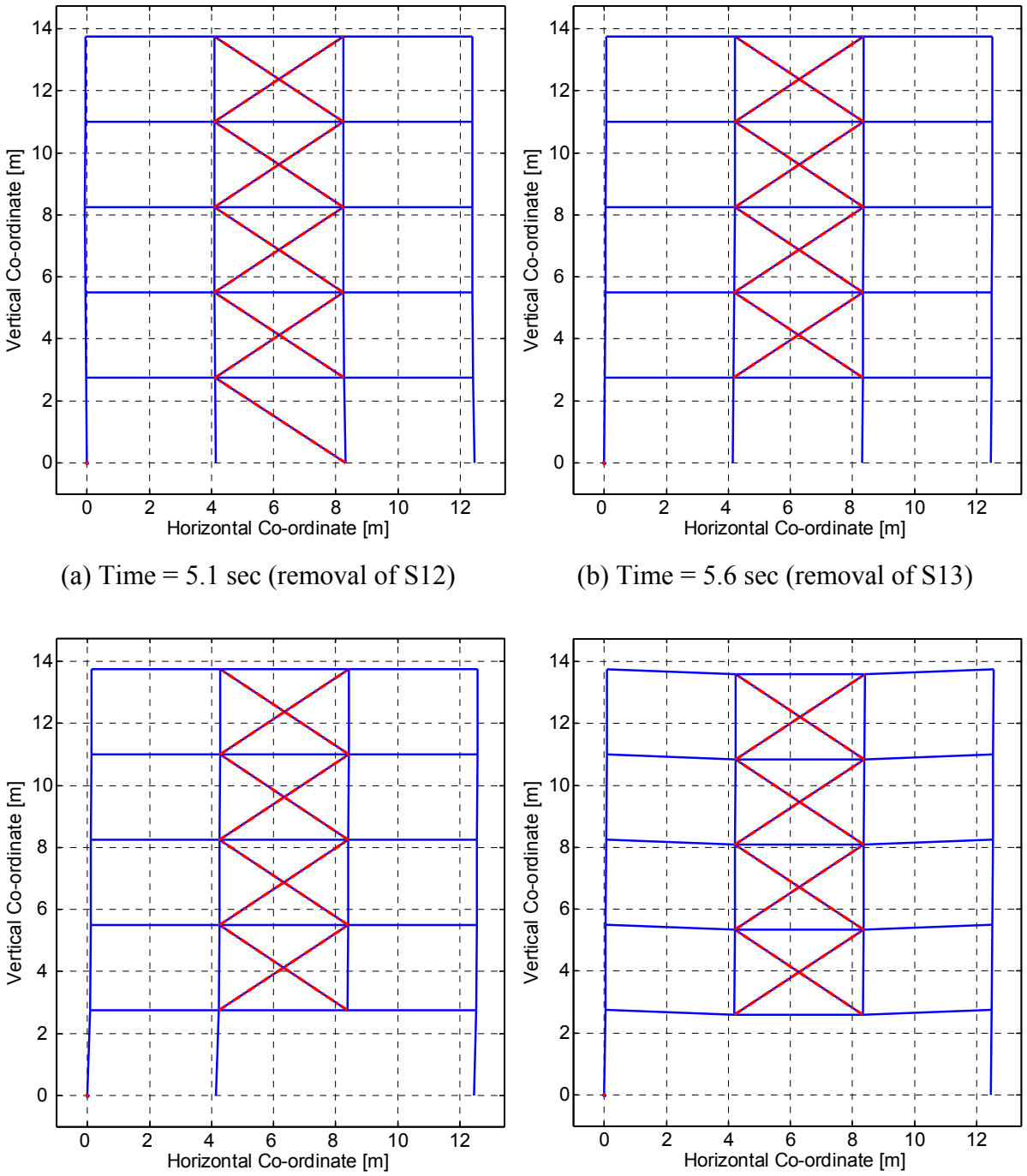

(a) Time = 5.1 sec (removal of S12)

(b) Time = 5.6 sec (removal of S13)

(c) Time = 6.8 sec (removal of C13)

(d) Time = 7.0 sec (removal of C12)

Fig. 7.17 Snapshots of deformed FE model geometry demonstrating early stages of collapse progression in reference five-story structural model (no amplification).

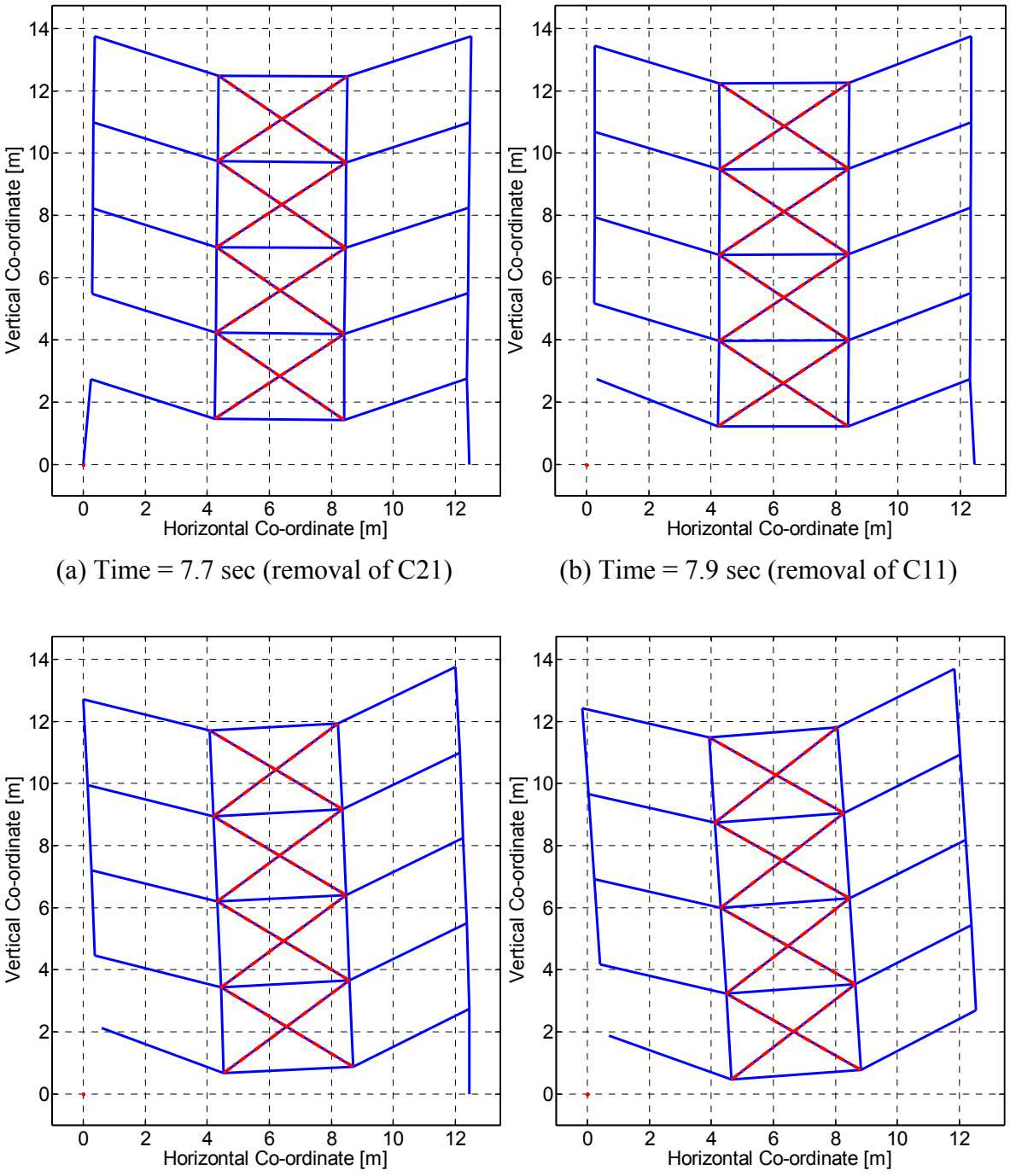

(a) Time = 7.7 sec (removal of C21)

(b) Time = 7.9 sec (removal of C11)

(c) Time = 8.2 sec (collapse mechanism)

(d) Time = 8.3 sec (free-fall)

Fig. 7.18 Snapshots of deformed FE model geometry demonstrating late stages of collapse progression in reference five-story structural model (no amplification).

7.2.6 Results and Discussion of Deterministic Sensitivity Analysis

The sensitivity of the progressive collapse response to parameter uncertainty is investigated using two output quantities, namely the simulated time at incipient collapse and the simulated maximum first-story drift prior to or at incipient collapse. The simulated time at incipient collapse exhibits more suitable characteristics for the objectives of this application. This is specifically because the effects of changing several system parameters result either in localizing the structural damage in the first story and thus decreasing the time at incipient collapse, or spreading the damage into the other stories of the structural system and thus delaying incipient collapse or avoiding it altogether. As a result, the change in the simulated time at incipient collapse is thought to be an effective measure for the influence of an uncertain parameter value on the system's vulnerability for progressive collapse. On the other hand, the simulated story drifts will likely exhibit a decrease in the cases in which global collapse is avoided. However, in cases where global collapse takes place, the magnitude of the simulated story drifts may not exhibit a predictable pattern with the induced change in uncertain system parameters. Instead, the maximum drift is controlled by local variables such as the axial load and the corresponding lateral deformation ductility of individual RC columns, and is thus not expected to be an effective sensitivity measure.

Figure 7.19 illustrates the Tornado diagram summarizing the sensitivity results for the simulated time at incipient collapse, with swings around the reference value of 7.891 sec ordered in an ascending fashion. The largest swing is associated with the earthquake intensity. Increasing the hazard level to 1/50 results in a stronger earthquake and earlier incipient collapse at 6.920 sec, whereas decreasing the hazard level to 3/50 results in no collapse for the 23.000 sec duration of the simulation where only the URM wall collapse is predicted in the first story. The next important uncertain parameter is the URM wall stiffness. The higher stiffness value results in larger forces being redistributed to columns C12 and C13 upon URM wall collapse, leading to earlier incipient collapse at 7.469 sec. On the contrary, the lower wall stiffness results in lower forces being redistributed to the columns of the infilled bay of the RC frame at URM wall collapse. In addition, the low-stiffness URM walls exhibit complete collapse in the second and third stories, and partial collapse (i.e., collapse of one diagonal strut) in the fifth story as well, which reduces the subsequent localization of damage and story drift demands in the first story.

This enables the structural system to survive the earthquake without gravity load collapse in any RC column, despite sustaining severe damage in the URM walls. The observed asymmetry in the swings of these two parameters around the reference value is because one case of each resulted in global collapse, within the same time interval of high-amplitude ground shaking as the reference case, while the other case of each resulted in no global collapse.

Next in importance to the URM wall stiffness is the distributed mass on the structure in terms of the live load factor (LL). The assumption of full occupancy results in higher gravity-induced axial loads on the RC columns (i.e., lower lateral drift capacities) and the URM walls. This leads to the collapse of at least one diagonal strut in each of the first four stories and to slightly earlier incipient collapse at 7.681 sec. On the other hand, the assumption of no occupancy results in lower gravity-induced axial loads on the RC columns and URM wall. As a result, the structural system survives the first interval of high-amplitude shaking and incipient collapse is delayed until 16.37 sec. The observed asymmetry in the swing of this parameter around the reference value is because the case of maximum occupancy resulted in global collapse within the same time interval of high-amplitude shaking as the reference case, while the case of no occupancy resulted in delaying the occurrence of incipient collapse until the second time interval of high-amplitude shaking (see Fig. 7.8).

The least-important parameter for the time at incipient collapse in terms of uncertainty is the viscous damping ratio. No fundamental change in the time, extent of localization, or overall mechanism of incipient collapse is observed as a result of changing the damping ratio in the range between 2% and 10%.

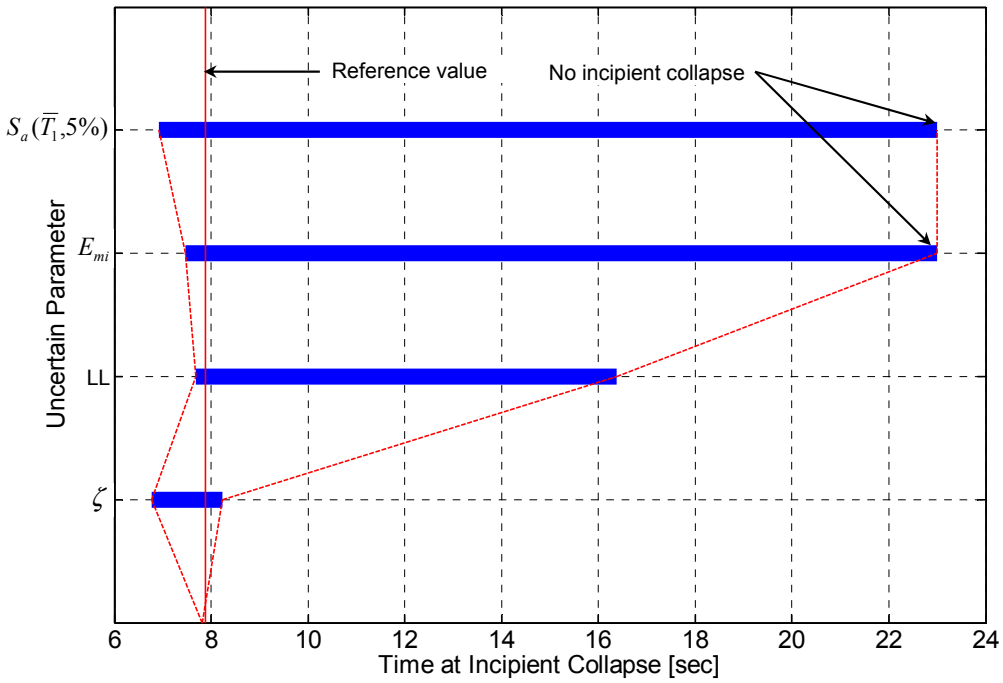

Fig. 7.19 Tornado diagram for simulated sensitivity of time at incipient collapse.

Figure 7.20 illustrates the swings of the simulated first-story drift, with the uncertain parameters ordered according to their relative importance established by the simulated time at incipient collapse in Figure 7.19. The comparison with Figure 7.19 serves to demonstrate that the use of story drift is ineffective in assessing the ranking of uncertain parameters in terms of their importance for progressive collapse behavior in simulations involving direct removal of a collapsed FE. Except for the least-important uncertain parameter, i.e., the viscous damping ratio, the magnitude of the swings is in opposite order to that of Figure 7.19. The most important parameter, the earthquake intensity and the corresponding seismic hazard level, possesses the second-shortest swing. In addition, the computed swing is oddly offset from the reference value. This is because the low-intensity earthquake results in no collapse and a much smaller first-story drift than the reference value, while the high-intensity earthquake results in earlier formation of the soft-story collapse mechanism and thus a slightly smaller first-story drift than the reference value prior to incipient collapse. The largest simulated swing in the first-story drift is associated with the uncertainty in occupancy in terms of the live load factor. This is attributed to the effect of the resulting increase in the column axial load on the lateral displacement ductility and thus on

the lateral drift capacity at collapse of individual columns (e.g., the axial force-lateral drift limit curve). Furthermore, the simulated drift values corresponding to the two cases where no global collapse took place (i.e., minimum earthquake intensity and minimum URM wall stiffness) are oddly larger than the drift value simulated for the case of maximum occupancy which nevertheless resulted in global collapse. Thus, the simulated time at incipient collapse is deemed more effective than the simulated maximum story drift as a sensitivity measure in this application.

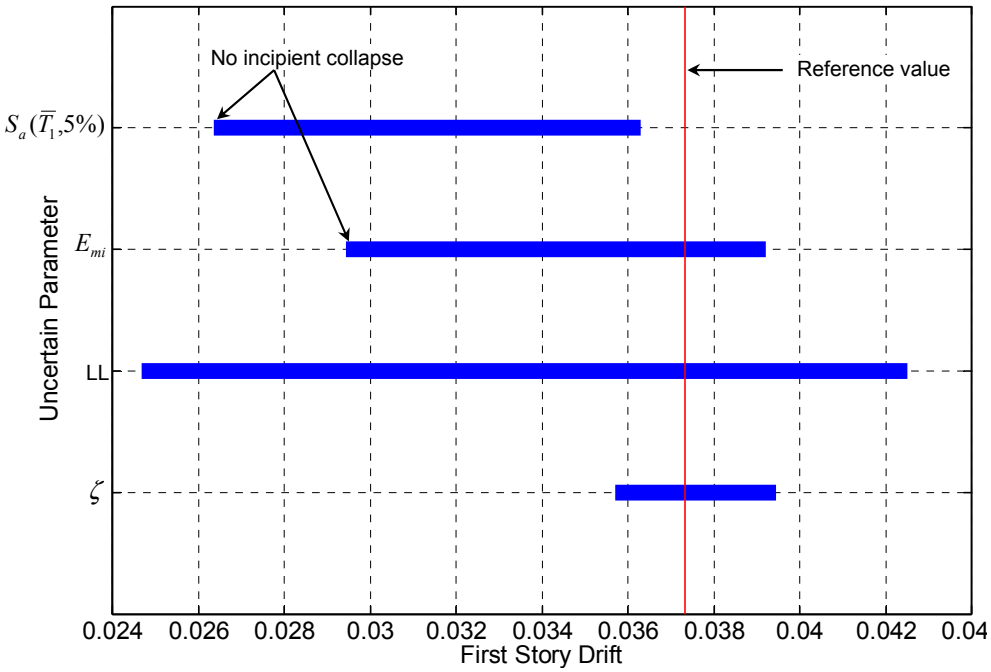

Fig. 7.20 Diagram of unordered swings for simulated sensitivity of first-story drift.

It warrants commenting that the swings representing sensitivity in the simulated time at incipient collapse for the first two uncertain parameters in Figure 7.19 are close in magnitude, and that both parameters include a minimum-value case where incipient collapse was avoided. However, in the case of the lower-stiffness URM wall, the survival of the structural system comes at the expense of more extensive propagation of URM wall collapse into the structure and a larger maximum first-story drift demand than in the case of the lower-intensity ground motion record (see Fig. 7.20). Moreover, the minimum URM wall stiffness corresponds to a 0.997 confidence interval of possible values, while the minimum ground motion intensity corresponds

to decreasing the reference hazard level by only one percentage point of being exceeded in 50 years. Thus, the most important uncertain parameter with regard to the possibility of progressive collapse is the earthquake hazard level. However, the most important system parameter for the investigated test-bed structural system investigated, which determines the vulnerability to progressive collapse (and spread of damage) during a given seismic event at a specified hazard level, is the stiffness of the URM wall.

7.3 APPLICATION C: PROBABILISTIC PROGRESSIVE COLLAPSE ASSESSMENT OF ONE-STORY RC FRAME/URM WALL SYSTEM

In Section 7.2, the sensitivity of the simulated time at incipient collapse of the five-story test-bed structural system presented in application B was investigated with respect to an estimated range of uncertainty in the system parameters and seismic hazard level. According to this investigation, it was observed that the uncertainty in the input ground motion intensity as characterized by the seismic hazard level is of paramount relative importance to the outcome of progressive collapse simulation. Application C investigates further the effect of uncertainty in the ground motion characteristics. This is conducted using an ensemble of selected ground motion records belonging to the same earthquake in order to generate empirical probability values for reaching specified limit states of collapse progression in the simulated test-bed structural system when subjected to these ground motion records. This ensemble is presented in Section 7.3.1, and consists of two horizontal components of seven strong motion records obtained during the 1994 Northridge earthquake. The resulting fourteen ground motion records are selected from closely spaced recording stations located at sites with nearly similar soil conditions and nearly equal distances from the surface projection of the fault rupture plane that triggered the earthquake. However, the time-history profile and intensity of the individual ground motion records show considerable difference from one recording site and orientation to the other. The differences in the ensemble of ground motion records represent a measure of the aleatory uncertainty in the input ground motion to a structural system located within the same geographic area due to the site location and orientation of the structure. Aleatory uncertainty is inherent in nature and cannot be influenced (i.e., reduced) by increasing the number or quality of observations.

The FE model used in application A (see Section 7.1) is subjected to the ensemble of 14 ground motion records, each scaled to represent 7 seismic hazard levels in application C. The effect of the complexity in the ground motion scaling technique is explored by investigating two scaling procedures to compute two distinct sets of seismic intensity measures (presented in Section 7.3.2). The FE model of the test-bed structural system is then subjected to the ensemble of scaled ground motion records. The results from the simulations are used to construct fragility curves for each of four collapse limit states (defined in Section 7.3.3). Each fragility curve represents the conditional probability of reaching the corresponding limit state given the value of the adopted seismic intensity measure corresponding to a specified hazard level. An empirical probability is defined as the number of simulations in which the corresponding limit state is reached divided by the total number of simulations per hazard level, i.e., 14 in this application. Due to the large number of simulations involved and the associated cost in terms of computational time, the probabilistic analysis is conducted for the FE model representing the one-story test-bed structural system previously defined in Section 7.1.

7.3.1 Selection and Characteristics of Ground Motion Records

A building site location is considered in the region affected by the Northridge (1994) earthquake in Los Angeles. The selected building site is located near the intersection of Golden State Highway (Interstate 5) and the San Diego Freeway (Interstate 405), and has the latitude and longitude coordinates of 34.3(N) and -118.5(W), respectively, 43.0 km away from the epicenter of the earthquake. Ground motion acceleration records obtained from seven recording stations during the earthquake have been documented and used without scaling in Ghannoum (2007) and Moehle et al. (2005). These records were utilized in a preliminarily exploration of the influence of the orientation and site-to-site variability of ground motion records from the same earthquake (i.e., intra-event variability) on the dynamic behavior and simulated collapse of a three-story RC frame structural system with shear-deficient reinforcement in two out of four RC columns (Moehle et al. 2005). The selected recording station sites are all closely located within a distance of 5.2 to 6.5 km from the fault rupture plane, and have nearly similar soil conditions and NEHRP soil classification C and D (ICC 2003). The two orthogonal components of the horizontal ground

motion at each recording station yield a total of 14 records. The locations of the selected building site and recording stations are indicated on the map of the earthquake locality in Figure 7.21. The recording station designations and site information are listed in Table 7.7.

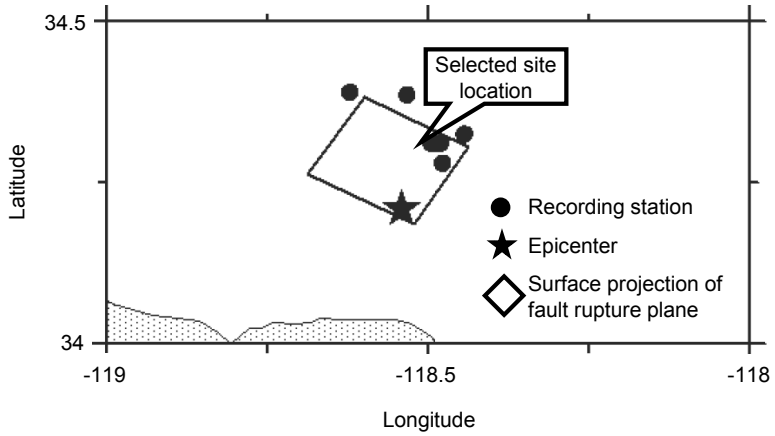

Fig. 7.21 Northridge (1994) earthquake locality showing recording stations (Moehle et al. 2005) and selected building site location.

Table 7.7 Summary of ground motion recording stations used in application C.

Recording station	Code	R_{ru} [km]*	V_{S30} [m/s]**
Jensen Filter Plant	JEN	5.4	373
Newhall Fire Station	NWH	5.9	269
Newhall West Pico Canyon Road	WPI	5.5	286
Rinaldi Receiving Station	RRS	6.5	282
Sylmar Converter Station	SCS	5.3	251
Sylmar Converter Station East	SCE	5.2	371
Sylmar Olive Grove Medical Center	SYL	5.3	441

* Distance from fault rupture plane

** Average shear-wave velocity in the top 30 m of soil

The horizontal ground motions are recorded in two orthogonal directions, which are not coincidental at each recording station. Hence, the two components of each record are referred to as "Component 1" and "Component 2." Components 1 are chosen as the direction per record in which the elastic spectral acceleration response is higher for the test-bed structural system. An average value of the elastic spectral acceleration response $S_a(\overline{T}_1,5\%)$ is computed for a vibration period range of 0.121–0.192 sec, corresponding to the FE model's fundamental vibration period with the diagonal strut elements included and removed, respectively. These elastic spectral acceleration values are used in comparing and classifying the ground motion components in Table 7.8, as well as in the scaling of individual ground motion components in the next section. The elastic spectral acceleration responses of each ground motion component group are illustrated in Figure 7.22. The values of the elastic spectral acceleration and peak ground acceleration corresponding to each ground motion component are listed in Table 7.8.

It can be observed from both Table 7.8 and Figure 7.22 that the intra-event variability significantly affects the characteristics of these ground motion components. For example, the elastic spectral acceleration value for JEN292 is nearly double that of its orthogonal component JEN022, and nearly triple that of WPI046 in the same component group (see Table 7.8). It can also be observed that the spread in the elastic spectra of individual ground motion components around the mean spectra generally increases as the fundamental vibration period increases, i.e., with the expected progression of damage and element removal from the FE model (see Fig. 7.22). It can also be observed that NWH090 is classified as a Component 1, while SYL090, measured in the same orientation, is classified as a Component 2 because the elastic spectral acceleration response of NWH090 and SYL360 records are higher than those of NWH360 and SYL090 records, respectively (see Table 7.8). These observations suggest that there are no clear independent effects of site location and measurement orientation, and that an interaction effect between these two factors exists.

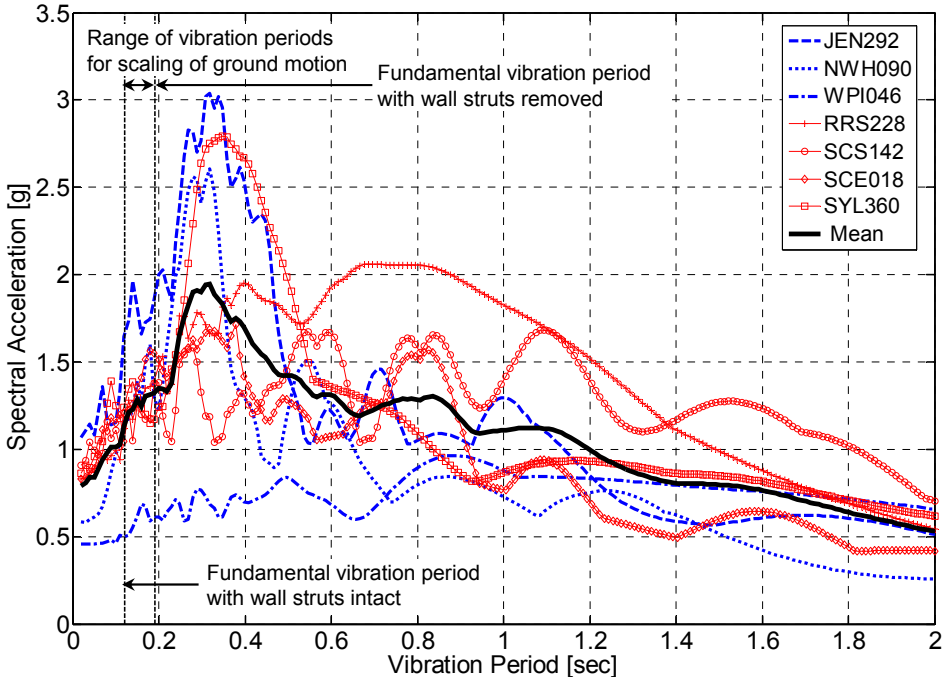

(a) Components 1

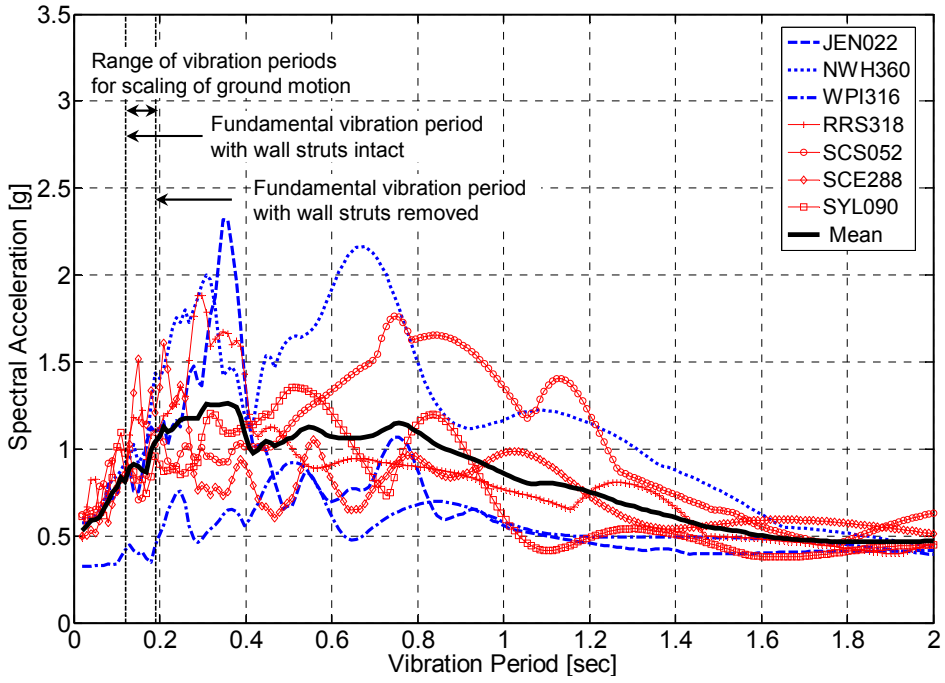

(b) Components 2

Fig. 7.22 Elastic 5%-damped response spectra of records used in application C.

Table 7.8 Unscaled seismic intensity measures of records used in application C.

Component 1			Component 2		
Record	PGA [g]	$S_a(\overline{T}_1,5\%)$ [g]	Record	PGA [g]	$S_a(\overline{T}_1,5\%)$ [g]
JEN292	1.023870	1.8011	JEN022	0.570622	0.9417
NWH090	0.583030	1.3155	NWH360	0.589780	1.0988
WPI046	0.454930	0.5943	WPI316	0.325431	0.4173
RRS228	0.825195	1.2973	RSS318	0.486504	1.0854
SCS142	0.897237	1.2291	SCS052	0.612467	0.8901
SCE018	0.828279	1.3825	SCE288	0.493035	1.2162
SYL360	0.843306	1.2507	SYL090	0.604490	0.8726

7.3.2 Hazard-Specific Scaling Procedures for Ground Motion Records

In the present application, each component of the ground motion records presented in the previous section is treated as an independent ground motion record. The intra-event variability in the time-history profile between individual records is thus considered due to site location and building orientation combined. The scaling of individual components is based on the USGS uniform hazard curves for seismic intensity measures (USGS 2002). Two different ground motion scaling procedures are investigated to explore the influence of the complexity in the scaling procedure on the robustness of the fragility analysis. The first procedure is based on matching the PGA as the adopted seismic intensity measure of individual records (see Table 7.8) to the hazard-specific values listed in Table 7.9. The second procedure is based on matching the magnitude of the system-specific elastic spectral acceleration response $S_a(\overline{T}_1,5\%)$ as the adopted seismic intensity measure of individual records (see Table 7.8) to the hazard-specific values listed in Table 7.9. The hazard-specific elastic spectral acceleration values are linearly averaged from the two values computed at approximate fundamental vibration periods of 0.1 and 0.2 sec to represent the change in stiffness of the FE-simulated structural system upon removal of the diagonal struts, as previously discussed in Sections 7.2.3 and 7.3.1. The first procedure is thus less complex than the second one, since it does not consider the dynamic characteristics of the

structural system in assessing the seismic intensity measure corresponding to each hazard level, and is therefore more straightforwardly appealing to use. The second procedure involves the estimation of the structural system's dynamic properties and expected progression of major local collapse events leading to potential global collapse before selecting the ground motion scaling factors. This procedure may be made even more complex if the mechanism of collapse is significantly sensitive to the values of the scaling factors being computed. In the present application, the significant difference in lateral stiffness between the URM wall and the RC frames result in collapse always being initiated in the URM walls.

Table 7.9 Hazard-specific seismic intensity measures at selected building site location.

Hazard Level	1/50	2/50	3/50	5/50	10/50	20/50	50/50
RP [years]	4975	2475	1642	975	475	224	72
PGA [g]	1.8407	1.5887	1.4344	1.2339	0.9676	0.6790	0.2706
$S_a(0.1,5\%)$ [g]	3.6857	3.1366	2.7767	2.3784	1.8124	1.2484	0.5058
$S_a(0.2,5\%)$ [g]	4.6824	3.8789	3.4726	2.9261	2.2447	1.5323	0.6389
$S_a(\overline{T}_1,5\%)$ [g]	4.1841	3.5078	3.1247	2.6523	2.0286	1.3904	0.5724

7.3.3 Definition of Collapse Limit States

Four collapse limit states are investigated in application C, defined as follows:

1. In-plane failure of the URM wall: defined by the collapse and removal of at least one diagonal strut from the FE model;
2. Out-of-plane collapse of the URM wall: defined by the collapse and removal of both diagonal struts from the FE model;
3. Partial collapse of the structural system: defined by the collapse and removal of the beam-column elements representing at least two RC columns;
4. Complete collapse of the structural system: defined by the collapse and removal of the beam-column elements representing all six RC columns.

The in-plane failure of the URM wall refers to major, continuous diagonal cracking and/or corner crushing developing in one and/or opposite directions of the URM wall that effectively eliminate the URM wall's capacity to transfer lateral loads while maintaining a reduced capacity to transfer gravity loads and out-of-plane bending moments. The out-of plane collapse of the URM wall refers to disintegration and loss of the URM wall integrity altogether. During the analysis it was observed that, for the structural system being considered, partial collapse (limit state 3) almost always led to complete collapse (limit state 4), due to the structural system's inability to dynamically redistribute gravity loads after the loss of the URM wall and two of its RC columns. Therefore, collapse limit state 3 can be considered redundant for this specific application.

7.3.4 Results and Discussion

The empirical probability of reaching each of the four previously defined collapse limit states in the simulated one-story test-bed structural system due to exposure to a seismic event similar to the 1994 Northridge earthquake in the neighborhood of the building site location is illustrated using the multiple fragility curves in Figure 7.23. Figure 7.23a represents the fragility curves conditioned on the specified hazard levels defined in terms of PGA. It can be observed that even at relatively frequent hazard levels (20/50), the probability of in-plane failure of the URM wall exceeds 0.1, and this probability quickly approaches near-certainty (>0.9) as the hazard level becomes rarer than 3/50. The probability of out-of-plane collapse of the URM wall exceeds 0.1 only at hazard levels rarer than 10/50, and would only exceed 0.9 at a hazard level rarer than 1/50. As discussed earlier, the probabilities of partial and complete collapse are almost identical, with one exception at the 2/50 hazard level; hence only the more important limit state of complete collapse is referred to in this discussion. The probability of complete collapse remains lower than 0.2 for frequent hazard levels up to 3/50 or less. It then increases steadily and reaches a maximum of 0.57 at the 1/50 hazard level.

Figure 7.23b represents the fragility curves conditioned on the specified hazard levels defined in terms of the elastic spectral acceleration. It can be observed that the probabilities of in-plane failure and out-of-plane collapse in the URM wall, as well as partial collapse in the RC

frame are non-zero even at the most frequent hazard level of 50/50 (i.e., the ground motion scaling factors for the 50/50 hazard level are generally higher when computed based on the elastic spectral acceleration than when based on the PGA). The probability of in-plane URM wall failure increases steadily, and rapidly reaches approximately 0.8 at the 10/50 hazard level, after which it exhibits little to no increase before increasing again to 1.0 at the 1/50 hazard level. The probability of out-of-plane collapse of the URM wall, however, increases steadily and rapidly to 0.5 at the 10/50 hazard level. Afterwards, it increases slowly up to the 2/50 hazard level, before resuming a rapid increase to exceed 0.9 at the 1/50 hazard level. The probabilities of partial and complete collapse are identical for hazard levels less frequent than 50/50. The probability of complete collapse increases steadily from 0.0 at the 50/50 hazard level to 0.43 at the 5/50 hazard level; afterwards it exhibits little increase and momentarily stabilizes at 0.5 between the 3/50 and 2/50 hazard levels, before exhibiting a rapid increase to approximately 0.7 at the 1/50 hazard level.

The fragility curves illustrated in Figure 7.23 suggest that the effect of intra-event variability is an important factor on the ability to reliably predict the progressive collapse outcome of the one-story test-bed structural system. The structural system has been subjected to ground motion components recorded at multiple orientations in similar site locations and soil conditions during the same earthquake. Nevertheless, these components represented different intensities and exhibited large variation in a time-history profile and the elastic response spectra. The variability in the ground motion components is reduced by scaling them to common intensity measures (i.e., PGA and elastic spectral acceleration) at each hazard level for the selected building site location. However, for each hazard level between 10/50 and 2/50, the probability of reaching each limit state is larger than zero and less than 1.0. Thus, the simulation results using at least one scaled ground motion component have reached all limit states, whereas the results using another similarly scaled component have not reached any. These results emphasize the paramount importance of addressing this intra-event variability in a fundamental manner within the framework of PBEE in order to develop consistent and unified selection and scaling procedures for the ground motion records being used in computational simulations of structural collapse.

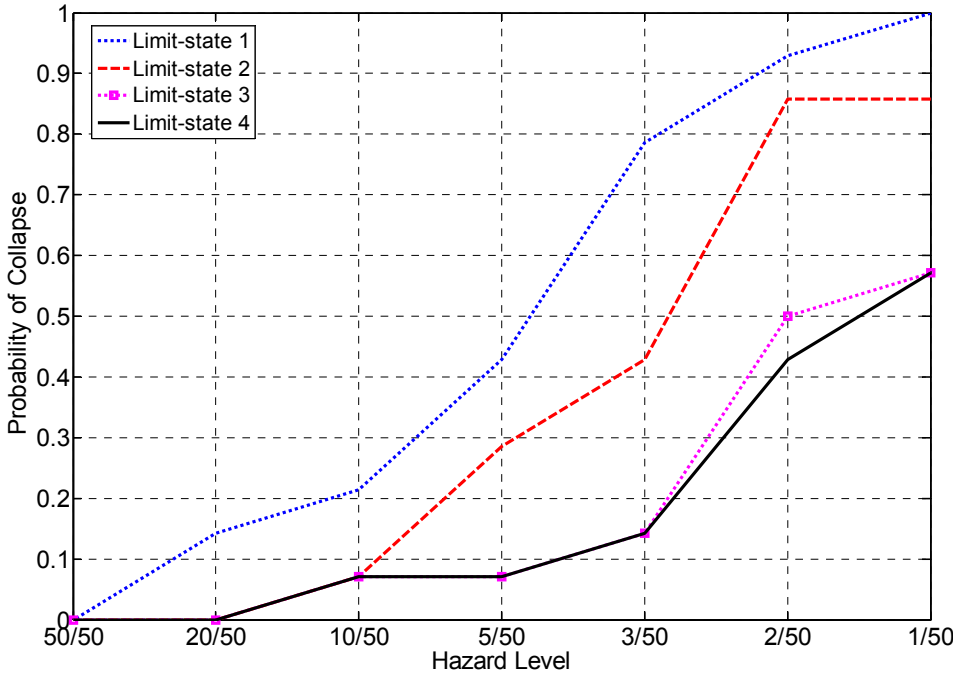

(a) Hazard levels characterized by PGA

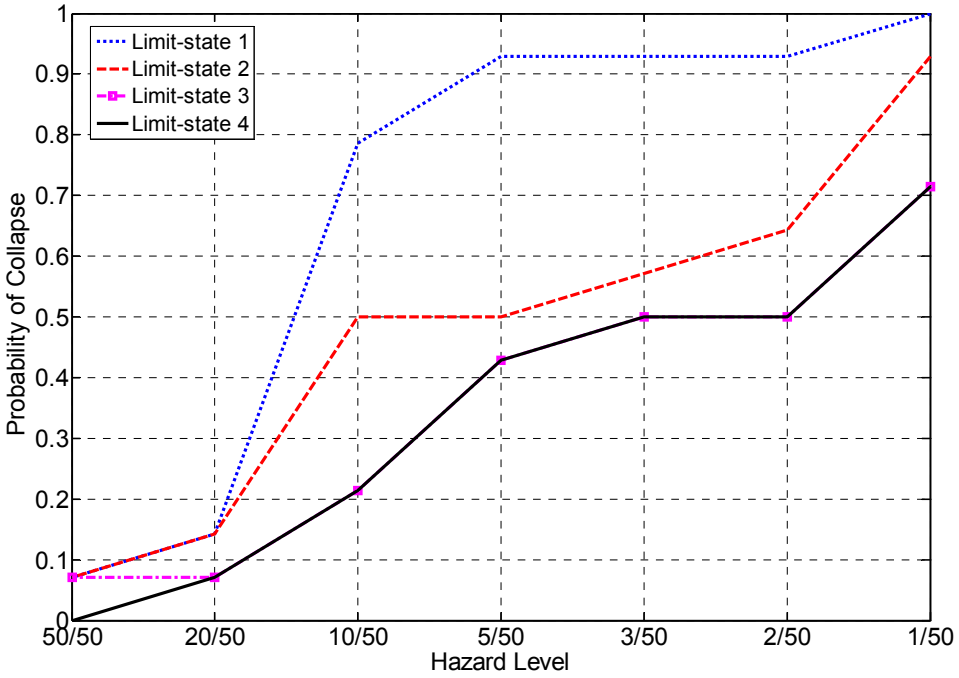

(b) Hazard levels characterized by $S_a(\overline{T}_1,5\%)$

Fig. 7.23 Fragility curves for individual collapse limit states of application C.

The comparison between Figure 7.23a and b is represented in Figure 7.24, where the fragility plots for limit states 1 and 4 are compared for the two ground motion scaling procedures. In this comparison, the hazard level is represented by the corresponding return period in years, shown in linear scale in Figure 7.24a and in logarithmic scale in Figure 7.24b. This comparison reveals that the computed probabilities of reaching each limit state are generally higher or equal for both hazard levels when using the elastic spectral acceleration as an intensity measure than when using the PGA. This means that the use of PGA for estimating the expected collapse losses due to seismic events, although temptingly less complex, is likely to result in lower predicted probabilities of collapse in this application. This is because the computed ground motion scaling factors for each hazard level are found to be generally higher when computed based on the elastic spectral acceleration for the test-bed structural system than when based on the PGA. In addition, the resulting fragility curves in Figure 7.24a exhibit more similar trends with the increase in return period using $S_a(\overline{T}_1,5\%)$ scaling for both limit states, consisting of convex functions whose slopes are monotonically decreasing (except for the last point which represents a very rare event, i.e., once in 4750 years). Meanwhile, the PGA-scaled fragility curves, with the exception of the longest return period, exhibit dissimilar trends: an approximately linear trend for limit state 1 where the slope alternately increases and decreases in between return periods, and a concave function for limit state 4 whose slope is monotonically increasing. This discrepancy in trends may be due to the elastic spectral acceleration being closely related to the dynamic characteristics of the structural system in addition to the ground motion characteristics, and having thus more relevance to the structural system's seismic behavior. This is especially so for the current test-bed structural system, since it does not have the added complexity of higher modes of vibration and its dynamic response is foremost controlled by its fundamental mode and period of vibration.

The comparison between the fragility curves in Figure 7.24b with the return periods plotted using a logarithmic scale exhibits different characteristics. With the exception of the shortest and the longest return periods, the $S_a(\overline{T}_1,5\%)$-scaled fragility curves still exhibit parallel trends consisting of convex functions with monotonically decreasing slopes for both limit states. Hence, early increases in the return period's logarithm result in relatively large increases in the computed probability of collapse, while later increases in the return period's logarithm result in

limited increases in this probability. Moreover, the PGA-scaled fragility curves now exhibit parallel trends consisting of concave functions with monotonically increasing slopes. Contrary to the $S_a(\overline{T}_1,5\%)$-scaled fragility curves, early increases in the return period's logarithm result in a relatively small increase in the computed probability of collapse, while later increases in the return period's logarithm result in relatively large increases in this probability. The observations in the current paragraph emphasize the previous conclusion about the scaling based on the elastic spectral acceleration resulting in higher estimates of the probability of collapse than the scaling based on the PGA for this application. At very short (i.e., <250) and very long (i.e., >2500) return periods, the aforementioned opposite trends result in the fragility results from the two different scaling procedures intersecting for limit state 1 and becoming commensurate for limit state 4.

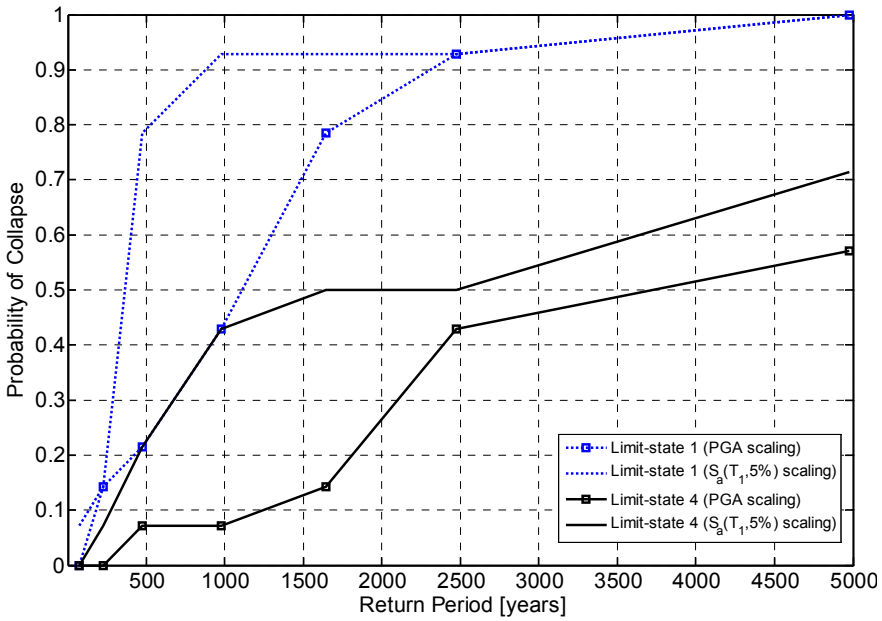

(a) Linear scale for return period

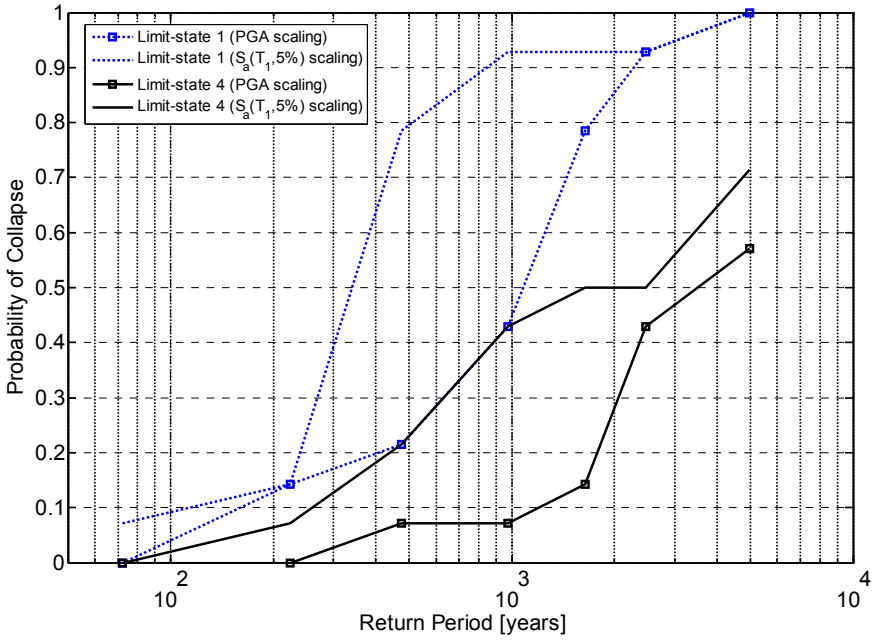

(b) Logarithmic scale for return period

Fig. 7.24 Comparison between PGA- and $S_a(\overline{T}_1,5\%)$-scaled fragility curves.

7.4 SUMMARY

In this chapter, three application studies were presented for progressive collapse FE simulations using the computational developments presented in the previous chapters of this report. The object of each of the three applications was one of two RC frame/URM wall test-bed structures located at a specific site in Los Angeles. In the first application, deterministic computational simulations were successfully performed for progressive collapse in a one-story test-bed structural system consisting of three RC frames connected by a RC slab and infilled with a URM wall in the middle frame. The FE model of the structural system was calibrated using results from a physical test structure previously subjected to shake-table experiments. The simulations were performed using the component models developed to predict damage progression and gravity-load collapse due to seismically deficient RC column details that were artificially introduced into the FE structural model. The hitherto modified FE model was subjected to two hazard-specific levels of scaled ground motion record from Düzce (1999) earthquake. Direct element removal of the collapsed columns and URM wall was successful in simulating the dynamic force redistribution to the intact part of the computationally modeled structural system and the resulting momentary changes in its fundamental period of vibration. The two ground motion scales resulted in significant differences in the predicted collapse sequence and eventual global collapse mechanism, emphasizing the sensitivity of the response to the input ground motion intensity and the need for a feasible probabilistic approach in the context of performance-based evaluation.

In the second application, a deterministic computational simulation and a sensitivity study were successfully performed for progressive collapse response in a five-story test-bed structural system consisting of one three-bay RC frame infilled with a URM wall in the middle bay. First, a set of reference system parameters (i.e., mass, URM wall stiffness and viscous damping) was defined for the structural system. Next, a deterministic progressive collapse simulation established the reference progressive collapse response of the FE-modeled five-story structural system subjected to a ground motion record from the 1999 Düzce earthquake, which has been scaled in accordance with a reference hazard level. The effect of collapse progression on the simulated individual story and overall drifts, the evolution of modal vibration periods, and the estimated time at incipient collapse were investigated. Finally, a deterministic sensitivity

analysis was conducted using the Tornado diagram analysis method to assess the influence and relative importance of uncertainty in the aforementioned system parameters and hazard level (i.e., ground motion intensity factor) on the variables characterizing the simulated progressive collapse response of the FE model, namely the simulated time at incipient collapse and the maximum first-story drift. A comparison of the results indicated that the use of time at incipient collapse is more effective in assessing the sensitivity of progressive collapse to—and demonstrates better correlation with the induced changes in—the uncertain parameters. The analysis of the sensitivity results identified the uncertainty in ground motion intensity and the associated hazard level as the most important sources of uncertainty in the outcome of the progressive collapse simulation. Moreover, for the given input seismic event, the most important uncertain system parameter was concluded to be the stiffness of the URM wall.

In the third application, a probabilistic study was performed to assess the influence of intra-event variability (i.e., site location and building orientation) on the outcome of progressive collapse simulations of the one-story test-bed structural system at different seismic hazard levels. Fourteen ground motion records, occurring in different orientations at closely spaced recording stations located in sites with similar soil conditions during the Northridge (1994) earthquake, are scaled to correspond to seven specified hazard levels at the building site location. Two sets of scaled ground motion records were obtained using as seismic intensity measures either the PGA or the elastic 5%-damped first-mode spectral accelerations. Four limit states characterizing the extent of collapse in the FE-modeled structural system were developed. An empirically computed probability of reaching each limit state in the FE model conditioned on each hazard level was defined and used to construct corresponding fragility curves for the test-bed structural system. The results indicated that intra-event variability is an important factor in determining the outcome of computational progressive collapse simulations even for ground motion records obtained from closely spaced locations and scaled to correspond to the same hazard level. In addition, the computed fragility curves resulted in higher estimates of the progressive collapse probability for all limit states of the test-bed structural system when the hazard levels were defined using the elastic spectral acceleration than when they were defined using the peak ground acceleration.

8 Summary, Conclusions, and Future Extensions

8.1 SUMMARY

Computational tools for the simulation of progressive collapse, divided into component and system levels, are developed. Development, implementation, and calibration of constitutive laws and damage models for material and cross-section behavior at the component level are discussed in Chapters 2–4. Component models are combined to model the behavior of reinforced concrete (RC) columns with seismically deficient details in Chapter 5, where simulated results are compared with results from laboratory tests. An algorithm for the identification and direct removal of collapsed elements from a structural model during a computational simulation is developed, implemented, and demonstrated using a benchmark problem in Chapter 6. The component models and element removal algorithm are used together to conduct system-level progressive collapse studies in Chapter 7.

Three analytical material models and one confined cross-section model are introduced to represent the effect of seismically deficient details and retrofit by fiber-reinforced polymer (FRP) composites on the hysteretic behavior for RC columns whose collapse is dominated by axial-flexure interaction. An analytical constitutive material model is developed, implemented, and calibrated for the axial stress-strain behavior of longitudinal reinforcing bars susceptible to buckling. This model accounts for the lateral restraining effect of the transverse reinforcement in computing the critical length and stress at the onset of buckling. Moreover, the model considers a consistent strain decomposition approach to simulate the post-buckling softening behavior, and incorporates hysteretic stress reduction to predict steel bar fracture using a damage model based

on low-cycle fatigue. It is calibrated using published experimental data for reinforcing steel bars subjected to monotonic and cyclic loads. A second analytical constitutive material model is developed, implemented, and calibrated for the axial stress-strain behavior of lap-spliced reinforcing bars. This model combines a strain decomposition approach based on the equilibrium of axial and shear bond stresses along the splice region with a developed constitutive law for hysteretic bond-slip behavior of the lap-splice. This constitutive law represents a hysteretic bond-slip relationship, which accounts for the effect of confining stress and hysteretic degradation on the bond-slip behavior. The predictions of the calibrated lap-splice material model compares well with published experimental data of reinforcing bars embedded in concrete. A third analytical constitutive model is developed, implemented, and calibrated for the hysteretic behavior of FRP-confined, steel-confined, and unconfined concrete. This model enforces lateral strain compatibility between the confined concrete and the confining medium (external jacket or internal transverse reinforcement), and accounts for hysteretic strength degradation using a stress-reduction factor and a damage index based on dissipated energy and maximum compressive strain. This analytical model is calibrated using published experimental data of concrete cylinders subjected to monotonic and cyclic uniaxial compressive loading.

A fourth analytical model is implemented to describe the spatial distribution of confining stresses within a fiber-discretized FRP-confined circular RC cross section subjected to general axial and flexural loads. This analytical model is based on the equilibrium of bond stresses between the cross section perimeter and the confining jacket, and the derived confining stress distribution is shown to be equivalent to a power law. The predictions of this cross-section model compare well with laboratory test measurements from a specifically designed series of four column tests. Two material-aggregated damage indices are proposed for describing the degradation in axial force and bending moment strength of fiber-discretized cross sections, and to serve as removal criteria for RC columns whose collapse is dominated by flexure-axial interaction. An existing analytical model is adopted from the literature to establish element removal criteria for RC columns whose collapse is dominated by shear-axial interaction.

The implementation of the computational development is carried out in an object-oriented environment using the software platform OpenSees. The details of the object-oriented implementation of the component-level developments, the resulting hierarchical class

relationships, and the capabilities for expanding the existing library to include further component models are comprehensively discussed.

The implemented constitutive material and cross-section models are successfully integrated to develop computational models of previously tested seismically deficient RC columns. The experimentally observed response of as-built and FRP-retrofitted RC column specimens from four published experimental programs is satisfactorily reproduced computationally. The range of deficient column behavior examined in the experimental programs include the failure of transverse steel reinforcement, the loss of confinement to the concrete core, the failure of lap-splices, the buckling of longitudinal bars, in addition to the fracture and rupture in internal spirals and external FRP composites used for retrofit. The relationship between the proposed cross-section damage indices and the observed collapse limit states and damage progression with the increase in lateral displacement values is investigated.

The system-level developments include the formulation, implementation, and computational verification of a dynamically compatible computational element removal algorithm. The mechanics of removing a collapsed finite element (FE) from the structural model during an ongoing simulation are formulated using the principles of dynamic equilibrium, which characterize how this removal affects the transient kinematics of the damaged structural system and the dynamic redistribution of forces. The implemented element removal algorithm accounts for the redistribution of internal forces and masses from collapsed elements and the removal of applied external loads from removed components, in addition to independently tracking the motion of the collapsed elements in order to detect subsequent collision with the intact part of the structural model. The numerical robustness of the implemented element removal algorithm is computationally tested and verified using an idealized structural system of trussed cantilever beams subjected to seismic excitation. The results from the computational study confirm the numerical robustness and functionality of the implemented algorithm, while highlighting the sensitivity of the progressive collapse outcome to the uncertainty in the structural system parameters.

The component-level and system-level developments are combined to conduct three demonstration applications of progressive collapse FE simulations of seismically deficient RC frame structures infilled by unreinforced masonry (URM) walls. Two test-bed structural systems

are investigated, namely a one-story and a five-story RC frame infilled with URM walls representative of residential construction details common in the 1960s. In the first application, a deterministic computational simulation is successfully performed for the progressive collapse in the one-story test-bed structural system subjected to two hazard-specific levels of scaled ground motion using a record from the Düzce (1999) earthquake. The results from the FE model of the structural system are compared with results from a previous shake-table experiment, and then modified to simulate seismically deficient RC column details. The two ground motion scales result in significant differences in the predicted collapse sequence and eventual global collapse mechanism. In the second application, a deterministic computational simulation and a sensitivity study are performed for the progressive collapse response in the five-story test-bed structural system. The deterministic progressive collapse simulation establishes the response of the structural system subjected to a ground motion record from the Düzce (1999) earthquake, relative to a reference set of typically unknown system parameters (i.e., mass, URM wall stiffness, and viscous damping) and seismic hazard level. The relative importance of the uncertainty in the unknown parameter values is then established using the Tornado diagram method as a form of deterministic sensitivity analysis. In the third application, a probabilistic study is performed to assess the influence of intra-event variability (i.e., site location and building orientation) on the outcome of progressive collapse simulations of the one-story test-bed structural system, assumed to exist in a building site located in Los Angeles County and subjected to different seismic hazard levels. Fragility curves are developed for four progressive collapse limit states using an empirically defined probability of being reached during the FE simulation, conditioned on seven different hazard levels. A set of fourteen ground motion records obtained from closely spaced recording sites during the Northridge (1994) earthquake is used. The probabilistic study additionally investigates the effect of the ground motion scaling method by considering as seismic intensity measures both the peak ground acceleration and the first-mode elastic spectral acceleration, resulting in two independent sets of scaled records and two corresponding sets of fragility curves.

8.2 CONCLUSIONS

The major findings of this report can be listed in the following general points. It should be noted that these conclusions are limited to the specific cases studied:

- The distribution and effect of confining stresses in a RC cross section can be accurately simulated using the proposed analytical model for fiber-discretized cross sections. In as-built columns with seismically deficient details, the effect of the confining stresses is important in predicting the non-ductile stress-strain response of constituent fibers. In FRP-retrofitted RC columns, the effects of confining stresses and the stress state in the confining FRP composite are important in estimating the improved strength and ductility.
- The confinement-sensitive uniaxial behavior of concrete, buckling-prone longitudinal steel bars, and lap-spliced steel bars can be accurately modeled using the developed and calibrated constitutive material models.
- In a study of as-built and FRP-retrofitted seismically deficient RC columns, the developed constitutive material and cross-section models successfully reproduce the lateral load capacity, the deformation level at the initiation of failure in non-ductile details, the effects of FRP-retrofitting, and the fracture and the rupture in the transverse steel and the FRP reinforcement.
- The proposed cross-section damage indices exhibit good correlation with the observed collapse limit states and damage progression in modeled RC column specimens whose collapse is dominated by axial-flexure interaction.
- Internal force redistribution from collapsed structural elements can be simulated by considering the dynamic equilibrium of forces and the kinematically compatible transient behavior of the damaged structural system as it tries to reach a new equilibrium state. The dynamic amplification of element deformation demands associated with element removal suggests that progressive collapse assessment methods based on alternative path analysis or similarly involving quasi-static redistribution of internal forces are not conservative in their approximation. This conclusion is limited to cases where structural members collapse suddenly, which has not always been demonstrated in laboratory seismic tests.
- The computational implementation of the developed component models and element removal algorithm exhibits a robust and stable numerical behavior, and is made readily

extensible by its object-oriented architecture.

In addition, the major findings drawn from the study of the investigated test-bed structural systems can be summarized in the following points:

- The presence of an infill wall plays a leading role in determining the strength, stiffness, and seismic demand forces and displacements of RC frame/URM wall structural systems. Being significantly stiffer than bare RC frames, the resulting decrease in the fundamental vibration period affects the seismic displacement and demand forces, the majority of which are resisted by the relatively stiffer URM wall until its collapse. The collapse of the URM wall significantly increases the fundamental vibration period of the structural system and modifies its dynamic characteristics and the resulting seismic force and deformation demands.
- The relatively low ductility of the URM wall results in suddenly increased force demands on the columns of the infilled frame after the URM wall collapses, and subsequent localization of damage and deformation demands leading to the possible formation of soft-story collapse mechanisms.
- The use of the time at incipient collapse to quantify the effect of uncertain system parameters on the progressive collapse response and to conduct sensitivity analysis is a more effective measure, both theoretically and practically, than the use of maximum inter-story drifts.
- Among uncertain system parameters, the stiffness of the URM wall is found to have the largest influence on the outcome of a progressive collapse simulation using a specific ground motion record, followed by the system mass and then, with minimal influence, the viscous damping ratio.
- The aforementioned sensitivity of progressive collapse to the change in the URM wall stiffness, within essentially its entire uncertain range, is approximately comparable to the sensitivity to a relatively small change in the considered seismic hazard level, namely a ±1% probability of being exceeded in 50 years.
- The fragility analysis results indicate that intra-event variability is a very important phenomenon in determining the outcome of computational progressive collapse simulations.

- The simulated fragility curves exhibit significant sensitivity to the ground motion scaling procedure used. The use of elastic spectral acceleration results in higher estimates of the progressive collapse probability than the use of peak ground acceleration.

8.3 FUTURE EXTENSIONS

This study can be further pursued in the following directions:

- Development of an analytical model for RC columns whose collapse is dominated by shear-axial interaction based on constitutive modeling and computational mechanics.
- Implementation of methods to modify the type or internal degrees of freedom of an element during the course of an ongoing simulation, e.g., conversion of a beam-column element to a truss element after the complete loss of flexural capacity at the ends of the original beam-column element.
- Development of component models for modeling the degrading behavior and collapse criteria of structural members other than these considered here, such as beam-column joints and the membrane action of floor elements.
- Modification of the OpenSees data structure to allow the automatic time-efficient identification of dangling nodes after element removal.
- In-depth investigation of the numerical properties of the equations of motions in mathematical models representing progressively collapsing systems as regards to their numerical stability and accuracy, especially with respect to the effect of viscous damping coefficients on higher modes of vibration.
- Implementation of new methods in OpenSees to enable automatic time-efficient identification of collisions by comparing, after each converged time-step, the deformed geometry of the damaged FE model and the collapsed elements during their free-fall.
- Implementation of a 3D confined cross-section model for use with recently developed 3D strut-and-tie models for explicit modeling of the out-of-plane collapse of URM walls.
- Optimization of the numerical implementation of the developed component models to enhance the numerical efficiency and reduce the simulation times for the FE models containing large numbers of degrees of freedom. This optimization is of particular

importance given the envisioned probabilistic assessment framework requiring an extensive number of computational simulations, which can be rendered unfeasible by the associated processing time.

- Investigation of other commonly used building structural systems to identify the system parameters significantly affecting their progressive collapse behavior, and to establish the sensitivity and the order of importance of the different uncertain parameters governing the structural response.
- Research on the reliability of existing ground motion selection and scaling methods, leading to the establishment of system-specific procedures for the selection and scaling of appropriate records for use in simulation-based progressive collapse assessment.
- Identification of an appropriate probabilistic performance-based earthquake engineering framework for reliably conducting progressive collapse simulation-based assessment. This framework should identify the sufficient number and characteristics of ground motion records to be used and establish clear provisions to account for unknown system parameters.

References

ACI (1963). *Standard Building Code Requirements for Reinforced Concrete.* ACI 318-63. American Concrete Institute, Detroit, Michigan, USA.

ACI (2002). *Building Code Requirements for Structural Concrete and Commentary.* ACI 318-02 and ACI 318R-02. American Concrete Institute, Farmington Hills, Michigan, USA**.**

Ahmad, S.H. and Shah, S.P. (1982). Stress-Strain Curves of Concrete Confined by Spiral Reinforcement. *ACI Journal* **79**(6): 484-490.

Altoontash, A. (2004). Simulation and Damage Models for Performance Assessment of Reinforced Concrete Beam-Column Joints. Ph.D. Report, Stanford University.

Ang, A.H.-S. and Tang, W.H. (1975). *Probability Concepts in Engineering Planning and Design* - Volume 1: Basic Principles. John Wiley and Sons.

Attard, M.M. and Setunge, S. (1996). Stress-Strain Relationship of Confined and Unconfined Concrete. *ACI Materials Journal* **93**(5): 432-442.

Attolico, A., Biondi, S., Nuti, C. and Petrangeli, M. (2000). Influence of Buckling of Longitudinal Rebars in Finite Element Modeling of Concrete Structures Subjected to Cyclic Loading. *Proceedings - 12th World Conference on Earthquake Engineering*. Auckland, New Zealand, NZSEE Silverstream.

Ayoub, A. and Filippou, F.C. (1999). Mixed Formulation of Bond-Slip Problems under Cyclic Loads. *ASCE Journal of Structural Engineering* **125**(6): 661-671.

Bae, S., Mieses, A.M. and Bayrak, O. (2005). Inelastic Buckling of Reinforcing Bars. *ASCE Journal of Structural Engineering* **131**(2): 314-321.

Balan, T.A., Filippou, F.C. and Popov, E.P. (1998). Hysteretic Model of Ordinary and High-Strength Reinforcing Steel. *ASCE Journal of Structural Engineering* **124**(3): 288-297.

Bauschinger (1886). Repeated Loads. *Engineer*.

Bayrak, O. and Sheikh, S.A. (2001). Plastic Hinge Analysis. *ASCE Journal of Structural Engineering* **127**(9): 1092-1100.

Bazant, Z.P., Gettu, R., Jirasek, M., Barr, B.I.G., Carol, I., Carpinteri, A., Elices, M., Huet, C., Mihashi, H., Nemati, K.M., Planas, J., Ulm, F.-J., Van Mier, J.G.M., Van Vliet, M.R.A., Burtscher, S., Chiaia, B., Dempsey, J.P., Ferro, G., Gopalaratnam, V.S., Prat, P., Rokugo, K., Saouma, V.E., Slowik, V., Vitek, L. and Willam, K. (2004). Rilem TC QFS Quasibrittle Fracture Scaling and Size Effect - Final Report. *Materials and Structures/Materiaux et Constructions* **37**(272): 547-568.

Bazant, Z.P. and Oh, B.H. (1983). Crack Band Theory for Fracture of Concrete. *Materials and Structures/Materiaux et Constructions* **16**(93): 155-177.

Berry, M.P. and Eberhard, M.O. (2005). Practical Performance Model for Bar Buckling.*ASCE Journal of Structural Engineering* **131**(7): 1060-1070.

Binici, B. (2005). An Analytical Model for Stress-Strain Behavior of Confined Concrete. *Engineering Structures* **27**(7): 1040-1051.

Binici, B. and Mosalam, K.M. (2007). Analysis of Reinforced Concrete Columns Retrofitted with Fiber Reinforced Polymer Lamina. *Composites Part B: Engineering* **38**(2): 265-276.

Brown, J. and Kunnath, S.K. (2004). Low-Cycle Fatigue Failure of Reinforcing Steel Bars. *ACI Materials Journal* **101**(6): 457-466.

Chang, G. and Mander, J.B. (1994). *Seismic Energy Based Fatigue Damage Analysis of Bridge Columns: Part I - Evaluation of Seismic Capacity*. NCEER Technical Report 94-0006.

Cho, J.-Y. and Pincheira, J.A. (2006). Inelastic Analysis of Reinforced Concrete Columns with Short Lap Splices Subjected to Reversed Cyclic Loads. *ACI Structural Journal* **103**(2): 280-290.

Chopra, A.K. (2001). *Dynamics of Structures: Theory and Application to Earthquake Engineering*. Prentice Hall, Upper Saddle River, NJ, USA.

Chung, H.-S., Yang, K.-H., Lee, Y.-H. and Eun, H.-C. (2002). Strength and Ductility of Laterally Confined Concrete Columns. *Canadian Journal of Civil Engineering* **29**(6): 820-830.

Coffin, J., L.F. (1962). Low Cycle Fatigue -- Review. *Applied Materials Research* **1**(3): 129-141.

Coleman, J. and Spacone, E. (2001). Localization Issues in Force-Based Frame Elements. *ASCE Journal of Structural Engineering* **127**(11): 1257-1265.

Cornelissen, H.A.W., Hordijk, D.A. and Reinhardt, H.W. (1985). Experimental Determination of Crack Softening Characteristics of Normalweight and Lightweight Concrete. in *Fracture Mechanics and Structural Aspects of Concrete*. HERON **31**(2): 45-56.

Crawford, J.E. (2002). *Retrofit Methods to Mitigate Progressive Collapse.* Technical Report TR-02-7. Karagozian & Case, Glendale, CA, USA.

Crisfield, M.A. (1990). Consistent Co-Rotational Formulation for Non-Linear Three-Dimensional Beam Elements. *Computer Methods in Applied Mechanics and Engineering* **81**(2): 131-150.

Crisfield, M.A. and Moita, G.F. (1996). Unified Co-Ratational Framework for Solids, Shells and Beams. *International Journal of Solids and Structures* **33**(20-22): 2969-2992.

Dhakal, R.P. and Maekawa, K. (2002a). Modeling for Postyield Buckling of Reinforcement. *ASCE Journal of Structural Engineering* **128**(9): 1139-1147.

Dhakal, R.P. and Maekawa, K. (2002b). Path-Dependent Cyclic Stress-Strain Relationship of Reinforcing Bar Including Buckling. *Engineering Structures* **24**(11): 1383-1396.

Dhakal, R.P. and Maekawa, K. (2002c). Reinforcement Stability and Fracture of Cover Concrete in Reinforced Concrete Members. *ASCE Journal of Structural Engineering* **128**(10): 1253-1262.

El-Dash, K.M. and Ahmad, S.H. (1995). Model for Stress-Strain Relationship of Spirally Confined Normal and High-Strength Concrete Columns. *Magazine of Concrete Research* **47**(171): 177-184.

Eligehausen, R., Popov, E.P. and Bertero, V.V. (1983). Behavior of Deformed Bars Anchored at Interior Joints under Seismic Excitations. *Proceedings - 4th Canadian Conference on Earthquake Engineering*. Vancouver, BC, Canada 70-80.

Elkhoraibi, T. (2007). Generalized Hybrid Simulation Framework for Structural Systems Subjected to Seismic Loading. PhD Report, University of California, Berkeley.

Ellingwood, B.R. (2006). Mitigating Risk from Abnormal Loads and Progressive Collapse. *Journal of Performance of Constructed Facilities* **20**(4): 315-323.

Elwood, K.J. (2002). Shake Table Tests and Analytical Studies on the Gravity Load Collapse of Reinforced Concrete Frames. PhD Report, University of California, Berkeley.

Elwood, K.J. (2004). Personal Communication.

Elwood, K.J. and Moehle, J.P. (2005). Axial Capacity Model for Shear-Damaged Columns. *ACI Structural Journal* **102**(4): 578.

Engstrom, B., Magnuson, J. and Huang, Z. (1998). Pull-out Bond Behavior of Ribbed Bars in Normal and High-Strength Concrete with Various Confinements. in *Bond Development of Reinforcement*. ACI **SP-118**(10): 215-242.

Fenves, G.L., McKenna, F., Scott, M.H. and Takahashi, Y. (2004). An Object-Oriented Software Environment for Collaborative Network Simulation. *Proceedings - 13th World Conference on Earthquake Engineering*. Vancouver, BC, Canada.

Filippou, F.C. and Fenves, G.L. (2004). Methods of Analysis for Earthquake-Resistant Structures. in *Earthquake Engineering from Engineering Seismology to Performance-Based Engineering*. Bozorgnia, Y. and Bertero, V., Eds. CRC Press.

Filippou, F.C. and Zulfiqar, N. (1990). *Models of Critical Regions in Reinforced Concrete Frames under Earthquake Excitations.* EERC Technical Report 90-06.

Ghannoum, W. (2007). Experimental and Analytical Dynamic Collapse Study of a Reinforced Concrete Frame with Light Transverse Reinforcements. PhD Report, University of California, Berkeley.

Gilmour, J.R. and Virdi, K.S. (1998). Numerical Modeling of the Progressive Collapse of Framed Structures as a Result of Impact or Explosion. *Proceedings - 2nd International PhD Symposium in Civil Engineering*, Budapest, Hungary.

Gomes, A. and Appleton, J. (1997). Nonlinear Cyclic Stress-Strain Relationship of Reinforcing Bars Including Buckling. *Engineering Structures* **19**(10): 822-826.

Grierson, D.E., Safi, M., Xu, L. and Liu, Y. (2005a). Simplified Methods for Progressive-Collapse Analysis of Buildings. *Proceedings - 2005 Structures Congress and the 2005 Forensic Engineering Symposium - Metropolis and Beyond*. New York, NY, USA, ASCE 2279-2286.

Grierson, D.E., Xu, L. and Liu, Y. (2005b). Progressive-Failure Analysis of Buildings Subjected to Abnormal Loading. *Computer-Aided Civil and Infrastructure Engineering* **20**(3): 155-171.

Gupta, A. and Krawinkler, H. (2000). Dynamic P-Delta Effects for Flexible Inelastic Steel Structures. *ASCE Journal of Structural Engineering* **126**(1): 145-154.

Haselton, C.B. and Deierlein, G.G. (2005). Benchmarking Seismic Performance of Reinforced Concrete Frame Buildings. *Proceedings - 2005 Structures Congress and the 2005 Forensic Engineering Symposium - Metropolis and Beyond*. New York, NY, USA, ASCE 1891-1902.

Hashemi, A. and Mosalam, K.M. (2006). Shake-Table Experiment on Reinforced Concrete Structure Containing Masonry Infill Wall. *Earthquake Engineering and Structural Dynamics* **35**(14): 1827-1852.

Hashemi, A. and Mosalam, K.M. (2007). *Seismic Evaluation of Reinforced Concrete Buildings Including Effects of Masonry Infill Walls. PEER Technical Report* 2007/100.

Hashemi, S.A. (2007). Seismic Evaluation of Reinforced Concrete Buildings Including Effects of Masonry Infill Walls. PhD Report, University of California, Berkeley.

Hawkins, N.M., Lin, I.J. and Jeang, F.L. (1982). Local Bond Strength of Concrete for Cyclic Reversed Loadings. in *Bond in Concrete* Applied Science Publications, London, England, 151-161.

Henry, L. (1998). Study of Buckling of Longitudinal Bars in Reinforced Concrete Bridge Columns. MS Thesis, University of California, Berkeley.

Houghton, D.L. and Karns, J.E. (2002). Post 9-11 Multi-Hazard Mitigation in Steel Frame Structures as a Function of Connection Geometry. *Proceedings - 71st International Convention of SEAOC*. Santa Barbara, CA, USA.

Huang, Z., Engstrom, B. and Magnuson, J. (1996). Experimental and Analytical Studies of the Bond Behavior of Deformed Bars in High Strength Concrete. *Proceedings - 4th International Symposium of High-Strength/High-Performance Concrete*. Paris, France, 1115-1124.

ICC (2003). *International Building Code*. International Code Council, Falls Church, VA, USA.

Ilki, A. and Kumbasar, N. (2003). Compressive Behaviour of Carbon Fibre Composite Jacketed Concrete with Circular and Non-Circular Cross-Sections. *Journal of Earthquake Engineering* **7**(3): 381-406.

Imran, I. and Pantazopoulou, S.J. (2001). Plasticity Model for Concrete under Triaxial Compressions. *ASCE Journal of Engineering Mechanics* **127**(3): 281-290.

Kaewkulchai, G. and Williamson, E.B. (2004). Beam Element Formulation and Solution Procedure for Dynamic Progressive Collapse Analysis. *Computers and Structures* **82**(7-8): 639-651.

Kaewkulchai, G. and Williamson, E.B. (2006). Modeling the Impact of Failed Members for Progressive Collapse Analysis of Frame Structures. *ASCE Journal of Performance of Constructed Facilities* **20**(4): 375-383.

Kim, Y. and Kabeyasawa, T. (2004). Dynamic Test and Analysis of an Eccentric Reinforced Concrete Frame to Collapse. *Proceedings - 13th World Conference on Earthquake Engineering*. Vancouver, BC, Canada.

Krauthammer, T., Hall, R.L., Woodson, S.C., Baylot, J.T., Hayes, J.R. and Sohn, Y. (2002). Development of Progressive Collapse Analysis Procedure and Condition Assessment for Structures. *Proceedings - National Workshop on Prevention of Progressive Collapse*. Multihazard Mitigation Council of the National Institute of Building Sciences, Rosemont, IL, USA.

Lee, T.-H. and Mosalam, K.M. (2005). Seismic Demand Sensitivity of Reinforced Concrete Shear-Wall Building Using FOSM Method. *Earthquake Engineering and Structural Dynamics* **34**(14): 1719-1736.

Lokuge, W.P., Sanjayan, J.G. and Setunge, S. (2003). Triaxial Test The results of High-Strength Concrete Subjected to Cyclic Loading. *Magazine of Concrete Research* **55**(4): 321-329.

Lokuge, W.P., Sanjayan, J.G. and Setunge, S. (2004). Constitutive Model for Confined High Strength Concrete Subjected to Cyclic Loading. *ASCE Journal of Materials in Civil Engineering* **16**(4): 297-305.

Lokuge, W.P., Sanjayan, J.G. and Setunge, S. (2005). Stress-Strain Model for Laterally Confined Concrete. *ASCE Journal of Materials in Civil Engineering* **17**(6): 607-616.

Lowes, L.N., Moehle, J.P. and Govindjee, S. (2004). Concrete-Steel Bond Model for Use in Finite Element Modeling of Reinforced Concrete Structures. *ACI Structural Journal* **101**(4): 501-511.

Lu, Y., Gu, X. and Guan, J. (2005). Probabilistic Drift Limits and Performance Evaluation of Reinforced Concrete Columns. *ASCE Journal of Structural Engineering* **131**(6): 966-978.

Lynn, A.C. (2001). *Seismic Evaluation of Existing Reinforced Concrete Building Columns*. PhD Report, University of California, Berkeley.

Ma, R. and Xiao, Y. (1999). Seismic Retrofit and Repair of Circular Bridge Columns with Advanced Composite Materials. *Earthquake Spectra* **15**(4): 747-764.

Mander, J.B., Priestley, M.J.N. and Park, R. (1984). *Seismic Design of Bridge Piers*. Research Report 84-02, University of Canterbury, Christchurch, New Zealand

Mander, J.B., Priestley, M.J.N. and Park, R. (1988). Theoretical Stress-Strain Model for Confined Concrete. *ASCE Journal of Structural Engineering* **114**(8): 1804-1826.

Manson, S.S. (1979). Inversion of the Strain-Life and Strain-Stress Relationships for Use in Metal Fatigue Analysis. *Fatigue of Engineering Materials and Structures* **1**(1): 37-57.

Massone, L.M. and Wallace, J.W. (2004). Load-Deformation Responses of Slender Reinforced Concrete Walls. *ACI Structural Journal* **101**(1): 103-113.

MATLAB (2007). *Getting Started with Matlab 7 (Release 2007b)*. The MathWorks, Inc., Natick, MA, USA.

Mau, S.T., Elwi, A.E. and Zhou, S.-Z. (1998). Analytical Study of Spacing of Lateral Steel and Column Confinement. *ASCE Journal of Structural Engineering* **124**(3): 262-269.

Mazzoni, S., Mckenna, F., Scott, M.H. and Fenves, G. (2004). Opensees User's Manual. *www.opensees.berkeley.edu*.

McKenna, F. (1997). Object-Oriented Finite Element Programming: Frameworks for Analysis, Algorithms, and Parallel Computing. PhD Report, University of California, Berkeley.

Menegotto, M. and Pinto, P. (1973). Method of Analysis for Cyclically Loaded Reinforced Concrete Plane Frames Including Changes in Geometry and Non-Elastic Behavior of Elements under Combined Normal Force and Bending. *Proceedings - Symposium on Resistance and Ultimate Deformability of Structures Acted on by Well Defined Repeated Loads*. IABSE: 13, 15-22.

Mirmiran, A. and Shahawy, M. (1997a). Behavior of Concrete Columns Confined by Fiber Composites. *ASCE Journal of Structural Engineering* **123**(5): 583-590.

Mirmiran, A. and Shahawy, M. (1997b). Dilation Characteristics of Confined Concrete. *Mechanics of Cohesive-Frictional Materials* **2**(3): 237-249.

Mitra, N. and Lowes, L.N. (2007). Evaluation, Calibration, and Verification of a Reinforced Concrete Beam-Column Joint Model. *ASCE Journal of Structural Engineering* **133**(1): 105-120.

Mizuno, K., Nakamura, H. and Higai, T. (1999). Analytical Study on the Factors Affecting the Behavior of RC Members Subjected to the Cyclic Loading. *Transactions of the Japan Concrete Institute* **21**: 281-286.

Moehle, J., Ghannoum, W. and Bozorgnia, Y. (2005). Collapse of Lightly Confined Reinforced Concrete Frames During Earthquakes. *Proceedings - NATO Science for Peace Workshop in Advances in Earthquake Engineering for Urban Risk Reduction*. Istanbul, Turkey, Springer 317-332.

Monti, G., Filippou, F.C. and Spacone, E. (1997a). Analysis of Hysteretic Behavior of Anchored Reinforcing Bars. *ACI Structural Journal* **94**(3): 248-261.

Monti, G., Filippou, F.C. and Spacone, E. (1997b). Finite Element for Anchored Bars under Cyclic Load Reversals. *ASCE Journal of Structural Engineering* **123**(5): 614-623.

Monti, G. and Nuti, C. (1992). Nonlinear Cyclic Behavior of Reinforcing Bars Including Buckling. *ASCE Journal of Structural Engineering* **118**(12): 3268-3284.

Monti, G. and Spacone, E. (2000). Reinforced Concrete Fiber Beam Element with Bond-Slip. *ASCE Journal of Structural Engineering* **126**(6): 654-661.

Mosalam, K.M., Talaat, M. and Binici, B. (2007a). Computational Model for FRP-Confined RC Members. *Proceedings - 8th International Conference on Fiber Reinforced Polymers Reinforcement for Concrete Structures*. University of Patras, Greece.

Mosalam, K.M., Talaat, M. and Binici, B. (2007b). A Computational Model for Reinforced Concrete Members Confined with Fiber Reinforced Polymer Lamina: Implementation and Experimental Validation. *Composites Part B: Engineering* **38**(5-6): 598-613.

NEHRP (2001). NEHRP Recommended Provisions for Seismic Regulations for New Buildings and Other Structures. Washington, DC, USA, Building Seismic Safety Council.

Newmark, N.M. (1959). Method of Computation for Structural Dynamics. *ASCE Journal of the Engineering Mechanics Division* **85**(EM3, Part 1): 67-94.

Ngo, D. and Scordelis, A.C. (1967). Finite Element Analysis of Reinforced Concrete Beams. *ACI Journal* **64**(3): 152-163.

Pantazopoulou, S.J. (1995). Role of Expansion on Mechanical Behavior of Concrete. *ASCE Journal of Structural Engineering* **121**(12): 1795-1805.

Nilson, A.H. (1971). Internal Measurements of Bond Slip. *ACI Journal* **69**(7): 439-441.

Parent, S. and Labossiere, P. (2000). Finite Element Analysis of Reinforced Concrete Columns Confined with Composite Materials. *Canadian Journal of Civil Engineering* **27**(3): 400-411.

Park, R., Kent, D.C. and Sampson, R.A. (1972). Reinforced Concrete Members with Cyclic Loading. *ASCE Journal of the Structural Division* **98**(ST7): 1341-1360.

Park, Y.-J. and Ang, A.H.-S. (1985). Mechanistic Seismic Damage Model for Reinforced Concrete. *ASCE Journal of Structural Engineering* **111**(4): 722-739.

PEER (1997). Pacific Earthquake Engineering Research Center Mission Statement. *www.peer.berkeley.edu*.

Pivonka, P., Lackner, R. and Mang, H.A. (2000). Numerical Analyses of Concrete Subjected to Triaxial Compressive Loading. *Proceedings - European Congress on Computational Methods in Applied Science and Engineering*. 1-26.

Popovics, S. (1973). Numerical Approach to the Complete Stress-Strain Curve of Concrete. *Cement and Concrete Research* **3**(5): 583-599.

Porter, K.A. (2003). An Overview of PEER's Performance-Based Earthquake Engineering Methodology. *Proceedings - 9th International Conference on Application of Statistics and Probability in Civil Engineering (ICASP)*. San Francisco, CA, USA, Civil Engineering Risk and Reliability Association (CERRA).

Powell, G. (2005). Progressive Collapse: Case Studies Using Nonlinear Analysis. *Proceedings - 2005 Structures Congress and the 2005 Forensic Engineering Symposium - Metropolis and Beyond*. New York, NY, USA, ASCE 2185-2198.

Pramono, E. and William, K. (1989). Fracture Energy-Based Plasticity Formulation of Plain Concrete. *ASCE Journal of Engineering Mechanics* **115**(6): 1183-1204.

Pretlove, A.J., Ramsden, M. and Atkins, A.G. (1991). Dynamic Effects in Progressive Failure of Structures. *International Journal of Impact Engineering* **11**(4): 539-546.

Priestley, M.J.N. and Park, R. (1987). Strength of Ductility of Concrete Bridge Columns under Seismic Loading. *ACI Structural Journal* **84**(1): 61-76.

Priestley, M.J.N. and Seible, F. (1991). *Seismic Assessment and Retrofit of Bridges.* Technical Report SSRP 91/03. University of California, San Diego.

Priestley, M.J.N., Verma, R. and Xiao, Y. (1994). Seismic Shear Strength of Reinforced Concrete Columns. *ASCE Journal of Structural Engineering* **120**(8): 2310-2328.

Pujol, S. (2002). Drift Capacity of Reinforced Concrete Columns Subjected to Displacement Reversals. PhD Report, Purdue University.

Pujol, S., Ramirez, J. and Sozen, M. (1999). Drift Capacity of Reinforced Concrete Columns Subjected to Cyclic Shear Reversals. in *Seismic Response of Concrete Bridges*, Michigan, ACI **SP-187**: 255-274.

Pujol, S., Sozen, M. and Ramirez, J. (2000). Transverse Reinforcement for Columns of Reinforced Concrete Frames to Resist Earthquakes. *ASCE Journal of Structural Engineering* **126**(4): 461-466.

Ramsden, M. (1987). Dynamic Effects in the Progressive Failure of Lattice Structures. PhD Report, University of Reading, UK.

Razvi, S. and Saatcioglu, M. (1999). Confinement Model for High-Strength Concrete. *ASCE Journal of Structural Engineering* **125**(3): 281-288.

Reinhardt, H.W. and Van der Veen, C. (1992). Splitting Failure of a Strain-Softening Material Due to Bond Stresses. *Proceedings - International Workshop on the Applications of Fracture Mechanics to Reinforced Concrete*. Turin, Italy.

Ricles, J.M., Yang, Y.-S. and Priestley, M.J.N. (1998). Modeling Nonductile R/C Columns for Seismic Analysis of Bridges. *ASCE Journal of Structural Engineering* **124**(4): 415-424.

Rodriguez, M.E., Botero, J.C. and Villa, J. (1999). Cyclic Stress-Strain Behavior of Reinforcing Steel Including Effect of Buckling. *ASCE Journal of Structural Engineering* **125**(6): 605-612.

Rubiano-Benavides, N. (1998). *Predictions of the Inelastic Seismic Response of Concrete Structures Including Shear Deformations and Anchorage Slip*. PhD Report, University of Texas, Austin.

Saatcioglu, M. and Razvi, S.R. (1992). Strength and Ductility of Confined Concrete. *ASCE Journal of Structural Engineering* **118**(6): 1590-1607.

Saenz, N. and Pantelides, C.P. (2007). Strain-Based Confinement Model for FRP-Confined Concrete. *ASCE Journal of Structural Engineering* **133**(6): 825-833.

Salem, H.M. and Maekawa, K. (2004). Pre- and Postyield Finite Element Method Simulation of Bond of Ribbed Reinforcing Bars. *ASCE Journal of Structural Engineering* **130**(4): 671-680.

Sargin, M., Ghosh, S. and Handa, V. (1971). Effects of Lateral Reinforcement upon the Strength and Deformation Properties of Concrete. *Magazine of Concrete Research* **23**(75-76): 99-110.

Schonberg, W.P., Keer, L.M. and Woo, T.K. (1987). Low Velocity Impact of Transversely Isotropic Beams and Plates. *International Journal of Solids and Structures* **23**(7): 871-896.

Seible, F., Priestley, M.J.N., Hegemier, G.A. and Innamorato, D. (1997). Seismic Retrofit of RC Columns with Continuous Carbon Fiber Jackets. *ASCE Journal of Composites for Construction* **1**(2): 52-62.

Sezen, H. (2002). Seismic Response and Modeling of Reinforced Concrete Building Columns. PhD Report, University of California, Berkeley.

Sezen, H. and Moehle, J.P. (2004). Shear Strength Model for Lightly Reinforced Concrete Columns. *ASCE Journal of Structural Engineering* **130**(11): 1692-1703.

Shames, I.H. and Cozzarelli, F.A. (1997). *Elastic and Inelastic Stress Analysis*. Taylor and Francis, Washington, DC, USA.

Sheikh, S. and Uzumeri, S.M. (1982). Analytical Model for Concrete Confinement in Tied Columns. *ASCE Journal of the Structural Division* **108**(ST12): 2703-2722.

Sheikh, S.A. and Yau, G. (2002). Seismic Behavior of Concrete Columns Confined with Steel and Fiber-Reinforced Polymers. *ACI Structural Journal* **99**(1): 72-80.

Smith, S.S., William, K.J., Gerstle, K.H. and Sture, S. (1989). Concrete over the Top, or: Is There Life after Peak? *ACI Materials Journal* **86**(5): 491-497.

Spacone, E., Filippou, F.C. and Taucer, F.F. (1996a). Fibre Beam-Column Model for Non-Linear Analysis of R/C Frames: Part I. Formulation. *Earthquake Engineering & Structural Dynamics* **25**(7): 711-725.

Spacone, E., Filippou, F.C. and Taucer, F.F. (1996b). Fibre Beam-Column Model for Non-Linear Analysis of R/C Frames: Part Ii. Applications. *Earthquake Engineering & Structural Dynamics* **25**(7): 727-742.

Starossek, U. (1999). Progressive Collapse Study of a Multi-Span Bridge. *Structural Engineering International*. IABSE **16**(2): 121-125.

Starossek, U. (2006). Progressive Collapse of Bridges-Aspects of Analysis and Design. *Proceedings - International Symposium on Sea-Crossing Long-Span Bridges*. Mopko, Korea.

Talaat, M. and Mosalam, K.M. (2007). On Bond Failure by Splitting of Concrete Cover Surrounding Anchored Bars. *Proceedings - Fracture Mechanics of Concrete and Concrete Structures*. Catania, Italy, Taylor & Francis Group, 789-797.

Teng, J.G. and Lam, L. (2004). Behavior and Modeling of Fiber Reinforced Polymer-Confined Concrete. *ASCE Journal of Structural Engineering* **130**(11): 1713-1723.

Tepfers, R. (1979). Cracking of Concrete Cover Along Anchored Deformed Reinforcing Bars. *Magazine of Concrete Research* **31**(106): 3-12.

Terenzani, L., Mosalam, K.M. and Russo, G. (2001). Loaded Concrete Columns. *Draft Report* (unpublished). University of California, Berkeley.

Timoshenko, S. and Gere, J. (1961). *Theory of Elastic Stability*, McGraw-Hill Book Company, New York, NY, USA.

USGS (2002). USGS Probabilistic Hazard Curves. *http://earthquake.usgs.gov/research/hazmaps/design/*.

Vamvatsikos, D. and Cornell, C.A. (2002). Incremental Dynamic Analysis. *Earthquake Engineering and Structural Dynamics* **31**(3): 491-514.

Vamvatsikos, D. and Cornell, C.A. (2004). Applied Incremental Dynamic Analysis. *Earthquake Spectra* **20**(2): 523-553.

Van Mier, J.G. (1997). *Fracture Processes of Concrete*. CRC Press.

Virdi, K.S. and Beshara, F.B. (1992). Numerical Simulation of Building Decommission as a Progressive Collapse Process. *Proceedings - 3rd International Conference on Decommissioning and Demolition*. UMIST, UK.

Viwathanatepa, S. (1979). *Bond Deterioration of Reinforcing Bars Embedded in Confined Concrete Blocks*. PhD Report, University of California, Berkeley.

Welch, B., Jones, K. and Hobbs, J. (2003). *Practical Programming in Tcl and Tk*. Prentice Hall.

Wu, C.-L., Loh, C.-H. and Yang, Y.-S. (2006). Shake Table Tests on Gravity Load Collapse of Low-Ductility RC Frames under near-Fault Earthquake Excitation. in *Advances in Experimental Structural Engineering*. Itoh and Aoki, Eds. 725-732.

Xiao, Y. and Ma, R. (1997). Seismic Retrofit of Reinforced Concrete Circular Columns Using Prefabricated Composite Jacketing. *ASCE Journal of Structural Engineering* **123**(10): 1357-1364.

Yankelevsky, D.S. and Reinhardt, H.W. (1989). Uniaxial Behavior of Concrete in Cyclic Tension. *ASCE Journal of Structural Engineering* **115**(1): 166-182.

Zareian, F. and Krawinkler, H. (2007). Assessment of Probability of Collapse and Design for Collapse Safety. *Earthquake Engineering & Structural Dynamics*. **36**(16): 1901-1914.

Zhao, J. and Sritharan, S. (2007). Modeling of Strain Penetration Effects in Fiber-Based Analysis of Reinforced Concrete Structures. *ACI Structural Journal* **104**(2): 133-141.

Zineddin, M. and Krauthammer, T. (2007). Dynamic Response and Behavior of Reinforced Concrete Slabs under Impact Loading. *International Journal of Impact Engineering* **34**(9): 1517-1534.

Appendix A: Tcl Input Commands for Developed OpenSees Classes

OpensSees Tcl input commands are introduced according to the following order:

Command ReqArgs String $Value … <OptArgs (= Def) –Switch $Value …>

where,

Command	Command name to invoke the object constructor
ReqArgs	Required arguments for the command
String	Keyword argument of the command (e.g., element type)
$Value…	Numerical variables representing the values of arguments
OptArgs	Optional arguments for the command, some have default values
Def	Default value (if any) of optional argument
-Switch	String preceded by "-" to specify an optional command entry

A.1 *CONFINEDFIBERSEC2D* CLASS

section RCFiber $secTag <-Hoop $hoopTag> <-Conf -$pow=2> <-e3max $fractStrain> {#fiber data}

$secTag	Integer identifying the cross section being defined
$hoopTag	Integer identifying pre-defined hoop uniaxial material
-pow	Integer power of the confining stress distribution function, 0 = constant
$fractStrain	Strain corresponding to fracture of hoops, used to compute damage index
#fiber data	List of fiber areas, locations, material tags, etc. (refer to OpenSees user's manual). Material tag of the first group of fibers to be defined must be that of the core

concrete. Additional core concrete fibers can be defined later (e.g., for irregularly shaped cross sections) within the fiber-section block using the same material tag.

A.2. *UNIAXIALCONFINEDMATERIAL* SUBCLASSES

A.2.1 ConfinedConcrete

uniaxialMaterial ConcreteBLE $matTag $fc $ec $Ec $fu $eu $ft $et0 $lc $Gfc $pc <$nu=0.2 $dmgTag=0 $prstrs=0 $hoopTag=0 $alphae=0>

$matTag	Integer identifying the material being defined
$fc	Compressive strength
$ec	Strain corresponding to compressive strength
$Ec	Initial Young's modulus
$fu	Residual strength, ignored in current implementation
$eu	Strain corresponding to residual strength, ignored in current implementation
$ft	Tensile strength
$et0	Strain corresponding to complete loss of tensile capacity
$lc	Localization length (fraction of plastic hinge length)
$Gfc	Compressive fracture energy
$pc	Hysteretic loop controller, recommended $pc = 1.445-0.0035$fc [MPa]
$nu	Initial Poisson's ratio
$dmgTag	Integer tag of pre-defined associated damage object
$prstrs	External prescribed confining stress, if any
$hoopTag	Integer tag of pre-defined associated hoop uniaxial material
$alphae	Power of normalized dissipated energy-based envelope reduction factor

A.2.2 SteelRebar

uniaxialMaterial SteelRebar $matTag $esh $sh/eu $barTag $barDiam $hoopSpac <$hoopTag=0 $beta=1 $recRatio=-2 $e3max=0.1 $eult=0.13 $mf=0 $af=0>

$matTag	Integer identifying the material being defined

$esh	Strain at the beginning of strain-hardening, enter as negative value to include post-yielding reduction in stiffness prior to buckling and as positive value to ignore
$sh/eu	Terminal inelastic to elastic stiffness ratio if entered as a positive value, or strain at which to compute this ratio if negative value
$barTag	Integer tag of pre-defined material representing bar's constitutive law
$barDiam	Diameter of reinforcing bar
$hoopSpac	Spacing of hoops
$hoopTag	Integer tag of pre-defined associated hoop uniaxial material
$beta	Efficiency multiplier for hoop stiffness
$recRatio	User-defined maximum tensile strain recovery ratio for buckled bars, set magnitude >1 to enforce Equation (2.35), positive values indicate constant recovery ratio (not recommended), negative value indicate linearly varying recovery ratio (recommended)
$e3max	Strain corresponding to minimum stiffness in the restraining hoops
$eult	Fracture strain (for Coffin-Manson damage model), 0 = no fracture
$mf	Power of Coffin-Manson damage index
$af	Power of Coffin-Manson stress-reduction factor

A.2.3 LapSplice

uniaxialMaterial LapSplice $matTag $hoopSpac $barDiam $barTag $taomax <$e3max=0.00125 $rnot=2 $hoopTag = 0 umax=0.25[mm] $pinchRatio=0 $kr=0 $ueRatio=0.5 $EunRatio=1 uult=10 $alphap=0 $alphapn=0 $gmax=0.9 $gmin=0.7>

$matTag	Integer identifying the material being defined
$hoopSpac	Spacing of hoops
$barDiam	Diameter of reinforcing bar
$barTag	Integer tag of pre-defined material representing bar's constitutive law
$taomax	Maximum bond strength
$rnot	Bond-slip shape parameter, 2.0 for Grade 60 steel, 1.5 for Grade 40 steel

$hoopTag	Integer tag of pre-defined associated hoop uniaxial material
$umax	Slip displacement corresponding to maximum bond stress
$pinchRatio	Ratio of pinched reloading stiffness to initial bond-slip stiffness
$kr	Ratio of residual stress to unloading stress upon strain reversal
$ueRatio	Ratio of elastic slip displacement to maximum slip displacement $umax
$EunRatio	Ratio of unloading stiffness to initial bond-slip stiffness
$alphap	Power of slip-based stress-reduction factor for maximum-slip cycle, α_p
$alphapn	Power of slip-based stress-reduction factor for internal slip cycles, α_{pn}
$gmax	Reloading stress factor for slip cycles reentering before elastic slip, $\gamma_{p,\max}$
$gmin	Reloading stress factor for slip cycles reentering at large slip, $\gamma_{p,\min}$

A.3 *REMOVERECORDER* CLASS

A.3.1 Element Removers

recorder Collapse <–ele $ele1…$elen> <-eleRange $eleStart $eleFin> <-slave –ele slave1 … –eleRange $slaveStart $slaveFin> <-sec $sec1…$secn> <-time> <-crit $critID1 $critThresh1 …> <-file $filename>

$ele1..$elen	Integer(s) identifying the elements being checked for collapse
$eleStart	Integer identifying the first element in a range
$eleFin	Integer identifying the last element in a range
$slave1…	Integer(s) identifying the elements that need to be removed if all elements defined in this set are removed (typically, the interior elements of multi-element columns)
$slaveStart	Integer identifying the first slave element in a range
$slaveFin	Integer identifying the last slave element in a range
$sec1…$secn	Critical cross section identifiers, use dummy integer for truss and similar elements
$critID1	Potential collapse modes to be checked, Options are: axialDI = axial damage index, flexure-axial mode flexureDI = flexure damage index, flexure-axial mode axialLS = axial limit state, shear-axial mode

shearLS = shear limit state, shear-axial mode

maxStrain = maximum elongation

minStrain = maximum shortening

$critThresh1 Threshhold values for the selected criteria

$filename File name for element removal log. Only one log file is constructed for all recorder commands. The first file name input to a collapse recorder command will be used and any subsequent file names are ignored.

A.3.2 Node Removers

recorder Collapse –ele $ele1<…$elen> –node $node

$ele1…$elen Integers identifying connected elements

$node Node number be removed when all elements defined in the command are removed

Appendix B: Simplified Modeling of Impact Force and Duration

The illustration in Figure 5.14 demonstrates the steps of determining the time of collision and duration of impact between truss element 3 after its collapse and the rest of the intact structure of the benchmark problem presented in Chapter 6. At the time of collapse of element 3, t_0, the kinetics of the separated end-node from element 3 (i.e., node 1b) are obtained from the last converged state of the structural system. The displacements, velocity, and acceleration can be used to compute the angular position, velocity, and acceleration at time t_0 (Fig. 5.14a). These quantities represent initial conditions for the collision problem being considered. The angular position of the collapsed truss element at any time $\theta(t)$ is governed by the following differential equation,

$$I_M \ddot{\theta} + Mg\frac{L}{2}\cos\theta = 0 \tag{B.1}$$

where I_M is the element's mass moment of inertia about end-node 4 (i.e., $I_M = ML^2/3$), M is the element's mass, and L is the element's length. With the initial conditions $\theta(t_0) = \theta_0$ and $\dot{\theta}(t_0) = \dot{\theta}_0$, the solution for $\theta(t)$ is computed and compared to the position of node 9 until collision is determined. The time at collision is denoted t_c, and the corresponding kinematics of node 1b are $\theta(t_c) = \theta_c$ and $\dot{\theta}(t_c) = \dot{\theta}_c$. These latter quantities constitute the initial conditions for the impact problem.

The equations of motion governing the collapsed element and the damaged structure during impact are coupled and difficult to solve. Impact is assumed to take place at one point (collision of node 1b and node 9). Assume that $R(t)$ is the resulting reaction force between the two bodies at the point of collision and that $R(t)$ is a function of the resulting relative displacements between u of the impacting (collapsed) element and u_s of the impacted structure.

For simplicity, assume that both impacting and impacted bodies have one scalar DOF each. Hence, the coupled equations of motion take the form

$$M\ddot{u} + R(u - u_s) = 0 \tag{B.2}$$

$$M_s\ddot{u}_s - R(u - u_s) + F(u_s) = 0 \tag{B.3}$$

where M and M_s are the masses of impacting and impacted bodies, respectively, $F(u_s)$ is the structural resisting force in the impacted structure, and viscous damping is ignored. The assumption of soft impact states that $|u_s| << |u|$ and allows Equations (B.2) and (B.3) to be uncoupled as follows:

$$M\ddot{u} + R(u) = 0 \tag{B.4}$$

$$M_s\ddot{u}_s - R(u) + F(u_s) = 0 \tag{B.5}$$

Hence, Equation (B.4) can be solved to compute the impacting element's displacement u and the resulting impact force $R(u)$, which can then be used in Equation (B.5) to solve for the impacted structure's displacement u_s and induced resisting force demands $F(u_s)$. Assuming soft-impact, and hence negligible relative deformation at the point of collision, the structural response of the collapsed truss element after impact is modeled upon collision as a beam supported at nodes 4 and 9 with a proportion of mass $M_1 = 0.5M$ allocated to inserted node 1c at mid-span (see Fig. 5.14b). This assumption excludes the occurrence of punching of the intact structure and/or disintegration of the collapsed element upon collision. Hence, the governing differential equation becomes

$$M_1\ddot{u} + Ku + M_1 g\cos\theta = 0 \tag{B.6}$$

where $K = 48EI/L^3$ is the beam's flexural stiffness, i.e., the applied force at mid-span required to produce a unit transverse displacement. This differential equation can be solved using the initial conditions $\theta(t_c) = \theta_c, u(t_c) = 0, \dot{u}(t_c) = \dot{\theta}_c L/2$ to compute $u(t)$. The reaction force on the beam at nodes 9 and 4 are thus computed as

$$R(t) = u(t)\frac{K}{2} \tag{B.7}$$

If we assume that there is no friction during collision, the forces at node 9 due to the

impact and additional gravity load can thus be computed from equilibrium as

$$F_I(t) = \frac{R(t)}{\cos\theta(t)} + M_2 g \cong \frac{R(t)}{\cos\theta_c} + M_2 g \tag{B.8}$$

where $M_2 = 0.25M$ is the proportion of element mass lumped at each of nodes 4 and 1b. Finally, the duration of impact Δt_I is computed as one half of the natural vibration period of the subsystem illustrated in Figure 5.14b, which is the time duration required for the collapsed element to bounce back after the collision and be on the verge of rebounding off the intact structure. Hence

$$\Delta t_I = \pi\sqrt{\frac{0.5M}{K}} \tag{B.9}$$

It is unrealistic to assume that the impacting element will rebound off the intact structure as in an elastic collision. Instead there is likely to be a short interval of highly damped transient response including brief rebounds and collisions of decreasing magnitude before it comes to a steady-state of applying its gravity load equally to nodes 4 and 9 as vertical reaction forces. The effect of damping in this short duration is difficult to predict, especially with further inelasticity expected to take place in the impacting element and locally in the impacted intact structure resulting in significant energy dissipation. Hence, a practical and conservative assumption is made that the impacting element after one half cycle of vibration undergoes negligible transient response that is ignored and the steady-state reaction forces are applied directly. This results in a sinusoidal temporal variation of impact load on the intact structural system as illustrated in Figure 5.14c.

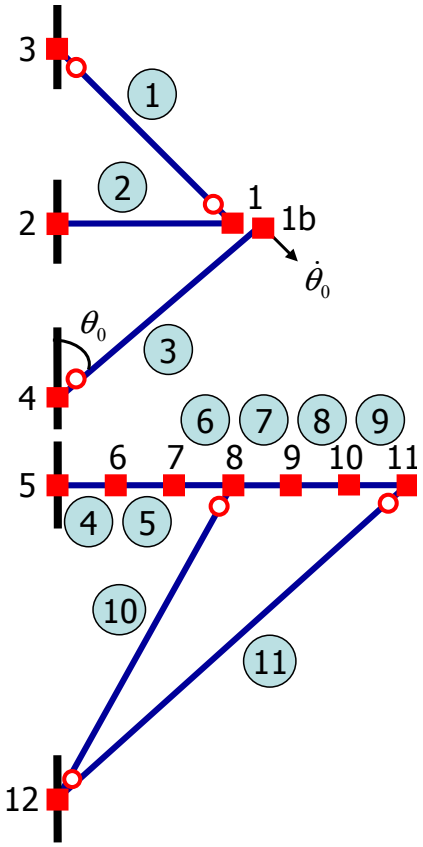

(a) at time $t = t_0$

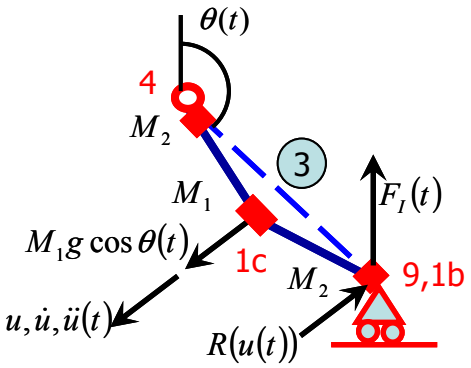

(b) at time $t_c \le t \le t_c + \Delta t_I$

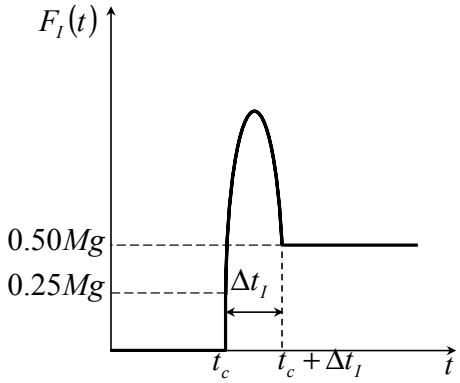

(c) Temporal variation of impact force

Fig. B.1 Demonstration of collision and impact modeling.

PEER REPORTS

PEER reports are available from the National Information Service for Earthquake Engineering (NISEE). To order PEER reports, please contact the Pacific Earthquake Engineering Research Center, 1301 South 46th Street, Richmond, California 94804-4698. Tel.: (510) 665-3405; Fax: (510) 665-3420.

PEER 2007/11 *Bar Buckling in Reinforced Concrete Bridge Columns.* Wayne A. Brown, Dawn E. Lehman, and John F. Stanton. February 2008.

PEER 2007/10 *Computational Modeling of Progressive Collapse in Reinforced Concrete Frame Structures.* Mohamed M. Talaat and Khalid M. Mosalam. May 2008.

PEER 2007/09 *Integrated Probabilistic Performance-Based Evaluation of Benchmark Reinforced Concrete Bridges.* Kevin R. Mackie, John-Michael Wong, and Božidar Stojadinović. January 2008.

PEER 2007/08 *Assessing Seismic Collapse Safety of Modern Reinforced Concrete Moment-Frame Buildings.* Curt B. Haselton and Gregory G. Deierlein. February 2008.

PEER 2007/07 *Performance Modeling Strategies for Modern Reinforced Concrete Bridge Columns.* Michael P. Berry and Marc O. Eberhard. April 2008.

PEER 2007/06 *Development of Improved Procedures for Seismic Design of Buried and Partially Buried Structures.* Linda Al Atik and Nicholas Sitar. June 2007.

PEER 2007/05 *Uncertainty and Correlation in Seismic Risk Assessment of Transportation Systems.* Renee G. Lee and Anne S. Kiremidjian. July 2007.

PEER 2007/03 *Beam-Column Element Model Calibrated for Predicting Flexural Response Leading to Global Collapse of RC Frame Buildings.* Curt B. Haselton, Abbie B. Liel, Sarah Taylor Lange, and Gregory g. Deierlein. May 2008.

PEER 2007/02 *Campbell-Bozorgnia NGA Ground Motion Relations for the Geometric Mean Horizontal Component of Peak and Spectral Ground Motion Parameters.* Kenneth W. Campbell and Yousef Bozorgnia. May 2007.

PEER 2007/01 *Boore-Atkinson NGA Ground Motion Relations for the Geometric Mean Horizontal Component of Peak and Spectral Ground Motion Parameters.* David M. Boore and Gail M. Atkinson. May. May 2007.

PEER 2006/12 *Societal Implications of Performance-Based Earthquake Engineering.* Peter J. May. May 2007.

PEER 2006/11 *Probabilistic Seismic Demand Analysis Using Advanced Ground Motion Intensity Measures, Attenuation Relationships, and Near-Fault Effects.* Polsak Tothong and C. Allin Cornell. March 2007.

PEER 2006/10 *Application of the PEER PBEE Methodology to the I-880 Viaduct.* Sashi Kunnath. February 2007.

PEER 2006/09 *Quantifying Economic Losses from Travel Forgone Following a Large Metropolitan Earthquake.* James Moore, Sungbin Cho, Yue Yue Fan, and Stuart Werner. November 2006.

PEER 2006/08 *Vector-Valued Ground Motion Intensity Measures for Probabilistic Seismic Demand Analysis.* Jack W. Baker and C. Allin Cornell. October 2006.

PEER 2006/07 *Analytical Modeling of Reinforced Concrete Walls for Predicting Flexural and Coupled–Shear-Flexural Responses.* Kutay Orakcal, Loenardo M. Massone, and John W. Wallace. October 2006.

PEER 2006/06 *Nonlinear Analysis of a Soil-Drilled Pier System under Static and Dynamic Axial Loading.* Gang Wang and Nicholas Sitar. November 2006.

PEER 2006/05 *Advanced Seismic Assessment Guidelines.* Paolo Bazzurro, C. Allin Cornell, Charles Menun, Maziar Motahari, and Nicolas Luco. September 2006.

PEER 2006/04 *Probabilistic Seismic Evaluation of Reinforced Concrete Structural Components and Systems.* Tae Hyung Lee and Khalid M. Mosalam. August 2006.

PEER 2006/03 *Performance of Lifelines Subjected to Lateral Spreading.* Scott A. Ashford and Teerawut Juirnarongrit. July 2006.

PEER 2006/02 *Pacific Earthquake Engineering Research Center Highway Demonstration Project.* Anne Kiremidjian, James Moore, Yue Yue Fan, Nesrin Basoz, Ozgur Yazali, and Meredith Williams. April 2006.

PEER 2006/01 *Bracing Berkeley. A Guide to Seismic Safety on the UC Berkeley Campus.* Mary C. Comerio, Stephen Tobriner, and Ariane Fehrenkamp. January 2006.

PEER 2005/16 *Seismic Response and Reliability of Electrical Substation Equipment and Systems.* Junho Song, Armen Der Kiureghian, and Jerome L. Sackman. April 2006.

PEER 2005/15 *CPT-Based Probabilistic Assessment of Seismic Soil Liquefaction Initiation.* R. E. S. Moss, R. B. Seed, R. E. Kayen, J. P. Stewart, and A. Der Kiureghian. April 2006.

PEER 2005/14 *Workshop on Modeling of Nonlinear Cyclic Load-Deformation Behavior of Shallow Foundations.* Bruce L. Kutter, Geoffrey Martin, Tara Hutchinson, Chad Harden, Sivapalan Gajan, and Justin Phalen. March 2006.

PEER 2005/13 *Stochastic Characterization and Decision Bases under Time-Dependent Aftershock Risk in Performance-Based Earthquake Engineering.* Gee Liek Yeo and C. Allin Cornell. July 2005.

PEER 2005/12 *PEER Testbed Study on a Laboratory Building: Exercising Seismic Performance Assessment.* Mary C. Comerio, editor. November 2005.

PEER 2005/11 *Van Nuys Hotel Building Testbed Report: Exercising Seismic Performance Assessment.* Helmut Krawinkler, editor. October 2005.

PEER 2005/10 *First NEES/E-Defense Workshop on Collapse Simulation of Reinforced Concrete Building Structures.* September 2005.

PEER 2005/09 *Test Applications of Advanced Seismic Assessment Guidelines.* Joe Maffei, Karl Telleen, Danya Mohr, William Holmes, and Yuki Nakayama. August 2006.

PEER 2005/08 *Damage Accumulation in Lightly Confined Reinforced Concrete Bridge Columns.* R. Tyler Ranf, Jared M. Nelson, Zach Price, Marc O. Eberhard, and John F. Stanton. April 2006.

PEER 2005/07 *Experimental and Analytical Studies on the Seismic Response of Freestanding and Anchored Laboratory Equipment.* Dimitrios Konstantinidis and Nicos Makris. January 2005.

PEER 2005/06 *Global Collapse of Frame Structures under Seismic Excitations.* Luis F. Ibarra and Helmut Krawinkler. September 2005.

PEER 2005//05 *Performance Characterization of Bench- and Shelf-Mounted Equipment.* Samit Ray Chaudhuri and Tara C. Hutchinson. May 2006.

PEER 2005/04 *Numerical Modeling of the Nonlinear Cyclic Response of Shallow Foundations.* Chad Harden, Tara Hutchinson, Geoffrey R. Martin, and Bruce L. Kutter. August 2005.

PEER 2005/03 *A Taxonomy of Building Components for Performance-Based Earthquake Engineering.* Keith A. Porter. September 2005.

PEER 2005/02 *Fragility Basis for California Highway Overpass Bridge Seismic Decision Making.* Kevin R. Mackie and Božidar Stojadinović. June 2005.

PEER 2005/01 *Empirical Characterization of Site Conditions on Strong Ground Motion.* Jonathan P. Stewart, Yoojoong Choi, and Robert W. Graves. June 2005.

PEER 2004/09 *Electrical Substation Equipment Interaction: Experimental Rigid Conductor Studies.* Christopher Stearns and André Filiatrault. February 2005.

PEER 2004/08 *Seismic Qualification and Fragility Testing of Line Break 550-kV Disconnect Switches.* Shakhzod M. Takhirov, Gregory L. Fenves, and Eric Fujisaki. January 2005.

PEER 2004/07 *Ground Motions for Earthquake Simulator Qualification of Electrical Substation Equipment.* Shakhzod M. Takhirov, Gregory L. Fenves, Eric Fujisaki, and Don Clyde. January 2005.

PEER 2004/06 *Performance-Based Regulation and Regulatory Regimes.* Peter J. May and Chris Koski. September 2004.

PEER 2004/05 *Performance-Based Seismic Design Concepts and Implementation: Proceedings of an International Workshop.* Peter Fajfar and Helmut Krawinkler, editors. September 2004.

PEER 2004/04 *Seismic Performance of an Instrumented Tilt-up Wall Building.* James C. Anderson and Vitelmo V. Bertero. July 2004.

PEER 2004/03 *Evaluation and Application of Concrete Tilt-up Assessment Methodologies.* Timothy Graf and James O. Malley. October 2004.

PEER 2004/02 *Analytical Investigations of New Methods for Reducing Residual Displacements of Reinforced Concrete Bridge Columns.* Junichi Sakai and Stephen A. Mahin. August 2004.

PEER 2004/01 *Seismic Performance of Masonry Buildings and Design Implications.* Kerri Anne Taeko Tokoro, James C. Anderson, and Vitelmo V. Bertero. February 2004.

PEER 2003/18 *Performance Models for Flexural Damage in Reinforced Concrete Columns.* Michael Berry and Marc Eberhard. August 2003.

PEER 2003/17 *Predicting Earthquake Damage in Older Reinforced Concrete Beam-Column Joints.* Catherine Pagni and Laura Lowes. October 2004.

PEER 2003/16 *Seismic Demands for Performance-Based Design of Bridges.* Kevin Mackie and Božidar Stojadinović. August 2003.

PEER 2003/15 *Seismic Demands for Nondeteriorating Frame Structures and Their Dependence on Ground Motions.* Ricardo Antonio Medina and Helmut Krawinkler. May 2004.

PEER 2003/14 *Finite Element Reliability and Sensitivity Methods for Performance-Based Earthquake Engineering.* Terje Haukaas and Armen Der Kiureghian. April 2004.

PEER 2003/13 *Effects of Connection Hysteretic Degradation on the Seismic Behavior of Steel Moment-Resisting Frames.* Janise E. Rodgers and Stephen A. Mahin. March 2004.

PEER 2003/12 *Implementation Manual for the Seismic Protection of Laboratory Contents: Format and Case Studies.* William T. Holmes and Mary C. Comerio. October 2003.

PEER 2003/11 *Fifth U.S.-Japan Workshop on Performance-Based Earthquake Engineering Methodology for Reinforced Concrete Building Structures.* February 2004.

PEER 2003/10 *A Beam-Column Joint Model for Simulating the Earthquake Response of Reinforced Concrete Frames.* Laura N. Lowes, Nilanjan Mitra, and Arash Altoontash. February 2004.

PEER 2003/09 *Sequencing Repairs after an Earthquake: An Economic Approach.* Marco Casari and Simon J. Wilkie. April 2004.

PEER 2003/08 *A Technical Framework for Probability-Based Demand and Capacity Factor Design (DCFD) Seismic Formats.* Fatemeh Jalayer and C. Allin Cornell. November 2003.

PEER 2003/07 *Uncertainty Specification and Propagation for Loss Estimation Using FOSM Methods.* Jack W. Baker and C. Allin Cornell. September 2003.

PEER 2003/06 *Performance of Circular Reinforced Concrete Bridge Columns under Bidirectional Earthquake Loading.* Mahmoud M. Hachem, Stephen A. Mahin, and Jack P. Moehle. February 2003.

PEER 2003/05 *Response Assessment for Building-Specific Loss Estimation.* Eduardo Miranda and Shahram Taghavi. September 2003.

PEER 2003/04 *Experimental Assessment of Columns with Short Lap Splices Subjected to Cyclic Loads.* Murat Melek, John W. Wallace, and Joel Conte. April 2003.

PEER 2003/03 *Probabilistic Response Assessment for Building-Specific Loss Estimation.* Eduardo Miranda and Hesameddin Aslani. September 2003.

PEER 2003/02 *Software Framework for Collaborative Development of Nonlinear Dynamic Analysis Program.* Jun Peng and Kincho H. Law. September 2003.

PEER 2003/01 *Shake Table Tests and Analytical Studies on the Gravity Load Collapse of Reinforced Concrete Frames.* Kenneth John Elwood and Jack P. Moehle. November 2003.

PEER 2002/24 *Performance of Beam to Column Bridge Joints Subjected to a Large Velocity Pulse.* Natalie Gibson, André Filiatrault, and Scott A. Ashford. April 2002.

PEER 2002/23 *Effects of Large Velocity Pulses on Reinforced Concrete Bridge Columns.* Greg L. Orozco and Scott A. Ashford. April 2002.

PEER 2002/22 *Characterization of Large Velocity Pulses for Laboratory Testing.* Kenneth E. Cox and Scott A. Ashford. April 2002.

PEER 2002/21 *Fourth U.S.-Japan Workshop on Performance-Based Earthquake Engineering Methodology for Reinforced Concrete Building Structures.* December 2002.

PEER 2002/20 *Barriers to Adoption and Implementation of PBEE Innovations.* Peter J. May. August 2002.

PEER 2002/19 *Economic-Engineered Integrated Models for Earthquakes: Socioeconomic Impacts.* Peter Gordon, James E. Moore II, and Harry W. Richardson. July 2002.

PEER 2002/18 *Assessment of Reinforced Concrete Building Exterior Joints with Substandard Details.* Chris P. Pantelides, Jon Hansen, Justin Nadauld, and Lawrence D. Reaveley. May 2002.

PEER 2002/17 *Structural Characterization and Seismic Response Analysis of a Highway Overcrossing Equipped with Elastomeric Bearings and Fluid Dampers: A Case Study.* Nicos Makris and Jian Zhang. November 2002.

PEER 2002/16 *Estimation of Uncertainty in Geotechnical Properties for Performance-Based Earthquake Engineering.* Allen L. Jones, Steven L. Kramer, and Pedro Arduino. December 2002.

PEER 2002/15 *Seismic Behavior of Bridge Columns Subjected to Various Loading Patterns.* Asadollah Esmaeily-Gh. and Yan Xiao. December 2002.

PEER 2002/14 *Inelastic Seismic Response of Extended Pile Shaft Supported Bridge Structures.* T.C. Hutchinson, R.W. Boulanger, Y.H. Chai, and I.M. Idriss. December 2002.

PEER 2002/13 *Probabilistic Models and Fragility Estimates for Bridge Components and Systems.* Paolo Gardoni, Armen Der Kiureghian, and Khalid M. Mosalam. June 2002.

PEER 2002/12 *Effects of Fault Dip and Slip Rake on Near-Source Ground Motions: Why Chi-Chi Was a Relatively Mild M7.6 Earthquake.* Brad T. Aagaard, John F. Hall, and Thomas H. Heaton. December 2002.

PEER 2002/11 *Analytical and Experimental Study of Fiber-Reinforced Strip Isolators*. James M. Kelly and Shakhzod M. Takhirov. September 2002.

PEER 2002/10 *Centrifuge Modeling of Settlement and Lateral Spreading with Comparisons to Numerical Analyses***.** Sivapalan Gajan and Bruce L. Kutter. January 2003.

PEER 2002/09 *Documentation and Analysis of Field Case Histories of Seismic Compression during the 1994 Northridge, California, Earthquake.* Jonathan P. Stewart, Patrick M. Smith, Daniel H. Whang, and Jonathan D. Bray. October 2002.

PEER 2002/08 *Component Testing, Stability Analysis and Characterization of Buckling-Restrained Unbonded Braces™.* Cameron Black, Nicos Makris, and Ian Aiken. September 2002.

PEER 2002/07 *Seismic Performance of Pile-Wharf Connections.* Charles W. Roeder, Robert Graff, Jennifer Soderstrom, and Jun Han Yoo. December 2001.

PEER 2002/06 *The Use of Benefit-Cost Analysis for Evaluation of Performance-Based Earthquake Engineering Decisions*. Richard O. Zerbe and Anthony Falit-Baiamonte. September 2001.

PEER 2002/05 *Guidelines, Specifications, and Seismic Performance Characterization of Nonstructural Building Components and Equipment*. André Filiatrault, Constantin Christopoulos, and Christopher Stearns. September 2001.

PEER 2002/04 *Consortium of Organizations for Strong-Motion Observation Systems and the Pacific Earthquake Engineering Research Center Lifelines Program: Invited Workshop on Archiving and Web Dissemination of Geotechnical Data, 4–5 October 2001*. September 2002.

PEER 2002/03 *Investigation of Sensitivity of Building Loss Estimates to Major Uncertain Variables for the Van Nuys Testbed.* Keith A. Porter, James L. Beck, and Rustem V. Shaikhutdinov. August 2002.

PEER 2002/02 *The Third U.S.-Japan Workshop on Performance-Based Earthquake Engineering Methodology for Reinforced Concrete Building Structures*. July 2002.

PEER 2002/01 *Nonstructural Loss Estimation: The UC Berkeley Case Study.* Mary C. Comerio and John C. Stallmeyer. December 2001.

PEER 2001/16 *Statistics of SDF-System Estimate of Roof Displacement for Pushover Analysis of Buildings.* Anil K. Chopra, Rakesh K. Goel, and Chatpan Chintanapakdee. December 2001.

PEER 2001/15 *Damage to Bridges during the 2001 Nisqually Earthquake.* R. Tyler Ranf, Marc O. Eberhard, and Michael P. Berry. November 2001.

PEER 2001/14 *Rocking Response of Equipment Anchored to a Base Foundation.* Nicos Makris and Cameron J. Black. September 2001.

PEER 2001/13 *Modeling Soil Liquefaction Hazards for Performance-Based Earthquake Engineering.* Steven L. Kramer and Ahmed-W. Elgamal. February 2001.

PEER 2001/12 *Development of Geotechnical Capabilities in OpenSees*. Boris Jeremi . September 2001.

PEER 2001/11 *Analytical and Experimental Study of Fiber-Reinforced Elastomeric Isolators*. James M. Kelly and Shakhzod M. Takhirov. September 2001.

PEER 2001/10 *Amplification Factors for Spectral Acceleration in Active Regions.* Jonathan P. Stewart, Andrew H. Liu, Yoojoong Choi, and Mehmet B. Baturay. December 2001.

PEER 2001/09 *Ground Motion Evaluation Procedures for Performance-Based Design.* Jonathan P. Stewart, Shyh-Jeng Chiou, Jonathan D. Bray, Robert W. Graves, Paul G. Somerville, and Norman A. Abrahamson. September 2001.

PEER 2001/08 *Experimental and Computational Evaluation of Reinforced Concrete Bridge Beam-Column Connections for Seismic Performance*. Clay J. Naito, Jack P. Moehle, and Khalid M. Mosalam. November 2001.

PEER 2001/07 *The Rocking Spectrum and the Shortcomings of Design Guidelines.* Nicos Makris and Dimitrios Konstantinidis. August 2001.

PEER 2001/06 *Development of an Electrical Substation Equipment Performance Database for Evaluation of Equipment Fragilities*. Thalia Agnanos. April 1999.

PEER 2001/05 *Stiffness Analysis of Fiber-Reinforced Elastomeric Isolators.* Hsiang-Chuan Tsai and James M. Kelly. May 2001.

PEER 2001/04 *Organizational and Societal Considerations for Performance-Based Earthquake Engineering.* Peter J. May. April 2001.

PEER 2001/03 *A Modal Pushover Analysis Procedure to Estimate Seismic Demands for Buildings: Theory and Preliminary Evaluation.* Anil K. Chopra and Rakesh K. Goel. January 2001.

PEER 2001/02 *Seismic Response Analysis of Highway Overcrossings Including Soil-Structure Interaction.* Jian Zhang and Nicos Makris. March 2001.

PEER 2001/01 *Experimental Study of Large Seismic Steel Beam-to-Column Connections.* Egor P. Popov and Shakhzod M. Takhirov. November 2000.

PEER 2000/10 *The Second U.S.-Japan Workshop on Performance-Based Earthquake Engineering Methodology for Reinforced Concrete Building Structures.* March 2000.

PEER 2000/09 *Structural Engineering Reconnaissance of the August 17, 1999 Earthquake: Kocaeli (Izmit), Turkey.* Halil Sezen, Kenneth J. Elwood, Andrew S. Whittaker, Khalid Mosalam, John J. Wallace, and John F. Stanton. December 2000.

PEER 2000/08 *Behavior of Reinforced Concrete Bridge Columns Having Varying Aspect Ratios and Varying Lengths of Confinement.* Anthony J. Calderone, Dawn E. Lehman, and Jack P. Moehle. January 2001.

PEER 2000/07 *Cover-Plate and Flange-Plate Reinforced Steel Moment-Resisting Connections.* Taejin Kim, Andrew S. Whittaker, Amir S. Gilani, Vitelmo V. Bertero, and Shakhzod M. Takhirov. September 2000.

PEER 2000/06 *Seismic Evaluation and Analysis of 230-kV Disconnect Switches.* Amir S. J. Gilani, Andrew S. Whittaker, Gregory L. Fenves, Chun-Hao Chen, Henry Ho, and Eric Fujisaki. July 2000.

PEER 2000/05 *Performance-Based Evaluation of Exterior Reinforced Concrete Building Joints for Seismic Excitation.* Chandra Clyde, Chris P. Pantelides, and Lawrence D. Reaveley. July 2000.

PEER 2000/04 *An Evaluation of Seismic Energy Demand: An Attenuation Approach.* Chung-Che Chou and Chia-Ming Uang. July 1999.

PEER 2000/03 *Framing Earthquake Retrofitting Decisions: The Case of Hillside Homes in Los Angeles.* Detlof von Winterfeldt, Nels Roselund, and Alicia Kitsuse. March 2000.

PEER 2000/02 *U.S.-Japan Workshop on the Effects of Near-Field Earthquake Shaking.* Andrew Whittaker, ed. July 2000.

PEER 2000/01 *Further Studies on Seismic Interaction in Interconnected Electrical Substation Equipment.* Armen Der Kiureghian, Kee-Jeung Hong, and Jerome L. Sackman. November 1999.

PEER 1999/14 *Seismic Evaluation and Retrofit of 230-kV Porcelain Transformer Bushings*. Amir S. Gilani, Andrew S. Whittaker, Gregory L. Fenves, and Eric Fujisaki. December 1999.

PEER 1999/13 *Building Vulnerability Studies: Modeling and Evaluation of Tilt-up and Steel Reinforced Concrete Buildings.* John W. Wallace, Jonathan P. Stewart, and Andrew S. Whittaker, editors. December 1999.

PEER 1999/12 *Rehabilitation of Nonductile RC Frame Building Using Encasement Plates and Energy-Dissipating Devices.* Mehrdad Sasani, Vitelmo V. Bertero, James C. Anderson. December 1999.

PEER 1999/11 *Performance Evaluation Database for Concrete Bridge Components and Systems under Simulated Seismic Loads.* Yael D. Hose and Frieder Seible. November 1999.

PEER 1999/10 *U.S.-Japan Workshop on Performance-Based Earthquake Engineering Methodology for Reinforced Concrete Building Structures.* December 1999.

PEER 1999/09 *Performance Improvement of Long Period Building Structures Subjected to Severe Pulse-Type Ground Motions*. James C. Anderson, Vitelmo V. Bertero, and Raul Bertero. October 1999.

PEER 1999/08 *Envelopes for Seismic Response Vectors.* Charles Menun and Armen Der Kiureghian. July 1999.

PEER 1999/07 *Documentation of Strengths and Weaknesses of Current Computer Analysis Methods for Seismic Performance of Reinforced Concrete Members.* William F. Cofer. November 1999.

PEER 1999/06 *Rocking Response and Overturning of Anchored Equipment under Seismic Excitations.* Nicos Makris and Jian Zhang. November 1999.

PEER 1999/05 *Seismic Evaluation of 550 kV Porcelain Transformer Bushings.* Amir S. Gilani, Andrew S. Whittaker, Gregory L. Fenves, and Eric Fujisaki. October 1999.

PEER 1999/04 *Adoption and Enforcement of Earthquake Risk-Reduction Measures.* Peter J. May, Raymond J. Burby, T. Jens Feeley, and Robert Wood.

PEER 1999/03 *Task 3 Characterization of Site Response General Site Categories.* Adrian Rodriguez-Marek, Jonathan D. Bray, and Norman Abrahamson. February 1999.

PEER 1999/02 *Capacity-Demand-Diagram Methods for Estimating Seismic Deformation of Inelastic Structures: SDF Systems.* Anil K. Chopra and Rakesh Goel. April 1999.

PEER 1999/01 *Interaction in Interconnected Electrical Substation Equipment Subjected to Earthquake Ground Motions.* Armen Der Kiureghian, Jerome L. Sackman, and Kee-Jeung Hong. February 1999.

PEER 1998/08 *Behavior and Failure Analysis of a Multiple-Frame Highway Bridge in the 1994 Northridge Earthquake.* Gregory L. Fenves and Michael Ellery. December 1998.

PEER 1998/07 *Empirical Evaluation of Inertial Soil-Structure Interaction Effects.* Jonathan P. Stewart, Raymond B. Seed, and Gregory L. Fenves. November 1998.

PEER 1998/06 *Effect of Damping Mechanisms on the Response of Seismic Isolated Structures.* Nicos Makris and Shih-Po Chang. November 1998.

PEER 1998/05 *Rocking Response and Overturning of Equipment under Horizontal Pulse-Type Motions.* Nicos Makris and Yiannis Roussos. October 1998.

PEER 1998/04 *Pacific Earthquake Engineering Research Invitational Workshop Proceedings, May 14–15, 1998: Defining the Links between Planning, Policy Analysis, Economics and Earthquake Engineering.* Mary Comerio and Peter Gordon. September 1998.

PEER 1998/03 *Repair/Upgrade Procedures for Welded Beam to Column Connections.* James C. Anderson and Xiaojing Duan. May 1998.

PEER 1998/02 *Seismic Evaluation of 196 kV Porcelain Transformer Bushings.* Amir S. Gilani, Juan W. Chavez, Gregory L. Fenves, and Andrew S. Whittaker. May 1998.

PEER 1998/01 *Seismic Performance of Well-Confined Concrete Bridge Columns.* Dawn E. Lehman and Jack P. Moehle. December 2000.

ONLINE REPORTS

The following PEER reports are available by Internet only at http://peer.berkeley.edu/publications/peer_reports.html

PEER 2007/101 *Generalized Hybrid Simulation Framework for Structural Systems Subjected to Seismic Loading.* Tarek Elkhoraibi and Khalid M. Mosalam. July 2007.

PEER 2007/100 *Seismic Evaluation of Reinforced Concrete Buildings Including Effects of Masonry Infill Walls.* Alidad Hashemi and Khalid M. Mosalam. July 2007.